The Numerical Simulation
of Nonlinear Waves
in a Hydrodynamic Model Test Basin

University of Twente

Jaap-Harm Westhuis

THE NUMERICAL SIMULATION OF NONLINEAR WAVES IN A HYDRODYNAMIC MODEL TEST BASIN

Jaap-Harm Westhuis

Figure cover: photograph of the Seakeeping and Manoeuvering Basin at MARIN (Wageningen, The Netherlands) merged with a graph of measured (solid line) and simulated (dots) wave elevation using the algorithm of this thesis.

This thesis was typeset using $\LaTeX\,2_\varepsilon$.

THE NUMERICAL SIMULATION OF NONLINEAR WAVES IN A HYDRODYNAMIC MODEL TEST BASIN

PROEFSCHRIFT

ter verkrijging van
de graad van doctor aan de Universiteit Twente,
op gezag van de rector magnificus,
prof.dr. F.A. van Vught,
volgens besluit van het College voor Promoties
in het openbaar te verdedigen
op vrijdag 11 mei 2001 te 16:45 uur

door

Jaap-Harm Westhuis

geboren op 23 augustus 1973
te Amsterdam.

DIT PROEFSCHRIFT IS GOEDGEKEURD DOOR DE PROMOTOR

PROF.DR.IR. E.W.C. VAN GROESEN
(FACULTEIT DER TOEGEPASTE WISKUNDE)

'*Men hoeft niet te slagen om te volharden,*
noch te hopen om te ondernemen.'

Willem van Oranje

Abstract

This thesis describes the development of a numerical algorithm for the fully nonlinear simulation of free-surface waves. The aim of the research is to develop, implement and investigate an algorithm for the deterministic and accurate simulation of two-dimensional nonlinear water waves in a model test basin. The simulated wave field may have a broad-banded spectrum and the simulations should be carried out by an efficient algorithm in order to be applicable in practical situations. The algorithm is based on a combination of Runge-Kutta (for time integration), Finite Element (boundary value problem) and Finite Difference (velocity recovery) methods. The scheme is further refined and investigated using different models for wave generation, propagation and absorption of waves.

The accuracy and stability of the numerical scheme are investigated and the numerical dispersion error is determined for several discretisation parameters. It was found that stable, second order accurate discretisations can be obtained using first order Finite Elements and second order Finite Differences. The results also showed that a global projection method, using Finite Elements for velocity recovery, results in unstable discretisations. By a suitable choice of the grid density parameter the dispersion error of a small amplitude regular numerical wave can be annihilated by cancellation of errors. A physically relevant error measure for broad banded wave simulations is introduced and mass and energy conservation show to be sufficiently small for accurate simulations.

Wave generation methods based on models of physical wave makers and methods for numerical wave generation are described and evaluated. The discrete wave board transfer functions for flap- and piston-type wave generators are determined and it is concluded that the numerical wave generator produces slightly higher waves than expected from continuous analysis. It was also found that application of the algorithm to wave simulation may result in unstable discretisations for specific geometries in combination with certain numerical grids.

Measurements that were performed on the reflection properties of beaches in the model basin are compared to a numerical wave absorption method. The introduced absorption method consists of combined pressure damping, horizontal grid stretching and application of a Sommerfeld condition. Strict energy decay is guaranteed and the combination allows for effective absorption for a broad range of frequencies. Reflection

coefficients smaller than 0.7 % can be achieved at relative low computational cost. It is also shown that by suitable choice of parameters the combined absorption method can reasonably approximate the measured reflections on artificial beaches in the basin.

The algorithm was further applied to several benchmark tests confirming the validity of the results. Also the direct comparison with measurements showed satisfactory agreement.

The numerical scheme was used to investigate the long time evolution of nonlinear wave groups. The efficiency and accuracy of the algorithm allowed to explore the dynamics of these waves on an unprecedented time and spatial scale. This has led to detailed information and new insights in the long time evolution of bichromatic wave groups and served as a basis for further experimental and analytical investigations.

A study on the propagation of a confined wave group over a bottom topography, the disintegration of a confined wave train and an elaborate study involving numerous measurements and simulations on the evolution of bichromatic wave groups are presented. The disintegration of a wave train in groups has been observed, but the complete splitting into clearly separated groups cannot be rigorously confirmed by the numerical results. Investigation of the evolution of a confined (NLS-soliton) wave group over a bottom topography showed the defocussing of the group and the generation of a large free solitary wave. The long time evolution of bichromatic waves showed spatial periodic variations of the wave spectrum, indicating recurrence. An appropriate scaling was experimentally constructed that relates the ratio of amplitude and original frequency difference ($\Delta\omega/q$) to the observed spatial recurrence periods. Examination of the envelope evolution of the bichromatic waves show the splitting of the original envelope in two distinguishable envelopes. These distinguished groups are observed to interact in at least two qualitatively different ways, both showing envelope recurrence.

Preface

Since the spring of 1997 I have enjoyed the freedom of doing research in the topic of my choice. This opportunity was given to me by the combined effort of my promotor professor Brenny van Groesen (University of Twente) and René Huijsmans, senior researcher at the Maritime Research Institute Netherlands (MARIN). I greatly appreciate their efforts and support, and their flexibility to grant me the freedom in doing some unrelated research. The PhD position was financed by the KNAW (Royal Netherlands Academy of Arts and Sciences) under grant number 95-BTM-29 (LabMath) and the additional financial support from MARIN is acknowledged.

During this project I was stationed at MARIN, Wageningen. There I have enjoyed the company of many (PhD-)students from different nationalities, many who I still frequently encounter. I would like to thank all of them for their pleasant company and cheerful moments. The last years bear the most fresh memories and during this time I have had the pleasure of having three distinctly different personalities as room mates. I would like to thank Albert Ballast, Anne Boorsma and Jie Dang for the fine discussions, meals and 'sporting events' that made up a significant part of our workday.

A special word of thanks is addressed to Andonowati, Agus Suryanto, Helena Margeretha, Edi Chayono and Robert Otto who have actively participated in the research program LabMath and whose contributions and discussions provided valuable material for my research. Although most of my time was spent at MARIN, I frequently visited the Department of Mathematics at the University of Twente. I have enjoyed the conversations with Wilbert, Timco, Barbera, Stephan and Frits and wish to express my special thanks to the help and support from the secretaries: Marielle, Miranda and Carole.

The last years, working hours have taken up a large part of the week. The remaining time that I spent with friends and family have given me great pleasure and knowledge that cannot be found in text books. I want to thank my two paranimfs, Rogier and Jasper, for their friendship and efforts, but most of all I want to thank Aster...

<div align="right">

Zeist, 13-02-2001
Jaap-Harm Westhuis

</div>

ix

Contents

Notations

In the table below, the notations used throughout this thesis are listed in alphabetic order of their first symbol (first the notations starting with a Roman symbol then the notations starting with a Greek symbol). Besides a short description of the notation, the section where the notation is introduced is given for further reference.

Notations starting with a Roman symbol

a	amplitude of a regular wave [section 3.1]
$\bar{a}$	stroke amplitude of a wave board to generate a linear regular wave with amplitude a [subsection 4.1.1]
a_w	half breadth of the wedge wave maker [section 4.2]
$a(\cdot,\cdot)$	bilinear form [subsection 2.2.4 and appendix A]
A	amplitude of the wave envelope [subsection 3.1.2 and section 6.2]
$\mathbf{A}$	Matrix resulting from linearisation of the discretised equations [subsection 3.2.2, subsection 4.1.4 and subsection 5.4.2]
$b(\cdot,\cdot)$	bilinear form [subsection 2.2.4 and appendix A]
$\mathbf{b}$	matrix resulting from the linearisation of the discretisation of the driving terms [subsection 4.1.4]
c	phase velocity of a regular wave [section 3.1]
c_g	group velocity of a linear wave group [section 3.1]
c_s	velocity parameter in the Sommerfeld condition [subsection 5.3.1]
$c.c.$	complex conjugated of the previous expression
C_j	coefficient of an evanescent mode [subsection 4.1.1]
d	parameter describing the geometry of a flap-piston wave maker [subsection 4.1.1]
d_w	depth of the wedge wave maker [section 4.2]
$\mathcal{D}$	index set containing the node numbers associated with grid points on the free surface [subsection 2.2.4]
e	measurement error in reflection coefficient [subsection 5.2.1]
E	discrete energy [section 3.4]

$f(\cdot)$	function defining the Dirichlet data on Γ_D [section 2.2.4 and appendix A]
$\tilde{f}$	vector function containing the dynamic equations as $\mathbf{q}_t = \tilde{f}(\mathbf{q}, t)$ [subsection 2.2.2]
$\vec{F}$	a force [subsection 2.1.1]
g	gravitational constant [subsection 2.1.1]
$g(\cdot)$	function defining the Neumann data on Γ_N [subsection 2.2.4 and appendix A]
$\hat{g}$	vector containing the coefficients of the approximation of $g(\cdot)$ [subsection 4.1.4].
h	the water depth
h_{grid}	grid refinement parameter [subsection 3.2.3]
H	wave height (crest to through distance) [subsection 3.1.2]
$H^1(\Omega)$	function space [subsection 2.2.4 and appendix A]
$H^{\pm 1/2}(\Gamma)$	function space [subsection 2.2.4 and appendix A]
$\mathcal{I}$	index set containing the node numbers in $\mathcal{V}$ that do not belong to $\mathcal{D}$ or $\mathcal{S}$ [subsection 2.2.4]
k	wavenumber of regular wave $k = 2\pi/\lambda$ [subsection 3.1.1]
$\tilde{k}$	complex wavenumber of a linearly damped regular wave [subsection 5.4.1]
$\bar{k}$	averaged wavenumber in bichromatic wave [section 6.3]
l	parameter describing the geometry of a flap-piston wave maker [subsection 4.1.1]
L	total length of computational domain
L_B	length of beach without horizontal stretching of the grid [subsection 5.3.3]
L_{eff}	length of beach with horizontal stretching of the grid [subsection 5.3.3]
M	discrete mass [section 3.4]
$\vec{n}$	vector normal to a surface (pointing outward) [subsection 2.1.2]
nx	number of nodes in horizontal direction [subsection 3.2.1]
nz	number of nodes in vertical direction [subsection 3.2.1]
N_i	Finite Element base function associated with global node number i [subsection 2.2.4]
$\mathcal{N}$	index set containing the node numbers associated with grid points on Γ^N [subsection 4.1.4]
p	(fluid) pressure [subsection 2.1.1]
$p[FEM]$	polynomial order of the base functions used in the finite element approximation for Φ [subsection 3.2.2]
$p[FD]$	polynomial order on which the finite difference scheme to approximate Φ_z is based [subsection 3.2.2]

q	amplitude of a single wave component in a regular wave
$\bar{q}$	flap stroke amplitude resulting in a wave amplitude q [subsection 6.3.1]
$\mathbf{q}$	vector containing the discrete variables involved in time integration [subsection 2.2.2 and subsection 3.2.2]
r	reflection coefficient [subsection 5.2.1]
R	dispersion operator [subsection 5.4.1]
$\vec{s}$	vector tangential to a surface [subsection 2.2.5]
$\mathcal{S}$	index set containing the node numbers associated with grid points on the Sommerfeld boundary [subsection 5.4.2]
$\mathcal{S}'$	surface tension [subsection 2.1.2]
$\mathcal{S}'_0$	linearised surface tension [subsection 3.1.1]
t	time [subsection 2.1.1]
T	wave period ($T = \frac{2\pi}{\omega}$) [subsection 3.1.1]
T_{mod}	modulation period (period of a wave group) [subsection 6.3.1]
u	horizontal velocity [subsection 3.1.2]
$\vec{v}$	fluid velocity vector [subsection 2.1.1]
$\mathcal{V}$	index set containing all node numbers [subsection 3.2.2]
x	horizontal coordinate [subsection 2.1.1]
z	vertical coordinate [subsection 2.1.1]

Notations starting with a Greek symbol

$\alpha(x)$	coefficient of the pressure damping term $\alpha(x)\Phi_z$ [subsection 5.3.2]
α_i	polynomial coefficients of $\alpha(x) = \alpha_0 + \alpha_1 x + \alpha_2 x^2$ [subsection 5.3.2]
β	parameter governing the vertical grid density [subsection 3.2.1]
β'	coefficient in front of the linear term $A_{\xi\xi}$ in the Non Linear Schrödinger equation [subsection 3.1.2 and section 6.2]
γ	parameter governing the horizontal grid stretching in the dissipation zone [subsection 5.3.3]
γ'	coefficient in front of the nonlinear term $|A|^2 A$ in the Non Linear Schrödinger equation [subsection 3.1.2 and section 6.2]
γ_s	surface tension coefficient [subsection 2.1.2]
Γ	boundary of the domain Ω [subsection 2.2.4 and appendix A]
Γ^D	part of Γ on which Dirichlet data is specified [subsection 2.2.4 and appendix A]
Γ^N	part of Γ on which Neumann data is specified [subsection 2.2.4 and appendix A]
δ	small perturbation parameter $(h/\lambda)^2$ [subsection 3.1.2]
δ'	relative frequency of modulation disturbance $\frac{\omega'-\omega}{\omega}$ [subsection 6.3.3]

Δk	wavenumber difference in bichromatic wave [section 6.3]
Δt	discrete time step [subsection 2.2.2]
Δx	horizontal mesh width [subsection 3.2.2]
Δz	vertical mesh width [section 3.2.1]
$\Delta\omega$	frequency difference in bichromatic wave [section 6.3]
ΔT	period difference in bichromatic wave [section 6.3]
ϵ	perturbation parameter a/h [section 3.1.2]
ε	perturbation parameter ka [section 6.2]
ξ	slow spatial variable in moving frame of reference $\xi = \varepsilon\,(x - c_g t)$ [subsection 3.1.2 and section 6.2]
η	function describing the free surface elevation [subsection 2.1.2]
$\hat{\eta}$	vector containing the z-coordinate of the boundary nodes on the free surface [subsection 3.2.2]
θ	phase function [subsection 3.1.2]
λ	wavelength ($\lambda = \frac{2\pi}{k}$) [subsection 3.1.1]
μ	eigenvalue of $\mathbf{A}$ [subsection 3.2.2]
$\tilde{\mu}$	zero'th order approximation of the dispersion operator R. $R\phi \approx \tilde{\mu} \cdot \phi$ [subsection 5.4.1]
μ'	dynamic viscosity [subsection 2.1.1]
ν	kinematic viscosity [subsection 2.1.1]
∇	gradient operator. $\nabla = (\partial_{x_1}, \ldots, \partial_{x_n})^T$, where n is dimension of the spatial domain X of the function $\vartheta\,(x \in X; t)$ on which ∇ operates.
ρ	fluid density [subsection 2.1.1]
σ	relative phase velocity error resulting from discretisation [subsection 3.3.1]
$\hat{\sigma}$	Parameter controlling the length of the tangential free surface grid correction vector [subsection 2.2.1]
$\sigma(a,b)$	maximum value of σ for $a \leq \lambda \leq b$. [subsection 3.3.2]
τ	slowly varying time $\tau = \varepsilon^2 t$ [section 6.2]
ϕ	linear free surface potential [subsection 5.3.2]
φ	vector containing the potential values at the discrete grid points. An additional superscript denotes a restriction of φ to the index set symbolised by the superscript.
Φ	velocity potential [subsection 3.2.2]
$\hat{\Phi}$	discrete approximation of Φ [subsection 2.2.4]
Ψ	acceleration potential $\Psi = \Phi_t$ [section 4.2]
ω	regular wave frequency [subsection 3.1.1]
$\bar{\omega}$	averaged frequency in bichromatic wave [section 6.3]
Ω	open domain in $\mathbb{R}^d$, $d = 2, 3$ [section 2.1].
$\hat{\Omega}$	discrete approximation of Ω. [subsection 2.2.4]
$\vec{\Omega}$	fluid vorticity $\vec{\Omega} = \nabla \times \vec{v}$ [subsection 2.1.1]

Chapter 1

Introduction

1.1   A hydrodynamic laboratory

A hydrodynamic laboratory is a complex of facilities in which maritime structures such as freight carriers, ferries and oil riggs are tested on a model scale. Before the actual construction, owners and designers need precise information about the hydrodynamic properties of their design. Questions as whether or not the contract velocity of the design will be achieved are answered by testing in a model test basin. Other important aspects such as safety, maneuverability and controllability can also be investigated at this stage.

A hydrodynamic laboratory usually has several facilities that are used for different testing purposes. When the hull resistance of a ship needs to be determined, a model is towed through still water. To obtain information about dynamic properties such as the stability and e.g. the maximum roll angles, model tests are performed in a seakeeping basin. In a seakeeping basin waves and possibly wind are generated while the ship is kept at a fixed position or sails through the tank. Although there are situations were the ship is towed by a carriage, most of the model tests are performed by self propulsion. These models have active rudders, stabilising fins or propellers that should allow for a steady course through the basin, while the carriage moves over the model and facilitates the measurements. These towing tanks are usually narrow basins and do therefore not allow for simultaneous manoeuverability testing. The new SMB (Seakeeping and Manoeuvering Basin) at MARIN (Maritime Research Institute Netherlands) has the unique capability to combine manoeuvering and seakeeping model tests (Fig. 1.1 on the following page). The construction of the SMB started in 1998 and was operational in mid 1999. It is a 170x40x5 $[m^3]$ water basin with 330 individually controlled wave maker segments on two sides and artificial beaches on the opposing sides. A giant carriage spanning the 40 meter width can follow a vessel sailing through the basin at a maximum speed of 6 [m/s].

Figure 1.1: *The new Seakeeping and Manoeuvering Basin (SMB) at MARIN, Wageningen. The individual controllable segments of the wave maker on the long side are clearly visible on the foreground.*

To evaluate the hydrodynamic properties of the ship the reaction of the vessel to a certain external force is measured. In seakeeping tests one is mainly interested in the ship motions and forces due to loads caused by waves.

In order to meaningfully test their ship, designers need to specify in what wave conditions the ship should be tested. A ferry operating solely in the North Sea between England and the Netherlands does not need to be tested for tropical hurricane waves. Every geographical area has its own wave characteristics, which are captured in a low dimensional model with the significant period (T_s) and the significant wave height (H_s) as the most important dimensions. At the basis for these low dimensional models is most of the time a 'linear' interpretation of reality. The waves are thought to consist of a summation of regular waves and the parameters governing the dynamics of ships are thought to have a linear dependence on the amplitude of the waves. Although for many situations this is an accurate and useful model of reality, it does not adequately describe extreme situations in which nonlinear interactions between waves significantly influence the wave field. Model testing under extreme conditions is however becoming more and more relevant for designers. Besides the generation of waves for regular testing in 'linear seas' it therefore becomes increasingly important to be able to generate extreme wave conditions at a prescribed position in the tank. To generate these conditions, accurate wave generation hardware and steering algorithms are essential. The new facilities of MARIN are equipped with sufficiently accurate hardware. Every segment of the wave maker is controlled by an individual electric motor allowing for precise control of the wave board position.

In 1997 the Mathematical Physics group of the department of Mathematics at the
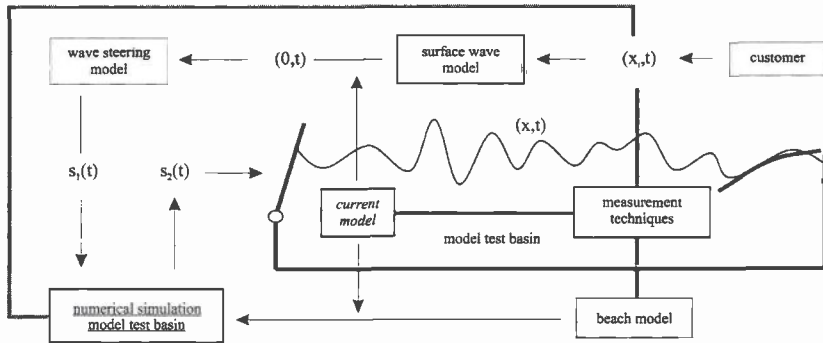
Figure 1.2: *Relation between the different components of the LabMath project.*

University of Twente together with MARIN and the Indonesian Hydrodynamic Laboratory (IHL) started the LabMath program. The aim of this program was to develop applicable mathematics for the better controllability of the wave and current generation at hydrodynamic laboratories. The program consisted of four projects: (i) the development of nonlinear surface wave models, (ii) experimental wave measurement techniques, (iii) modelling and simulation of wave-current interaction and (iv) fully nonlinear numerical simulation of waves in a basin.

The relation between these projects is schematically depicted in Fig. 1.2. Assume that a specified spatial temporal wave pattern $\eta(x_i, t)$ in the basin is desired. By using a suitable (nonlinear) surface model, a steering signal for the wave makers is derived. Then, a fully numerical simulation is used to investigate whether or not the proposed steering signal will produce the desired wave characteristics. If not, the steering signal to the wave maker has to be adapted and the new signal can again be numerically evaluated. Finally the steering signal is sent to the wave makers in the physical basin and measurements must show whether or not the specified spatial-temporal pattern is indeed produced. If this process would have been performed by trial and error in the physical basin, valuable tank-time would have been consumed. The fully numerical simulation also allows for easy parameter variation studies and the wave data is available on a fine spatial-temporal resolution, not achievable by measurement techniques in the physical basin. This high resolution data can be used for the development and validation of simplified free-surface models. It is stressed however, that continuous cross validation with physical experiments is essential and that the validity limits of the models should always be carefully examined. The measurements that are performed in the model test basin are also used to provide information for the development of the mathematical models that describe the artificial beaches and the wave-current interaction.

The efforts of the LabMath project have been focused on two-dimensional (depth and longitudinal direction) flow in the model basin. Follow-up research projects to extend the results and numerical algorithms to a three-dimensional basin have been granted.

Preliminary results of the three-dimensional simulations, performed by the author, showed promising results and indicated that the algorithm can indeed be effectively used for 3d wave simulations. As part of the LabMath project Eddy Cayhono is working on nonlinear surface models (see e.g. van Groesen *et al.* (2001)) and Helena Margeretha researches mathematical models that describe wave current interaction (see e.g. Margeretha *et al.* (2001)). Some aspects of the measurement techniques have been treated in Westhuis (1997) and further research and development on these techniques was performed by MARIN.

This thesis reports on the development of the numerical algorithm for fully nonlinear simulation of waves in a two-dimensional model basin. In summary, the aim of this research project was to develop, implement and investigate an algorithm for the (i) deterministic and accurate simulation of (ii) two dimensional nonlinear waves (no breakers) (iii) synthesised from a broad banded spectrum (iv) in a hydrodynamic model test basin (v) by an efficient algorithm allowing simulations to be performed in overnight jobs.

We conclude this section by quoting prof. Bernard Molin who was the invited speaker for the 22nd George Weinblum Memorial Lecture (Molin (1999)): "As the oil industry moves into deeper waters, the need for cross-validation of results from numerical codes and model tests becomes more acute. In 1000 or 2000 m water depths, it is not possible to test a complete production system (FPSO + risers and moorings) at an appropriate scale, and a combined use of numerical software and model test results becomes necessary. This means that the wave systems produced in the numerics and in the tank must be perfectly known and controlled. If they cannot be made to be identical, then one should know how to manage the numerical and experimental tools to cope with their differences."

1.2   Numerical simulation of nonlinear waves

The numerical simulation of nonlinear waves follows from the mathematical model that is used to describe the wave dynamics. Based on the continuum hypothesis, the conservation of mass and momentum in an isothermal flow lead to the *Navier-Stokes equations* for the fluid velocity, pressure and density. These equations simplify to *Euler's equations* for the velocity if the fluid is considered inviscid. An additional assumption on the incompressibility and the irrotationality of the fluid allows for the introduction of a velocity potential that completely determines the velocity field (*potential flow model*). Under the conditions leading to the potential flow model, the equations that describe the evolution of the air-water interface can be expressed in terms of the potential and the shape of the interface itself. Further assumptions on the shape of this surface and the water depth lead to numerous *free-surface models*, in which all quantities are restricted to the free surface. As will be motivated in Section 2.1 the potential flow model provides an adequate description for the surface dynamics for nonlinear water waves. The assumptions leading to the more simple

surface models conflicts with the design criteria mentioned at the end of the previous section. It is however stressed that for specific situations, surface wave models can accurately describe (nonlinear) wave dynamics.

The numerical simulation of nonlinear water waves using the potential-flow assumption has been studied since the mid 1970's. Longuet-Higgins & Cokelet (1976) were the first to simulate an asymmetric overturning deep water wave. They used a conformal mapping approach with space periodic boundary conditions and an artificial pressure distribution to enforce the breaking. Since then, many researchers have taken up the topic of nonlinear wave simulation, often in combination with wave-body interaction. Extensive reviews on the topic of wave simulation are given by Yeung (1982) and Tsai & Yue (1996). More recently Kim *et al.* (december, 1999) reviewed the research on the development of Numerical Wave Tanks (NWT's). In a NWT, the emphasis is both on wave simulation and wave-body interaction and aims at the replacement (*not* simulation) of an experimental model basin (also called Experimental Wave Tank). Because of the availability of these extensive and recent reviews, no literature overview is presented here. References are given throughout this thesis when appropriate.

Most numerical methods for potential flow wave simulation are based on the mixed Eulerian-Lagrangian method (employed by Longuet-Higgins & Cokelet (1976)) to separate the elliptic Boundary Value Problems (BVP) from the dynamic equations at the free surface. The vast majority of available numerical schemes that simulate free-surface potential-flow, approximate the BVP using a Boundary Integral (BI) formulation. This formulation is then discretised using Boundary Elements (BE) (e.g. Dommermuth *et al.* (1988) [2d constant panel method], Romate (1989) [3d second-order panel method], Grilli *et al.* (1989) [2d higher order boundary elements] and Celebi *et al.* (1998) [3d desingularised BI]. Other methods to solve the BVP are Finite Difference [FD] and Finite Element [FE] methods to discretise the potential-flow field equations. In FD methods (e.g. Chan (1977) and DeSilva *et al.* (1996)) the geometry is usually mapped to a rectangular domain to efficiently implement the numerical scheme. This is not necessary for the FE methods, but although the FE method has been widely used in steady state (viscous) flow problems and linearised free surface problems (e.g. Washizu (1982)) it did not receive much attention in nonlinear potential flow problems until recently (e.g. Wu & Eatock Taylor (1994) [fixed walls] and Cai *et al.* (1998) [fixed walls and mapping to a rectangular domain]). The use of FE methods in viscous numerical free surface simulation was also recently reported by Braess & Wriggers (2000). Finally, the spectral method based on a Taylor expansion of the Dirichlet-Neumann operator developed by Graig & Sulem (1993) is mentioned as an alternative to the BE, FD and FE methods. For numerical studies involving wave breaking in potential flow we refer to Vinje & Brevig (1981), Dommermuth *et al.* (1988), Banner (1998) and Tulin & Waseda (1999) [experimental data and numerical simulations] and Guignard *et al.* (1999) [shoaling of solitary wave]. Many authors (e.g. Longuet-Higgins & Cokelet (1976) [BE], Dold (1992) [BE], Wu & Eatock Taylor (1994) [FE] and Robertson & Sherwin (1999) [FE]) report on the appearance of saw-tooth instabilities during numerical simulation. In order to simulate wave prop-

agation over sufficiently long time, additional smoothing of the intermediate results or regridding is used to avoid numerical instabilities.

The numerical algorithm and implementation presented in this thesis differs from the previously reported schemes in the combination of the following aspects:

- a direct (no mapping) field discretisation of the successive boundary value problems using a Finite Element method with a successive velocity recovery using Finite Differences.

- marginally stable linearised spatial discretisation due to the combination of Finite Elements and Finite Differences (no smoothing necessary).

- the inclusion in the numerical simulation of a model for artificial beaches that are used in the experimental wave tank.

- a focus on the simultaneous accurate simulation of nonlinear waves of different wavelength on a single numerical grid.

- a modular, object-oriented algorithm for the implementation of the geometry, allowing for the separated development, implementation and testing of e.g. wave makers and numerical beaches.

1.3   Contents and outline of the thesis

This section describes the main contents of the thesis and serves as an outline for quick reference to the appropriate (sub)sections. The results of the investigations have been ordered as follows. Chapter 2 describes the mathematical model and numerical algorithm, Chapter 3 investigates the numerical simulation of waves without the influence of artificial wave generation and/or absorption. These latter two topics are treated in Chapter 4 and Chapter 5 respectively. In Chapter 6 the numerical algorithm is used to investigate the long-time evolution of wave groups and the final Chapter 7 contains concluding remarks and recommendations for further research.

Many of the captions of the figures in this thesis contain a list of numerical parameters that were used to perform the presented simulation from which the presented results have been derived. Although this might distract the reader from the intention of the figure, this data is provided to enable the repeating of the numerical simulations by other researchers. An important aim of the presentation of the research has been to provide sufficient information for complete reconstruction of all presented results.

In the following subsections the content of Chapters 2-6 is summarised. The first paragraph of each section contains a brief abstract describing the structure of the chapter in relation to its section division. The next paragraphs in the subsection discuss the contents of the chapter in more detail and in relation to its subsection structure.
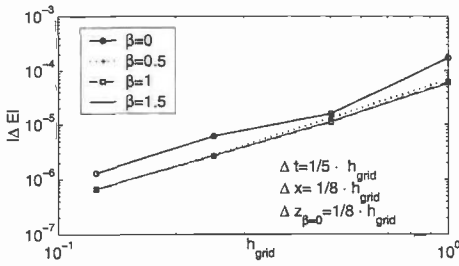
(a) Spatial-temporal grid refinement for linear Finite Elements and second order Finite Differences. The log-log graph shows that energy-norm error is proportional to h_{grid}^2.
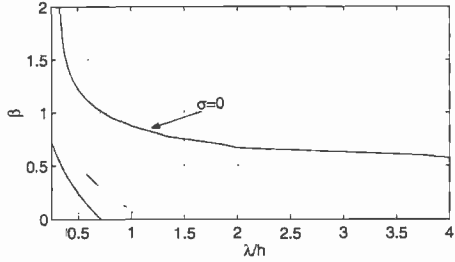
(b) The $\sigma = 0$ curve connects the values of the grid density parameter β for which the phase velocity of the numerical wave equals the exact linear phase velocity.

Figure 1.3: *Two figures from Chapter 3. (a) Grid refinement study in Subsection 3.2.3 on page 60. (b) analysis of discrete dispersion relation in Subsection 3.3.1 on page 63.*

Chapter 2 - Governing equations

The aim of this chapter is to introduce the equations that describe the free-surface dynamics [2.1], the numerical algorithms to approximate the solution of these equations [2.2] and the implementation of this algorithm in a compututational method [2.3].

In Section 2.1 the field equations describing potential flow are derived [2.1.1] and the assumptions leading to these equations are discussed. Next, the equations governing the free-surface dynamics are derived [2.1.2] resulting in the final set of governing equations. Section 2.2 starts by describing the numerical treatment of the free surface [2.2.1] and the resulting structure of the top-level time-marching scheme [2.2.2]. This time marching scheme consists of the repeated construction and solution of a boundary-value problem followed by a velocity recovery step. The use of field methods versus boundary-integral methods to solve the boundary value problems are compared [2.2.3] and based on this comparison the choice for the Finite Element Method is motivated and further discussed in detail [2.2.4]. For the velocity recovery methods [2.2.5] a global projection method and finite differences are discussed.

The chapter ends with some brief comments on the object-oriented structure of the implementation in Section 2.3 and the definition of the scope of the investigations in Section 2.4 for Chapters 3,4 and 5.

Chapter 3 - Free-surface waves

The focus of Chapter 3 is on the analysis of the numerical methods introduced in the previous chapter with respect to free surface waves in a basin with natural boundaries. After a brief introduction of some relevant equations for the description of (nonlinear) wave propagation [3.1] the accuracy and stability of the numerical scheme are investigated [3.2]. To further quantify the numerical errors and the effect of the discretisation parameters, the error of the discrete dispersion relation is established [3.3]. The stability and error analysis of the previous sections are mainly based on the linearisation of the discretised equations. In order to assess the accuracy of the fully nonlinear discretisation, the discrete mass and energy conservation is investigated [3.4]. The chapter ends with some applications [3.5] and the conclusions [3.6] of this chapter.

In Section 3.1 the linearised free-surface equations and the resulting dispersion relation for linear waves [3.1.1] are derived. Next, the deep water Stokes waves and the Boussinesq, KdV and NLS equations [3.1.2] are introduced for future reference. Section 3.2 starts with the introduction of the gridding [3.2.1] and the introduction of the vertical grid density parameter β. The effect of this parameter and other numerical parameters on the stability of the numerical scheme is then investigated [3.2.2]. First the spatial discretisation of the governing equations are linearised and a Von Neumann stability analysis is performed. The results show that scheme is marginally stable when Finite Differences are used as a velocity-recovery method. The use of a global projection method can however lead to unstable spatial discretisations and is therefore rejected as a suitable method. Next the stability of the discretisation of the time integration is investigated. The growth rates of eigenvectors due to 4-stage and 5-stage Runge-Kutta methods are determined and compared when applied to the linearised spatial discretisation. It is concluded that a 5-stage method is preferable over a 4-stage method. After these discussions on the stability of the linearised discretised equations, the convergence of the nonlinear discretisation is investigated by a systematic grid refinement study [3.2.3] showing that the numerical scheme is second-order accurate (see also Fig. 1.3 on the preceding page). Section 3.3 starts by introducing the relative dispersion error σ [3.3.1] and investigates the effect of the grid on this parameter. It is shown that for a specified wavelength this error can be made zero due to cancellations (see also Fig. 1.3 on the page before). To investigate the quality of the simulation of a broad banded wave spectrum, the maximum error $\sigma(a, b)$ over a range of wavelength on a single grid is introduced [3.3.2] and the effect of the numerical parameters is examined. Analysis of the computational complexity of first and second order FE implementations and extensive variations of the FD polynomial orders and other grid parameters result in a graph in which the minimal achievable $\sigma(1/4, 4)$ error as a function of the computational effort is given. The results show that by suitable choice of the nonuniform grid distribution and the FD polynomial order, a reduction in the $\sigma(1/4, 4)$ error by a factor 100 can be achieved given the same computational effort. This allows for accurate simulations over realistic time scales of a complete wave basin in overnight jobs.

To further investigate the quality of the nonlinear simulation, the effect of numerical parameter variations on the discrete mass and energy evolution is investigated in Section 3.4. It is concluded that the discrete mass and energy are very slowly decreasing functions of time and are positively influenced by choosing the nonuniform grid configurations. Section 3.5 of this chapter describes two applications of the numerical method. The first application discusses the results of a benchmark problem on the evolution of a nonlinear sloshing waves [3.5.1]. The second application concerns the simulation of the splitting of solitary waves over a bottom topography [3.5.2]. At the end of the chapter the conclusions of the investigations are summarised [3.6].

Chapter 4 - wave generation

Chapter 4 is concerned with the numerical simulation of wave generation. A distinction is made between wave generation methods based on models of physical wave makers (such as flap- and piston-type [4.1] and heaving wedge [4.2] wave makers) and methods based on numerical velocity generation models [4.3].

In Section 4.1 the numerical simulation of flap- and piston wave makers is discussed. Upon presenting a linear model describing both wave makers [4.1.1], the numerical modelling is discussed in more detail [4.1.2]. The gridding around the wave maker and the treatment of the free-surface grid points near the wave maker are examined. A grid convergence study is performed [4.1.3] to investigate the correct implementation of the numerical scheme. Similar to the linear analysis of Chapter 3, the discretisation of the wave generator is constructed [4.1.4] and the discrete Biésel transfer functions - relating the wave board stroke and the wave amplitude - are determined. Also, the wave envelope near the wave board, that is largely determined by evanescent modes, is determined from linear analysis and compared to continuous results (see also Fig. 1.4 on the following page). It is concluded that even for relative fine (with respect to the previous chapter) horizontal and vertical grid resolution, the discrete transfer function for high frequencies is overpredicted by the discretisation. For accurate simulations, the discrete transfer functions should therefore be used when wave board steering signals are synthesised from a target wave spectrum. Based on the linear analysis it is also shown that in the present formulation, the intersection grid point between the wave maker and free surface should be treated analogous to the free-surface grid points.

In Section 4.2 the results on a comparative study on a forced heaving wedge wave maker are presented. After some remarks on the computation of the force on the wetted wedge, a linear stability analysis [4.2.1] is performed on the discretisation. This study showed and erratic stability behavior that sensitively depends on the grid. The section on the wedge wave maker is concluded by presenting the results of the comparison [4.2.2] with other numerical methods. In general good mutual agreement was found between the results of fully nonlinear codes. Section 4.3 treats two practical numerical wave generation methods. First a combined flux-displacement wave maker
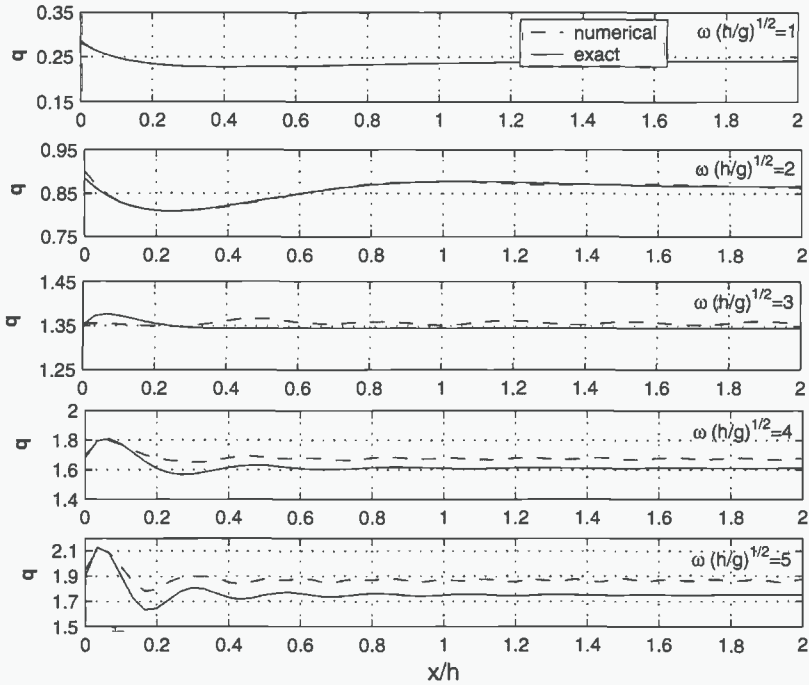
Figure 1.4: *Comparison between the exact and a numerical solution of the (linear) wave envelope near the wave maker. Accurate representation of the evanescent modes is necessary to simulate the effects of nonlinear interactions near the wave maker (from Subsection 4.1.4 on page 97)*

is introduced [4.3.1] in which the wave generation is partially governed by wave board displacement and partially by numerical flux generation. The second numerical wave generation method implements a combined generating potential with a Sommerfeld condition [4.3.2] to absorb reflected waves with the same frequency as the generated wave. It is shown by transient generation of a small standing wave that this is an adequate wave generator for small amplitude waves. This chapter on wave generation ends with the gathered conclusions [4.4] from the previous sections.

Chapter 5 - wave absorption

The main emphasis in Chapter 5 is on the numerical simulation of wave absorption. First the absorption of waves in a hydrodynamic basin [5.1] is examined. Then the measurements that were performed at the beaches of the new seakeeping and manoeuvering basin at MARIN [5.2] is presented. These measurements are later compared to results of numerical wave absorption methods [5.3] and the most promising methods are further analyzed [5.4]. The results of the simulations, analysis and measurements

are then compared and discussed [5.5].

In Section 5.1 a brief overview on passive [5.1.1] and active [5.1.2] wave absorbers in a physical basin is presented. Then, in Section 5.2, the measurements that were performed on the concepts for the artificial beaches of the new SMB are treated. First the method to determine the reflection coefficient (r.c.) [5.2.1] is described. This description includes the measurement setup and two different methods (envelope modulation and spectral decomposition) to extract the r.c.'s from the data. The results for two artificial beaches are presented [5.2.2] that show relative large unexplained scattering of the data probably caused by measurement and r.c. model assumptions.

The next Section 5.3 introduces several methods for numerical wave absorption. The Sommerfeld condition [5.3.1], the energy dissipation zone [5.3.2] based on pressure damping, the horizontal grid stretching and their combination are discussed in more detail. The combined absorption zone is expected to provide the most efficient and robust numerical wave absorption and it is shown that energy decay in this zone is guaranteed. The reflection coefficients of the combination are first determined by using a continuous approximation [5.4.1] of the linearised equations for constant, linear and parabolic damping functions. This continuous analysis is based on a plane wave assumption and uses an approximation $\tilde{\mu}$ for the dispersion operator R in the linear damping zone. Next, the reflection coefficients are determined from analysis of the linearised discretised equations [5.4.2]. The effect of the additional damping terms and Sommerfeld condition on the discrete spectrum is determined and it is shown that the envelope modulation method to determine the r.c.'s provides accurate results when used in combination with the linearised discretised equations. The intersection point between the free surface and the boundary on which the Sommerfeld condition is defined is investigated and it is shown that artificial eigenvectors appear in the discretisation. Based on the analysis of these additional vectors it is concluded that the implementation of the intersection point as a Sommerfeld condition is preferable over the treatment of this point as a free-surface particle. Following this discussion, the effect of the additional equations following from discretisation of the Sommerfeld condition on the stability of the time integration is investigated. It is shown that the Sommerfeld condition can impose a severe restriction on the time step and that the local horizontal mesh width Δx^0 near the Sommerfeld boundary should be significantly larger in order not to influence the stability of a simulation without a Sommerfeld condition. Discrete analysis of the polynomial damping functions showed characteristic difference in r.c.'s for constant and linear damping functions but similar results for linear and parabolic damping functions. The combined effect of damping, stretching and Sommerfeld condition showed that high-frequency waves can significantly reflect from the stretched grid, but that this can be compensated by a suitable choice of the damping coefficient. The stretching allows for large damping zones with relative few grid points thus providing an efficient method.

In Section 5.5 the resulting estimates for the r.c. based on the analysis in previous sections is discussed. Comparison of the continuous approximations and the converged numerical approximations [5.5.1] showed that for constant damping functions
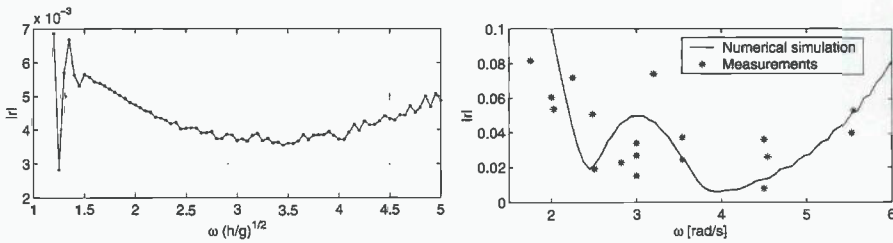
(a) Configuration to approximate a transparant beach. Reflection coefficients smaller than 0.7% are achieved over a wide range of frequencies at the cost of extending the computational domain with two times the depth.

(b) Configuration to approximate the measured reflection coefficients. The combination of the stretching, damping and Sommerfeld condition is used to tune the numerical reflection curve to the measurements.

Figure 1.5: *Reflection coefficients from the combined absorbing zone developed in Chapter 5. A distinction is made between a transparent numerical beach (Subsection 5.5.2 on page 159) and the simulation of the artificial beach in a model test basin (Subsection 5.5.3 on page 161).*

good mutual agreement is achieved for high-frequency waves but that the continuous model generally gives higher r.c. estimates than the discrete results. As it has been checked that the numerical results have converged, the difference can only be contributed to the plane wave assumption underlying the continuous analysis. For linear damping functions the agreement between the continuous and discrete results is poor. Although both methods show the same trends, the quantitative differences are large. It is shown that the result is quite sensitive to the dispersion operator approximation and it is thus concluded that this approximation in combination with the plane wave assumption leads to wrong predictions of the reflection coefficients. Based on the discrete investigations, a combination of parameters is selected that results in minimal reflection coefficients [5.5.2] over the significant range of wavelength at the computational cost of extending the domain with two times the depth (see also Fig. 1.5). Through extensive parameter variation studies, a combination was selected that reasonably fits the scattered reflection coefficients that were previously measured [5.5.3] (see also Fig. 1.5). The chapter ends with Section 5.6 in which the conclusions of this chapter are summarised.

Chapter 6 - wave groups

In Chapter 6 the developed numerical scheme, including wave generation and absorption is used to study the long time evolution of nonlinear wave groups. After an introduction and a literature review [6.1] the propagation of confined wave group [6.2]
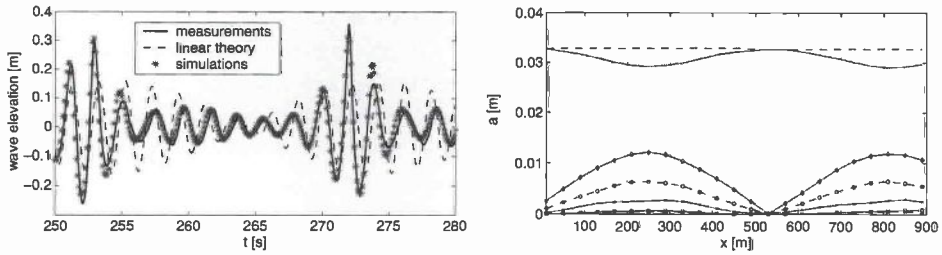
(a) Comparison of measurements (solid line), numerical simulations with the methods of this thesis (dots) and linear theory (dotted line).

(b) The nonlinear spatial evolution of the spectral components of a bichromatic wave (see Subsection 6.3.2 on page 184 and Fig. 6.15 on page 196).

Figure 1.6: *The evolution of nonlinear bichromatic wave groups.*

over an uneven bottom topography is studied. Next, a more extensive study involving numerous measurements and simulations on the evolution of bichromatic wave groups [6.3] is presented. The conclusion of these investigations are summarised at the end of this chapter [6.4].

In Section 6.1 the literature on the evolution of modulated wave trains [6.1.1] and bichromatic waves [6.1.2] is reviewed. Section 6.2 then starts with the motivation for the study of confined wave groups and introduces the coefficients governing the Nonlinear Schrödinger (NLS) equation. A numerical simulation of a disintegrating wave train shows the splitting in solitary wave groups but the anticipated separation is not observed on the investigated time scale. Next, the construction of an initial solution for the propagation of a confined solitary wave group [6.2.1] is investigated. The sub- and super harmonics that are freed when the first-order component of the NLS solitary wave group solution is imposed are identified. After these additional waves have propagated sufficiently far from the main group, this group is isolated and used for the investigation of the effect of depth variation [6.2.2]. The result of the increasing depth is the freeing of a bound long wave and the defocussing of the wave group which transforms in a wave train on shallow water.

Section 6.3 starts with some notations used for the investigation of the evolution of a periodically generated bichromatic wave group. First, a number of measurements [6.3.1] are presented that have been performed at the High Speed Basin at MARIN. These measurements clearly show the steepening of the waves at the front of the group of steep bichromatic waves. These measurements are then compared to the results of numerical simulations (that actually preceded the measurements) and excellent agreement [6.3.2] is observed (see also Fig. 1.6). To investigate the long time evolution, the dimensions of the numerical basin are then stretched far beyond the realm of a physical model basin. The spatial evolution of different energy modes

are identified (see also Fig. 1.6) and the results of the numerical simulations are presented in these low-dimensional representations of the wave group evolution. The non-stationary behavior of the bichromatic wave group evolution is investigated [6.3.3] in three different ways. First the spatial recurrence period of the different modes is identified and an appropriate scaling is found to unify the results. Next the relation with the Benjamin-Feir instability of nonlinear deep water wave trains is examined. Although some correspondence is found, the growth factors of the side bands cannot be completely explained by this theory. Finally the evolution of the wave envelope is investigated. The results of the fully nonlinear numerical simulation are compared to simulations using the NLS equation as an Initial Boundary Value Problem (IBVP). Opposed to the usual spatial periodic simulation of the NLS, the IBVP approach recovers the asymmetric evolution and when corrected with the nonlinear Stokes group velocity, good quantitative agreement is found. Investigation of the wave group envelope evolution from the fully nonlinear simulations, also showed two typically different long-time envelope behavior, (i) the splitting of the original wave in two groups in which one is periodically overtaken by the other and (ii) the splitting in two wave groups in which one periodically bounces between its neighbouring groups. All the results of these investigations on nonlinear wave group evolution are summarised in the final section [6.4] of the chapter.

Chapter 2

Mathematical Model and Numerical Algorithm

The simulation of waves in a hydrodynamic model test basin requires four stages of development. Firstly a mathematical model to describe the relevant physical process in the basin needs to be constructed, resulting in a set of governing equations with additional boundary and initial conditions. Next, these equations are either solved exactly or, when no exact solution is available, the solution of these equations is approximated using a numerical algorithm. After verifying the stability and consistency of the numerical algorithm, this algorithm needs to be implemented in a computer code and finally the applicability of the numerical algorithm and the validity of the results needs to be established. In this chapter the mathematical model and algorithm are described for the simulation of free-surface waves without addressing issues related to wave generation and absorption. These latter aspects and the numerical analysis involving stability and validation will be dealt with in the subsequent chapters.

2.1 Mathematical model

To describe and investigate the evolution of waves in a laboratory, a mathematical model is constructed. The mathematical model is based on the equations of fluid mechanics for which many classical textbooks, e.g. Lamb (1932) and Landau & Lifshitz (1987) are available. In this section the equations governing the dynamics of water with a free surface will be derived to introduce the notations and clarify the assumptions. The classical water-wave problem consists of solving the Euler equations in the presence of a free surface. The field equations will be derived in Subsection 2.1.1. The nonlinear evolution of waves is governed by the boundary conditions at the free surface which are introduced in Subsection 2.1.2.

2.1.1   Field equations

The starting principle for the derivation of the equations of fluid mechanics are the conservation of mass and momentum. The flow is assumed isothermal and therefore the conservation of energy is not considered. For a fixed control volume Ω mass conservation is expressed as

$$\frac{\partial}{\partial t} \int_{\Omega} \rho d\Omega + \int_{S} \rho \vec{v} \cdot \vec{n} dS = 0, \tag{2.1}$$

where $\rho(\vec{x}, t)$ is the fluid density, $\vec{v}(\vec{x}, t)$ the fluid velocity and $\vec{n}$ the outward normal. Applying Gauss' divergence theorem, the surface integrals can be transformed into volume integrals and allowing the contol volume to become infinitesimally small leads to the differential form

$$\frac{\partial \rho}{\partial t} + \nabla \cdot (\rho \vec{v}) = 0, \tag{2.2}$$

which for icompressible flow reduces to

$$\nabla \cdot \vec{v} = 0. \tag{2.3}$$

Newton's second law of motion states that the change in momentum equals the total force acting on the control volume,

$$\frac{\partial}{\partial t} \int_{\Omega} \rho \vec{v} d\Omega + \int_{S} \rho \vec{v} \vec{v} d\Omega = \int_{S} T \cdot \vec{n} dS + \int_{\Omega} \rho \vec{g} d\Omega, \tag{2.4}$$

where for Newtonian fluids and incompressible flow the stress tensor T (molecular rate of transport of momentum) is given as $T = -pI + 2\mu'D$ (p is the static pressure, I is the unit tensor, D is the rate of strain tensor and μ' is the dynamic viscosity). Only gravity is considered as a body force and is acting in negative z-direction, $\vec{g} = (0, 0, -g)^{T}$. Using Gauss' divergence theorem the integral form of the conservation equation can be expressed in differential form as

$$\frac{\partial \rho \vec{v}_i}{\partial t} + \nabla \cdot (\rho \vec{v}_i \vec{v}) = \nabla \cdot T_i + \rho \vec{g}_i. \tag{2.5}$$

For Newtonian fluids and incompressible flow this reduces to

$$\rho \frac{\partial \vec{v}_i}{\partial t} + \rho \nabla \cdot (\vec{v}_i \vec{v}) = -(\nabla p)_i + \mu' \nabla \cdot \nabla \vec{v}_i + \rho \vec{g}_i. \tag{2.6}$$

To motivate further simplification of Eq. (2.6) the vorticity $\vec{\Omega}$ is introduced as

$$\vec{\Omega} = \nabla \times \vec{v}. \tag{2.7}$$

A velocity field is called irrotational if $\vec{\Omega} = 0$. Taking the material derivative of $\vec{\Omega}$ and substitution of Eq. (2.6) results in the vorticity transport equation

$$\frac{d\vec{\Omega}}{dt} = \left(\vec{\Omega} \cdot \nabla \right) \vec{v} + \nu \nabla \cdot \nabla \vec{\Omega}. \tag{2.8}$$

In Eq. (2.8), $\nu = \frac{\mu'}{\rho}$ is the kinematic viscosity. From Eq. (2.8) one can observe that in the absence of viscosity (i.e. $\mu' = 0$) an initialy irrotational velocity field $((\nabla \times \vec{v})\,|_{t=0} = 0)$ will remain irrotational for all time. Both for numerical simulations as for experiments in the laboratory, the initial state of the velocity field is rest (and thus irrotational), and therefore the velocity field will remain irrotational if viscous effects are neglected completely and for all times.

In the presence of viscosity but with an initial irrotational velocity field, diffusion will mainly occur near the boundaries, because variations in the second derivative of the velocities will be largest there due to the no-slip boundary condition. However, the oscillatory nature of wave phenomena, ensures that the direction of the flow often changes, so most of the inward diffusion will be restricted to a thin boundary layer. The thickness of this Stokes boundary layer is of order $\mathcal{O}\left(\sqrt{\frac{\nu}{\omega}}\right)$ where ω is the frequency of the wave motion in [rad/s]. As the kinematic viscosity of water is of order 10^{-6} $[m^2/s]$ and the frequencies are typically of order 1, the boundary layer thickness is of order 10^{-3} [m]. Therefore the viscous effect are considered negligible small with respect to the wave lengths of interest ($\lambda > 1$ [m]). However, when large second order spatial derivatives of the velocity occur (e.g. near breaking situations or other violent fluid motion) or very long time scales are considered, the inward diffusion may become significant. For references and applications of the simulation of low Reynolds numbers free-surface flows, we refer to Tsai & Yue (1996).

For an irrotational vector field $\vec{v}$ a scalar potential function Φ exists such that

$$\vec{v} = \nabla\Phi. \tag{2.9}$$

Substitution of Eq. (2.9) in Eq. (2.3) leads to the Laplace equation for the potential Φ,

$$\nabla \cdot \nabla\Phi = 0. \tag{2.10}$$

In the next section the free surface will be introduced and the boundary conditions at the free surface are derived.

2.1.2   Free-surface boundary conditions

Assume that the open domain $\Omega \subset \mathbb{R}^d$ has a boundary Γ that marks the fluid-air interface. Free-surface flow is usually considered as a limiting case of a two-phase flow in which the dynamics of one phase (in this case air), is greatly simplified or ignored. In this case, the velocity field of the air is considered zero and a constant atmospheric pressure is assumed. This leads to two conditions at the free-surface interface: the kinematic and the dynamic condition.

When the continuity equation Eq. (2.3) is integrated over a control volume $\Omega(t)$ whose

boundary $S(t)$ moves in time we find

$$\int_{\Omega(t)} \nabla \cdot (\rho \vec{v}) d\Omega = 0 \qquad (2.11)$$

and using Leibniz rule one derives

$$-\int_S \rho \vec{v}_b \cdot \vec{n} dS + \int_S \rho \vec{v} \cdot \vec{n} dS = 0 \qquad (2.12)$$

where $\vec{v}_b$ represents the velocity with which the integration boundary moves. From Eq. (2.12) the following condition for the boundary velocity can be directly obtained

$$\int_S (\vec{v} - \vec{v}_b) \cdot \vec{n} dS = 0. \qquad (2.13)$$

This condition states that at the boundary the normal component of the fluid velocity has to be equal to the normal component of the free-surface velocity,

$$\vec{v} \cdot \vec{n} = \vec{v}_b \cdot \vec{n}. \qquad (2.14)$$

The boundary condition Eq. (2.14) is a kinematic relation and therefore the condition, when applied to the free surface, is usually referred to as the kinematic boundary condition.

The second boundary condition follows from the continuity of the normal stresses at the water-air interface and from contributions due to surface tension. If viscous effects are neglected (as is assumed) this results in a relation between the pressure of water and that of the air and the forces due to surface tension,

$$p_{\text{water}} - p_{\text{air}} = -S'. \qquad (2.15)$$

The force due to the surface tension is proportional to the mean curvature of the surface. If the surface is implicitly defined, this may be defined directly in terms of the two radii of curvature. When the surface is considered to be a function $\eta(\mathbf{x}, t)$ of the horizontal coordinates $\mathbf{x}$ [1] and time, the mean curvature can be expressed in terms of derivatives of η as

$$S' = \gamma_s \nabla \cdot \left(\frac{\nabla \eta}{\sqrt{1 + |\nabla \eta|^2}} \right). \qquad (2.16)$$

The factor γ_s is the surface tension and for water has a value of $7.3 \ 10^{-2}$ [N/m] (at T=293 [K]). It will be shown in Section 3.1.1 that the effect of surface tension can be neglected with respect to the scales of interest in the present study. When Eq. (2.15) is applied to the free surface, it is referred to as the dynamic boundary condition. We will proceed by expressing the kinematic and dynamic boundary conditions (2.14)-(2.15) in terms of the velocity potential Φ.

---

[1] Here we have used the notation $\vec{x} = (\mathbf{x}, z)$, to distinguish the horizontal coordinate $\mathbf{x}$ (one- or two-dimensional, depending on the dimension of $\vec{x}$) from the vertical coordinate z.

Substitution of the potential definition Eq. (2.9) in the momentum equation Eq. (2.6) and ignoring viscosity results in

$$\frac{\partial \nabla \Phi}{\partial t} + (\nabla \Phi \cdot \nabla) \nabla \Phi + \frac{1}{\rho} \nabla p - \vec{g} = 0 \tag{2.17}$$

which can be expressed as

$$\nabla \left(\frac{\partial \Phi}{\partial t} + \frac{1}{2} |\nabla \Phi|^2 + \frac{p}{\rho} + gz \right) = 0. \tag{2.18}$$

Integration of Eq. (2.18) results in the Bernoulli equation

$$\frac{\partial \Phi}{\partial t} + \frac{1}{2} |\nabla \Phi|^2 + \frac{p}{\rho} + gz = f(t) \tag{2.19}$$

from which the integration constant $f(t)$ can be eliminated by redefining Φ.

Denoting $\eta(\mathbf{x}, t)$ as the free-surface boundary between water and air, and substituting Eq. (2.15) in Eq. (2.19) the dynamic boundary condition at the free surface can be written as

$$\frac{\partial \Phi}{\partial t} + \frac{1}{2} |\nabla \Phi|^2 + \frac{p_{air} - \mathcal{S}'}{\rho} + g\eta = 0 \quad \text{on} \ \ z = \eta(\mathbf{x}, t). \tag{2.20}$$

The kinematic boundary condition Eq. (2.14) can also be formulated in terms of η and Φ as

$$\nabla \Phi \cdot [-\eta_x, -\eta_y, 1] = \eta_t(\mathbf{x}, t) \quad \text{on} \ \ z = \eta(\mathbf{x}, t) \tag{2.21}$$

which is usually expressed as

$$\eta_t = \Phi_z - \eta_x \Phi_x - \eta_y \Phi_y \quad \text{on} \ \ z = \eta(\mathbf{x}, t). \tag{2.22}$$

Assuming the fluid to be incompressible and inviscid with an irrotational velocity field and assuming the free-surface boundary between water and air to be a single-valued function of the horizontal coordinate and time, the following equations govern the motion of the free surface

$$\vec{v} = \nabla \Phi \tag{2.23a}$$

$$\nabla \cdot \nabla \Phi = 0 \quad \text{in} \ \Omega \tag{2.23b}$$

$$\nabla \Phi \cdot \vec{n} = V_n \quad \text{on} \ \Gamma \tag{2.23c}$$

$$\tag{2.23d}$$

$$\frac{\partial \Phi}{\partial t} + \frac{1}{2} |\nabla \Phi|^2 + \frac{p_{air} - \mathcal{S}'}{\rho} + g\eta = 0 \quad \text{on} \ \ z = \eta(\mathbf{x}, t) \tag{2.23e}$$

$$\eta_t = \Phi_z - \eta_x \Phi_x - \eta_y \Phi_y \quad \text{on} \ \ z = \eta(\mathbf{x}, t) \tag{2.23f}$$

For a treatment on the existence, uniqueness and regularity of a solution of the Laplace boundary-value problem on a domain with corners confer e.g. Kawohl (1980). When initial conditions for the potential and the free surface are added, equations (2.23a)-(2.23f) define a well-posed initial value boundary problem for η and Φ.

2.2   Numerical algorithm

In general no exact solution is available to equations (2.23a)-(2.23f). In these situations, discretisation methods can be used to find the solution of the free-surface equations. A discretisation method approximates the differential equations by a set of algebraic equations. The numerical solution belongs to a finite-dimensional (mathematical) space and usually provides results at discrete locations in time and/or space.

2.2.1   Free surface

For references to the simulation of nonlinear free-surface flow we refer to the review papers of Scardovelli & Zaleski (1999), Dias & Kharif (1999), Tsai & Yue (1996), Yeung (1982) and Schwartz & Fenton (1982). For an overview of numerical methods applied to a more general class of problems in fluid mechanics the book of Ferziger & Perić (1999) could be consulted. Kim *et al.* (1999) recently presented a review paper specifically related to the development of numerical wave tanks. In Scardovelli & Zaleski (1999) the methods to solve free-surface flow are categorised by the use of the grid employed to subdivide Ω in small elements as follows:

- Fixed grid methods: The fixed grid methods can be subdivided in two subcategories

    - Marker methods. Free-surface markers are used to define the interface surface in a fixed grid environment, see e.g. Unverdi & Tryggavson (1992)

    - Volume of Fluid (VOF) Methods. In these methods the free surface is the result of an evaluation of the fraction of fluid in a grid volume. The VOF algorithm solves the problem of updating the volume fraction given the fixed grid, the velocity field and the fractions at the previous time step. There are basically two methods for approximating the free-surface interface from these volume fractions. A simple line interface calculation (SLIC) and a piecewise linear interface construction method (PLIC). Both methods however construct discontinuous approximations of the free-surface interface. These kind of methods have been applied successfully to 'green water' and sloshing applications (see e.g. Fekken *et al.* (1999) and van Daalen *et al.* (1999)). For an extensive literature survey on VOF methods for free-surface flow problems see Scardovelli & Zaleski (1999).

Because of the way the free surface is approximated, the Marker methods and VOF methods are also referred to as surface-capturing techniques.

- Grid-free methods: To eliminate problems related to fixed or moving grid methods (partial) grid elimination methods such as Boundary-Integral Methods (BIM) and the Particle-in-Cell (PIC) method (originally by Harlow (1964)) have been developed. Another promising framework in which the coupling between particles and the grid is not retained is the Smoothed Particle Hydrodynamics (SPH) method by Monaghan (1992). In this latter method the differential equations are solved using particles and smoothing kernels that define the intensity of interaction between particles. Although initially developed for astrophysical applications, this method can also be used to solve free surface problems (Monaghan (1994)). The SPH method has recently been adopted by Fontaine *et al.* (2000) to successfully simulate the breaking of waves (including plunging jets and splashing). For a recent overview to grid-free methods we refer to Belytschko *et al.* (1996). It is noted that a grid free method that does not eliminate the grid on the free surface (like a boundary-integral method), can be referred to as a surface-tracking technique.

- Moving-grid methods: In these methods the grid is allowed to move, thus letting the grid itself define the free-surface position. The motion of the grid in a mixed manner between the Lagrangian motion and the fixed Eulerian point of view (the Arbitrary Lagrangian Eulerian method, ALE) was first introduced by Hirt *et al.* (1974). In contrast to surface-capturing techniques, moving grid methods are also referred to as surface-tracking techniques.

In this thesis a surface-tracking method is used for the following reasons. Firstly, the position and velocity of the free surface are of principal interest and for an interface-tracking method this interface is well-defined and can be more accurately calculated. Secondly, the aim of the simulations is not to capture complicated phenomena such as spilling, breaking and splashing of waves in which case a fixed grid or grid-free method might be more suitable.

Since the first successful numerical methods in the simulation of fully nonlinear free-surface waves by Longuet-Higgins & Cokelet (1976), use has been made of the mixed-Eulerian-Lagrangian (MEL) procedure in which the solution of the spatial equations are solved in the Eulerian (fixed grid) frame and the integration of the free-surface boundary conditions is performed in the Lagrangian manner. Integration in the Lagrangian frame implies that the grid points that are on the free surface are identified with material particles and thus move with the velocity field. A complete Lagrangian treatment of the free-surface grid points however leads to loss of control over the grid density (see e.g. Broeze (1993)) and might thus adversely affect stability and accuracy. Therefore an Arbitrary Lagrangian Eulerian (ALE) method is used with respect to the boundary points. The ALE method was initially developed by Hirt *et al.* (1974) for discretising the Navier Stokes equations and its implementation was considerably more complicated than needed for our purposes. After a Lagrangian integration of
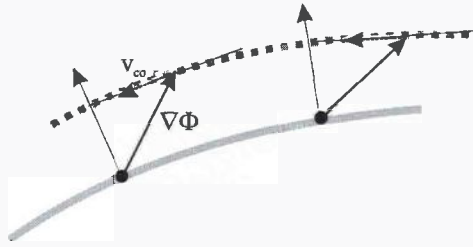
Figure 2.1: *The grid displacement on the boundary follows from the material displace-ment corrected with a tangential correction vector.*

the variables, including the grid points, the grid is adjusted and the variables associ-ated with the grid points are updated in such a way that the conservation laws are satisfied. The final displacement of the grid points at the free surface thus follows from a correction to the displacement of the material points (see also Fig. 2.1).

The grid velocity correction on the free surface cannot be chosen arbitrary. Eq. (2.14) states that the normal component of the fluid velocity has to equal the normal com-ponent of the free-surface velocity. Therefore, mass conservation is not violated (in the infinitesimal case) as long as the velocity of a free-surface grid point is corrected with a velocity vector tangential to the free surface. It should be noted that for fi-nite time step Δt the tangential correction vector is not perpendicular to the normal vector of the grid on which the Laplace problem is solved. Also, the tangential and normal vector might not be well-defined due to the discretisation of the free surface. Therefore the error in mass conservation will be of the same order of magnitude as the method for time-integration and surface approximation, although the truncation error might be slightly larger.

There is a degree of freedom in the length of the correction vector. Local grid cor-rection parameters $\hat{\sigma}_1$ and $\hat{\sigma}_2$ are introduced to indicate this freedom. The correction vector is tangential to the free surface and thus of the form

$$\vec{v}_{\text{cor}} = -\hat{\sigma}_1 \left[\begin{array}{c} \Phi_x \\ 0 \\ \Phi_x \eta_x. \end{array} \right] - \hat{\sigma}_2 \left[\begin{array}{c} 0 \\ \Phi_y \\ \Phi_y \eta_y. \end{array} \right] \tag{2.24}$$

For every grid point the parameterisation parameters have been normalised such that $\hat{\sigma}_j = 0$ corresponds to Lagrangian motion of the grid point, and $\hat{\sigma}_j = 1$ corresponds to only vertical motion of the grid point.

As the dynamic equations of the potential have been derived in the Eulerian frame of reference, the evolution of the potential Φ_i (subscript i now numbers the grid point and not the coordinates) needs to be updated with the actual grid motion. Given

the velocity $\nabla\Phi_i$ in grid point $\vec{x}_i$, the governing equation for the position of the grid point is thus given by

$$\frac{Dx_i}{Dt} = \nabla\Phi_i + \vec{v}_{\text{cor}}. \tag{2.25}$$

Using the dynamic boundary condition (2.23e) and ignoring surface tension the dynamic equation for Φ_i in x_i is given by

$$\frac{D\Phi_i}{Dt} = \partial_t\Phi_i + (\nabla\Phi_i + v_{\text{cor}}) \cdot \nabla\Phi_i \tag{2.26}$$

$$= \left(\frac{1}{2}\nabla\Phi_i - \hat{\sigma}_1 \begin{bmatrix} \Phi_x \\ 0 \\ \Phi_x\eta_x. \end{bmatrix} - \hat{\sigma}_2 \begin{bmatrix} 0 \\ \Phi_z \\ \Phi_z\eta_z. \end{bmatrix} \right) \cdot \nabla\Phi_i - gx_i \cdot \vec{z} \tag{2.27}$$

Notice that for $\hat{\sigma}_j = 1$ the non-zero, i.e. z-component, of Eq. (2.25) can be identified with the dynamics for η in Eq. (2.23f). Although analytically identical, the numerical implementation is slightly different as a direct discretisation of Eq. (2.23f) would lead to evaluation of η_x at the not-yet updated surface. The discretisation of Eq. (2.25) on the other hand determines η_x on the Lagrangian updated surface.

2.2.2 Time stepping

The set of equations (2.23a)-(2.23f) is elliptic in space and parabolic in time. Therefore, the numerical method to solve the spatial part of the equations is essentially different from the method to solve the time dependent part. Since the first successful numerical methods in the simulation of fully nonlinear free-surface waves by Longuet-Higgins & Cokelet (1976), use has been made of the so called mixed-Eulerian-Lagrangian (MEL) procedure in which the solution of the spatial equations are solved in the Eulerian (fixed grid) frame and the integration of the free-surface boundary conditions is performed in the Lagrangian manner. Following this well-established procedure the numerical algorithm is split in a time-integration part and a part concerning the solution of a boundary-value problem on a fixed geometry. After discretisation of the geometry and the equations, we are left with a set of algebraic equations (see also Section 3.2.2) that can be denoted as

$$\mathbf{q}_t = \tilde{f}(\mathbf{q}, t). \tag{2.28}$$

The vector $\mathbf{q}$ contains the free-surface-geometry and -potential and possibly other variables that have prescribed dynamics. Because the geometry of the domain and the boundary values are completely determined by $\mathbf{q}$, the solution of the Laplace problem is a function of $\mathbf{q}$ and incorporated in the function $\tilde{f}$. Whenever the function $\tilde{f}$ needs to be evaluated numerically, a boundary-value problem has to be solved. Given the time step Δt we denote the approximation of the solution $\mathbf{q}$ of Eq. (2.28) at time $i\Delta t$ as $\mathbf{q}_n = \mathbf{q}(n\Delta t)$.

There are several methods to numerically integrate Eq. (2.28) in time. Generally, these methods can be categorised in implicit and explicit methods depending on whether or not the equation for approximating q_n is implicit or explicit. Although implicit methods have the favorable property that they are unconditionally stable for linear $\tilde{f}$, they are more elaborate to implement. Another disadvantage of implicit methods to solve Eq. (2.28) is that they are based on an iterative scheme and thus many evaluations of $\tilde{f}$ are necessary which is computationally quite expensive. Several explicit time-integration methods have been used by several authors to solve the free-surface equations (Adams-Bashforth-Moulton formulae, Taylor series methods and Runge-Kutta methods). When time derivatives of the potential are also needed (e.g. for the evaluation of pressures) it may be beneficial to use a combination of a Runge-Kutta method and a Taylor series expansion (e.g. Broeze (1993)). The most widely used methods however are the Runge-Kutta methods which we have also adopted. The advantages of these methods are that they do not require derivatives of $\tilde{f}$ and that the approximation of q_n depends only on q_{n-1}. Moreover they are accurate and can be easily tuned for specific purposes (see also Section 3.2.2).

The explicit s-stage Runge-Kutta (RK) integration method determines the value of the vector q_{n+1} using the following formula

$$q_{n+1} = q_n + \Delta t_n \sum_{i=1}^{s} b_i f_i \qquad (2.29)$$

where

$$f_1 = \tilde{f}(q_n, t_n) \qquad (2.30)$$

$$f_i = \tilde{f}\left(q_n + \Delta t_n \sum_{j=1}^{i-1} a_{ij} f_j, \ t_n + c_i \Delta t_n\right). \qquad (2.31)$$

The coefficients a, b and c can be chosen freely and determine the order of the scheme. The presented Runge-Kutta method can be easily extended to include adaptive time steps and continuous output (cf. Dormand (1996) for details).

Although only four stages are needed to create a fourth order RK scheme, the degrees of freedom that are available in a fourth order 5-stage method can be used to minimize the principal (i.e. fifth) local truncation error term. The principal error is reduced by a factor of approximately 7 with respect to an optimal 4-stage fourth order RK formula. It is shown in Dormand (1996) that for a benchmark application (gravitational 2 body orbit problem) the additional computational effort is more than compensated for by the improvement in accuracy.

In Fig. 2.2 on the next page the numerical algorithm is visualised in which the solution of the Laplace BVP problem has explicitly been incorporated. The steps (A) and (F) are computational steps that follow from the Runge-Kutta formulae Eqs. (2.29)-(2.31). In step (E) the right-hand side of the discretised form of e.g. Eq. (2.25)-(2.27) is determined. Steps (B)-(D) are necessary to provide the velocity approximation
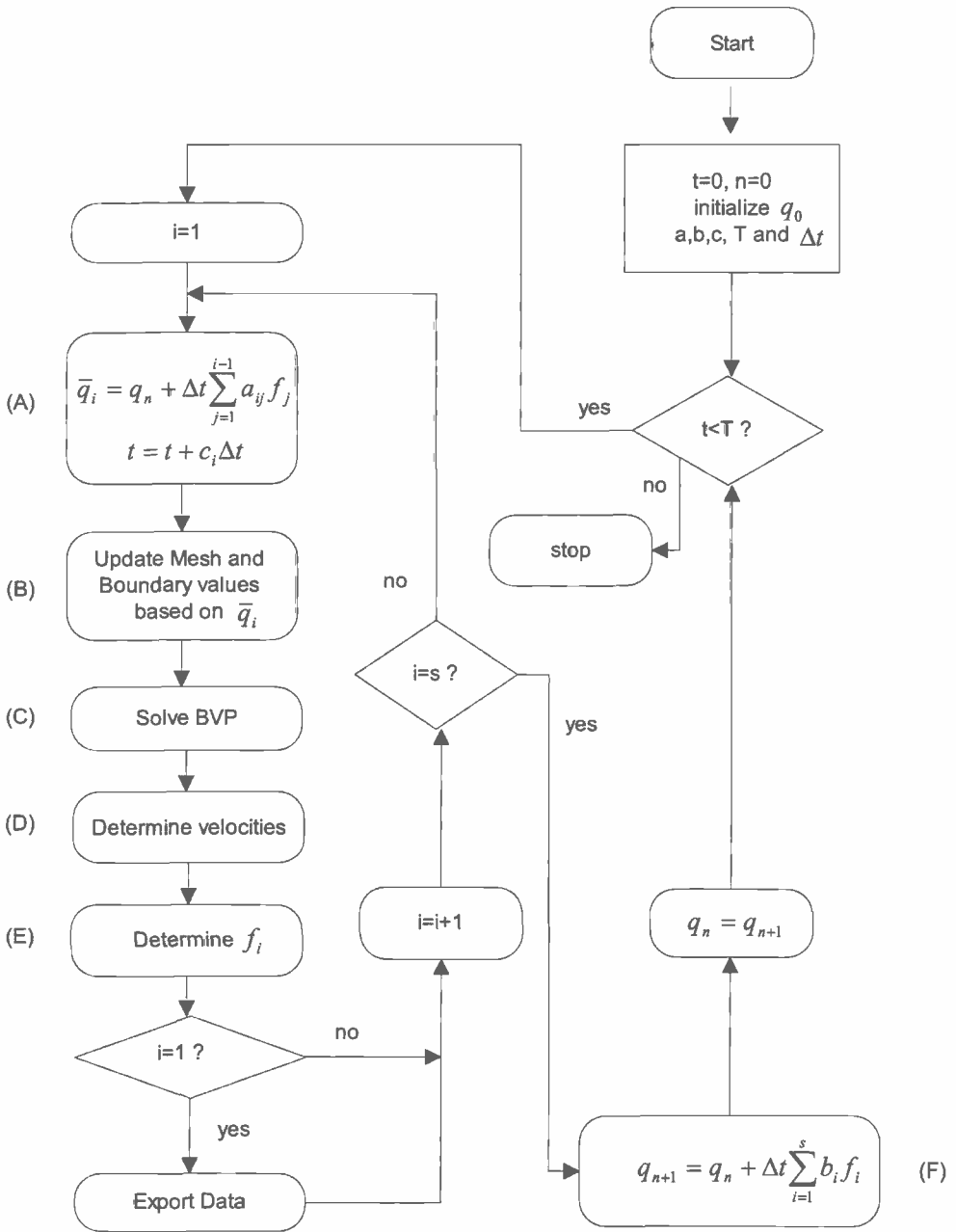
Figure 2.2: *Flow diagram of the numerical time stepping scheme using an explicit Runge-Kutta method.*

needed in step (E). The solution of the boundary-value problem in step (C) will be discussed in the next two subsections. Some aspects of the implementation of this algorithm will be further discussed in Section 2.3.

2.2.3   Field method versus Boundary-Integral method

So far, we have not commented on the approximation of the boundary-value problem. There are two main methods to solve the boundary-value problem for Laplace's equation in step (C): field methods and boundary-integral methods. The field methods can roughly be divided in finite-difference and finite-element methods (finite-volume methods are not taken into account, following the discussion at the start of Section 2.2). Although finite difference methods could be used, the implementation of such a method on a non-rectangular geometry and the implementation of the boundary conditions, makes this method less suitable than a Finite Element (FE) method. This section outlines the main advantages and disadvantages of a boundary-integral method versus a FE approximation of the field equations with respect to the simulation of waves in a model test basin.

Most of the existing numerical schemes to solve the free-surface equations are based on Boundary-Integral methods. A boundary-integral method (BIM) employs Green's theorem to reduce the differential equation in Ω to an integral equation on Γ. It therefore has the great advantage that the number of unknowns is much smaller than the number of unknowns of a field discretisation method. Another advantage of a boundary-integral method is that no effort has to be put in the gridding of Ω. However, the equations on Γ are more complicated than the field equations and the numerical methods to discretise them are relatively expensive in terms of floating-point operations. After discretisation, there is a direct global coupling between all the unknowns and in general no exact formula are available for evaluating the matrix coefficients. For a general introduction to integral equations in fluid mechanics see e.g. Power & Wrobel (1995) and for an application to free-surface simulation see e.g. the thesis of Romate (1989).

A field approximation of Laplace's equation by e.g. a finite element method (FEM) returns the solution throughout the domain and not only at the boundary. Its main disadvantages are that number of unknowns is much larger and one is concerned with the gridding of Ω. On the other hand, the computation of the matrix resulting from a FE discretisation is quite straightforward. For a large family of finite elements, exact and readily computable formulae are available for the matrix entries (see e.g. the appendix (B.1)).

Although it might seem that from a computational point of view a BIM is preferable over a FEM because of the reduced number of unknowns, this is not always true. It is stressed that the efficiency of a numerical method depends on its field of application. Therefore no general statement can be made about the efficiency of Boundary-Integral methods over Field-Discretisation methods or vice versa. Although it was found that

for the simulation of waves in a hydrodynamic model test basin, a FE method is highly efficient, studies concerning interaction with fixed or floating structures showed the effectiveness of a higher-order BI method (see e.g. Huijsmans *et al.* (1999)). In Cai *et al.* (1998) a heuristic comparison is given in which it is demonstrated that an approximate solution of the boundary-value problem for Laplce's equation can be obtained more efficiently by a FE discretisation. This is due to a combination of the sparse structure of the matrix arising from FE discretisation and the availability of good preconditioners.

In the following paragraphs this general heuristic comparison between a field discretisation and a boundary-integral equation and a relevant example with respect to a model test basin will be presented. At the end of this subsection we will mention some recent developments regarding other efficient solution methods of the Laplace boundary-value problem.

General heuristic comparison

The following heuristic comparison (mainly from Cai *et al.* (1998)) indicates that heuristically a FE based solution of Laplace's equation can be obtained more efficiently than a solution of a Boundary-Integral method. In the following we will simply refer to a FE based field discretisation method as FEM and to methods based on the Boundary-Integral equations as BIM.

Consider a square/box domain ($d = 2$, $d = 3$, respectively) with uniform grid with n grid points per spatial variable. The number of unknowns is then of order $\mathcal{O}(n^{d-1})$ for BIM and order $O(n^d)$ for FEM. The matrix associated with the linear system that follows from a boundary-integral description is dense, meaning that most matrix entries are non-zero. The number of non-zero entries per row in a FEM matrix is independent of n and therefore one matrix-vector multiplication for the FEM matrix needs $\mathcal{O}(n^d)$ multiplications, whereas one matrix-vector multiplication with the BIM matrix needs $\mathcal{O}(n^{2(d-1)})$ multiplications. The BIM-matrix is in general well conditioned, so an appropriate iterative solution procedure converges in a number of iterations independent of n. Therefore the total computational costs for one solution of the linear system associated with a BIM approximation is $\mathcal{O}(n^{2(d-1)})$.

A FEM matrix is in general not well conditioned; the matrix associated with the FE discretisation of Laplace's problem (on the square domain) has a spectral condition number κ that is $\mathcal{O}(1/h^2) = \mathcal{O}(n^2)$ (independent of d and the order of Finite Elements used (cf. e.g. Axelsson & Barker (1984))). Since for a Conjugate Gradient Method the number of iterations is $\mathcal{O}(\sqrt{\kappa})$, the total computational effort for a FEM approximation using a CG-method is $\mathcal{O}(n^{d+1})$. One might conclude that, on basis of this heuristic comparison, a BIM is more efficient for $d = 2$ and BIM and FEM are equally efficient for $d = 3$ when iterative solvers are used.

When a preconditioner is applied to the system of equations arising from FEM, the

spectral condition number of the resulting system can be greatly reduced. Especially in the case when no breaking of waves occurs, the fluid domain can be efficiently mapped to a rectangular domain, and an optimal preconditioner can be constructed which results in a uniform spectral condition number. This specific preconditioner is based on the fact that the transformed Laplace operator is spectrally close to the untransformed Laplace operator. The precondition step can in that case be performed by a so-called fast solver (e.g. FFT) that requires slightly more than $\mathcal{O}(n^d)$ computations.

Other preconditioners, such as the incomplete Cholesky factorisation also lead to almost uniform spectral condition numbers. Such a factorisation can be efficiently carried out at $O(n^d)$ cost. For a recent review on preconditioning techniques in computational fluid dynamics we refer to Turkel (1999). An optimal preconditioner, under mild conditions, for second order self-adjoint elliptic problems is presented in e.g. Axelsson & Vassilevski (1990). Another possibility to construct efficient solvers is by means of a domain embedding technique, cf. e.g. Börgers & Widlund (1990). When such near optimal preconditioners are used, the computational costs for a FEM and BIM are of the same order for $d = 2$. For $d = 3$ the BIM is a factor n more expensive than the FEM.

In the next paragraph, a representative example will be given to illustrate the computational effort for the two-dimensional situation. In this example, the linear system resulting from the FEM discretisation will be solved by a Gaussian Elimination procedure for symmetric and banded matrices. This method requiers $\mathcal{O}(nb^3)$ floating-point operations where b is the bandwidth of the matrix and is thus only more efficient than the optimaly preconditioned CG method if $b^3 \ll n$.

Numerical Wave Tank example

Assume that the model basin is 180 [m] long and 5 [m] deep. This geometry is discretised by 1000 points in the horizontal direction and 15 points in the vertical direction (these are realistic values). Discretisation of boundary-integrals requires at least one full matrix, which means that approximately $4 \cdot 10^6$ matrix entries need to be stored. For a linear FEM on a triangular grid, the number of non-zero matrix entries is approximately $5 \cdot 10^4$. This small number is due to the sparsity and symmetry of the matrix. A solution of a linear system with this FE matrix can be obtained using a Symmetric Gaussian Elimination procedure in approximately $5 \cdot 10^6$ floating-point operations. For the BI matrix a *single* matrix vector multiplication already takes approximately $4 \cdot 10^6$ floating-point operations. In general, several ($\gg 10$) matrix-vector multiplications have to be performed to obtain a solution of this system iteratively. It is clear that even if the construction of the matrix entries is not taken into account, a FE approximation on a regular grid can be obtained at lower computational effort than a BI approximation.

Of course the accuracy of the approximation needs also to be taken into account for

a full comparison. Such a comparison of the accuracy would be very elaborate, but when e.g. the FE grid in the above example is refined by a factor 2, the resulting number of non-zero matrix entries would be slightly less than $2 \cdot 10^5$. The number of floating-point operations to solve the system using the Symmetric Gauss Elimination procedure would be less than $7 \cdot 10^7$. In this case, the FE method is computational equivalent to the solution of a BI matrix when the BI system converges to the same precision within 17 iterations. Remark however that the solution of the compared FE discretisation is directly available on the whole domain at a *twice* as dense mesh using an inefficient solver. Finally it should be noted that the condition number of the BI matrix rapidly deteriorates when the aspect ratio of the domain increases.

It is not the intention to give a general comparison between Finite Element and Boundary-Integral methods, but the above example illustrates that it is a misunderstanding to think that a FE approximation is always computationally more expensive than a BI approximation. Of course, the above example is not conclusive and many aspects have not been touched upon. However, comparison with other computer codes based on integral equations indicated that for wave tanks (large aspect ratios) field approximations can be obtained more efficiently than boundary-integral approximations. These observations greatly contributed to the effort of developing a FE based numerical scheme for water wave simulations.

Recent developments

Recent developments (Nabors *et al.* (1994) and Scorpio *et al.* (National Academic Press, Washington DC)) have shown that a very efficient multi-pole expansion method based on a BIM can been constructed that has a computational and memory cost of $\mathcal{O}(n^{d-1})$. This method is based on the clustering of collocation points and sources and to replace their influence by a single multi-pole. However, this method requires some tuning and at this moment it is not clear to what extent it can be applied to numerical wave tank simulations. Domain decomposition techniques (cf. e.g. Wang *et al.* (1995) and de Haas & Zandbergen (1996)) for boundary-integral methods, can also improve the computational cost of a BIM considerably. The aim of the domain decomposition applied to Numerical Wave Tanks is to achieve a computational complexity that increases linearly with the length of the domain: an achievement already satisfied by a FE discretisation. Preliminary results indicate that both the multi-pole expansion and domain decomposition are less robust methods. However, these methods are continuously under development and the availability of a general and robust $\mathcal{O}(n^{d-1})$ numerical scheme would be of great practical value.

In the case of FE methods, multigrid solution methods have become increasingly popular in the last years. The implementation of a multigrid FEM to nonlinear wave problems is however not straightforward due to the non-rectangular geometry and the large aspect ratio of the domain. Implementation of a CG solver with a V-cycle multigrid preconditioner to three-dimensional flow simulations, showed that straightforward Jacobi preconditioning was more efficient (in terms of total computational

time) for a wave tank geometry. For a unifying treatment of domain decomposition techniques using, among others, multigrid methods for elliptic equations we refer to Smith *et al.* (1997).

Some of the considerations mentioned in the previous paragraphs have already been mentioned in Westhuis (1997) and were used as a starting point of this research. We have therefore not further investigated the use of boundary-integral methods and focused on the development of a finite element method. In the next subsection, the approximation of the solution of the boundary-value problem using the Finite Element Method will be presented.

2.2.4   Finite Element Method

The solution of the Laplace boundary-value problem is approximated using a Finite Element Method. This method is well established and many textbooks (e.g. Connor & Brebbia (1976), Brezzi & Fortin (1991) and Zienkiewicz & Taylor (1994)) are available on the subject. The method employs the weak formulation of the boundary-value problem which can often be found directly by minimizing the appropriate energy functional. For notations and definitions of the used spaces we refer to the appendix (A).

Weak formulation

Assume that the open set Ω has a bounded Lipschitz continuous boundary Γ. Consider the following bilinear form $a(\cdot, \cdot)$ on Ω:

$$a(u, v) = \int_{\Omega} \nabla u \cdot \nabla v \, d\Omega. \tag{2.32}$$

Furthermore, assume that the boundary $\Gamma = \Gamma^D \cup \Gamma^N$ consists of two disjunct parts. On Γ^D a Dirichlet condition is defined and Γ^N is equipped with a Neumann condition. Consider the two following problems:

(A) Find a function Φ that satisfies for given $g \in H^{-1/2}(\Gamma^N)$ and $f \in H^{1/2}(\Gamma^D)$

$$\Delta\Phi = 0 \qquad \text{in } \Omega \tag{2.33a}$$
$$\Phi = f \qquad \text{on } \Gamma^D \tag{2.33b}$$
$$\nabla\Phi \cdot n = g \qquad \text{on } \Gamma^N \tag{2.33c}$$

(B) Find a function $\Phi \in H^1(\Omega)$ such that

$$\Phi - \Phi_D \in H^1_{0,\Gamma^D} \tag{2.34a}$$
$$a(\Phi - \Phi_D, v) = -a(\Phi_D, v) + \langle g, v \rangle_\Gamma \qquad \forall v \in H^1_{0,\Gamma^D} \tag{2.34b}$$

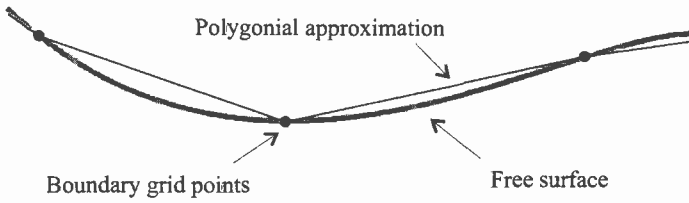for a given $\Phi_D \in H^1(\Omega)$ that satisfies $\gamma_D \Phi_D = f$

Figure 2.3: *Visualisation of the relation between boundary grid points (see also Fig. 2.1 on page 22), free surface and boundary of the polygonal approximation of the domain*

In appendix A the necessary definitions and theorems are presented to show that problems **(A)** and **(B)** are equivalent for $a(\cdot, \cdot)$ as in Eq. (2.32) and have a unique solution Φ. The duality bracket $\langle \cdot, \cdot \rangle_\Gamma$ is an extension of the scalar product on $L^2(\Gamma_D)$, i.e. for $g, v \in L^2(\Gamma)$ one can identify $\langle g, v \rangle_\Gamma$ with $\int_\Gamma g(s)v(s)\ ds$

The spaces used in problem **(A)** and **(B)** are infinite dimensional. In order to obtain a numerical approximation $\widehat{\widehat{\Phi}}$ of Φ a suitable finite-dimensional subspace needs to be defined that does not violate the assumptions under which the equivalence of **(A)** and **(B)** was proven. There are many choices for these subspaces, but we will focus on the classical finite-element spaces of piecewise polynomial functions. In the following, we will explicitly assume that Ω lies in the two-dimensional plane.

Firstly, the geometrical approximation $\widehat{\Omega}$ of the domain Ω is assumed to be polygonal, and is thus a geometric approximation of the contour of the actual fluid domain. The vertices of the polygonal located at the free-surface coincide with the boundary grid points introduced at the beginning of this section. Next a triangulation $\mathcal{T}$ on $\widehat{\Omega}$ is defined as

$$\widehat{\Omega} = \bigcup_{K \in \mathcal{T}} K \tag{2.35}$$

such that any two triangles K_1 and K_2 in $\mathcal{T}$ are either disjoint or share at most one side or one vertex. The classical FE subspaces consist of piecewise (on every triangle) polynomials. The order of the polynomial is denoted as p. The subspace of piecewise continuous polynomials with the H^1-norm is denoted as $V \subset H^1\left(\widehat{\Omega}\right)$. Every triangle K contains several (depending on p) nodes. A single node can belong to multiple triangles. These nodes are thought to have a global numbering and the set $\mathcal{V}$ is constructed as the junction of all node-indices. Every node i is associated with a position x_i and a function N_i. This function is defined such that

1. $N_i(x_i) = 1$

2. $N_i(x)$ is polynomial of order p on every triangle K_j to which node i belongs and $N_i(x) = 0$ on all other triangles.

3. $N_i(x_n) = 0$ for all nodes $n \neq i$ that share a triangle with node i.

As a result, all N_i are independent and (with an additional constraint on the relative positions of the nodes i) span the space V.

As the finite dimensional subspace $V_0 \subset H^1_{0,\Gamma_D}$ the space spanned by the base function N_i for which $N_i(x_j)$ is zero when x_j is a boundary grid point belonging to Γ^D is constructed. The following index sets are now defined:

$$\mathcal{I} = \{i \mid N_i \in V_0\}, \tag{2.36a}$$
$$\mathcal{D} = \{i \mid N_i \in V \setminus V_0\}. \tag{2.36b}$$

The function Φ_D is approximated with the base functions belonging to the subset $\mathcal{D}$ and its approximation is denoted as

$$\hat{\Phi}_D = \sum_{i \in \mathcal{D}} \beta_i N_i. \tag{2.37}$$

Correspondingly, the unknown $\phi = \Phi - \Phi_D$ is approximated by

$$\hat{\phi} = \sum_{i \in \mathcal{I}} \alpha_i N_i. \tag{2.38}$$

The coefficients β_i are determined in such a way that $\hat{\Phi}_D$ approximates f on Γ^D, which is achieved by choosing $\beta_i = f(x_i)$ for all $i \in \mathcal{D}$. Problem **(B)** can be completely restated with respect to V and V_0 and therefore from the unique approximation $\hat{\phi}$ that satisfies

$$a(\hat{\phi}, v) = -a(\hat{\Phi}_D, v) + \int_\Gamma g(s)v(s)\ ds \quad \forall v \in V_0 \tag{2.39}$$

the approximation $\hat{\Phi} = \hat{\phi} + \hat{\Phi}_D$ of the discretised boundary value problem for Laplace's equation can be constructed.

Substitution of Eq. (2.37) and Eq. (2.38) in Eq. (2.39) results in

$$\sum_{i \in \mathcal{I}} \alpha_i\, a(N_i, N_j) = -\sum_{i \in \mathcal{D}} \beta_i\, a(N_i, N_j) + \int_\Gamma g(s)N_j(s)\ ds \quad \forall j \in \mathcal{I} \tag{2.40}$$

where the statement $\forall v \in V_0$ has been replaced by the equivalent statement $\forall N_j$ $j \in \mathcal{I}$. Equation (2.40) is a linear system in α_i that can be solved in order to obtain the approximate solution $\hat{\Phi}$. The efficient construction of the base functions and exact formulae to determine the integrals $a(N_i, N_j)$ are given in appendix B.1. It is well known that for complete polynomials of order p the truncation error of the approximation is $\mathcal{O}(h^{p+1})$, where h is the typical grid width.

The use of higher-order FE's

Although the implementation of second and higher order polynomial base functions in the piecewise continuous approximation on a rectangular geometry is straightforward,

this is not the case for a curved geometry. If the triangular element family, described in appendix B.1 is used, the resolution of the geometrical approximation is reduced when the number of degrees of freedom (DOF) is kept constant. The use of parametric elements, in which the shape of the element is expressed in terms of the same base functions that interpolate the unknowns on the element, can be used to create piecewise polynomial surfaces. However, a drawback is that exact analytical integration on the element is not possible and a numerical integration method should be applied. Another complication is that in some boundary nodes the potential solution is locally C^1 continuous while in other boundary points it is not. This inconsistent treatment of boundary points can lead to undesired effects. The use of a mixed formulation of the boundary-value problem, in which both the potential and the velocity are approximated, does not lead to more accurate results for the velocity if the same polynomial order for both approximations is used (cf. Zienkiewicz & Taylor (1994) p.321) than when the velocity is recovered directly using a global projection method.

Another possibility for a higher order FE is the use of C^1 continuous representation of the boundary and potential approximation instead of the C^0 family described in the appendix. An advantage would be that a continuous velocity approximation is directly available from the FE solution. The computational complexity would however increase considerably and it should be investigated whether or not this is a worthwhile trade-off. It is noticed that a C^1 triangular element needs a fifth-order polynomial base function, requiring 21 degrees of freedom. Currently, non-rectangular C^N finite elements with $N \geq 2$ are not available at all. A promising application of higher order elements could be the C_B^N elements, developed by Givoli & Vigdergauz (1994). These elements are used at boundaries only, where they locally represent the potential by C^N continuous base functions. In the interior of the domain standard C^0 elements can be used. The C_B^N elements were originally constructed for the implementation of higher-order absorbing boundary conditions. However, they also might be useful as free surface elements in numerical water wave simulations. The applicability of higher order parametric hp, triangular C^1 or C_B^N elements for free-surface simulation is not further examined in this thesis because of the satisfactory results that were obtained using linear elements (see also Chapter 3).

2.2.5   Velocity recovery

The result of the solution of Eq. (2.40) is the approximation of the potential Φ. Numerical evaluation of the dynamic and kinematic boundary conditions Eqs. (2.25)-(2.27) however, requires an approximation of the velocity at the free surface. Direct differentiation of the potential approximation results in a lower order, discontinuous velocity with inferior accuracy. To achieve more accurate derivatives several recovery techniques are available. Among them are nodal averaging and global projection techniques using the original polynomial expansions (e.g. Wu & Eatock Taylor (1995) for an application of global projection to wave simulation). More recently Zienkiewicz & Zhu (1992) proposed a local projection technique on a patch of elements using a

single polynomial expansion of the function describing the derivatives (the so-called Super Convergent Patch Recovery Technique [SCPRT], see also Babuska *et al.* (1996)). The convergence of the recovered velocity using the SCPRT can be an order *higher* than the order of convergence of the potential. Another possibility to recover the velcoity at the free surface is the use of local finite differences (see e.g. Cai *et al.* (1998)). In the following paragraphs we introduce the global projection method and the local finite difference method that have been used as velocity recovery methods.

Global projection method

The direct differentiation of the potential in general results in an approximation of the velocity field of an order lower than the approximation of the potential. As pointed out by Greaves *et al.* (1997), one possibility to improve the accuracy of the velocity for evaluation of the kinematic and dynamic boundary conditions, is to find the best approximation of $\nabla\Phi$ in the same space as the approximation in which $\widehat{\Phi}$ was determined. This method can also be interpreted as a resampling of the velocity at the Gauss-Legendre integration points. It is well known that at these integration points the FEM approximation converges one order faster. It is therefore general practice (cf. Zienkiewicz & Taylor (1994), p.348) to sample the velocities (strains) at these integration points to obtain a more accurate approximation of the velocity field than by direct differentiation of the potential representation.

The approximation $\widehat{\Phi}$ of the potential Φ is of the form

$$\widehat{\Phi} = \sum \phi_i N_i \tag{2.41}$$

and therefore, by direct differentiation, the velocity field is approximated by

$$\widehat{\nabla\Phi} = \sum \phi_i \nabla N_i \tag{2.42}$$

The resampled recovery of the velocity, denoted as $\widehat{v}$, is also represented in terms of the polynomial base function as

$$\widehat{v} = \sum v_i N_i \tag{2.43}$$

and the coefficients v_i are determined from the minimisation of the functional

$$D(\widehat{v}) = \frac{1}{2} \int_{\widehat{\Omega}} |\widehat{\nabla\Phi} - \widehat{v}|^2 d\Omega. \tag{2.44}$$

The minimisation of this convex functional directly leads to the following algebraic equation for $\widehat{v}$

$$\int_{\widehat{\Omega}} (\widehat{\nabla\Phi} - \widehat{v}) N_i d\Omega = 0 \quad \forall i \in \mathcal{V}. \tag{2.45}$$

Substitution of Eq. (2.42) and Eq. (2.43) in Eq. (2.45) results in

$$\int_{\widehat{\Omega}} \sum_{j\in\mathcal{V}} v_j N_j N_i d\Omega = \sum_{j\in\mathcal{V}} \nabla N_j N_i d\Omega \quad \forall j \in \mathcal{V}. \tag{2.46}$$

from which the coefficients v_j can be directly obtained.

This method was implemented by Otto (1999) as a velocity recovery option in the developed code (see also Section 2.3) that implements the numerical algorithm. He found by performing nonlinear numerical simulations that application of this method leads to unstable high-frequency waves. This was also observed by Wu & Eatock Taylor (1995) who however did not relate this to the specific implementation of this velocity approximation method. These authors circumvented the instabilities by smoothing the free surface after each time-integration. In Section 3.2.2 it is shown by linear stability analysis that it is the velocity approximation method that leads to an unstable numerical scheme. The super-convergent patch recovery is a local version of the global projection method in which the minimisation is performed over a patch of elements instead of the whole domain. Because of the disappointing results of the global projection method, the SCPRT was not further investigated.

Finite Difference recovery of the velocity

As an alternative to the global recovery method of the previous paragraph, a local Finite Difference (FD) method can be used to recover the velocity at the free surface. Many different FD scheme's (based on one- or two-dimensional polynomial approximations) can be developed and several have been investigated by Otto (1999). Here we introduce our original implementation and we will comment on extensions at the end of this section. The original finite difference scheme was based on independent approximation of the tangential derivative of the potential from the free-surface data only and on the one sided, one dimensional approximation of the non-tangential velocity at the free surface from the field solution. The truncation error in the finite difference scheme is of the same order as the order of the polynomials used for the construction of the scheme.

Fig. 2.4 on the following page illustrates the method to determine the tangential velocity for the case that quadratic polynomials are used. The method can and has been extended to polynomials of arbitrary order in a similar fashion. Assume that the positions of three grid points x_i, $i = -1, 0, 1$ are given at the free surface. The potential at these points is denoted as Φ_i, $i = -1, 0, 1$. As an approximation of the tangential derivative of the free surface at x_0, the tangential derivative of the quadratic polynomial through x_i, evaluated at x_0 is determined (Fig. 2.4(a)). This local approximation of the surface tangent at x_i is denoted s. To accurately calculate the polynomial coefficients, all calculations are performed in a local frame of reference with its origin at x_0 and its orientation such that local positive z-axis is normal to the line through x_{-1} and x_1. This orientation of the local frame of reference is illustrated by the arrow-frame depicted in the figure. Besides improved numerical accuracy, the procedure of first determining a local frame of reference also allows for a more general implementation of the method as we are not restricted to apply it to free surfaces that are a function of the spatial variable.
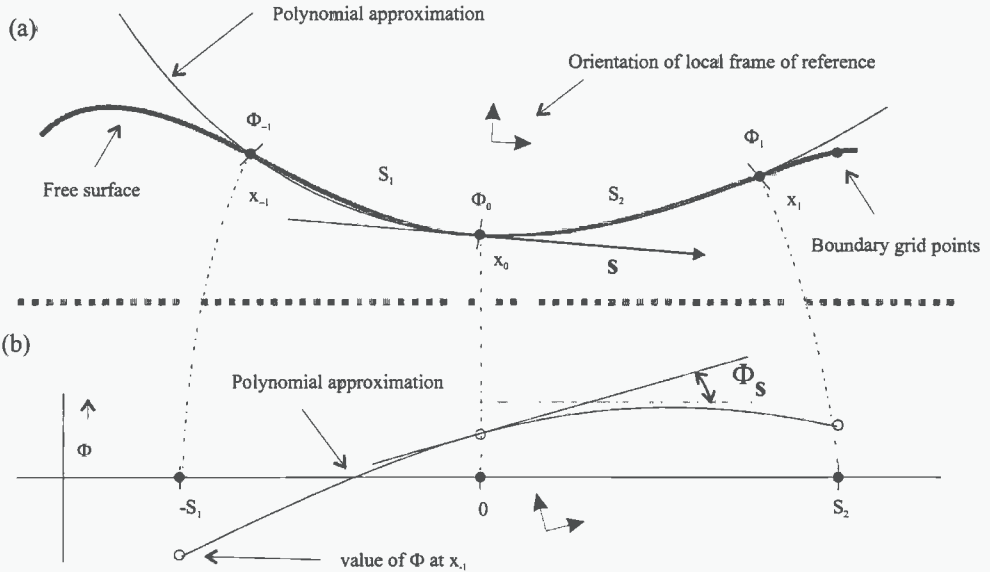
Figure 2.4: *Illustration of the quadratic method used to determine tangential vector s (a) and tangential derivative of the potential Φ_s at the free surface (b).*

The parameterisation along the local polynomial that approximates the free surface is denoted by s. In Fig. 2.4(b) the potential Φ_i is plotted as a function of s. To determine an approximation of the tangential derivative Φ in x_0, the same procedure is followed as described in the previous paragraph. After the polynomial approximation of Φ as a function of s has been constructed the derivative of this polynomial at the point x_0 is taken as the approximation for the value of the tangential derivative of Φ in x_i and denoted as $\widehat{\Phi}_s$.

The approximation of the non-tangential derivative of the potential at the free surface that is needed for the evaluation of the velocity, is determined in a similar manner. Below the free-surface nodes are situated on which the potential is known and through which polynomial approximations can be constructed in a similar way (see Fig. 2.5 on the next page). Using the technique described in the previous paragraphs, a non-tangential vector κ and the derivative of the potential along this vector can be determined. Of course in this case, the tangential vectors and derivatives are evaluated at the end nodes in stead of the central nodes.

The approximation of the velocity $\widehat{\nabla\Phi}_i$ at the free surface node x_i is thus obtained directly as a solution of

$$\widehat{\nabla\Phi}_i \cdot s \;=\; \widehat{\Phi}_s \tag{2.47}$$

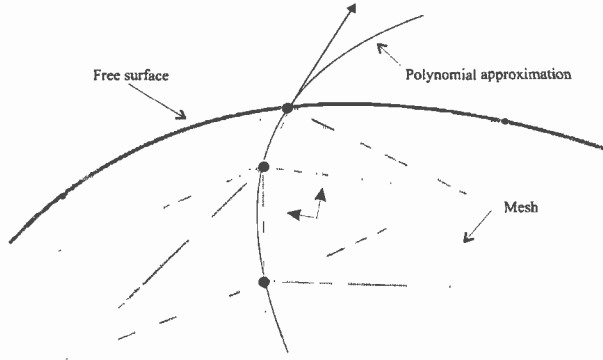$$\widehat{\nabla\Phi}_i \cdot \kappa \;=\; \widehat{\Phi}_\kappa. \tag{2.48}$$

Figure 2.5: *Illustration of the geometric configuration used to determine the non tangential vector and potential derivative at the free surface.*

Otto (1999) also investigated the use of 2-dimensional polynomials of different orders to directly interpolate the potential values at the nodes. The surface velocity approximation $\widehat{\nabla \Phi}$ is then determined by direct differentiation of this 2 dimensional polynomial. Based on extensive numerical simulations, he came to the following conclusions

- Higher-order ($p > 2$) 2-dimensional polynomials can lead to improved accuracy of simulations where fixed impermeable boundaries are modelled.

- Two-dimensional polynomial approximations result in less accurate or even unstable simulations when moving boundaries are involved in the simulation.

Further studies showed that the improved accuracy using higher-order polynomials can also be achieved using 1-dimensional polynomials and therefore the use of 2-dimensional polynomials to construct local finite difference formula was not further investigated.

2.3   Implementation

In this section the implementation of the numerical algorithm, depicted schematically in Fig. 2.2 on page 25, will be briefly discussed. Examination of the scheme shows that there are three levels of computation depending on the extent to which a step in the algorithm is global or local. At the highest level, the control of the complete loop itself and the implementation of step (C) is performed. At the intermediate level the computations that require local knowledge of the numerical grid, steps (B) and (D),

are situated. At the lowest level, the computations related to the time-integration of a single unknown q_i, steps (A), (E) and (F), are implemented. Components of this lowest level will be called particles and components of the intermediate level are called domains. The implementation of a component consists of the implementation of a data structure and the implementation of the interface with that data structure. The interface of all domains is identical and so is the interface of all particles. A domain may e.g. represent a model of the wave maker or of a numerical beach. Examples of particles are free-surface grid points but also numerical particles that implement e.g. a Sommerfeld condition. Components (of all levels) only share information through their interfaces, the actual implementation is thus hidden from other components. In Object Oriented (OO) programming methods, the blue print of a component (the data structure and interface) is called a class while an implementation (of the interface and actual data) of a class is called an object. Multiple objects can be constructed from a single class. New classes can be constructed from old classes by the concept of inheritance. The new class contains all functionality of its ancestor class and only additional interfaces and data structures are coded.

The OO programming approach to the implementation of the numerical algorithm allows to independently develop, implement and test domains and particles and then freely combine them into different configurations. A master-domain and master-particle have been developed that define all the necessary interfaces. Newly developed and implemented domains can be used without additional coding with existing domains as long as the new domain is inherited from this parent. The master-particle has also implemented all uniform operations , (A) and (F), so the only coding for new particles is the implementation of step (E). The same approach has been used for the implementation of the grid generation algorithms and the implementation of the Finite Element Method. The result is a clear, code efficient, maintainable and easy extendable computer program which proved of great value in the development, implementation and testing of over 20 different domains (different kind of wave generators, numerical beaches, naval structures, grid structures, finite elements, finite difference schemes, etc.) that can be used in arbitrary combinations.

2.4   Scope of the investigations

In this chapter Eqs. (2.23a)-(2.23f) governing the motion of the free surface on a layer of water have been derived. For many practical situations, the solution of these equations cannot be obtained exactly and numerical techniques are necessary to find an approximate solution. The numerical algorithm developed in this thesis is classified as a surface-tracking, mixed Eulerian-Lagrangian (MEL) method. It is based on the explicit time-integration of the dynamic and kinematic boundary conditions. The solution of the Boundary-Value Problem for the potential in the fluid is approximated using a Finite Element Method based on piecewise continuous polynomial approximations. The velocity is recovered from the potential using Finite

Differences or a global projection method.

The main aim of the investigations is to develop the numerical algorithm to include the generation and absorption of waves and to establish the accuracy, stability, applicability and efficiency of the numerical methods with respect to the simulation of nonlinear gravity waves in a hydrodynamic model test basin. Secondary, the investigations aim for a rationale to choose the free parameters in the numerical algorithm such as the numerical grid density, the polynomial orders of the FE and FD approximations and parameters related to the generation and absorption of waves, given practical limitations on e.g. the available computing time.

Chapter 3

Simulation of Free-Surface Waves

This chapter considers the numerical simulation of free-surface waves using the numerical algorithm introduced in the previous chapter. A complete model of waves in a hydrodynamic model test basin consists at least of three parts: the generation, the propagation and the absorption of waves. In this chapter we focus on the propagation of waves and therefore investigate the numerical scheme using the natural boundary conditions on the lateral walls. The natural boundary conditions correspond to fixed impermeable walls and the corresponding physical system is an open container filled with water and is given by

$$\nabla \Phi \cdot n = 0 \quad \text{on lateral boundaries.} \tag{3.1}$$

The numerical methods introduced in the previous chapter will be investigated for this boundary condition. The dispersive properties, stability and accuracy will be examined in order to ascertain the quality of the numerical solutions.

First some linear and nonlinear models of water wave propagation will be briefly introduced to provide reference solutions. Secondly, the rate of convergence and stability of the numerical scheme will be investigated. The effect of several velocity recovery and Finite Element schemes on the stability is examined. From analysis of the time integration, some results regarding the dissipative properties of the discretised equations are derived.

Next, the dispersive properties of the numerical scheme will be investigated. This dispersive investigation is based on the linearisation of the discretised governing equations. The influence of different numerical methods on the dispersion relation will be made quantitative. In relation to the accuracy the issue of computational complexity will be considered. Several nonlinear simulations are carried out to establish the mass and energy conserving properties of the numerical algorithm.

Finally, two applications of the numerical algorithm on problems with natural boundary conditions will be presented. The first application is related to a comparative study of a sloshing wave in an open container. The second application is a study of the splitting of solitary waves when propagating over an uneven bottom.

3.1 Linear and non-linear wave models

This section introduces the basic concepts of propagating linear water waves and some non-linear wave theories that will be used to investigate the result of the numerical simulations. Both linear and non-linear water waves are well-established fields of research and for an extensive overview we refer to the textbooks of Debnath (1994) and Dingemans (1997a,b). The following subsections are by no means extensive and only highlight some of the aspects of linear on nonlinear wave theory that are used in the course of this thesis.

3.1.1 Progressive periodic linear waves

Consider the free surface that is unbounded in the horizontal direction on a uniform layer of water with depth $z = -h$. The linearisation of the equations is performed in two steps to clarify the origin of the conditions for linearisation. Firstly, the quadratic terms in Φ and η in Eqs. (2.23b)-(2.23f) are discarded, but the equations are still evaluated at the free surface, resulting in

$$\Delta\Phi = 0 \qquad -h < z < \eta(\mathbf{x}, t) \tag{3.2a}$$

$$\Phi_t - \frac{S_0'}{\rho} + g\eta = 0 \qquad z = \eta(\mathbf{x}, t) \tag{3.2b}$$

$$\eta_t = \Phi_z \qquad z = \eta(\mathbf{x}, t) \tag{3.2c}$$

$$\Phi_z = 0 \qquad z = -h. \tag{3.2d}$$

In Eq. (3.2b) $S_0' = \gamma_s \nabla \cdot \nabla\eta$ is the linearisation of the surface tension S' defined in Eq. (2.16).

Using the standard technique of separation of variables a basic solution of Eq. (3.2a) satisfying the bottom boundary condition (3.2d) is sought as

$$\Phi(\mathbf{x}, z, t) = C_1 \left[\cosh(k(z + h))\right] \left[A_1 e^{i(\mathbf{k}\cdot\mathbf{x})} + A_2 e^{-i(\mathbf{k}\cdot\mathbf{x})}\right] T(t) \tag{3.3}$$

where the notation $k = |\mathbf{k}|$ has been used. Substitution of Eq. (3.3) in the linearised boundary equations (3.2b)-(3.2c) results in

$$\frac{\partial^2 T(t)}{\partial t^2} + \left(gk \tanh\left(k(\eta(\mathbf{x}, t) + h)\right)\left(1 + \frac{\gamma_s k^3}{\rho}\right)\right) T(t) = 0 \tag{3.4}$$

From Eq. (3.4) it is observed that the linearised boundary conditions around $z = \eta(\mathbf{x}, t)$ do not have a solution that can be obtained by the separation of variables, because clearly the equation for $T(t)$ is not independent of $\mathbf{x}$.

In order to construct a non-trivial solution, one needs to make a second linearisation that removes the spatial dependence from the argument of the tangent hyperbolic in Eq. (3.4). This can be achieved by the approximation

$$\tanh\left(k(\eta(\mathbf{x}, t) + h)\right) \simeq \tanh\left(kh\right) \tag{3.5}$$

which imposes the following two conditions on η:

$$\text{(A)} \quad |\eta| \ll h \qquad \text{(B)} \quad k\,|\eta| \ll 1$$

For deep water waves ($h \gg \lambda$) condition (A) is already satisfied and for shallow water waves ($kh \ll 1$) condition (B) is already satisfied. The conditions (A) and (B) result in the same set of equations that follow from evaluation of the boundary conditions (3.2b-3.2c) at $z = 0$ instead of $z = \eta$ (see e.g. Dingemans (1997a)). Under these conditions, transient solutions of Eqs. (3.2a)-(3.2d) subject to fixed, moving or oscillating pressure distributions or an initial surface displacement (initial value problems) can be obtained using combined Laplace (in time) and Fourier (in space) transformations (cf. e.g. Debnath (1994) Chapter 3).

When the conditions (A) and (B) for geometric linearisation are met, the solution $T(t)$ of Eq. (3.4) is harmonic and the frequency ω is related to the wavenumber $\mathbf{k}$ according to the dispersion relation

$$\omega^2 = \left(1 + \frac{\gamma_s k^2}{\rho g}\right) gk \tanh(kh). \tag{3.6}$$

Evaluation of the factor $\frac{\gamma_s k^2}{\rho g} \approx 2.94 \cdot 10^{-4}/\lambda^2$ shows that the influence of the surface tension is only relevant ($> 1\%$) for wavelengths smaller than approximately 17 [cm]. These waves are called capillary waves and are not in the regime of wave lengths typical for a hydrodynamic model test basin.

Ignoring the surface tension terms in Eq. (3.6) results in the well-known dispersion relation for free-surface water waves:

$$\omega^2 = gk \tanh(kh). \tag{3.7}$$

Final evaluation of the real-valued progressive wave solutions for Φ and η results in

$$\eta(\mathbf{x}, t) = a\cos(\mathbf{k} \cdot \mathbf{x} - \omega t) \tag{3.8a}$$

$$\Phi(\mathbf{x}, z, t) = \frac{ag}{\omega}\frac{\cosh(k(z-h))}{\cosh(kh)}\sin(\mathbf{k} \cdot \mathbf{x} - \omega t). \tag{3.8b}$$

From Eqs. (3.8a)-(3.8b) the velocity and pressure field can be easily obtained and limiting formulae for shallow and deep water are readily derived. It is noted that the

dispersion relation Eq. (3.7) also has infinitely many imaginary solutions ik_j. The corresponding solutions for Φ and η are called evanescent modes (see also Subsection 4.1.1). These evanescent modes are not progressive but decay exponentially in the horizontal direction.

Regular progressive linear waves are thus sinusoidal, propagate with a phase velocity $c(k) = \omega(k)/k$ and have an exponential decaying velocity profile in the negative z-direction. There is no mass transport due to the wave propagation and the dispersion relation Eq. (3.7) is independent of the amplitude. Another important parameter in linear wave theory is the group velocity which is defined as $c_g = \frac{\partial \omega}{\partial k}$.

The above travelling wave solutions were obtained on a domain that is unbounded in the horizontal coordinates. A similar analysis can be made for standing waves in a container. The additional boundary condition

$$\nabla \Phi \cdot n = 0 \tag{3.9}$$

is then applied at $x = 0$ and $x = L$, resulting in a countable number of linear standing wave solutions. The wave number and frequency of a standing wave solution also satisfy the dispersion relation Eq. (3.7). It is noted that under these boundary conditions no evanescent modes exist.

3.1.2   Nonlinear progressive wave models

Stokes (1847) was the first to establish the nonlinear solution for periodic wave trains on deep water. These solutions are based on systematic power series in the wave slope ka and are known as the Stokes expansions. Substitution of these expansions in the governing equations Eq. (2.23b) and (2.23e)-(2.23f results in a series solution of the free surface η for a steadily propagating nonlinear wave. The first three terms of the expansion for the elevation are given as

$$\eta = a \cos(\theta) + \frac{1}{2}ka^2 \cos(2\theta) + \frac{3}{8}k^2 a^3 \cos(3\theta) \tag{3.10}$$

where the phase function is defined as $\theta = (kx - \omega t)$. Levi-Civita (1925) proved that the power series are convergent if the ratio of amplitude to wavelength is sufficiently small, thus establishing the existence of permanent waves satisfying the exact nonlinear boundary conditions. Struik (1926) extended the proof of Levi-Civita to waves on finite water depth but it was Krasovskii (1960, 1961) who proved the existence of permanent periodic waves only to the restriction that their slope is less than the limiting value of 30 degrees. Later proofs of the existence are given by Keady & Norbury (1978) and Toland (1978).

The surface profile of these nonlinear solutions is trochoidal instead of sinusoidal and in contrast to linear waves, Stokes waves have a mean horizontal velocity (Stokes drift or Lagrangian mean velocity) which is $\mathcal{O}(\omega k a^2)$ in magnitude. Another noticeable

difference with respect to linear wave theory is the dispersion relation which is of the form (ignoring surface tension)

$$\omega^2 = gk\left(1 + a^2k^2 + \frac{5}{4}a^4k^4 + \mathcal{O}((ak)^6)\right) \tag{3.11}$$

and clearly depends on the amplitude. The consequence is that steep waves travel faster than less steep waves with the same wavelength. The wave height H for a regular Stokes wave is defined as the distance between crest and trough and its maximum on deep water is

$$\left(\frac{H}{\lambda}\right)_{\mathrm{max}} = 0.14 \ . \tag{3.12}$$

It should be noted that the Stokes expansion for shallow water is only valid for very small wave steepness. More precisely, the Stokes parameter (also called Ursell parameter)

$$\frac{a/h}{(kh)^2} \equiv \frac{1}{4\pi^2}\frac{a/h}{(h/\lambda)^2} \tag{3.13}$$

should be small (which is automatically satisfied for deep water waves). When the Stokes parameter is of order one, the nonlinear shallow water wave equations can be derived. Introducing the expansion parameters

$$\epsilon = a/h \tag{3.14}$$
$$\delta = h^2/\lambda^2 \tag{3.15}$$

and expanding the fluid potential in δ and substitution into the non-dimensional governing equations, retaining both order ϵ and δ terms, results (in one horizontal dimension) in the Boussinesq (1872) equations:

$$u_t + \epsilon u u_x + \eta_x - \frac{1}{2}\delta u_{txx} = 0 \tag{3.16a}$$

$$\eta_t + [u(1 + \epsilon\eta)]_x - \frac{1}{6}\delta u_{xxx} = 0. \tag{3.16b}$$

which are equivalent (in normalised variables and after regularisation) to the following equation (also called improved Boussinesq equation)

$$\frac{\partial\eta^2}{\partial t^2} - gh\frac{\partial\eta^2}{\partial x^2} = \frac{\partial^2}{\partial x^2}\left(\frac{3}{2}g\eta^2 + \frac{1}{3}h^2\frac{\partial\eta^2}{\partial t^2}\right). \tag{3.17}$$

When additional assumptions are made concerning the relative permanency of the waves and uni-directional propagation the following equations can be derived from Eq. (3.16a)-(3.16b)

$$\eta_t + (1 + \frac{3}{2}\epsilon\eta)\eta_x + \frac{1}{6}\delta\eta_{xxx} = 0 \tag{3.18}$$

which in dimensional variables becomes

$$\eta_t + \sqrt{gh}(1 + \frac{3}{2h}\eta)\eta_x + \frac{\sqrt{gh}h^2}{6}\eta_{xxx} = 0. \tag{3.19}$$

Equations (3.19) is known as the Korteweg & de Vries (1895) (KdV) equation and has been extensively studied. Both the Boussinesq and the KdV equations have periodic and solitary wave solutions (known as solitons for the KdV equation). The solitary solutions have a sech^2 profile and the periodic solutions are called cnoidal waves because of their typical cn^2 profile, where cn is the Jacobian elliptic function. The cnoidal waves have the same property as the Stokes waves, i.e. they have steeper crests and flatter troughs.

The Stokes expansion is only valid for $ak \ll (kh)^3$ (a small Stokes parameter Eq. (3.13)) and clearly the cnoidal wave solutions are only valid for small ϵ and δ. Rienecker & Fenton (1981) developed a numerical method to approximate the steadily progressive periodic wave solution of Eq. (2.23b)-(2.23f) based on a Fourier approximation of the potential. The advantage of this technique is that its only approximation is the truncation of the Fourier series and is thus (in contrast with the Stokes and cnoidal expansions) uniformly valid for all wavelengths.

Another widely used model equation for nonlinear wave propagation is the Non-Linear Schrödinger (NLS) equation. The equation describes the dynamic evolution of the slowly varying complex wave envelope A of a carrier wave with wavenumber k_0. I.e., in lowest order the solution is of the form

$$\eta(x, t) = A(x, t)e^{i(k_0 x - \omega t)} + \ c.c. \tag{3.20}$$

The NLS equation can be derived in different ways, e.g. by expansion of the nonlinear dispersion relation, Whitham's equations for the slow modulation of the wave amplitude (Chu & Mei (1970, 1971)), a multiple-scale expansion (Davey (1972), Hasimoto & Ono (1972)) or from the Resonant Interaction Equations (Phillips (1981)). The resulting NLS for the complex amplitude A (in a frame of reference moving with the linear group velocity) is

$$iA_\tau + \beta' A_{\xi\xi} - \gamma'|A|^2 A = 0 \tag{3.21}$$

where the values of β' and γ' depend on the dispersion relation (e.g. van Groesen (1998)).

3.2   Accuracy and stability

Every numerical solution contains errors. The important thing is to know how large these errors are and whether or not they are acceptable for the particular application. The reasons for differences between computed results and measurements are:

- Modelling errors: The differential equation contains approximations and ideal-isations

- Discretisation errors: Approximations are made in the discretisation process

- Iteration errors: The error in the iterative method used to solve the discretised equations

- Measurement errors

The first type of errors has already been discussed in Section 2.2 where the motivation for the simplified potential flow description has been given. The second kind of errors are usually difficult to quantify and are therefore described by the order of convergence of the method and by comparing approximations to known exact properties of the model equations. The third type of errors occurs when iterative procedures are used to solve the large (non-)linear systems arising from discretisations. In all iterative solutions used in this thesis, the iteration error (relative residu in is set to 10^{-12} and these errors are thus considered negligible with respect to the discretisation errors. For references on the iterative solution of (sparse) linear systems we refer to Barret *et al.* (1994) and Smith *et al.* (1997). The last type of errors results from imperfect measurement devices and indirect measurements techniques that make use of an (imperfect) model to post-proces the original measurements (see e.g. the analysis on the error in the measured reflection coefficient in Subsection 5.2.1).

In general the ultimate goal of a numerical scheme is to obtain a desired accuracy with least effort or the maximum accuracy with the available resources. As was pointed out in the introduction of this thesis one of the practical restrictions is that the computer code that implements the numerical scheme must run on a desktop computer and simulations need to be finished in overnight jobs. Therefore, we focus on the maximum accuracy with the available resources and verify whether or not the results can still be applied for practical situations.

As well-established methods are used to discretise the different elements of the partial differential equation, the consistency of the discretisation is taken for granted. Therefore the main concern of this section is the convergence and stability of the numerical scheme. For linear problems, stability and consistency imply convergence (Lax Equivalence Theorem) and investigation of the (linear) stability is therefore first performed. Secondly, the rate of convergence of the full set of discretised equations is investigated by systematic grid refinement. The analysis of stability and convergence depends on the used grid, and therefore the gridding algorithm for undisturbed wave propagation is first introduced.

3.2.1   Grid

A grid is a discrete representation of the geometric domain on which the problem is to be solved. In this thesis structured (also called regular) grids are used. A

(a) fixed triangular orientation   (b) alternating triangular orientation
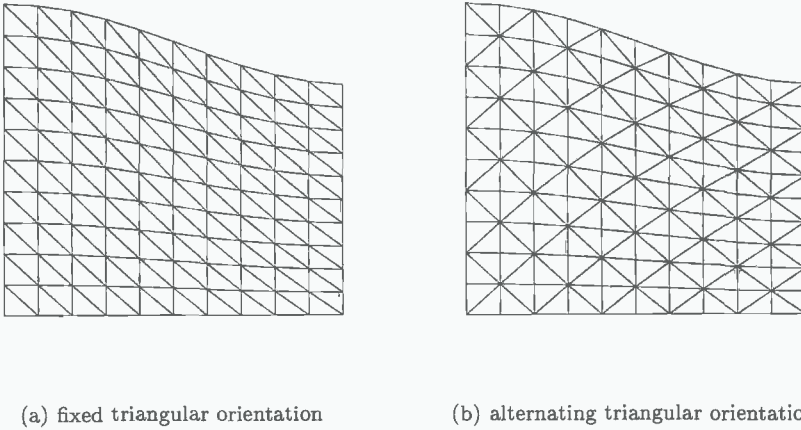
Figure 3.1: *Illustration of two regular gridding strategies. The node connectivity is not changed during simulations.*

regular grid consists of families of grid lines with the property that the members of a single family do not cross each other and cross each member of the other family only ones. In all simulations presented in this thesis structured grids of the H- type and block-structured grids are used.

As we do not consider overturning or breaking waves, no special attention is needed to grid these complex geometries. Fig. 3.1 shows two typical regular griddings (triangulations) of the domain. The nodes (intersections of the grid lines) are uniformly distributed over each vertical grid line. The position of the nodes thus depends on the free surface grid points and is not fixed during a numerical simulation. The element structure however, is unchanged and the connectivity of the nodes is thus static. Remark that despite the optical illusion, subfigure (a) and (b) of Fig. 3.1 differ only in node connectivity. In the next section the effect of this type of grids on the stability will be investigated.

Besides the triangular orientation of the elements in the grid, another variation used in the simulations is the vertical density of the nodes. As will be shown in the next sections, the use of a non-uniform grid in the depth is highly beneficial for the accuracy of the simulation. The level of redistribution of the grid points in the vertical direction is parameterised by a factor β. At a certain point on the free surface with x-coordinate x and z-coordinate η, the local depth is given by $h(x)$. The number of grid points in vertical direction is fixed, and denoted as nz. The successive distances Δz_i between two nodes on the vertical line increases with a certain rate β. The vertical mesh width of the i-th element in the negative z-direction is thus defined as

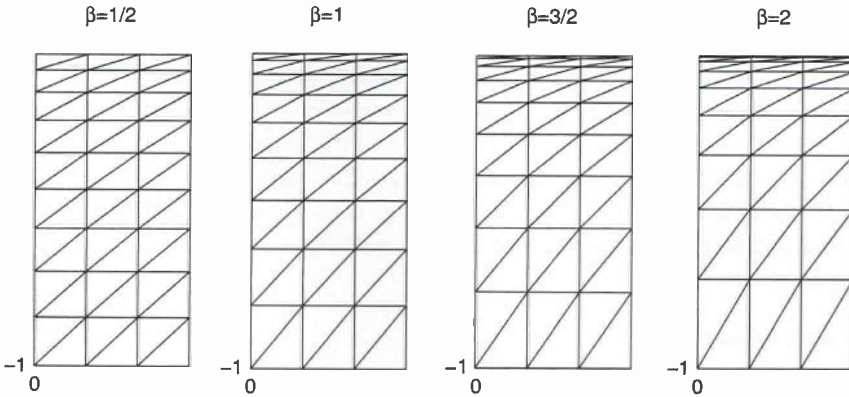$$\Delta z_i = \alpha \cdot i^\beta \quad i = 1 \ldots n_z - 1 \tag{3.22}$$

Figure 3.2: *Effect of the redistribution parameter β on the element density. The number of grid nodes is kept constant.*

where α is solved from

$$\sum_{i=1}^{nz-1} \alpha \cdot i^\beta = h(x) + \eta. \tag{3.23}$$

Fig. 3.2 shows the grid for different values of β. Of course, different possibilities exist to define the grid density, but the used method turned out to work quite well.

The algorithm for determining the grid based on the boundary nodes is identified by a set of two maps $\{\Xi, \Theta\}$. The map Ξ determines the position of the nodes that are not on the free surface boundary as a function of the position of the boundary nodes. The map Θ determines the node connectivity and maps the global node numbers to the local element node numbers associated with the nodal base functions on each element. All gridding algorithms used in this thesis are such that Ξ is a continuous map and Θ is time invariant.

3.2.2   Stability Analysis

In Section 2.2, the numerical methods and techniques have been introduced to discretise Eqs. (2.23b)-(2.23f). In this section we investigate the stability of the discretisation with respect to the natural boundary conditions. Rigorous results on the stability of the discretised nonlinear equations are not available. Instead the problem is split up in the stability of the time continuous, spatially discretised equations and the stability of the time integration method. It should be noted that the presented stability conditions are only necessary and not sufficient for stability of the nonlinear discretisation.

The Cauchy stability of the time continuous system is obtained by a Von Neumann

analysis of the linearised discrete equations. The stability of the time integration method is determined using standard Runge-Kutta results. In order to perform the Von Neumann analysis, the discretised equations need first to be derived in an appropriate form. It is noted that the stability of numerical wave simulations is certainly not a trivial topic. Almost all developers of numerical codes that implement some discretisation of the governing equations, mention the 'familiar' saw-tooth instability. This point-to-point instability results in growth of $2\Delta x$ waves and is removed from the solution by some kind of smoothing or filtering, cf. e.g. Longuet-Higgins & Cokelet (1976), Dold (1992) and Robertson & Sherwin (1999).

Discretised equations

Let the set of all nodes be denoted as $\mathcal{V}$ and the node numbers whose corresponding mesh nodes belong to the free-surface boundary be denoted by $\mathcal{D}$. The set of nodes not belonging to $\mathcal{D}$ is denoted as $\mathcal{I} = \mathcal{V} \setminus D$. The notation for the index sets is also used to map the node numbering as in

$$N_j^{\mathcal{I}} = N_{\mathcal{I}(j)} \tag{3.24}$$

As in the previous chapter, the functions N_i (see definition in 2.2.4) are the base functions associated with every node $i \in \mathcal{V}$. The approximation $\widehat{\Phi}$ is represented by these base functions as

$$\widehat{\Phi} = \sum_{i \in \mathcal{I} \cup \mathcal{D}} \varphi_i N_i. \tag{3.25}$$

The vector φ containing the scalar coefficients of the base functions is thought to be ordered as

$$\varphi = \begin{pmatrix} \varphi^{\mathcal{I}} \\ \varphi^{\mathcal{D}} \end{pmatrix} \tag{3.26}$$

The vector containing the position of the grid points on the free surface is denoted as

$$\eta = \begin{pmatrix} x \\ \widehat{\eta} \end{pmatrix}, \tag{3.27}$$

i.e. first a vector containing the x-coordinate of the grid points, then the vector containing the z-coordinate of the grid points.

The discretisation of the nonlinear kinematic and boundary conditions for a moving grid point on the free surface Eq. (2.25)-(2.27) can be expressed as

$$\frac{\mathrm{D}x}{\mathrm{D}t} = (1-\sigma)\mathbf{D}^x[\eta]\varphi^{\mathcal{D}} \tag{3.28a}$$

$$\frac{\mathrm{D}\widehat{\eta}}{\mathrm{D}t} = \mathbf{D}^z[\eta]\varphi^{\mathcal{D}} - \sigma\mathbf{D}^x[\eta]\varphi^{\mathcal{D}}\tilde{\mathbf{D}}^x\eta. \tag{3.28b}$$

$$\frac{\mathrm{D}\varphi^{\mathcal{D}}}{\mathrm{D}t} = \left(\frac{1}{2}\mathbf{D}^\nabla[\eta]\varphi^{\mathcal{D}} - \sigma\begin{pmatrix} \mathbf{D}^x[\eta]\varphi^{\mathcal{D}} \\ \mathbf{D}^x[\eta]\varphi^{\mathcal{D}}\tilde{\mathbf{D}}^x\eta \end{pmatrix}\right) \cdot \mathbf{D}^\nabla[\eta]\varphi^{\mathcal{D}} - g\widehat{\eta} \tag{3.28c}$$

In equation (3.28) the operators $\mathbf{D}^{\cdot}$ map the discrete values of η and x and $\widehat{\eta}$ to the approximations of the derivatives. When a solution of the boundary-value problem is involved, this operator depends on the geometry $\widehat{\Omega}$ and thus on η which is made explicit by using brackets.

$\mathbf{D}^z[\eta]$	maps the value of the free-surface potential nodes, through the approximation of the boundary-value problem and the recovery method of vertical velocity to the approximation of $\widehat{\Phi}_z$ at the boundary nodes.
$\mathbf{D}^x[\eta]$	idem for the approximation of $\widehat{\Phi}_x$
$\mathbf{D}^\nabla[\eta]$	approximation of the potential gradient as $(\mathbf{D}^x[\eta], \mathbf{D}^z[\eta])$
$\tilde{\mathbf{D}}^x$	maps η to the approximation of η_x at the boundary nodes.

In the previous section it was mentioned that all gridding algorithms depend continuously on η. Therefore the approximation of the solution of the boundary value problem depends continuously on η and thus do the operators governing the derivatives. These operators can thus be expanded around $\eta = 0$ as

$$\mathbf{D}^*[\eta] = \mathbf{D}^*[0] + \nabla_\eta \mathbf{D}^*[0]\eta + \mathcal{O}(\eta^2) \tag{3.29}$$

Linearisation of Eqs. (3.28) around $\eta = 0$ therefore leads to the following set of equations

$$
\begin{align}
x_t &= 0 \tag{3.30a}\\
\widehat{\eta}_t &= \mathbf{D}^z[0]\varphi^{\mathcal{D}} \tag{3.30b}\\
\varphi_t^{\mathcal{D}} &= -g\widehat{\eta}. \tag{3.30c}
\end{align}
$$

We now proceed by the explicit construction of $\mathbf{D}^z[0]$. Substitution of the natural boundary condition Eq. (3.1), i.e. substitution of $g \equiv 0$ in Eq. (2.40) results in the following equation for ϕ:

$$a\left(\sum_{i \in \mathcal{I}} \varphi_i N_i, N_j\right) = -a\left(\sum_{i \in \mathcal{D}} \varphi_i N_i, N_j\right) \quad \forall j \in \mathcal{I}. \tag{3.31}$$

This equation is written in matrix notation as

$$A_{\mathcal{I}\mathcal{I}}\varphi^{\mathcal{I}} = -A_{\mathcal{I}\mathcal{D}}\varphi^{\mathcal{D}} \tag{3.32}$$

where the matrices $A_{\mathcal{K}\mathcal{L}}$ are $\dim \mathcal{K} \times \dim \mathcal{L}$ matrices and the elements are given by

$$(A_{\mathcal{K}\mathcal{L}})_{ij} = a\left(N_{\mathcal{K}(i)}, N_{\mathcal{L}(j)}\right). \tag{3.33}$$

The solution φ is given by

$$\varphi^{\mathcal{I}} = -A_{\mathcal{II}}^{-1} A_{\mathcal{ID}} \varphi^{\mathcal{D}} \tag{3.34}$$

The linear operator that maps the values of φ to the approximation of the vertical derivative in the nodes of φ is denoted as D^z. The components of D^z are ordered as

$$D = \begin{bmatrix} D_{\mathcal{II}} & D_{\mathcal{ID}} \\ D_{\mathcal{DI}} & D_{\mathcal{DD}} \end{bmatrix}. \tag{3.35}$$

It now follows directly that

$$\mathbf{D}^z[0]\varphi^{\mathcal{D}} = [-D_{\mathcal{DI}}^z A_{\mathcal{II}}^{-1} A_{\mathcal{ID}} + D_{\mathcal{DD}}^z]\varphi^{\mathcal{D}} = L_{\mathcal{D}}\varphi^{\mathcal{D}} \tag{3.36}$$

The set of equations (3.30), ignoring the trivial part, can thus be written as

$$\frac{\partial}{\partial t} \begin{pmatrix} \widehat{\eta} \\ \varphi^{\mathcal{D}} \end{pmatrix} = \begin{pmatrix} 0 & L_{\mathcal{D}} \\ -gI & 0 \end{pmatrix} \begin{pmatrix} \widehat{\eta} \\ \varphi^{\mathcal{D}} \end{pmatrix} \tag{3.37}$$

For future convenience we will denote the linearised system of discrete equations as

$$\mathbf{q}_t = \mathbf{A}\mathbf{q} \tag{3.38}$$

In actual computations of $\mathbf{A}$, first all interactions $a(N_i, N_j)$ are calculated for all i, j. The different submatrices are formed by first applying permutation matrices to obtain the different numberings, defined by the different index sets. After the matrix is thus efficiently reordered, the submatrices are formed by simple restriction. The inverse matrix is not constructed by Gauss Elimination but by iterated solutions of the $|\mathcal{D}|$ linear equations defined by

$$-A_{\mathcal{II}}X = A_{\mathcal{ID}} \tag{3.39}$$

where use is made of a single Incomplete Cholesky Factorisation to provide a preconditioner. In this way the matrix $\mathbf{A}$ can be efficiently constructed.

Stability of the spatial discretisation

As is well known, the eigenvalues of the matrix $\mathbf{A}$ determine the stability of the system (3.38).

LEMMA 1 *Given the real $2n \times 2n$ matrix*

$$A = \begin{bmatrix} 0 & S \\ -I_n & 0 \end{bmatrix} \tag{3.40}$$

If S has eigenvalues ν_k, then the eigenvalues μ_k of A are given by $\mu_{\pm k} = \pm i\sqrt{\nu_k}$.

Proof. Using the determinant rule for the Schurr complement we find that

$$\det(\mu I_{2n} - A) = \det(\mu I_n) \det\left(\mu I_n - I_n (\mu I_n)^{-1}(-S)\right) \qquad (3.41)$$

$$= \mu^n \det(\mu I_n + \mu^{-1} S) \qquad (3.42)$$

$$= \det(\mu^2 I_n + S) \qquad (3.43)$$

So, μ is an eigenvalue of A if and only if μ^2 is an eigenvalue of $-S$. Therefore the spectrum of A consists of $\mu_{\pm k} = \pm i \sqrt{\nu_k}$, where ν_k are the eigenvalues of $-S$.   ∎

ASSUMPTION 2 *The meshing algorithm* $\{\Xi, \Theta\}$ *and velocity approximation* D^z *have the property that*

- Ξ *is a continuous function of the free-surface boundary nodes.*

- $-D^z_{\mathcal{DI}} A^{-1}_{\mathcal{II}} A_{\mathcal{ID}} + D^z_{\mathcal{DD}}$ *has positive real eigenvalues.*

THEOREM 3 *The linearised discretised equations (3.38) are Cauchy stable.*

Proof. From the definition of **A** in Eqs. (3.36)-(3.39), scaling of g and application of the previous lemma, it directly follows that the eigenvalues of **A** are all purely imaginary. Therefore all eigenvectors of the linear system do not grow in time and the Von Neumann criterion for Cauchy stability is satisfied.   ∎

Using Theorem 3, a computable criterion is available to determine the (linear) stability of the different FE/FD schemes. This criterion has been checked for many combinations of FD methods, FE base functions, triangular orientation of the grid and values of the density parameter β. These results will be discussed briefly in the next paragraph.

Firstly the stability of the numerical scheme is investigated when the original Finite Difference implementation (see Section 2.2.5) is used to approximate the vertical velocity at the free surface. The order of approximation of this velocity is $\mathcal{O}(h^p)$ where p is the order of the fitting polynomial. The polynomial order used for finite differencing to obtain $\widehat{\Phi}_z$ is denoted as $p[FD]$. The polynomial order of the base functions used in the Finite Element approximation is denoted as $p[FEM]$.

The parameters $p[FD]$, $p[FEM]$, β, the triangular orientation and the number of nodes nx and nz have been systematically varied. $p[FD]$ was varied between 1 and 4 and first and second order finite elements were investigated. The eigenvalues of **A** in equation (3.38) are plotted in Fig. 3.3 for some of these parameter combinations. All these combinations resulted in almost purely imaginary eigenvalues and are thus marginally stable. The fact that the eigenvalues do not exactly lie on the imaginary axis is related to the numerical computation of the eigenvalues. It was also found that the stability is not influenced by variations in the number of nodes in the horizontal
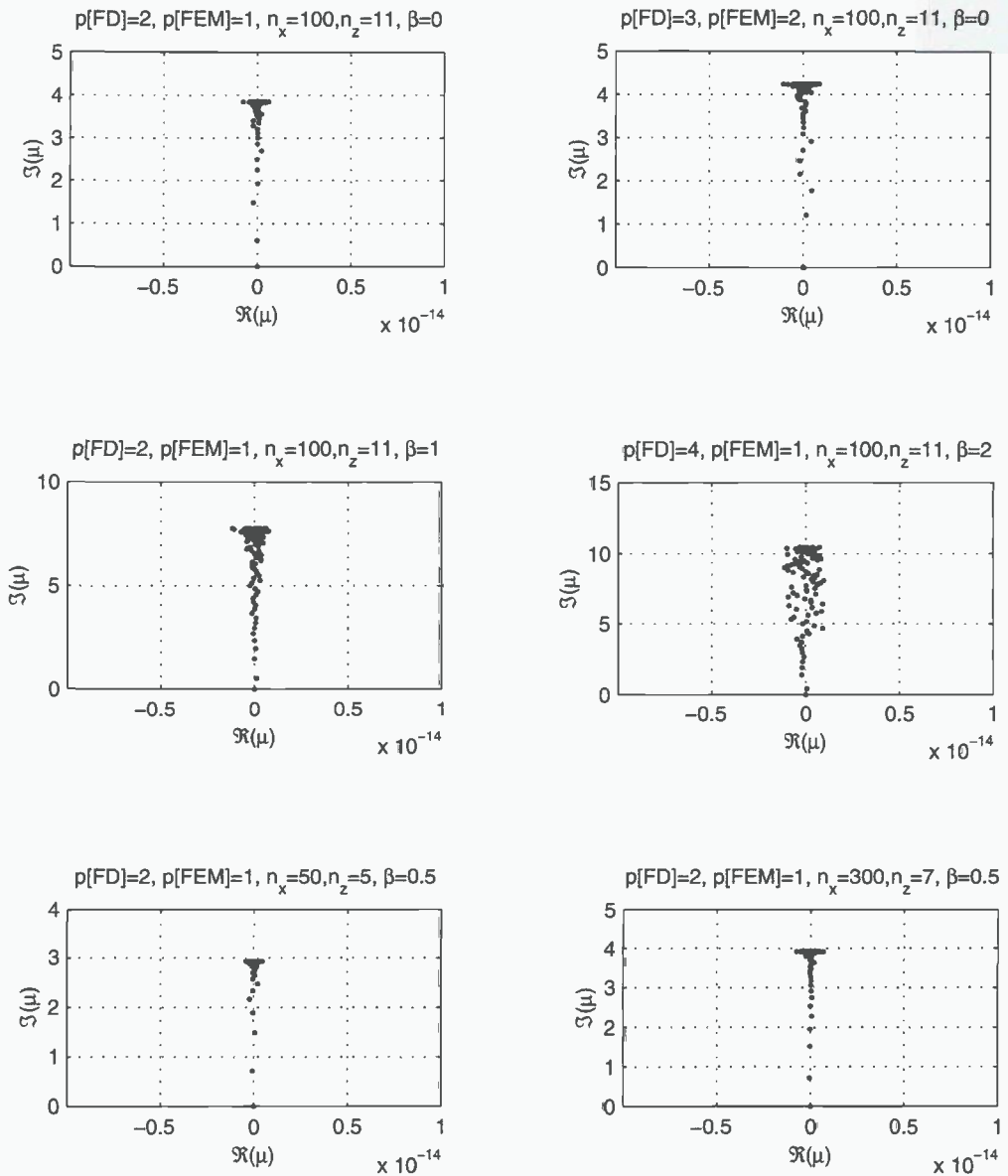
Figure 3.3: *Eigenvalues in the upper complex plane of* **A** *in Eq. (3.38) for different parameters using the 1-dimensional Finite Difference method for velocity recovery (see Section 2.2.5). Note that the horizontal axis is scaled with* 10^{-14}.
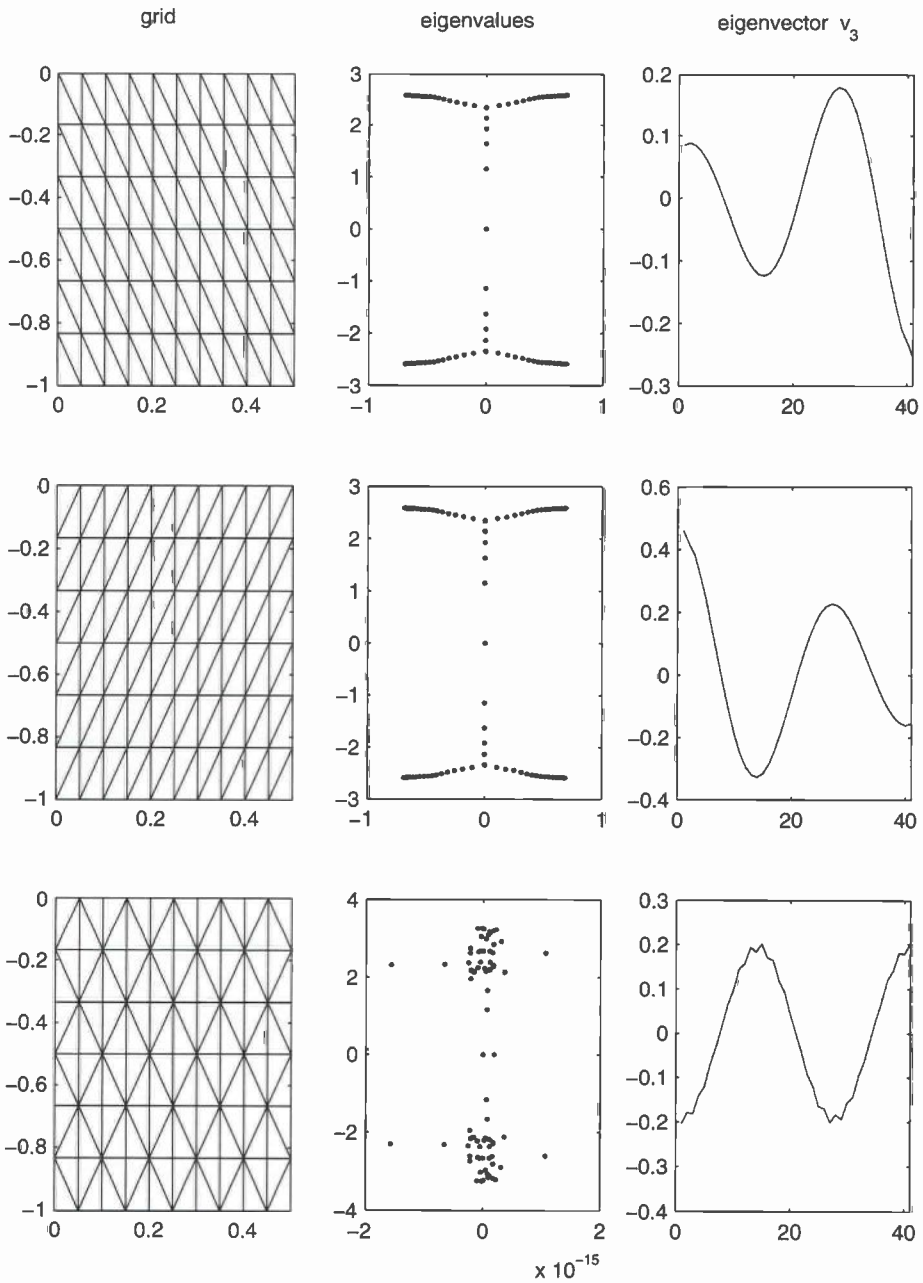
Figure 3.4: *Effect of the grid on the stability of the approximation when a global pro-
jection method is used for velocity recovery. The figure shows the grid (left
column), the corresponding eigenvalues of the linearised discretised equa-
tions (central column) and the eigenvector corresponding to k = 3 (right
column).*

and vertical direction (for fixed dimensions of the computational domain), the aspect ratio of the elements and orientation of the triangular elements.

Evaluation of the stability of the numerical algorithm when the global projection method (see Section 2.2.5) is used, revealed that this velocity recovery method can result in an unstable numerical scheme. This is illustrated in Fig. 3.4 in which the grid, the eigenvalues of Eq. (3.38) and the free-surface part of the (absolute value of the) eigenvector v_3 are visualised when linear finite elements are used. Clearly, the numerical scheme is unstable for the triangulations depicted in the first and second row of the figure. Some eigenvalues associated with the high frequency components have a positive real component. When the orientation of the triangulation is reversed, the spectrum stays identical, but the orientation of the eigenvector is also reversed. Further investigation of the eigenvectors indicated that the instability might be related to whether or not the free-surface corner grid point belongs to 1 or 2 elements. Indeed, when the grid was chosen such that the corner grid points belonged to a single element (third row in Fig. 3.4 on the preceding page), the eigenvalues were all found to be imaginary. However, examination of the eigenvector shows irregular point to point oscillations that are not present in the eigenvectors of the Finite Difference schemes.

Stability of the time integration

In the previous subsection the stability of the spatial discretisation was investigated while the time derivatives were considered to be exact. In this section the stability of the discretisation of the time integration using an explicit Runge-Kutta (RK) method (see also Section 2.2.2) is examined.

Consider the n-dimensional linear differential equation

$$q_t = \mathbf{A}q \tag{3.44}$$

In general one can show that for the s-stage RK formula Eq. (2.29)–(2.31) the following relation holds between two successive estimates of $q_n = q(n\Delta t)$

$$q_{n+1} = P(\Delta t \mathbf{A})q_n. \tag{3.45}$$

where P is called the stability polynomial. The dispersion (or phase) error is defined as

$$\epsilon_\phi(r) = r - \arg[P(r)] \tag{3.46}$$

and the method is said to be dispersive of order q if $\epsilon_\phi(r) = \mathcal{O}(r^{q+1})$. Here we refer to van der Houwen & Sommeijer (1972) and state that any m-stage p^{th} order RK method is dispersive of order $2\lfloor (p+1)/2 \rfloor$ and the maximal attainable order of dispersion is $2(m - p + \lfloor (p+1)/2 \rfloor)$; here $\lfloor x \rfloor$ denotes the integer part of x. In this reference a 5-stage third order RK method, defined by the Butcher arrays as in Table B.3, is presented that is indeed dispersive of order 8.

From straightforward analysis it is readily derived that a necessary and sufficient condition for stability of the time integration is that the eigenvalues μ of $\mathbf{A}$ lie in the RK stability region defined by $|P(\mu\Delta t)| \leq 1$. Applying the RK-scheme defined by Eq. (2.29)-(2.31) to the equation (3.44) directly leads to the stability polynomials P as a function of the parameters a, b and c. For the parameters tabulated in appendix B.2, we find the following polynomials P:

RK44M (Table B.1) $$P(r) = 1 + r + 1/2r^2 + 1/6r^3 + 1/24r^4 \qquad (3.47)$$

RK45M (Table B.2) $$P(r) = 1 + r + 1/2r^2 + 1/6r^3 + 1/24r^4 + 1/120r^5 \quad (3.48)$$

RK35D (Table B.3) $$P(r) = 1 + r + 1/2r^2 + 1/6r^3 + 71/1680r^4 + 1/112r^5 (3.49)$$

RK44M denotes the explicit 4-stage fourth order RK scheme with minimised principal error, RK45M the 5-stage fourth order scheme with minimised principal error and RK35D the 5-stage third order scheme with minimal dispersion (maximal dispersive order).

Fig. 3.5 shows the stability region in the upper half plane of the RK44M and RK45M schemes. In the left figure, one can observe that the stability region of the 5-stage scheme is slightly larger than the 4-stage scheme. The stability region of the RK35D scheme (not depicted) is similar to that of the RK45M scheme.

Close examination of the curves around $Re(\mu) = 0$ shows that the 5-stage stability region does not include a part of the imaginary axis close to the origin that is included by the stability region of the 4-stage scheme. Therefore an eigenvector with a pure imaginary eigenvalue μ will decrease in time due to a 5-stage scheme if

$$1.866 < \Delta t |Im(\mu)| < 3.395. \qquad (3.50)$$

and will increase otherwise. For a 4-stage scheme, this stability region on the imaginary axis is given by

$$\Delta t |Im(\mu)| \leq 2.8284 \qquad (3.51)$$

where 2.8284 is an approximation of $2\sqrt{2}$ and evaluated here numerically for comparison with Eq. (3.50). One can argue that the 5-stage method is not a suitable method for time integration of equation (3.38) because of the unstable region $[0, 1.866]$ on the imaginary axis [1]. However, the following observation needs to be taken into account. The value $|P(\cdot)|$ is a direct measure for the *actual* damping or growth of the eigenvectors of $\mathbf{A}$. In Fig. 3.6 on the next page one can observe the growth factor $|P(\Delta t\mu)|$ for μ that are purely imaginary and positive. From this figure two important observations can be made.

1. Both the 4-stage as the 5-stage method can result in drastic damping of eigenvectors (damping factor of approximately 0.5) with purely imaginary eigenvalues.

---

[1] It is noted that the presence of an unstable region on the imaginary axis is also found for the 4th order Adams-Bashforth-Moulton (ABM4) method
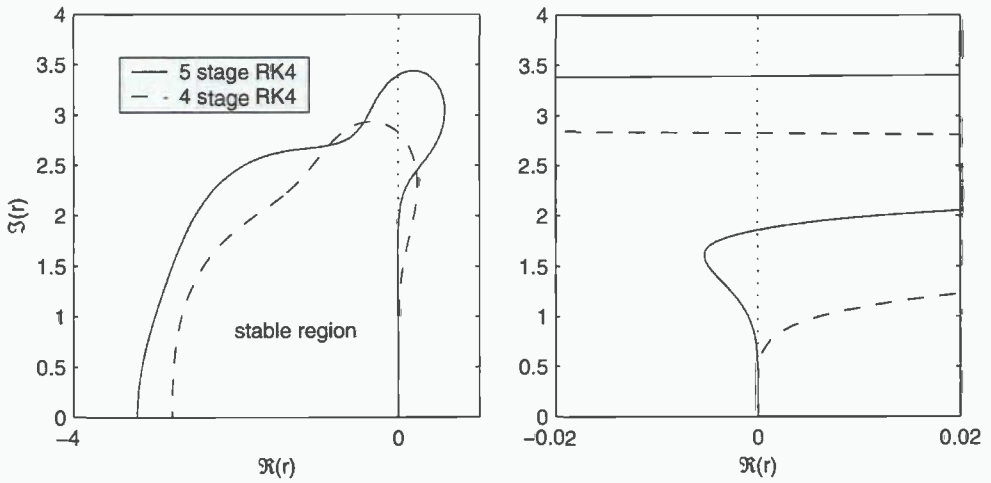
Figure 3.5: *Stability region of the 4-stage and 5-stage fourth order Runge-Kutta methods RK44M and RK45M. The right figure focuses on the stability regions around $\mu = 0$.*
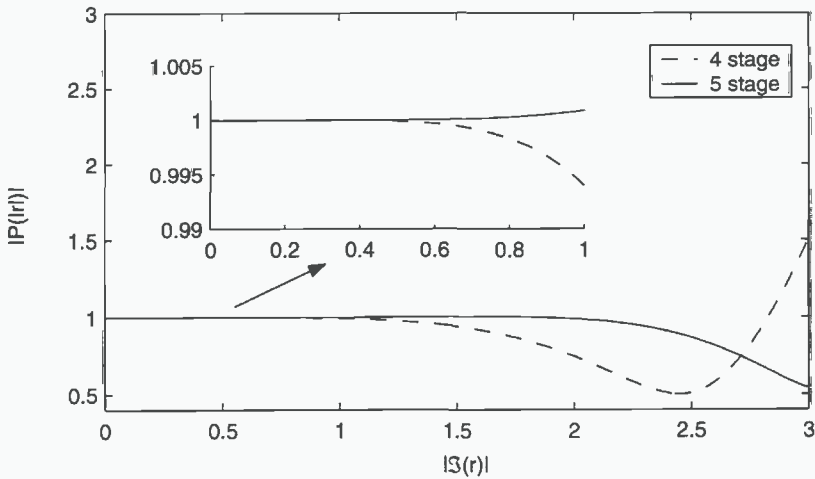

Figure 3.6: *The growth factor $|P(r)|$ along the imaginary axis $(\Re(r) = 0)$ for a 4- and 5-stage fourth order RK method.*
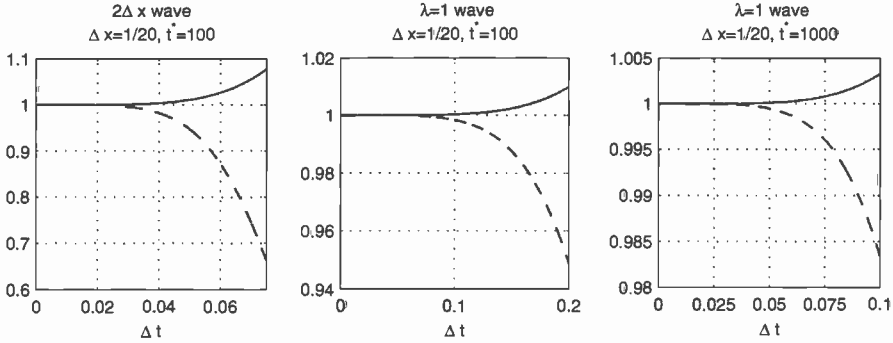
Figure 3.7: *The final growth factor after t^* of simulation time of (a) the fastest evolving mode ($t^* = 100$), (b) the mode corresponding to $\lambda = 1$ ($t^* = 100$) and (c) the same mode for $t^* = 1000$.*

2. In the region $0 < Im(r) < 1.886$, the maximum amplification factor of the 5-stage method is 1.0047 while the amplification factor of the 4-stage method for this value is approximately 0.9.

From linear theory (Section 3.1.1) it is readily verified that (in normalised variables) the maximum eigenvalue of the discrete system (the 'wave' that corresponds to a $2\Delta x$ wave length) is approximately $\sqrt{\pi/\Delta x}$. Therefore the maximum expected eigenvalue of A is $i\sqrt{\pi/\Delta x}$. For a simulation with time interval of length t^* and time step Δt, Eq. (3.52) can be used to obtain an a priori bound on Δt and horizontal spatial mesh width Δx in order to keep the total growth of every eigenvector for $t \in [0, t^*]$ within a desired bandwidth α.

$$\left| |P(i\Delta t\sqrt{\pi/\Delta x})|^{\frac{t^*}{\Delta t}} - 1 \right| \leq \alpha \tag{3.52}$$

Fig. 3.7 shows these final grow factors

$$|P(i\Delta t\omega|^{\frac{t^*}{\Delta t}} \tag{3.53}$$

for three frequencies ω and for specified t^* as a function of Δt. Graph (a) shows the growth of the eigenvector corresponding to the most unstable $2\Delta x$ wave after 100 units of simulation time. It can be observed that for $\Delta t < 0.08$ the artificial growth due to the 5-stage scheme does not exceed 10 %. In graph (b) it can be observed that a linear wave with $\lambda = 1$ grows with approximately 1 % when $\Delta T = \frac{1}{12}T_{\lambda=1} \approx 0.2$ for the 5-stage scheme. Using a 4-stage method, the wave amplitude decreases with approximately 5% for the same time step. In graph (c) this comparison is made for the same wavelength, only now over a simulation time of $t^* = 1000 \approx 400T_{\lambda=1}$ units. This graph shows that the final artificial amplification due to time integration of this wave after 400 periods is less than 5 promille if $\Delta < T/25$.

We conclude by noting that the application of both the RK44M, RK45M and RK35D schemes in the simulation of the nonlinear equations (3.28) resulted in stable simulations in the sense that no artificial blowup was observed. Actually, even the simulations using the 5-stage methods showed a small decrease in discrete energy (see also Section 3.4) indicating that the dissipative effects of the full nonlinear discretisation are stronger than the amplifying effect of the 5-stage scheme. Based on these observations and the small error of the RK45M method, the RK45M method is mostly used for time integration.

Conclusions

In this subsection the stability of the numerical discretisation has been investigated. The algebraic equations that discretise the partial differential equations have been derived and a linear von Neumann analysis was performed. For 1-dimensional Finite Differences as a velocity recovery method, the eigenvalues of the linearised system were found to lie on the imaginary axis, independent of the order of the investigated polynomial approximations of the Finite Differences and Finite Elements. Furthermore it was found that the orientation of the triangular elements and the grid density do not significantly ($< 10^{-14}$) influence the real component of the eigenvalues. Therefore, all investigated FEM/FD schemes have the property that the linearised discretised equations constitute purely oscillatory dynamics.

When a global projection method is used for the velocity recovery at the free surface, the total spatial discretisation is found to be unstable and dependent of the triangulation of the domain. Therefore this method is not suitable as a recovery method for the velocities at the free surface.

Next, the amplification of the eigenvectors due to the time discretisation using a RK method has been investigated. A 4-stage and a 5-stage method (both of fourth order) were compared. The 4-stage method has the property that all purely oscillatory modes are damped and specifically the high frequency components (as long as they are in the stability region). The 5-stage method has an interval on the imaginary axis on which these modes are amplified and therefore these modes are not stable. However, the accuracy of the 5-stage method is larger and, given the total simulation time, one can obtain bounds for the maximal amplification factor of every mode. Application to the nonlinear discretisation showed that in actual simulations the total energy slightly decreases (see also Section 3.4). Therefore the small amplification due to a 5-stage RK integration is always found to be compensated by the dissipation due to the (nonlinear) spatial discretisation.

3.2.3   Grid refinement

In the following all quantities are normalised by the depth and the gravitational constant. The order of convergence is determined by systematic grid refinement.

Following Roach (1994), the following remarks are made concerning the estimate of the order of convergence on refined grids.

- the grids must be refined substantially (at least 50%)

- the grid topology and relative spatial density of grid points should remain comparable on all grid levels

- the grids should be sufficiently fine that monotone convergence is obtained

For the grid refinement study, the order of the FE and FD polynomials is chosen to be 1 and 2, respectively, which results in second-order approximations of both the field solution and the boundary derivative approximation. We want to establish the overall accuracy of the scheme and therefore as a convergence measure, the difference in energy between the initial numerical solution and the energy after a fixed period of time ($t = 20$) is taken.

$$|\Delta E| = |E(20) - E(0)| \tag{3.54}$$

$$E(t) = \int_0^L \left\{ \int_{-1}^{\widehat{\eta}(x,t)} \frac{1}{2} \|\nabla \widehat{\Phi}(x,z,t)\|^2 dz + \frac{1}{2}\widehat{\eta}(x,t)^2 \right\} dx \tag{3.55}$$

The integrals in Eq. (3.55) are calculated over the discretised geometry, i.e. the junction of all FE triangles and all quantities are exactly integrated. As an initial condition we take the discretisation of the steady (i.e. $\Phi(x,z,0) = 0$) profile

$$\eta(x,0) = 0.1\cos(\pi x) \tag{3.56}$$

on a domain of length 2. The evolution of this standing wave is nonlinear because of the relative high steepness ($\frac{H}{\lambda} \approx 0.7 \left(\frac{H}{\lambda}\right)_{\max}$). The spatial and temporal grid size Δx, Δz and Δt for $\beta = 0$ are uniformly refined as

$$\left.\begin{array}{l} \Delta x = \frac{1}{8}h_{\text{grid}} \\ \Delta z = \frac{1}{8}h_{\text{grid}} \\ \Delta t = \frac{1}{5}h_{\text{grid}} \end{array}\right\} h_{\text{grid}} = 1, \frac{1}{2}, \frac{1}{4}, \frac{1}{8}. \tag{3.57}$$

In addition a refinement study is performed for different values of β (see also Fig. 3.2 on page 49 for a visual interpretation of the value of β) to investigate whether or not the order of convergence is influenced by the vertical distribution of mesh points. For this study, the factor h_{grid} is proportional to the number of grid points in the vertical direction as Δz is no longer a constant.

From Fig. 3.8 on the following page it is concluded that the overall scheme is of second order in the energy norm. Moreover, it is observed that increasing the value of β (i.e. a higher grid density near the free surface) results in more accurate computations and does not influence the order of the scheme. Further investigations showed that the obtained order of convergence does not change for higher-order FD approximations, confirming that the lowest order error (FE) is dominant.
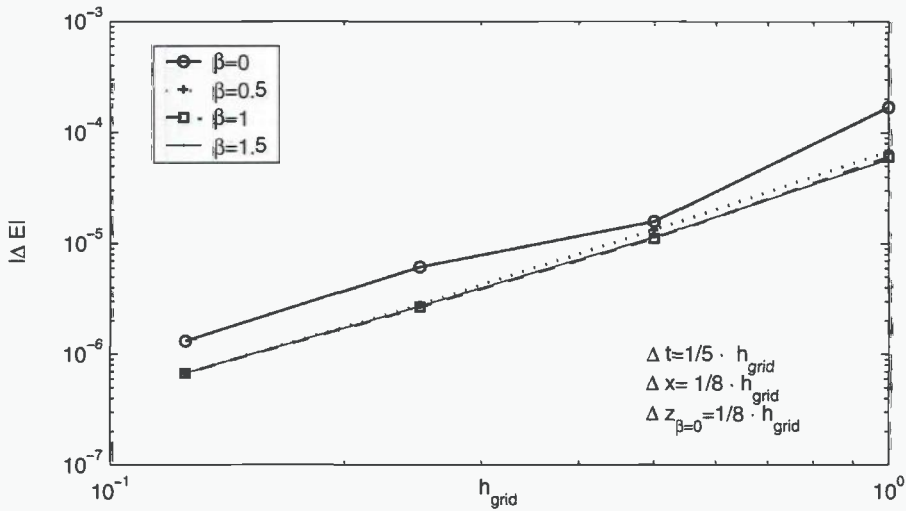
Figure 3.8: *Spatial-temporal grid refinement for first order Finite Elements and sec-*
ond order Finite Differences. It can be observed from the log-log plot that
the order of convergence in the energy norm is approximately 2 and inde-
pendent of β.

3.3   Dispersion relation

Although the above analysis, is indicative for the error and the accuracy of the nu-
merical scheme, it does not provide a global indication to the quality of the actual
numerical solutions. This section introduces an analysis of the numerical scheme,
that provides a quantitative insight in the performance of the scheme. It is not an
asymptotic investigation aimed to show some rate of convergence of the results. In-
stead, it provides a relation between the achievable results on overall accuracy given
the available computational effort and choice of numerical parameters.

The analysis of the stability of the linearised discrete equations (3.28) provides an
efficient method to evaluate the dispersive properties of the discretised equations. The
length scale, and therefore the wavenumber of the standing waves corresponding to the
eigenvectors, is exactly known. The eigenvalue μ_j that corresponds to a standing wave
with wavenumber k_j therefore constitutes the dispersion relation $\mu(k_j)$. This relation
evidently depends on the numerical parameters and therefore allows for a physical
significant criterion to assess the influence of these parameters. In this section, a
quantitative analysis of the dispersive properties due to spatial discretisation will
be presented. The analysis is performed on the linearised discretised equations and
provides a measure for the error in the phase velocity of the numerical waves. The
aim is to investigate what performance can be achieved given the available methods
and a restricted amount of computing power. First we will introduce the dispersion
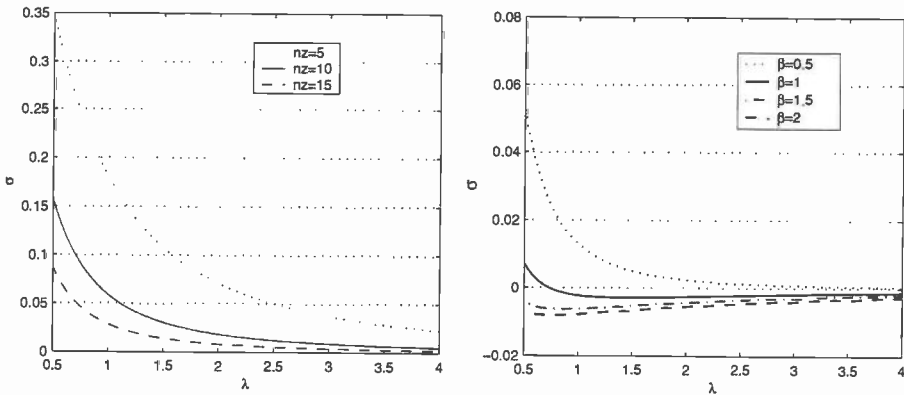
(a) Regular mesh (β = 0, nx/h=50, p[FEM]=1, p[FD]=2)

(b) Effect of β (nx/h=20, nz=10, p[FEM]=1, p[FD]=2).

Figure 3.9: *The relative phase velocity error of the linearised discretised equations for different numerical grids.*

error measure and its dependence on the wavenumber. Next, the dependence of this measure on the polynomial order of approximation of the finite difference and finite elements will be investigated.

3.3.1   Dispersion error σ

As a measure for the dispersion accuracy we introduce

$$\sigma(k) = \frac{\omega(k) - \mu_k}{\omega(k)} \tag{3.58}$$

where μ_k is the eigenvalue associated with an eigenvector with wavenumber k and $\omega(k)$ is the exact dispersion relation of linear gravity waves (see Eq. 3.7). Remark that $\sigma(k)$ can be interpreted as the relative error in the phase-velocity of the numerical wave.

Fig. 3.9(a) shows the graph of $\sigma(k)$ for a given set of numerical parameters on a uniform mesh ($\beta = 0$). As can be observed, the value of σ for shorter waves is much larger than the values for longer waves. This is due to the fact that the potential-flow solution for shorter waves has larger gradients near the free surface than the solution for longer waves. Therefore, the regular mesh represents the longer waves better and consequently, the approximation of the vertical velocity at the free surface is better. Remark also that the relative error in the phase-velocity for this configuration is rather high for shorter waves (up to 30%) which is unacceptable for practical simulations.
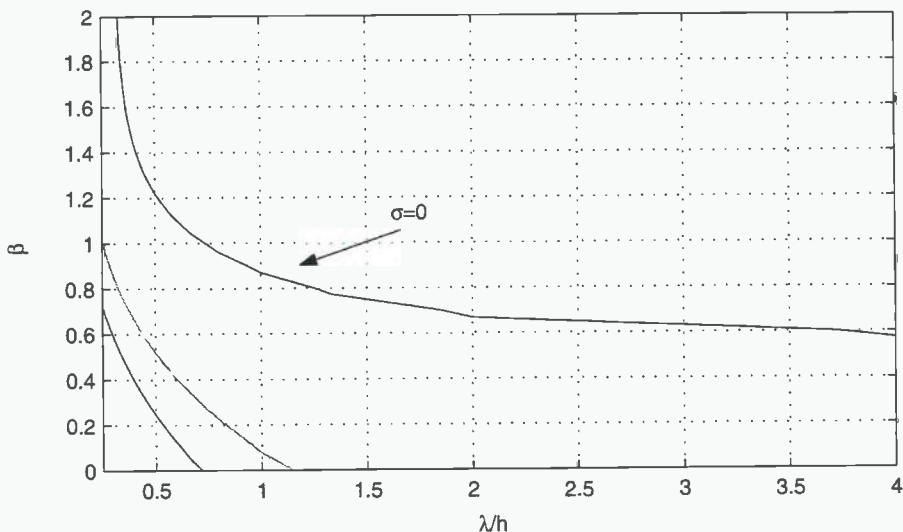
Figure 3.10: $\sigma = 0$ *curve where the phase velocity of the spatially discretised, linearised equations equals the continuous phase velocity. (nx/h=20, p[FEM]=1, p[FD]=2)*

In Fig. 3.9(b) the effect of β on the relative phase error is visualised for a particular configuration. Clearly, the phase error can be greatly reduced by a suitable choice of β. Remark that the choice of β does not influence the number of degrees of freedom of the total scheme.

It is also observed from Fig. 3.9 on the preceding page that a variation of β is a trade-off between the accuracy of the approximation of the solution of the Laplace problem and the accuracy of the Finite Difference approximation of the vertical velocity at the free surface. For small values of β, the resolution near the free surface is low, and approximation of the velocities for short waves is inaccurate. By increasing the resolution near the free surface, the approximation of the surface velocities increases but the resolution away from the free surface becomes coarser. For longer waves, the potential variations are not well resolved on these coarser grids, resulting in less accurate approximations of the potential and thus of the velocities.

Fig. 3.9(b) shows another remarkable aspect of the computational scheme: the factor β can be chosen such, that for a single regular wave, the phase error is zero. This is illustrated in Fig. 3.10 where the $\sigma = 0$ contour line is plotted as a function of the β and λ. It is thus possible to determine the grid density such that for a specific linear wave, the phase velocity of the linearised discretised equations equals the continuous linear phase velocity. This property was also found to be true for different values of nx/h, $p[FEM]$ and $p[FD]$.

3.3.2 Minimisation of $\sigma(1/4, 4)$

It was found in the previous section that for a FE/FD scheme, by a suitable choice of β, the relative dispersion error can be made zero. However, in practical applications, one is usually interested in the simulation of several waves simultaneously on the same numerical grid. Usually a complete wave spectrum containing many wave components is desired. To construct a measure that describes the dispersion quality over a range of waves, the maximum relative phase error is introduced as:

$$\sigma(a, b) = \max_{k \in [2\pi/b, 2\pi/a]} |\sigma(k)| \tag{3.59}$$

In other words, $\sigma(a, b)$ denotes the maximum relative error in the dispersion relation for waves with a wavelength between ah [m] and bh [m]. For uniform grids this maximum is always attained at the smallest wave $k = 2\pi/a$. However, as already can be observed from Fig. 3.9 on page 63, this is not necessarily the case when $\beta \neq 0$. The typical range of wavelengths in a hydrodynamic basin is about $[h/4, 4h]$. For some laboratories, these short waves may already fall in the capillary regime and one should then be careful to interpret the results.

The aim of this subsection is to derive a rationale for the different numerical parameters in the computational scheme given the available computational effort. The parameters that are varied are:

- the polynomial order of the Finite Elements used in the approximation of the field potential, $p[FEM] = 1, 2$.

- the polynomial order of the Finite Difference approximation of the vertical velocity at the free surface, $p[FD] = 1, .., 4$.

- the parameter governing the grid density near the free surface, $\beta = 0, \dots, 1.5$.

- the number of grid points in the horizontal direction per unit length, $nx = 15, \dots 100$.

- the number of grid points in the vertical direction, $nz = 7, \dots, 27$.

When first and second order Finite Elements are compared with respect to computational effort, the number of degrees of freedom (DOF) is kept constant. As a result, a triangle associated with a first-order FE approximation is twice as small than the one for a second-order approximation (see also Fig. 3.11 on the next page).

Floating point operations

In order to compare the computational effort, the floating point operations (flop) are determined to find a solution of the linear system arising from the FE discretisation.
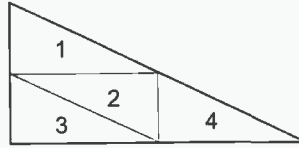
Figure 3.11: *Four first-order and one second-order triangular elements. When first-and second-order Finite Elements are compared, the number of degrees of freedom is kept constant and therefore the second-order element triangle is twice as large.*

The computation of this solution takes up the largest part of the approximation and therefore the computational effort to construct the matrix and to determine the FD approximations of the surface velocity are neglected. The actual needed computer time depends not only on the flop count but also on the type of computer (single processor, massively parallel processors or (parallel) vector processor). As has been mentioned in the introductory chapter, one of the design criteria is that the simulation software should run on a single PC which is usually equipped with a single processor. Therefore, the comparison using the flop count is also a direct measure for the computational time.

As a direct solver for the linear system arising from the discretisation of the boundary value problem, a symmetric banded Gauss elimination procedure with back substitution is adopted. The number of floating point operations for a single solution of the linear system using this method is counted as:

$$\text{flops}_{\text{sym. Gauss}} = nx \cdot B \cdot (8 + 7 \cdot B + B^2), \tag{3.60}$$

where B is the bandwidth of the matrix ($B = nz + 1$ for p[FEM]=1, $B \approx 2nz + 2$ for p[FEM]=2). As an iterative solver for the linear system a preconditioned conjugate gradient (PCG) method is used with incomplete Cholesky factors as a preconditioner. Both the CG as the Cholesky factorisation are specifically efficient for sparse, symmetric and positive definite matrices. The stop criterion for the PCG iterations was set to

$$\frac{\|Ax_i - b\|_2}{\|b\|_2} < \epsilon \tag{3.61}$$

where $\epsilon = 10^{-10}$ was chosen.

For the fill strategy in the incomplete Cholesky factorisation of the matrix $A = [a_1, a_2, \ldots, a_n]$, a drop tolerance criterion was taken. The drop tolerance level was set to $tol = 10^{-3}$. This implies that the elements for the upper triagonal R matrix of the decomposition are not stored if
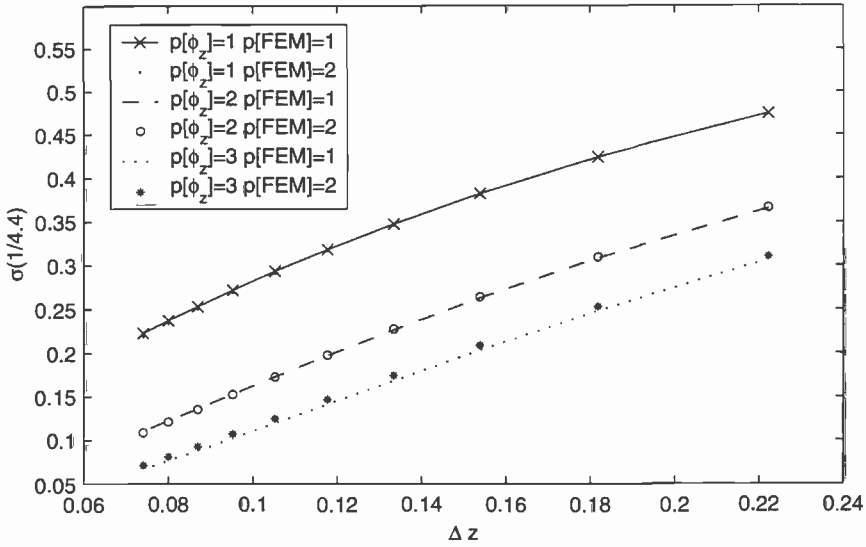
$$R_{ij} < tol \frac{\|a_j\|_2}{|R_{ii}|}. \tag{3.62}$$

Figure 3.12: *The effect of Δz, p[FEM] and p[FD] on the $\sigma(1/4, 4)$ dispersion error. ($\beta = 0$, $h = 1$, $g = 1$, $\Delta x = 1/40$)*

The number of non-zero elements in R is not *a priori* known and the exact number of iterations needed for convergence is also not known in advance. Therefore, the floating point count is performed *a postiori*.

Uniform grid

Firstly, we examine the $\sigma(1/4, 4)$ error for uniform grids, i.e. with $\beta = 0$. A systematic study where Δx, Δz, p[FEM] and p[FD] are varied, showed that the results for $\Delta x < 1/40$ are virtually independent of Δx. From this study, of which the results are presented in Fig. 3.12, the following observations are made:

- The effect of second-order Finite Elements is negligible with respect to the $\sigma(1/4, 4)$ error when compared to first-order FE's. Although a second-order FE approximation does have a positive effect on the longer waves (see Fig. 3.13 on the next page), the maximum dispersion error is attained at the smallest wave. The error is not, as one might expect, dominated by the Δx resolution.

- The effect of a higher-order FD scheme to approximate ϕ_z is positive and reduces the error significantly.

- For the investigated situations $\sigma(1/4, 4)$ depends almost linearly on Δz independent of p[FEM] and p[FD].
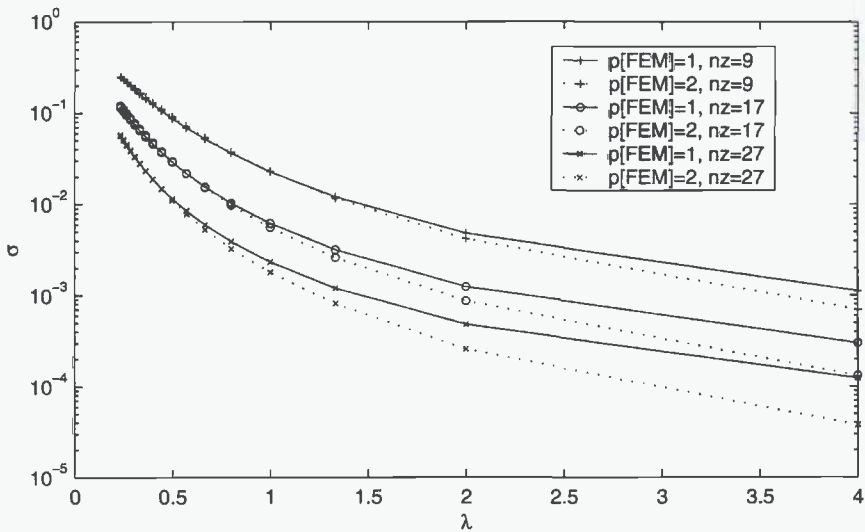
Figure 3.13: *The relative dispersion error σ as a function of the wave length λ for different numerical configurations on a uniform grid. ($\beta = 0$, p[FD]=3, $h = 1$, $g = 1$, $\Delta x = 1/40$)*

Fig. 3.14 on the facing page shows the maximum dispersion error as a function of the computational effort measured in flop's. The horizontal mesh width was kept constant and the increase in computational effort is the result of the uniform refinement of the grid in vertical direction.

As expected, the symmetric Gaussian elimination procedure combined with first-order Finite Elements is more efficient than the iterative solver for smaller (< 35) values of nz. Extrapolation of the curves, suggests that when a $\sigma(1/4, 4)$-error lower than 2 % is required, the iterative solver for linear elements becomes more efficient than the direct solver. The associated computational effort of $\approx 10^7$ floating point operations per 2 length units is however unacceptable given the operational constraints. When second (and higher) order FE's are used, an iterative solver is always found to be more efficient than a direct solver. However, it was already observed in the previous study that the effect of second order elements on this error measure is negligible.

A realistic 10 [min]simulation of a fully developed sea state would require a computational domain of length $L = 40h$ over $300T_{\lambda=1}$ with $\Delta t = \frac{1}{30}T_{\lambda=1}$ and $\Delta x = \frac{1}{30}$. On a pentium III 500 [Mhz] computer, such a simulation with a $\sigma(1/4, 4)$ error level of 5% on a uniform grid would require approximately 45 [hr] of computing time. Besides the fact that a 5% error in the phase velocity is still considered high, the necessary computing time exceeds the practical 'overnight-job' requirement. The achievable error level when 12 [hr] of computing time is available would be approximately 15%. The
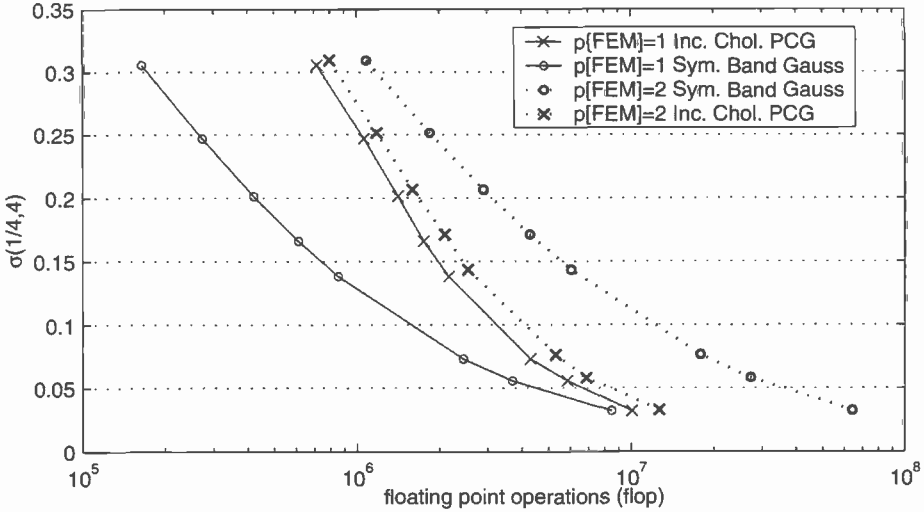
Figure 3.14: *The $\sigma(1/4, 4)$ error measure as a function of the computational effort ,*
$h = 1$, $g = 1$, $L = 2$, $p[FD] = 3$, $\Delta x = 1/60$

results indicate that for small ($< 5\%$) errors, the numerical algorithm on a uniform grid results in unacceptable long computing time. In the next paragraphs it will be shown that by choosing $\beta \neq 0$, large error reductions can be obtained while keeping the computational effort fixed. Acceptable levels of accuracy are feasible with linear elements and only 15 points in the vertical direction.

Nonuniform grid

The above analysis indicates that error levels of 3% are obtainable when a computational effort of $\approx 10^7$ floating point operations per 2 length units is invested. However, as could already be observed in Fig. 3.9 on page 63, increasing the local grid density near the free surface while keeping the number of DOF constant, can greatly improve the dispersive properties. In the following paragraphs this improvement is quantified for the $\sigma(1/4, 4)$ measure.

The $\sigma(1/4, 4)$ error was determined for the following combinations of parameters:
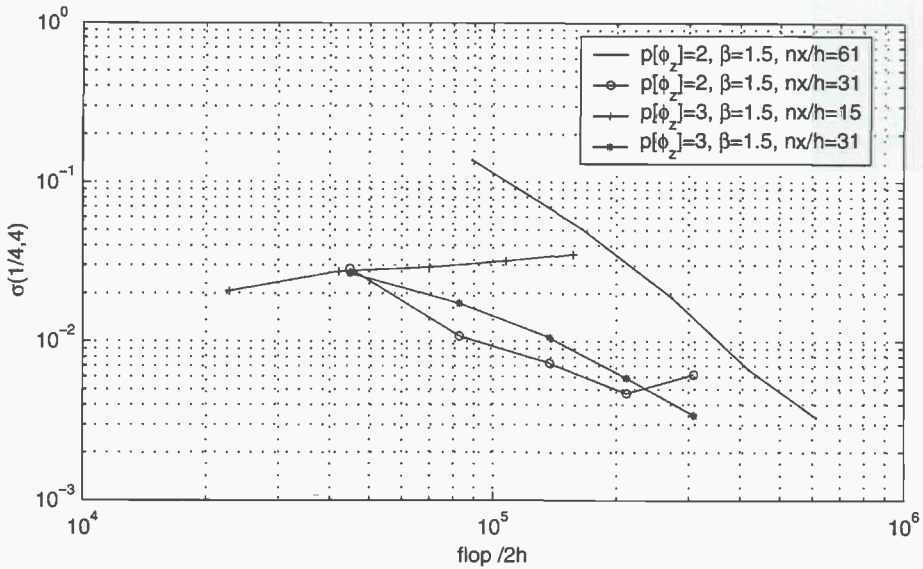
Figure 3.15: *'Optimal' curves from the parameter variation study. The curves visualize the achievable $\sigma(1/4, 4)$ error as a function of the computational effort. The markers on a curve correspond (in increasing flop direction) with $nz = 7, 9, 11, 13, 15$.*

param.	values
p[FEM]	1
p[FD]	2, 3, 4
β	0, 1/2, 3/4, 1, 5/4, 3/2
nx/h	15, 31, 61
nz	7, 9, 11, 13, 15

Systematic variation of these parameters resulted in a total of 270 discretisations. From these configurations it was observed that an increase of β from 0 to 1.5 generally resulted in a reduction of the error. The flop-$\sigma(1/4, 4)$ curves (as in Fig. 3.17 on page 72) where determined for all configurations. The four curves with the smallest errors are plotted in Fig. 3.15. For three configurations on these curves (flop=$(2 \times 10^4$, 1×10^5 and 2×10^5), the relative dispersion error σ is plotted as a function of the wavenumber λ in Fig. 3.16 on the facing page.

From this study and these figures a number of observations can be made. Firstly, it is observed that a redistribution of the grid can greatly improve the dispersion properties of the linearised discretised equations with respect to uniform grids. For example, if a computational effort of 2×10^5 is allowed, the minimal achievable $\sigma(1/4, 4)$-error on
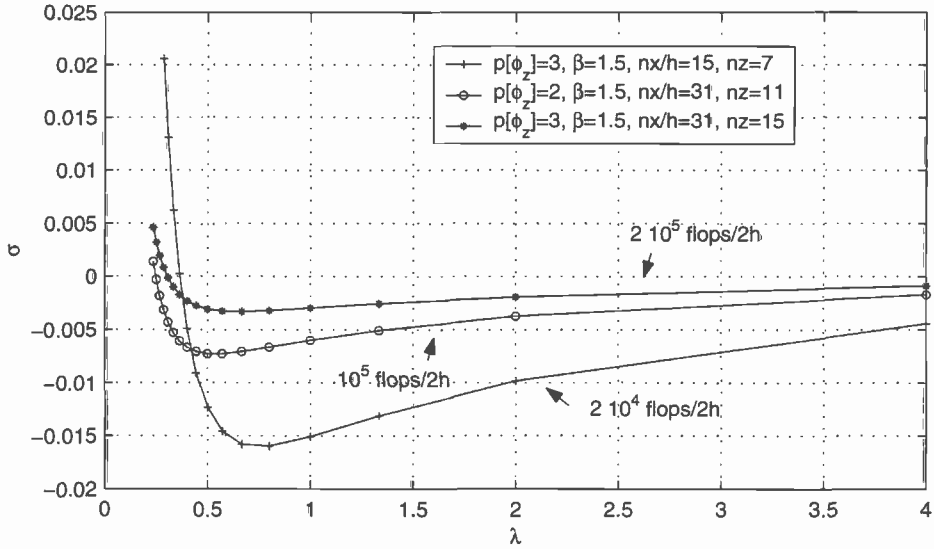
Figure 3.16: *The relative dispersion error σ as a function of the wave length λ for three configurations from Fig. 3.15 on the facing page.*

a uniform grid was found to be 2.5×10^{-1} (see Fig. 3.12 on page 67). For the optimal configuration using grid redistribution, the minimal achievable error is approximately 2.5×10^{-3}: an improvement of a factor 100. With the numerical configuration that requires $3 \times 10^{5}/(2h)$ flop's, the realistic simulation sketched at the end of the previous paragraph can be performed within 4.5 [hr] with an error level $< 0.3\%$.

Secondly, the curves of the investigated configurations showed that for $nx/h = 61$ the curves are a decaying function of nz, whereas for $nx/h = 15$ an increasing trend was observed for higher values of β (see also Fig. 3.17 on the following page). Thirdly, the fact that $\beta = 1.5$ for all optimal configurations does not allow for a general conclusion. For some configurations it was found that a lower value of β *ceteris paribus* was more efficient. In the case of $nx/h = 15$ the positive effect of β is also bounded by a different error source as can be observed from Fig. 3.17 on the next page. The curve that bounds the error from below was found to be independent of p[FD].

3.4   Mass and energy conservation

The results of the previous investigations are obtained by analysis of the linearised discretised equations. These results are quantitative and provide a rationale for the choice of a combination of methods and grid parameters. The analysis has provided a measure for small (linear) waves, the numerical method aims at the simulation of
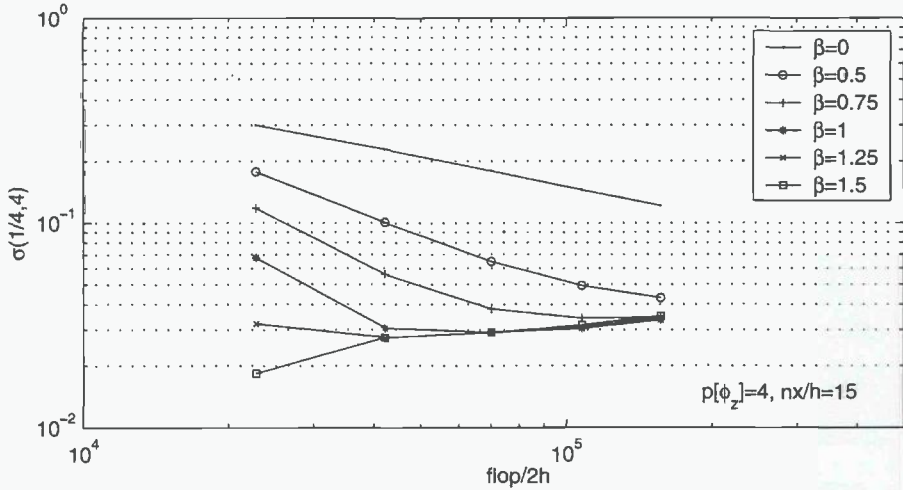
Figure 3.17: *The effect of β on the attainable $\sigma(1/4, 4)$ error curves. For larger β the error has a lower bound independent of p[FD].*

nonlinear waves. Therefore the global aspects of mass and energy conservation for nonlinear simulation will be further examined quantitatively in the next section. The discretised equations (3.28) are not the result of the variation of a discretised Hamiltonian energy and therefore, no exact energy conservation can be expected. However, convergence of the discretisations implies convergence to an energy conserving solution. In this section the deviations from mass and energy conservation are investigated as a function of the grid parameters and the numerical methods, similar as in the previous section. This section explicitly deals with nonlinear waves and therefore the wave height becomes a relevant parameter. Similar to the previous section, natural boundary conditions are used on the lateral boundaries. The simulation is performed using the following initial conditions for Φ and η.

$$\eta(x,0) \quad = \quad \frac{1}{2}H\cos(kx) \tag{3.63}$$

$$\Phi(x,z,0) \quad = \quad 0 \tag{3.64}$$

These initial conditions are discretised and as an energy error measure

$$E_{\text{rel}}(t) = \frac{E(t) - E(0)}{E(0) - E_0} \tag{3.65}$$

is taken, where $E(t)$ is the total discrete energy (see Eq. (3.55)) at time t and E_0 is the total potential energy of the system at rest (i.e. with $\eta \equiv 0$). As a measure for the mass deviations we take

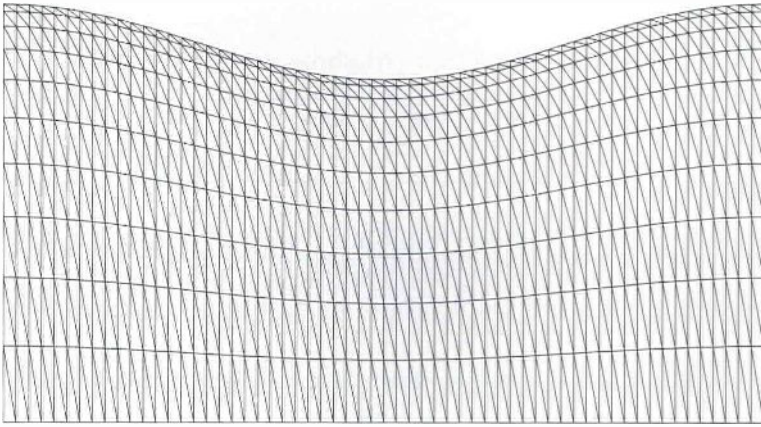$$M_{\text{rel}}(t) = \frac{M(t) - M(0)}{M(0)} \tag{3.66}$$

Figure 3.18: *Illustration of the grid used for the simulations to determine energy and mass conservation. ($nx/h = 31$, $nz = 11$, $\beta = 1$, $\lambda = 2$, $H/\lambda = 1/10$*

Fig. 3.18 shows a typical initial grid for the simulations performed to assess the mass and energy conservation.

It was found that in all simulations, the relative energy and mass oscillate around a trend line (see e.g. Fig. 3.19 on the following page). To characterize this behavior, the linear trend and the standard deviation of the $E(t)$ and $M(t)$ signals are determined. The length-interval over which the trend is computed is 50 periods of the linear standing wave associated with the initial conditions. The trend coefficient and standard deviation are determined for different configurations of the numerical algorithm. Given the orders of approximation and grid parameters, the evolution of an initial profile is determined for the combinations of steepness ($H/\lambda = 1/10$, $1/15$, $1/20$, $1/25$ and $1/30$) and wave length ($\lambda = 1/4$, $1/2$, $1, 2$ and 4).

From Fig. 3.20 on page 75 one can observe that for uniform grids, the linear trend coefficients of both the mass and the energy are quite small, even for steep waves. However, the standard deviation for the energy error is relatively large. For the shortest $\lambda = 1/4$ waves (resolved with only 7 grid points in the horizontal direction), the standard deviation can be as large as 0.3. Remark that this deviation is almost independent of the steepness of the initial wave. It is further observed that for this uniform grid, the standard deviation with respect to the relative mass error mainly depends on the steepness and not on the wavelength. In Fig. 3.21 on page 76 the evolution of the relative mass and energy deviations for an 'optimal' configuration
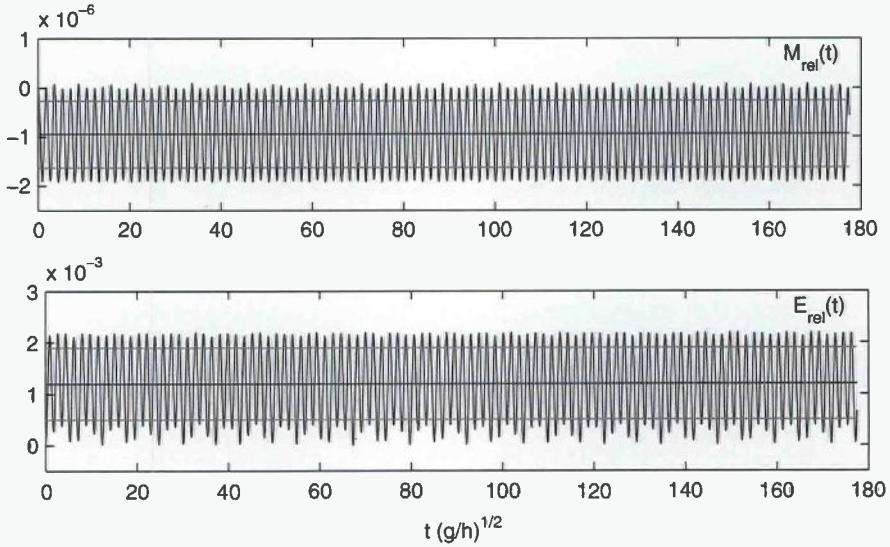
Figure 3.19: *The relative error of the energy Eq. (3.65) and mass Eq. (3.66) for a nonlinear standing wave. ($nx/h = 31$, $p[FEM]=1$, $p[FD]=2$, $nz = 11$, $\beta = 1.5$ $\Delta t = 0.06$, $\lambda = 2$, $H/\lambda = 1/30$*

found in the previous section is investigated. It is directly observed that the use of a nonuniform grid leads to an overall improvement when compared to Fig. 3.20 on the next page. Roughly speaking, all trend coefficients and standard deviations are reduced by a factor of 10. Remark that for the shorter waves the standard deviation is still independent of the steepness, indicating that the standard deviation is mainly related to the lack of horizontal resolution of the short waves.

Further studies where more grid points in the horizontal direction are used showed lower standard deviations. When $nx/h = 61$ grid points are used and the other parameters are kept constant, the standard deviation for the smallest wave can be reduced to 0.01. For this configuration the average trend coefficient for mass and energy are 10^{-9} and $10^{-5.5}$, respectively. The average standard deviations of the mass and energy are $10^{-6.5}$ and 10^{-3}, respectively.

The following trends with respect to the standard deviations of both mass and energy have been observed:

- The standard deviation decreases with the wave length. Clearly, this is an effect of the increase in spatial resolution per wavelength. From the results on the dispersion error (Fig. 3.16 on page 71), this improvement cannot be related to a better velocity approximation.

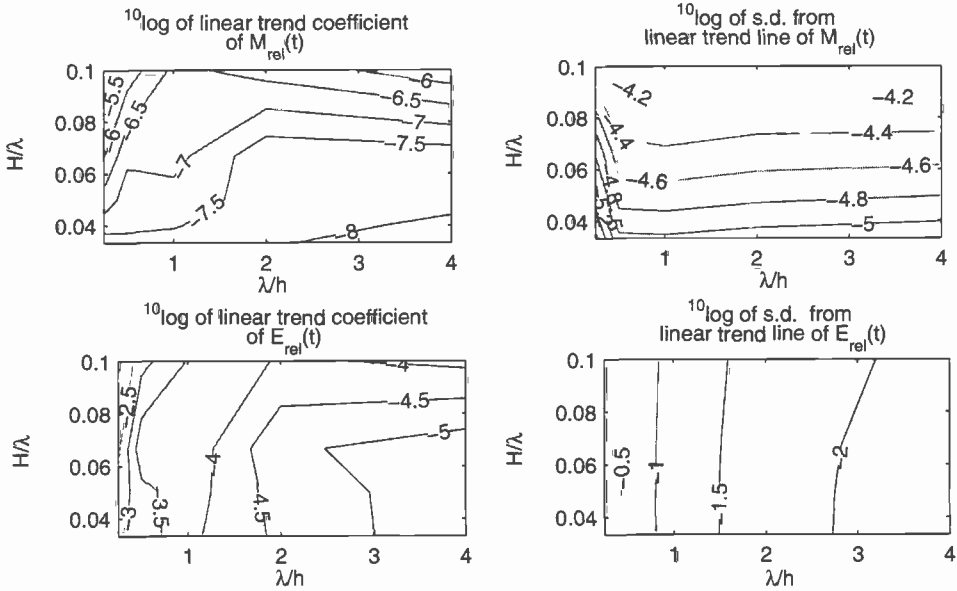- The standard deviation increases with the steepness. This is probably related

Figure 3.20: *The contour plots of the $^{10}\log$ of the trend coefficients (that have negative sign) and standard deviations for a uniform ($\beta = 0$) numerical grid. ($nx/h = 31$, $p[FD]=2$, $p[FEM]=1$, $nz = 11$, $\Delta t = 0.06$)*

to the truncation error of the geometrical and algebraic approximation of the horizontal derivatives at the free surface.

Investigations to whether or not the standard deviations are related to the local horizontal resolution near the fixed walls showed no relation. It is thus concluded that the deviations cannot be improved by local grid refinement near the horizontal walls.

3.5   Applications

In this section two applications of the numerical algorithm using natural boundary conditions will be described. The first application is related to a validational study on the sloshing of a wave in a rectangular container. The second application concerns the splitting of a solitary wave over an uneven bottom.
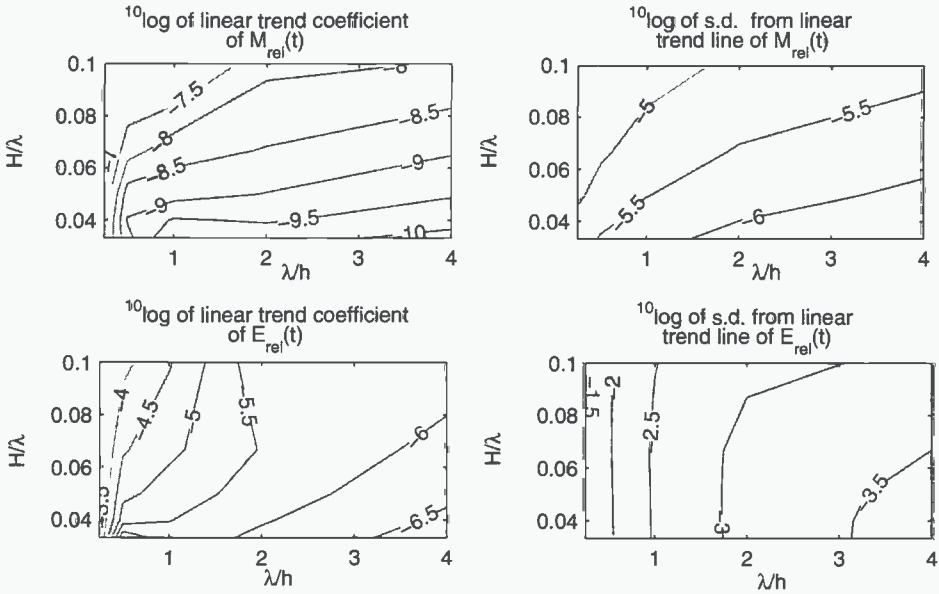
Figure 3.21: *The contour plots of the ^{10} log of the trend coefficients (that have negative sign) and standard deviations. The numerical configuration is identical to Fig. 3.20 on the page before except that the grid density $\beta = 1.5$.*

3.5.1   Comparative study on a sloshing wave

In 1994 Det Norske Veritas (DNV) initiated a comparative study for researchers involved in fully nonlinear water wave calculations (cf. Nestegård (1994)). One of the test cases in the comparative study was the calculation of a sloshing wave. Given the dimensions of the water tank ($h \times L = 70m \times 160m$) and the initially steady surface profile

$$\eta(x, 0) = 12 \left[1 - (x/53)^2\right] e^{-(x/76)^2}, \tag{3.67}$$

participants in the comparative study were asked to compute the surface elevation and horizontal and vertical surface velocities at $t = 9.2$ [s] at $x = 60$ [m]. In this subsection, the evolution of the initial condition Eq. (3.67) is computed to compare the results with the values obtained by the participants of the validation study. For the simulation, a regular grid of 15×160 nodes with a time step $\Delta t = 0.1$ and $\beta = 1.5$, p[FD]=2 was used. The space-time evolution of the initial condition Eq. (3.67) is plotted in Fig. 3.22 on the next page.

There were 7 participants that contributed to this comparative study. Most of the participants used methods based on the Boundary Integral Equation formulation. Table 3.1 summarizes the results of the participants added with the results obtained by using the numerical algorithm of the present thesis. As can be observed, the results
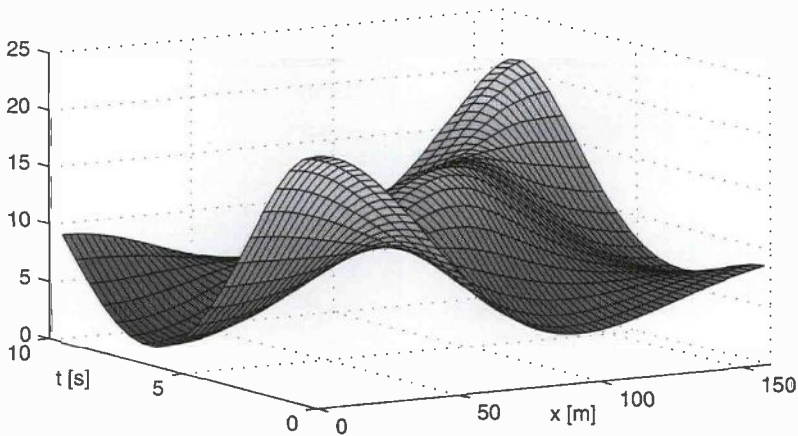
Figure 3.22: $x - t$ plot of the evolution following from the initial conditions (3.67) of the comparative study on sloshing waves.

of the presented method are in reasonable mutual agreement with the results obtained by the other participants.

3.5.2 Solitary wave propagation over uneven bottoms

In this section we describe an application of the developed numerical method for the problem of steadily propagating solitary waves and the splitting of such waves during run-up over a bottom. Although the problem is not on the typical scale of a hydrodynamic model test basin, it describes an interesting phenomena by itself. As the problem does not involve any special lateral boundary conditions, it can be used to investigate the applicability of the developed numerical scheme. As the propagation of solitary waves is a subtle balance between dispersion and nonlinearity, accurate simulation of the evolution of a solitary wave is only possible when both these aspects are well discretised.

The application of the numerical scheme to the splitting of a solitary wave is motivated by investigations of Pudjaprasetya (1996) and van Daalen *et al.* (1997). The splitting of solitary waves has been investigated since the seventies by Grimshaw (1970) and Johnson (1973) and we refer to Johnson (1994) for further references. In Pudjaprasetya (1996) a KdV model is developed to numerically simulate the evolution of a soliton over an uneven bottom. In van Daalen *et al.* (1997) this splitting is compared with fully nonlinear numerical simulations using a boundary-integral panel method developed by Romate (1989) and later improved by van Daalen (1993). Van Daalen *et al.* reported the fully nonlinear simulation of the splitting of solitary waves into 2 separated solitary waves after run-up. By introducing a larger change in depth,

part. nr.	$\eta(60, 9.2)$	$u(60, 9.2)$	$v(60, 9.2)$
1	-3.803	-2.456	-0.363
2	-3.860	-2.280	-0.560
3	-3.815	-2.414	-0.445
4	-3.759	-2.411	(-)0.602
5	-3.820	-2.417	-0.580
6	-3.803	-2.417	-0.572
7	-3.720	-2.480	-0.690
our result	**-3.788**	**-2.401**	**-0.561**

Table 3.1: Comparison of the surface elevation η, the horizontal velocity u and the vertical velocity v of the free surface at $t = 9.2$ [s], $x = 60$ [m] obtained by the participants in the comparative study of DNV (cf. Nestegård (1994)) with the results obtained by the present method.

splitting into three solitary waves is predicted by KdV models. However, this three-way splitting process has not been reproduced by numerical simulation of the fully nonlinear surface equations.

The simulations on solitary wave evolution in this section are performed to

- verify whether the developed numerical scheme can reproduce the results on the splitting of a single solitary wave into two solitary waves.

- investigate if the numerical scheme allows for the splitting of a solitary wave into *three* solitary waves. This has, to our knowledge, not yet been accomplished by other fully nonlinear surface wave simulations.

The geometric dimension for these simulations are $L = 300$ [m] and $h_0 = 0.5$ [m] and the total simulation time is 120 [s]. The value of the mesh parameter β is set at a value of 1.5 in accordance with the previous investigations. The polynomial orders are p[FEM]=1 and p[FD]=2, and the time step is chosen $\Delta t = 0.05$. The fixed horizontal mesh width is $\Delta x = 0.1$ [m] and the number of nodes in the vertical direction is fixed at $nz = 7$.

As an initial condition a steady profile is used

$$\eta(x, 0) = 0.215 \cdot \text{sech}(1.18 \cdot x). \tag{3.68}$$

This initial condition was constructed empirically with the aim to obtain a reasonable steady propagating solitary wave with a height of approximately 0.1 [m]. The result of the evolution of this initially steady solution is visualised in Fig. 3.23 on the preceding
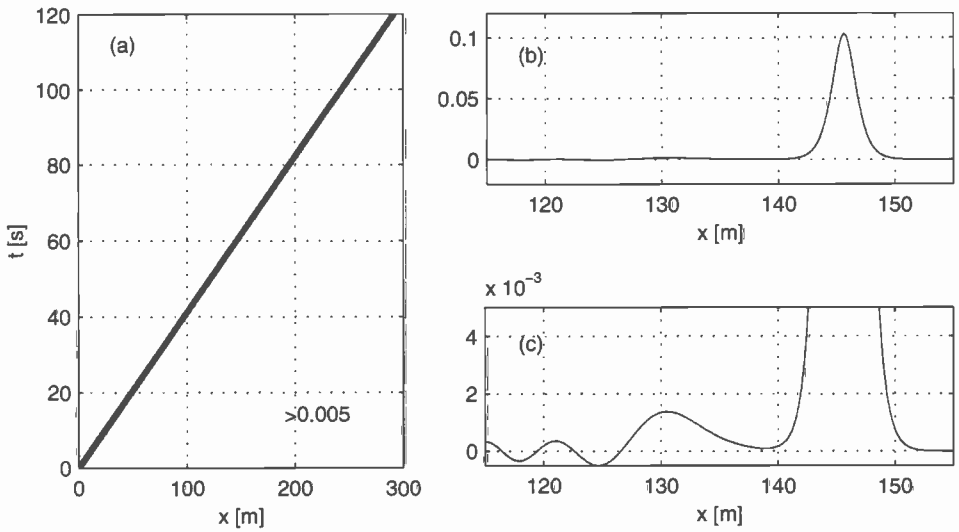
Figure 3.23: *Solitary wave propagation. (a) space-time plot of Eq. (3.68), $\eta(x,t) > 0.05H_{sol}$ is plotted. (b) snapshot of free surface. (c) Closeup of figure (b) around the oscillating tail.*
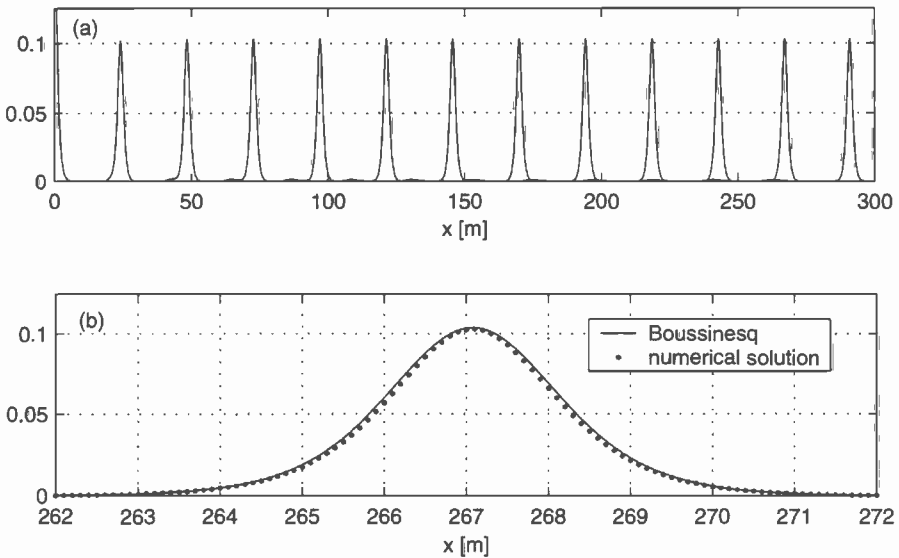

Figure 3.24: *(a) Different snapshots of the evolution of Eq. (3.68) (b) Comparison of the numerical solitary wave with an exact Boussinesq solitary wave solution Eq. (3.69)*

page and Fig. 3.24 on the page before.   From these figures the following observations
can be made

- In Fig. 3.23(a) the space-time evolution of the initial profile Eq. (3.68) is visu-
  alised by plotting all values $\eta(x,t) > 5 \ 10^{-3}$, i.e. 5% of the height of the solitary
  wave. The figure clearly shows an isolated wave moving at constant velocity.

- In Fig. 3.23(b) the spatial structure of the solitary wave for a fixed time step
  is shown. Although the solitary wave seems indeed the only free-surface distur-
  bance, closer examination of the tail of the solitary wave in Fig. 3.23(c), shows
  the presence of a wiggly tail. The amplitude of the oscillating tail decreases fur-
  ther away from the solitary wave and its maximal amplitude is approximately
  2% of the height of the solitary wave. The wiggling tail is a consequence of
  the way the solitary wave was generated. More sophisticated initial solutions,
  e.g. parts of analytical Rienecker-Fenton cnoidal solutions (cf. Rienecker &
  Fenton (1981) and van Daalen *et al.* (1997)), could be used to improve the com-
  pactness of the solitary wave. It turns out however, that the empirical solitary
  wave generation method by Eq. (3.68) is sufficient for describing the splitting
  phenomena.

- Fig. 3.24(a) also shows the constant shape of the solitary wave by plotting the
  surface elevation at regular time intervals. In Fig. 3.24(b) the numerical solution
  is compared to the exact solitary wave solution

$$\eta(x,t) = H \operatorname{sech}^2 \left(\frac{x - \sqrt{g(h+H)}t}{\sqrt{\frac{4h^3(1+H/h)}{3H}}} \right) \tag{3.69}$$

of the Boussinesq equation with improved frequency dispersion, Eq. (3.17) on
page 45.

The solitary wave solution Eq. (3.69) is translated to fit to the position of the
numerical solitary wave. Note however, that the width of the solitary wave solu-
tion (3.69) is fixed by the amplitude and therefore is not fitted. The comparison
between the analytic solitary wave of the improved Boussinesq equation and the
numerical wave is excellent. Comparison of the numerical wave with solitary
wave solutions of the Korteweg-de Vries (KdV) and the Benjamin-Bona-Mahony
(BBM, Benjamin *et al.* (1972)) equations showed less good agreement.

The velocity of the numerical solitary wave is approximately 2.427 [m/s], which is
in close agreement with velocities obtained from analytical models; KdV & BBM:
$c = \left(1 + \frac{H}{2h}\right)\sqrt{gh} = 2.436$ [m/s]; Boussinesq: $c = \sqrt{g(h+H)} = 2.426$ [m/s]. Remark
that the velocity of the Boussinesq model resembles more closely the velocity obtained
from the numerical simulation than the KdV and BBM velocity. The previous figures
and comparisons show that the empirically chosen initial condition Eq. (3.68) indeed
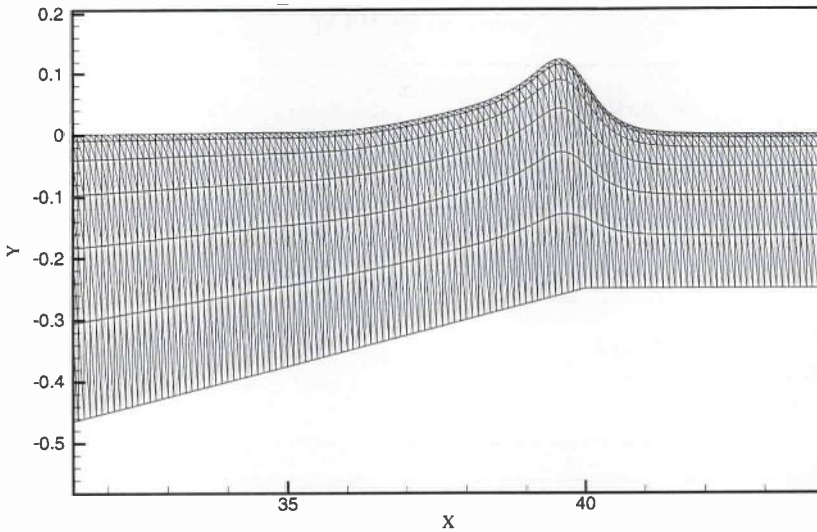produces a solitary wave and this solitary wave more closely resembles the solitary

Figure 3.25: *Illustration of the grid used for the simulation of solitary wave splitting over the bottom topography ($h_1 = 0.25$).*

solution of the improved Boussinesq equation than the solitary wave solution of the KdV and BBM equation.

As indicated in the introductory part of this section, the main interest is in the dynamics of this propagating solitary wave when the bottom topography contains a slope. The bottom increases linearly from the original depth $h_0 = 0.5$ [m] to a new water depth h_1. During the propagation over the slope, the wave will be partially reflected but the vast majority of the wave energy is transmitted. The solitary wave no longer 'fits' on the new depth and therefore disintegrates into solitary waves and radiation. Fig. 3.25 shows the grid around the solitary wave as it is propagating directly above the slope.

This process of wave splitting depends on the slope of the beach and the new water depth after the slope. In all simulations, the depth linearly increased from $h = 0.5$ at $x = 30$ to h_1 at $x = 40$ [m]. Fig. 3.26(a)-(e) show the numerical solutions at $t = 119$ [s] for different values of the final depth h_1. Clearly the original solitary wave deforms and for decreasing depths the splitting into new solitary waves is visible. Remark however that this process is quite gradual and that what appears to be a periodic tail just behind the original solitary wave in (a) and (b) can be identified with a new solitary wave in (c).

The distinct separation into two solitary waves (situation where $h_1 = 0.3068$) reported
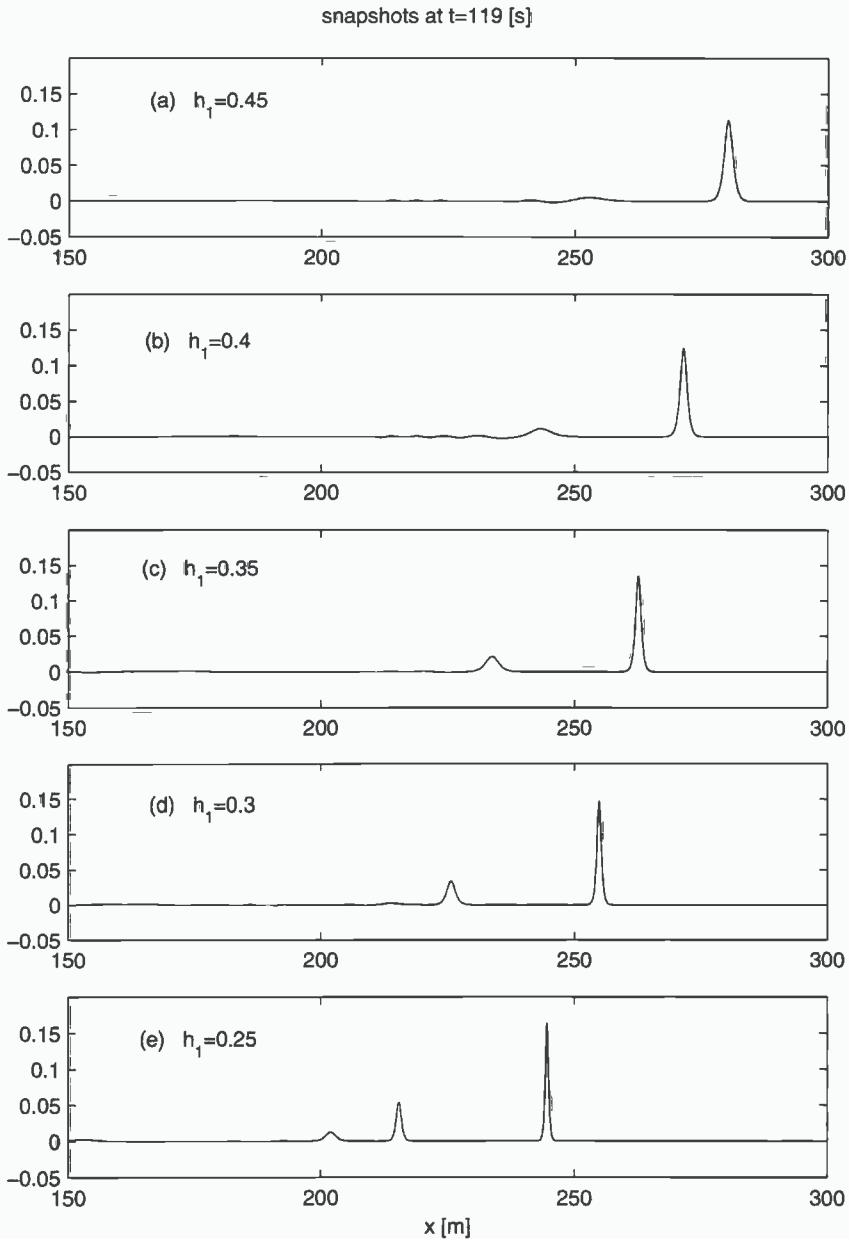
snapshots at t=119 [s]

Figure 3.26: *The solitary wave of Fig. 3.23 has run up a linear slope from $h_0 = 0.5$ to h_1 from $x = 30$ [m] to $x = 40$ [m]. The figures show snapshots of the free-surface elevation at $t = 119$ [s] for different final depths h_1.*
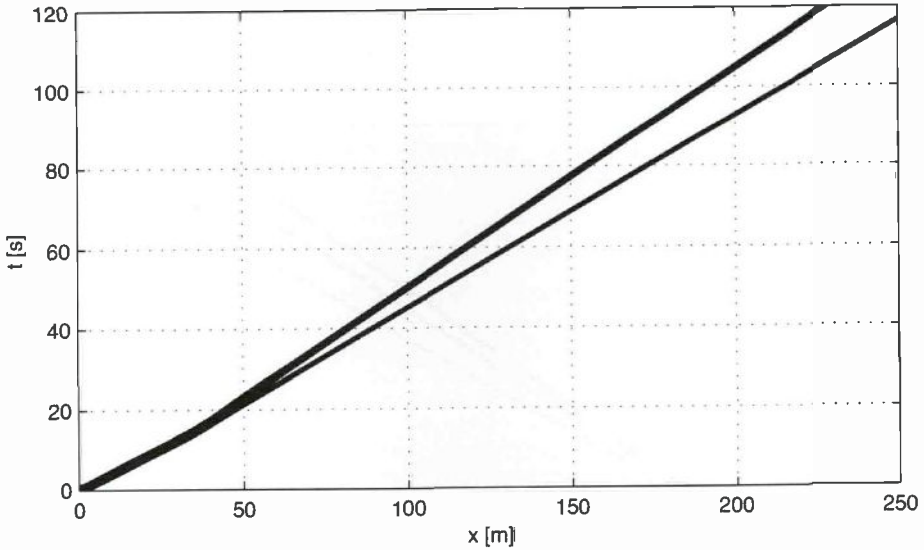
Figure 3.27: *x-t plot of the splitting of the solitary wave of Fig. 3.23(a) over a bottom slope (between $x = 30$ and $x = 40$ [m]) from a depth of $h_0 = 0.5$ to $h_1 = 0.3068$ [m] (see also Fig. 3.26 on the facing page(d)). $\eta(x,t) > 0.05H$ is plotted.*

by previous authors was reproduced. The splitting is visualised in Fig. 3.27 where only the values for $\eta > 0.005$ have been plotted.

As could be observed from Fig. 3.26(e), the splitting into three solitary waves is also found as a numerical solution of the nonlinear free-surface equations. This three-way splitting is visualised in Fig. 3.28 on the next page, in which again only the values larger than $0.05H$ are plotted. From this figure the difference in speed of the three identified solitary waves can be observed. The velocities of the split solitary waves are compared to the theoretical velocities of a Boussinesq solitary wave in Table 3.2. It is found that the velocities of the fully nonlinear solitary waves are in close agreement but differ slightly from the solitary wave solution of the Boussinesq equation with the same wave height.

3.6   Conclusions

We conclude this chapter by summarizing the main results obtained in the previous sections. All numerical results in this chapter were obtained with respect to natural boundary conditions.

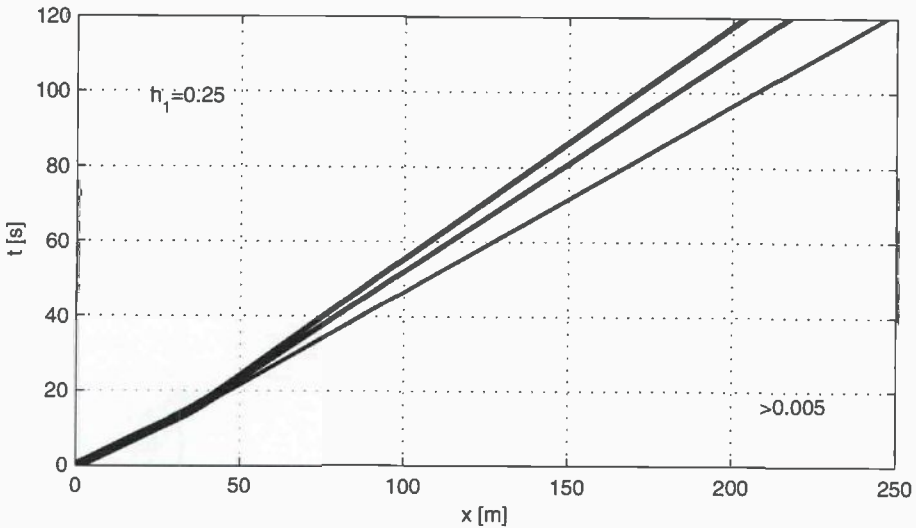It was found from linear Von Neumann stability analysis that the numerical scheme

Figure 3.28: *x-t plot of the splitting of the solitary wave over a bottom slope (between $x = 30$ and $x = 40$ [m]) from a depth of $h_0 = 0.5$ to $h_1 = 0.25$ [m] (see also Fig. 3.26(e)). $\eta(x,t) > 0.05H$ is plotted.*

Wave nr.	H_{num}	c_{full}	c_{Bq}
1	0.164	1.996	2.015
2	0.0538	1.710	1.726
3	0.0126	1.590	1.605

Table 3.2: *Wave height and velocities of the numerical solitary waves after splitting compared to the velocities of the Boussinesq solitary wave solutions with the same wave height.*

is stable for all investigated polynomial orders of the Finite Elements and Finite Differences, independent of the grid density and the orientation of the FE triangles. Moreover, it was found that the global projection method resulted in an unstable numerical scheme, specifically for the higher frequencies. This explains the need for additional smoothing when this method is used for velocity recovery.

Analysis of the Runge-Kutta time integration showed that in contrast to a 4-stage method, a 5-stage method results in growing solutions of the linearised discretised equations. However, actual amplification factors were found to be very small. In nonlinear simulations, it was always found that the energy slightly decreases and therefore it is concluded that the numerical dissipation caused by the geometric modelling compensates the amplifications due to the use of a 5-stage method.

A grid refinement study showed that for $p[FEM]=1$ and $p[FD]=2$ the numerical scheme is second-order accurate with respect to the energy.

A parameter variation study has been performed to examine the dispersive properties of the linearised discretised equations. A physically significant error measure σ has been introduced that corresponds to the relative error in the phase velocity of the numerical linear waves with respect to continuous linear waves. In practical applications many waves with different frequencies are simulated using one numerical grid. Therefore, the maximum dispersion error over a range of wave lengths was introduced. The limits for the wave lengths were set to $1/4$ to 4 times the water depth which contains the vast majority of waves generated in the laboratory.

It was found that by a suitable choice of grid density parameters and polynomial order of approximations of the FE's and FD's, the maximum relative error dispersion $\sigma(1/4, 4)$ can be reduced by a factor 100 for the same computational effort. It was also found that in the range of allowable computational effort the use of second-order Finite Elements does not lead to an efficiency improvement with respect to the $\sigma(1/4, 4)$ error.

Quantitative examination of the mass and energy conservation of the numerical algorithm showed that mass and energy very slowly decrease as a function of time. The relative error in the mass and energy has been computed for different wavelengths and wave steepness. The use of a nonuniform grid again showed significant reduction of the error. The amplitude of the oscillations of the energy error around its trend is mainly due to the horizontal resolution of the wave.

Two applications of the numerical algorithm to non-linear wave problems have been presented. A comparative study on the sloshing of a wave in a container showed good agreement with other numerical results. The second application concerned the splitting of a solitary wave over an uneven bottom. The previously reported splitting in two solitary waves was reproduced. By further decreasing the final depth, a splitting in three solitary waves was found to occur. The velocities of the solitary waves that result from the splitting process are in good agreement with theory.

Chapter 4

Simulation of Wave Generation

In the previous chapter the developed numerical scheme was investigated with respect to natural boundary conditions imposed at the lateral walls. These natural boundary conditions correspond to impermeable fixed walls. To introduce surface wave dynamics under these boundary conditions, an artificial initial condition on the free-surface elevation and velocity was imposed. In this chapter other methods will be investigated to generate free-surface dynamics in a numerical wave tank. The available methods are (e.g. Kim *et al.* (1999)):

1. Prescribed free-surface position and velocity; possibly with space periodic boundary conditions.

2. Discrete Internal Singularities.

3. Numerical velocity generation at the inflow boundary.

4. Wave-maker motion.

The prescribed free-surface technique (1) in combination with space periodic boundary conditions has been used to study the evolution of periodic signals on relative small computational domains (e.g. Longuet-Higgins & Cokelet (1976)). It is noted however, that the forced spatial periodicity may result in artificial evolution, especially when long time scales are involved. The discrete internal singularities method (2) was originally developed by Brorsen & Larsen (1987) for methods based on a boundary integral formulation. Recently, Clément (1999b) developed internal spinning dipoles generating uni-directional waves. In the following sections, the numerical velocity generation (3) and wave-maker motion technique (4) are examined, because these techniques are closely related to the actual wave generation process in a model basin.

The main emphasis is on the numerical aspects of wave generation. The actual steering of the wave makers, including the construction of second-order steering signals is discussed in detail by e.g. Schäffer (1996). In an experimental model basin, waves are usually generated using a wave maker. There are three types of wave makers: (a) piston-type wave makers (b) flap-type wave makers (c) plunger-type wave makers. At MARIN, flap-type wave makers are exclusively used for wave generation.

In Section 4.1 the flap and piston type wave makers are introduced and their implementation in the numerical scheme developed in the previous chapters is discussed. The numerical model is analyzed to determine stability and to obtain the discrete Biésel transfer functions relating the wave board stroke to the generated wave amplitude. In Section 4.2 the heaving wedge type wave maker is discussed. Linear stability analysis is performed and the results of a comparative study with other numerical methods are presented. In Section 4.3 two special implementations of numerical velocity generation are discussed. The results of this chapter are summarised in the concluding Section 4.4.

4.1   Flap- and piston-type wave maker

The most commonly used wave makers in model basins are the flap- and piston-type wave maker. The piston-type wave maker is a vertical board that oscillates in the horizontal direction. A flap-type wave maker is a hinged board that oscillates around a rotation point. The numerical simulation of these flap- and piston-type wave makers involves the movement of the grid near the oscilating wave board. In Subsection 4.1.4 the applicability of the discretisation is examined by comparing the results from the linearised discretised equations to results from the exact theory on linear waves generated by a wave maker.

The first theory on linear forced waves in water of finite depth was presented by Havelock (1929). Linearised solutions for both flaps and piston-type wave makers were later derived by Biésel (1951). These solutions are based on linearisation of both the free-surface elevation and the stroke of the waveboard. Since then, many extensions of this theory involving second-order contributions have been presented. A complete second-order wave-maker theory for planar wave makers has however been developed only recently by Schäffer (1996).

4.1.1   Linear theory

Following the wave-maker characterisation of Schäffer (1996), both flap- and piston type wave makers can be represented by the same linear model as

$$\Delta\Phi = 0 \qquad \text{in } \Omega \tag{4.1a}$$

$$\eta_t = \Phi_z \qquad \text{on } z = 0 \tag{4.1b}$$

$$\Phi_t = -g\eta \qquad \text{on } z = 0 \tag{4.1c}$$

$$\Phi_z = 0 \qquad \text{on } z = -h \tag{4.1d}$$

$$\Phi_x = g(z)T(t) \qquad \text{on } x = 0. \tag{4.1e}$$

with a radiation condition for $x \to \infty$. Both the kinematic and dynamic boundary conditions, as the stroke function of the wave board have been linearised. The type of wave generation is governed by the function $g(z)$ in Eq. (4.1e), which is defined as

$$g(z) = \begin{cases} 1 + \frac{z}{h+l} & \text{for } -(h-d) \le z \le 0 \\ 0 & \text{for } -h \le z \le -(h-d). \end{cases} \tag{4.2}$$

In Eq. (4.2), $z = -(h+l)$ is the center of rotation of the board and $d > 0$ is the elevation of the hinge over the bottom. If the center of rotation is below the bottom, then $d = 0$. The case $l = \infty$, $d = 0$ corresponds to a piston-type wave maker and the case where $l = -d < 0$ corresponds to a flap-type wave maker (see also Fig. 4.1 on the following page).

The general solution of the set of Eqs. (4.1a)-(4.1e) for a harmonic oscillating wave board, i.e. with $T(t)$ as

$$T(t) = i\bar{a}e^{-i\omega t}, \tag{4.3}$$

is given by

$$\Phi(x, z, t) = \frac{\bar{a}g}{\omega} \sum_{j=0}^{\infty} C_j \frac{\cosh\left(k_j(z+h)\right)}{\cosh\left(k_j h\right)} e^{i(k_j x - \omega t)} \tag{4.4a}$$

$$\eta(z, t) = \bar{a} \sum_{j=1}^{\infty} C_j e^{i(k_j x - \omega t)}, \tag{4.4b}$$

where the k_j's are solutions of

$$\omega^2 = gk_j \tanh\left(k_j h\right). \tag{4.5}$$

Of course, only the real part of these complex solutions corresponds to physical quantities. Remark that, unlike Eqs. (3.8a)-(3.8b) not only the progressive wave solution k_0 is incorporated, but also the so-called evanescent modes $k_j, \ge 1$. These evanescent modes correspond to imaginary solutions of the dispersion relation (4.5). The progressive mode is sinusoidal in the horizontal direction and hyperbolic in the depth, while the evanescent modes are sinusoidal in the depth and hyperbolic in the horizontal coordinate. The coefficients C_j are determined by substitution of Eqs. (4.4a) and (4.2) in Eq. (4.1e), multiplying by $-i\cosh\left(k_j(z+h)\right)$ and integrating the result
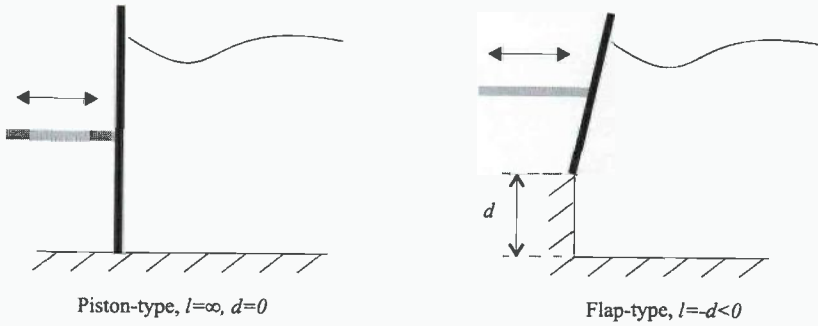
Figure 4.1: *A piston- and a flap-type wave maker, the values l and d of Eq. (4.2)
determine the wave-maker type.*

over the depth. This projection on the base functions $\cosh(k_j(z + h))$ leads to the
following formula for the coefficients C_j.

$$C_j = \sinh k_j h \frac{\Lambda_1(k_j)}{\Lambda_2(k_j)} \tag{4.6}$$

with

$$\Lambda_1(k_j) = \sinh(k_j h) - \frac{d+l}{h+l} \sinh(k_j d) + \frac{1}{h+l} \frac{\cosh(k_j d) - \cosh(k_j h)}{k_j} \tag{4.7}$$

$$\Lambda_2(k_j) = \frac{1}{2} [k_j h + \sinh(k_j h) \cosh(k_j h)]. \tag{4.8}$$

The function $C_0(\omega)$ is called the Biésel transfer function, which gives the relation
between the amplitude $\bar{a}$ of the wave board and the amplitude a of the progressive
wave as

$$a = C_0 \bar{a}. \tag{4.9}$$

Figs. 4.2 and 4.3 show the magnitude of the evanescent modes as a function of the
non-dimensionalised frequency for the wave-maker values $l = -d = -0.68$. These
values for l and d correspond to the flap-type wave makers used at the Seakeeping
and Manoeuvering Basin at MARIN. Clearly, the effect of the evanescent modes can
have a large influence on the total amplitude of the wave quantities at the wave
board. As pointed out by Schäffer (1996) it is therefore important to take the second-
order evanescent mode interactions into account when developing a second-order wave-
maker theory. In order to accurately simulate the generated waves in the fully non-
linear numerical algorithm, these evanescent modes need also to be well resolved on
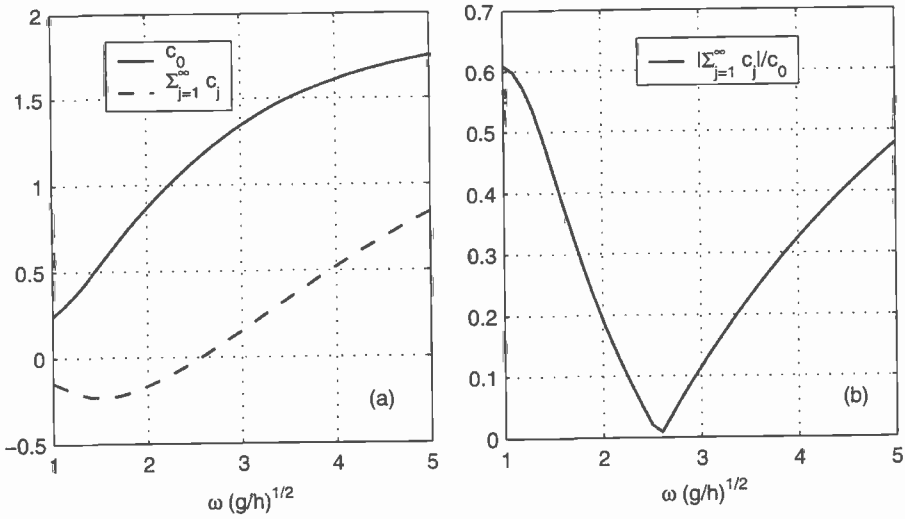the grid.

Figure 4.2: *(a) The Biésel transfer function C_0 and the total magnitude of the evanescent modes $i \sum_{j=1}^{\infty} C_j$ at $x = 0$ of Eq. (4.6), (b) The relative magnitude of the evanescent modes compared to the progressive mode. ($l = -d = -0.68$)*
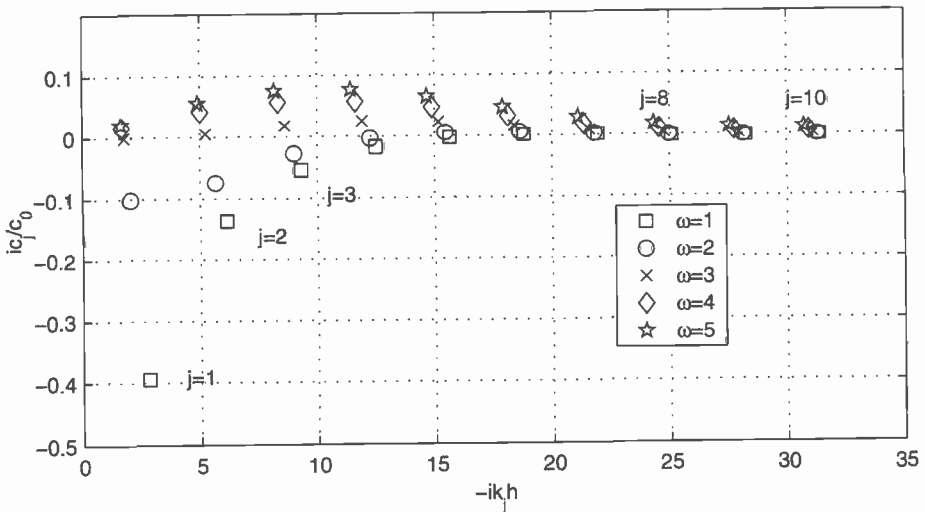

Figure 4.3: *The first 10 imaginary wavenumbers $-ik_j h$ and the corresponding relative contribution of the evanescent mode $C_j/|C_0|$ for different frequencies $l = -d = -0.68$.*
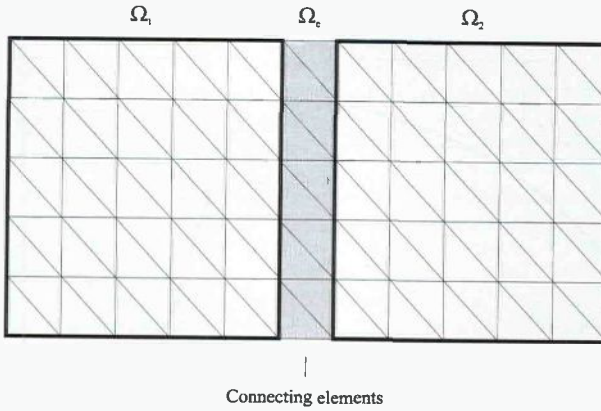
Connecting elements

Figure 4.4: *The stiffness matrices for Ω_1 and Ω_2 are constructed separately using natural boundary conditions on the interface. The matrices of $\widehat{\Omega} = \Omega_1 \cup \Omega_e \cup \Omega_2$ is constructed by the addition of the element contributions of Ω_e.*

4.1.2   Numerical modelling

It was already mentioned in Subsection 2.3 that the numerical modelling of the geometric domain is approached in a modular way. The geometry is e.g. split up in a wave-maker domain Ω_1 and a wave propagation domain Ω_2. These domains are independently developed and implemented in a computer code. All grid nodes are defined and controlled by the local domain grid generation algorithm. The finite elements are also locally constructed using natural boundary conditions ($\nabla\Phi \cdot n = 0$) on the lateral sides. Before proceeding with the global time marching scheme (see Fig. 2.2 on page 25), the highest level of the numerical algorithm connects the independent domains by adding elements as is schematically depicted in Fig. 4.4. The additional contribution to the interaction integrals $a(\cdot,\cdot)$ results in a change of the algebraic equations obtained from the FEM discretisation of the individual domains. For linear base functions, the combined new equations are identical to the equations obtained from direct FEM discretisation of the total domain $\widehat{\Omega} = \Omega_1 \cup \Omega_e \cup \Omega_2$. Remark that for higher-order elements (p[FEM]>2) also additional equations appear when the interface elements are added, due to the introduction of new base functions.

In the previous chapter, the performance of the numerical scheme on a domain with natural boundary conditions has been examined. In this section, the numerical grid and performance of the scheme for a flap wave maker is investigated. At the outflow boundary of the wave-maker domain, natural boundary conditions are imposed. This assures that (if the number of nodes in the vertical direction is identical) the wave maker can be connected directly to the propagation domain of the previous chapter. In this section we will introduce some grid structure parameters for the developed wave maker domain. Because the grid generation of a piston follows by analogy from the grid generation of the flap-type wave maker, only the grid structure of the
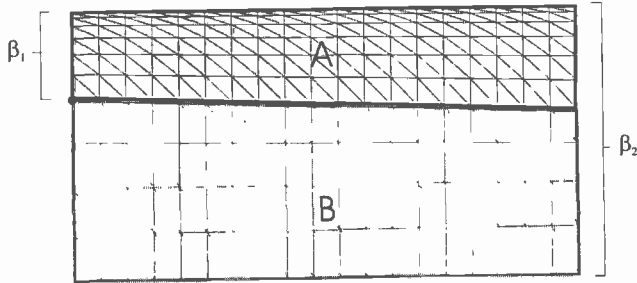
Figure 4.5: *The numerical grid near a flap wave maker. The structure of the grid is governed by the rotation point of the flap, the density factors β_1, β_2 and the fraction of grid points on the flap board.*

flap-type wave maker is introduced.

The structure of the grid around a flap wave maker is governed by (a) the rotation point of the flap, (b) the grid density parameters on the flap β_1 and on the outflow boundary β_2 and (c) the fraction of grid points on the flap. The grid is constructed from two regular blocks (topological equivalent to rectangular blocks) as depicted schematically in Fig. 4.5.

The grid generation of a block consists of two parts: (1) definition of the grid nodes on the four block-boundaries and (2) generation of the grid points inside the block. The boundaries of block A in Fig. 4.5 are defined by the free-surface boundary nodes, the node distribution on the flap and the node distribution on the outflow boundary. The lateral boundaries are defined by the grid distribution parameters β_1 and β_2 (see Eq. (3.22)-(3.23). The grid points on the lower horizontal boundary of block A are uniformly distributed over the block boundary.

The nodes in the interior of a block follow from a partition of the vertical lines connecting the nodes on the upper-horizontal block boundary and the lower horizontal block boundary. The distribution of the nodes on these lines varies linearly from the node distribution of the left boundary to the node distribution on the right boundary.

This process is formalised in the following way. Assume that the block consist of $Nx \times Nz$ nodes. The coordinates of the nodes of the grid are defined as $n(i,j) = (x_i, z_j)$. At the $i = 1$ boundary, the relative distance between the $j > 1$ node and the $j = 1$ node is given as

$$\Delta_1(j) = \frac{|n(1, Nz) - n(1, j)|}{|n(1, Nz) - n(1, 1)|},\tag{4.10}$$

and at the $j = Nx$ boundary, the relative distances are given as

$$\Delta_{Nx}(j) = \frac{|n(Nx, Nz) - n(Nx, j)|}{|n(Nx, Nz) - n(Nx, 1)|}.\tag{4.11}$$

The coordinates of the interior nodes $(1 < i < Nx, \ 1 < j < Nz)$ are now defined as

$$n(i,j) = n(i,1) + (n(i,Nz) - n(i,1)) \left(\frac{Nx - j}{Nx - 1} \Delta_1(j) + \frac{j - 1}{Nx - 1} \Delta_{Nx}(j) \right). \quad (4.12)$$

By this construction process a smoothly varying grid is generated that depends continuously on the position of the nodes of the flap and the nodes on the free surface. Remark that the grid is only well-defined if the left and right boundary have a small curvature. In all applications we consider, the left and right boundary of a block are straight lines, and the resulting grid is always well defined.

Grid points on the wave maker

The position of the grid points along the wave-maker board is determined from the position of the grid point at the intersection between the free surface and the wave maker. The distribution of the grid points from the rotation point to the intersection point is defined by β_1 (see also Eq. (3.22)-(3.23)). The motion of this intersection grid point is Lagrangian and its normal (with respect to the wave maker) velocity is prescribed by the motion of the wave maker. To obtain the velocity vector at this intersection point the tangential velocity along the wave board is determined using Finite Differences. The normal velocity at the nodes is determined from the prescribed angular-velocity of the board and the distance between the node and the rotation point. The normal velocity varies linearly over the wave board and is thus represented exactly by the restriction of first- or higher-order polynomial FE base functions to the boundary.

Free-surface grid points

If the grid points at the free surface are only allowed to move in the horizontal direction ($\hat{\sigma} = 1$ in Eq. (2.24)), the distance between the free-surface grid point at the wavemaker (which has to move completely Lagrangian, i.e. $\hat{\sigma} = 0$) and the first free-surface grid point can become very large or very small and even negative for large amplitudes of the wave board and small horizontal mesh width. Clearly the simulation halts as soon as the distance becomes negative and the free-surface node has 'penetrated' the wave-maker board.

To avoid this grid point collision problem there are several possibilities:

- Fixation of the horizontal position of the first free surface grid point such that it cannot be reached by the wave board. Although this avoids the collision problem for long and small regular waves it results in very inaccurate results for higher and shorter regular waves due to the extremely large local mesh width.

- Identification of all surface grid points with material points. Although this works for a short period of time, it will finally result in uncontrolled grid motion with possibly locally a very small mesh width, leading to unstable results if the time step is not adapted.

- Use a mixed Lagrangian description, e.g. setting $\hat{\sigma} = \frac{1}{2}$, for the first free-surface grid point and let the value of $\hat{\sigma}$ slowly reduce to $\hat{\sigma} = 0$ for the next free-surface points. This will solve the problem for a longer time than the previous solution, but there are still some problems involved. (1) the starting value of $\hat{\sigma}$ is arbitrary and (2) because the value of $\hat{\sigma}$ is non-zero, the grid point will partially behave as a material point and therefore experience an non-zero average velocity. When performing simulations for long time, we found that the latter effect becomes significant, leading to large local mesh width and finally to solution breakdown.

- To avoid the problems associated with the above possibilities, an active-grid procedure was developed. This procedure is based on a local and dynamic construction of $\hat{\sigma}$ such that the horizontal local grid velocity is a predefined factor of the horizontal grid velocity of the intersection point. This factor decreases linearly from 1 near the wave make to 0 at some specified distance from the wave maker.

The active-grid procedure is formalised as follows. Let the free-surface grid points be numbered as $(x_i, z_i), i = 0, \dots, n$. The grid point x_0 corresponds to the intersection point and its horizontal velocity is denoted as u_0. The desired horizontal grid velocity of x_i with $i > 0$ is

$$\frac{D}{Dt}x_i = (1 + \hat{\sigma}_i)(\Phi_x)_i = \frac{i}{n}u_0 \tag{4.13}$$

which defines $\hat{\sigma}_i$ dynamically for $\Phi_x \neq 0$ as

$$\hat{\sigma} = \frac{\frac{i}{nx}u_0 - (\Phi_x)_i}{(\Phi_x)_i}. \tag{4.14}$$

If $\Phi_x = 0$ then the value of $\hat{\sigma}$ is irrelevant and is set to zero. The result of the above dynamic and local definition of $\hat{\sigma}$ is that the grid stretches in the horizontal direction with the motion of the flap. This construction makes it possible to perform long time simulations using the wave maker with arbitrary fine grids near the wave maker and *a priori* bounds on the minimal/maximal grid width.

4.1.3   Grid convergence

To check the implementation of the wave maker a grid refinement study was performed for a typical wave. This refinement study was performed for several values β_1 of the grid distribution on the flap. The geometrical configuration was $h = 1$, $L = 10$, the gravitational constant g equals 1 and the rotation point of the flap was set at
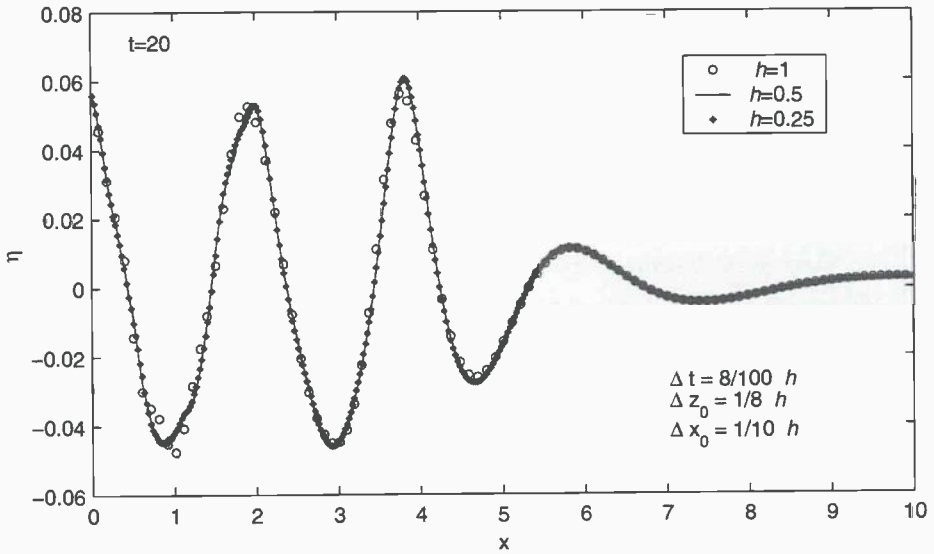
Figure 4.6: *Free-surface elevation at $t = 20$ for 3 refined grids ($g = 1$, $h = 1$, $A = 0.05$, $l = -d = -0.5$, $\omega=1.8$, $\beta_2 = 1$, p[FEM]=1, p[FD]=2).*

$z = -0.5$. A wave was generated with an intended amplitude (based on linear theory) of $A = 0.05$ with a frequency $\omega = 1.8$. The vertical grid distribution factor β_2 (see also Fig. 4.5 on page 93) at $L = 10$ is set to $\beta_2 = 1$. The grid was uniformly refined with a parameter h_{grid}. The following table gives the number of nodes in the vertical direction (nz) and the number of nodes above and including the rotation point (nz_1) and the number below the rotation point (nz_2) for the three refined grids.

h_{grid}	nz	nz_1	nz_2
1	9	6	3
1/2	17	11	6
1/4	33	21	11

The horizontal mesh width and time step depend on h_{grid} as $\Delta x = \frac{1}{10}h_{grid}$ and $\Delta t = \frac{8}{100}h_{grid}$. In Fig. 4.7 the grid near the wave maker is plotted at $t = 12$ for $h_{grid} = 1/2$ and $\beta_1 = 1$. The convergence was checked for $\beta_1 = 0, \frac{1}{4}, \ldots \frac{5}{4}$ (the grid distribution factor on the flap, see Fig. 4.5 on page 93). It was found that the surface elevation η at $t = 20$ converged for all investigated values of β_1. As an example Fig. 4.6 shows the free surface for three refined grids with $\beta_1 = 1$.
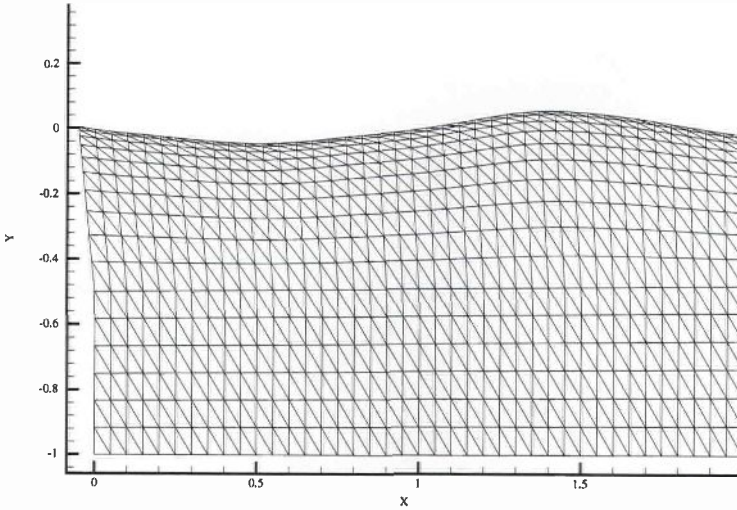
Figure 4.7: *Grid near the wave maker for one of the simulations in the convergence study.* $(t = 12, h_{grid} = 1/2, \beta_1 = 1)$

4.1.4 Linear analysis

This ssubsection is an extension of the linear analysis of Section 3.2.2. The same notation is used and not further introduced here. A new index set $\mathcal{N}$ is defined that holds the indices of all nodes (x_i, z_i) that are part of the wave-maker boundary Γ_W. Remark that there is exactly one node, the intersection point, that belongs to $\mathcal{N}$, but does not belong to $\mathcal{I}$. Moreover, this node belongs to $\mathcal{D}$ when the intersection point is considered as a part of the free surface.

Discretised equations

The normal velocity $g(z)$, see also Eq. (4.1e), along the boundary Γ^N is approximated by the restriction of the node functions N_i to Γ^N as

$$\widehat{g}(z) = \sum_{i \in \mathcal{N}} g_i N_i|_{\Gamma^N} \tag{4.15}$$

where the values of $\widehat{g} = g_i$ are simply determined as

$$g_i = g(z_i). \tag{4.16}$$

For notational convenience the bilinear form b is introduced as

$$b(g, v) = \langle g, v \rangle_{\Gamma^N} = \int_{\Gamma^N} g(s) v(s) ds. \tag{4.17}$$

Substitution of Eq. (4.15) and (4.17) in Eq. (2.40) leads to the following extension of Eq. (3.31),

$$a \left(\sum_{i \in \mathcal{I}} \varphi_i N_i, N_j \right) = -a \left(\sum_{i \in \mathcal{D}} \varphi_i N_i, N_j \right) + b \left(\sum_{i \in \mathcal{N}} g_i N_i |_{\Gamma^N}, N_j |_{\Gamma^N} \right) \ \forall j \in \mathcal{I}. \tag{4.18}$$

Similar to the introduction of the matrices $A_{\mathcal{KL}}$ in Eq. (3.33), the matrices $B_{\mathcal{KL}}$ are introduced as

$$(B_{\mathcal{KL}})_{ij} = b \left(N_{\mathcal{K}(i)} |_{\Gamma^N}, N_{\mathcal{L}(j)} |_{\Gamma^N} \right). \tag{4.19}$$

Analogous to the construction of Eq. (3.36) the following is readily derived,

$$\mathbf{D}^z[0] \widehat{\Phi^{\mathcal{D}}} = [-D^z_{\mathcal{DI}} A^{-1}_{\mathcal{II}} A_{\mathcal{ID}} + D^z_{\mathcal{DD}}] \varphi^{\mathcal{D}} + [D^z_{\mathcal{DI}} A^{-1}_{\mathcal{II}} B_{\mathcal{IN}}] \widehat{g} = L_{\mathcal{D}} \varphi^{\mathcal{D}} + L_{\mathcal{N}} \widehat{g}. \tag{4.20}$$

The linearised discretised equations for a wave generator are thus given by

$$\mathbf{q}_t = \mathbf{A}\mathbf{q} + \mathbf{b}\widehat{g}. \tag{4.21}$$

where the matrix $\mathbf{A}$ in Eq. (4.21) is identical to the matrix $\mathbf{A}$ in Eq. (3.36) and the matrix $\mathbf{b} = L_{\mathcal{N}}$. The linear stability of the equations including the discretisation of the wave maker is thus not affected by the wave maker. In Chapter 5 this linear analysis is extended to include an absorbing boundary (Sommerfeld condition). This boundary condition is completely transparent to progressive linear waves when the phase speed of the linear regular wave is provided. With this additional boundary condition the periodic solutions of the linearised discretised equations can be obtained. We are specifically interested in the envelope of the linear free-surface elevation, which is computed by first solving for time periodic solutions $\mathbf{q} = \tilde{\mathbf{q}} e^{i\omega t}$, given $\widehat{g} = \tilde{g} e^{i\omega t}$ as

$$(i\omega \mathbf{I} - \mathbf{A}) \tilde{\mathbf{q}} = \mathbf{b} \tilde{g}. \tag{4.22}$$

Eq. (4.22) is solved using a preconditioned Conjugate Gradient Squared (CGS) method with incomplete Cholesky factors (ICF) as preconditioners. When the drop tolerance of the ICF is set to 10^{-4} the relative residue converges typically to a value $< 10^{-12}$ within 10 iterations. The envelope is then determined as $|\tilde{\mathbf{q}}|$.

As the function $g(z)$ is normalised to 1 for $z = 0$, the Biésel transfer function of the numerical wave-maker model can be directly determined from the envelope amplitude $|\tilde{\mathbf{q}}|$. In Fig. 4.8 the numerical (from linear analysis of the discretised equations) and analytical (from Eq. (4.6)) Biésel functions are plotted for several grid configurations to illustrate the effect of the grid parameters β_1, nx/h and nz. The parameters that were kept constant are: p[FEM]=1, p[FD]=2, $L = 8$, $l = -d = -0.68$. When $nz = 11$ nodes are used in the vertical direction, the number of grid points on the flap nz_1 is

chosen to be 7 (corresponding to 5 elements). For the case that $nz = 21$ vertical nodes are used, the number of grid points on the flap is chosen as $nz_1 = 12$. In Fig. 4.9 on page 101 the Biésel transfer function is plotted for $nx/h = 25$ with $nz = 11$. From these figures the following observations are made.

- For small frequency waves, the relation between the exact and numerical Biésel function is satisfactory, but for high frequency waves, the numerical transfer functions are higher than the exact results.

- Increasing the number of grid points in the vertical direction leads to better approximation of the exact transfer function but a measurable difference is still present. Increasing the number of grid points in the horizontal direction leads to smoother curves around the high frequencies and a small overall improvement.

- Changing the grid distribution β_1 on the flap only shows significant improvement for high frequency waves and for sufficient horizontal resolution. However, for $nx/h = 25$ (fig. 4.9 on page 101) it is observed that the numerical estimate for high frequency waves ($\omega > 3$) corresponding to wave lengths smaller than 0.7, the estimated values severely deviate from the exact values for all values of β_1. The choice of $\beta_1 = 0$ and $\omega = 5$ ($\frac{nx}{\lambda_{\omega=5}} = 6$) even lead to a numerical solution without progressive waves.

- In all figures, it seems that for $\omega < 3$, the numerical values agree best with the exact values for $\beta_1 = 0$, whereas for the high frequencies $\beta_1 > 0$ seems to give the better results.

To further investigate to what extent the evanescent modes are resolved, the numerical and exact wave envelope near the free surface are plotted. In Fig. 4.10 the numerical and exact envelopes near the wave maker are shown for a modestly resolved grid configuration ($nx/h = 31$, $nz = 11$, $\beta_1 = 1.5$, $\beta_2 = 1.5$, $nz_1 = 8$, $l = -d = -0.68$). The exact result follows from Eq. (4.4b) where the first 10 evanescent modes have been used to approximate the infinite sum. As can be observed, the correspondence is quite satisfactory for $\omega\sqrt{h/g} = 1$ and $\omega\sqrt{h/g} = 2$ (corresponding with $\lambda > \frac{3}{2}h$). For $\omega\sqrt{h/g} = 3$ some deviations between the numerical and exact result can be observed. For higher frequencies $\omega\sqrt{h/g} = 4$ and $\omega\sqrt{h/g} = 5$ (corresponding to $\lambda < \frac{1}{2}h$) the shape of the envelopes is quite similar, but as was already observed from the previous figures, the numerical amplitude is higher than the theoretical amplitude.

Overall it is concluded that relative fine horizontal and vertical grids are necessary to accurately model the flap-type wave generation for high frequency waves compared to the grids needed for accurate wave propagation. This is most probably related to the larger velocity gradients occurring from the transition of the prescribed velocity field near the wave maker to the progressive wave velocity field. The results show however that reasonable results for the near field wave envelope can be achieved for the $l = -d = -0.68$ flap, if the grid density parameter is chosen as $\beta_1 = 1.5$ and $nz_1 \geq 8$ and $nx/h \geq 31$. It is however recommended that the linear analysis of the
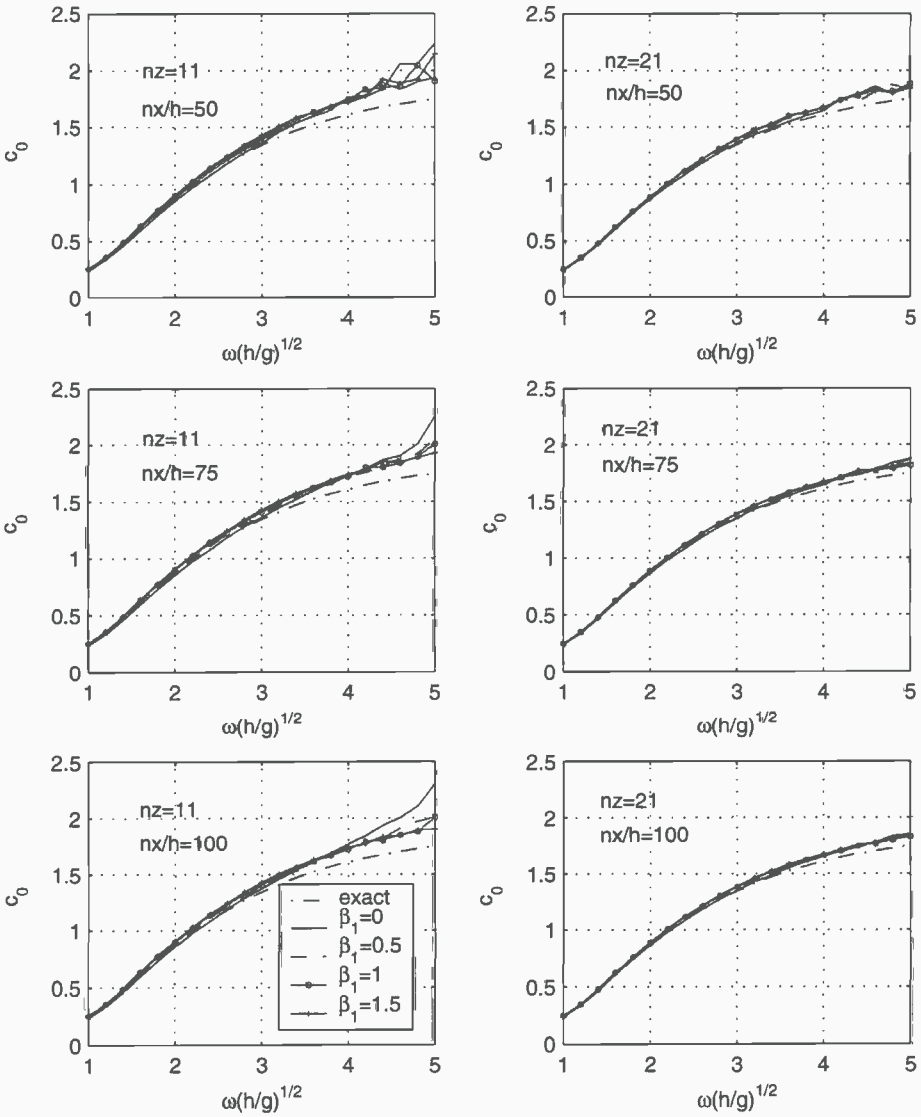
Figure 4.8: *The numerical and exact (from Eq. (4.6) Biésel transfer functions for different values of nz, β and nx/h. If $nz = 11$ then $nz_1 = 7$ and when $nz = 21$, $nz_1 = 12$. (p[FEM]=1, p[FD]=2, $L = 8$, $\beta_2 = 1.5$, $l = -d = -0.68$)*
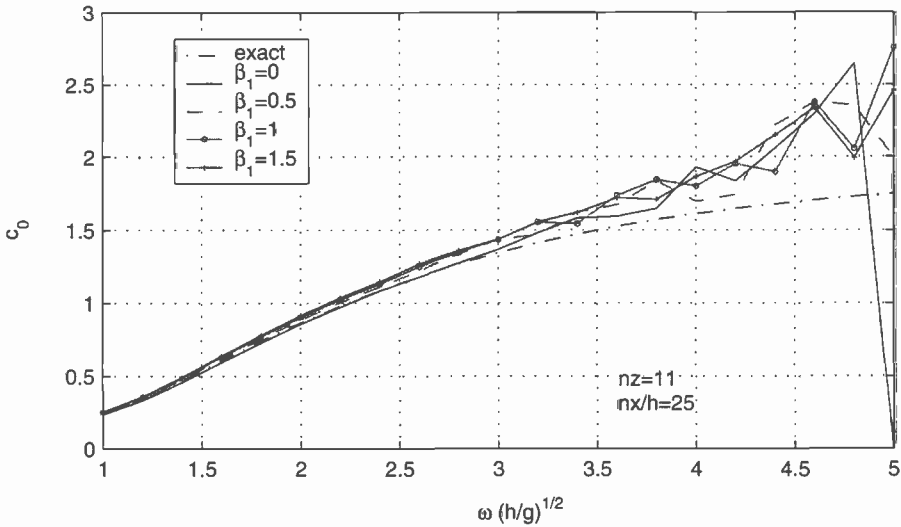
Figure 4.9: *The numerical and theoretical Biésel transfer functions for different values of β_1 for $nz = 11$, $nz_1 = 7$ and $nx/h = 25$.*

discretised equations outlined in Section 4.1.4 is used to construct the discrete transfer functions and that these are used instead of the exact Biésel transfer functions when numerical flap driving signals are generated from target wave spectra.

Intersection point

The surface grid point at the intersection between the free surface and the wave-maker board has to coincide with a material point. Therefore the motion of the intersection grid point x_{is} is described by the equation (see also Eq. (2.25) with $v_{cor} = 0$)

$$\frac{Dx_{is}}{Dt} = \nabla\Phi. \tag{4.23}$$

However, there appear to be two possibilities to treat the potential at the intersection point:

1. In the discretisation of the boundary value problem, the intersection point is considered to belong to Γ_D. In this case a Dirichlet condition has to be imposed at the intersection point. Because the intersection point is thus considered part of the free surface it is treated almost identical to free-surface nodes. The only difference is that the normal derivative of the potential is prescribed by a function instead of finite differences along the free surface.

2. The intersection point is treated as *not* belonging to Γ_D. In this case the potential at the intersection point is added as a degree of freedom to the equations.
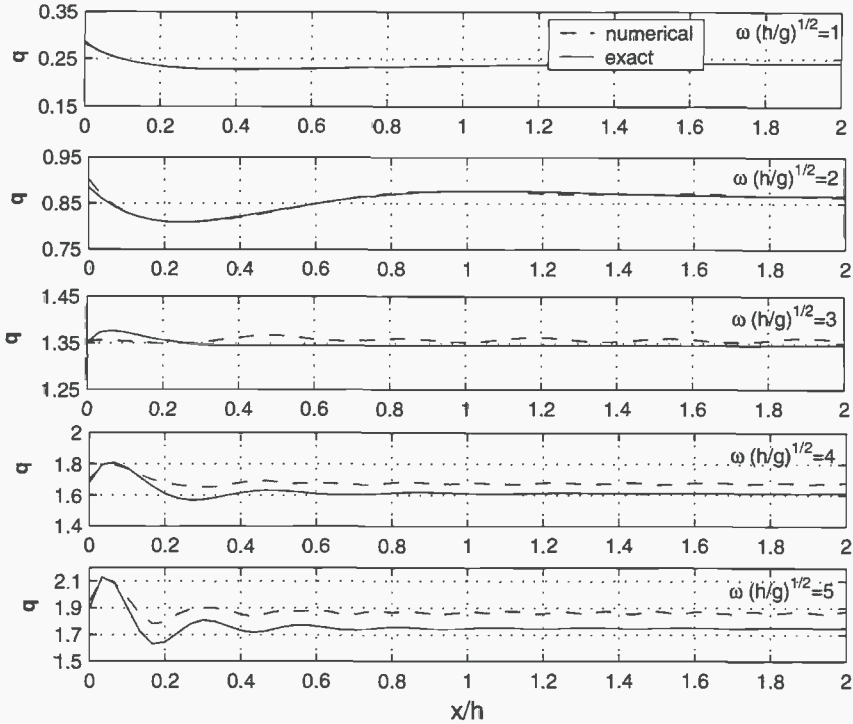
Figure 4.10: *Comparison between the exact (see Subsection 4.1.1 on page 88) and numerical wave envelope near the wave generator. (p[FEM]=1, p[FD]=2, $nx/h = 31$, $nz = 11$, $\beta_1 = 1.5$, $\beta_2 = 1.5$, $nz_1 = 8$, $l = -d = -0.68$)*

The potential at the intersection point follows from a solution of the boundary value problem with Dirichlet conditions prescribed on the free-surface nodes. Thus no dynamic equation for Φ at the intersection point is necessary. Again, for evaluation of the velocity at the free surface, the normal derivative is prescribed analytically.

Remark that the first implementation (Bernoulli at the intersection point) was chosen in Chapter 3. One of the reasons for this was the consistent treatment of the free-surface grid points when two domains are coupled as in Fig. 4.4 on page 92. More importantly, the second implementation leads to unstable simulations. Linear analysis of the second implementation requires some careful treatment of the grid points index sets $\mathcal{D}$ and $\mathcal{I}$ but can be performed analogous to the analysis in Section 4.1.4. An important difference is that the vectors for η and ϕ^D are not of the same length and that the matrix L_d is thus not longer square. In Fig. 4.11 on the next page the eigenvalues of the matrix associated with the linearised discretised equations are compared for the two different treatments of the intersection point. As can be observed, the second implementation leads to an unstable discretisation. This instability was
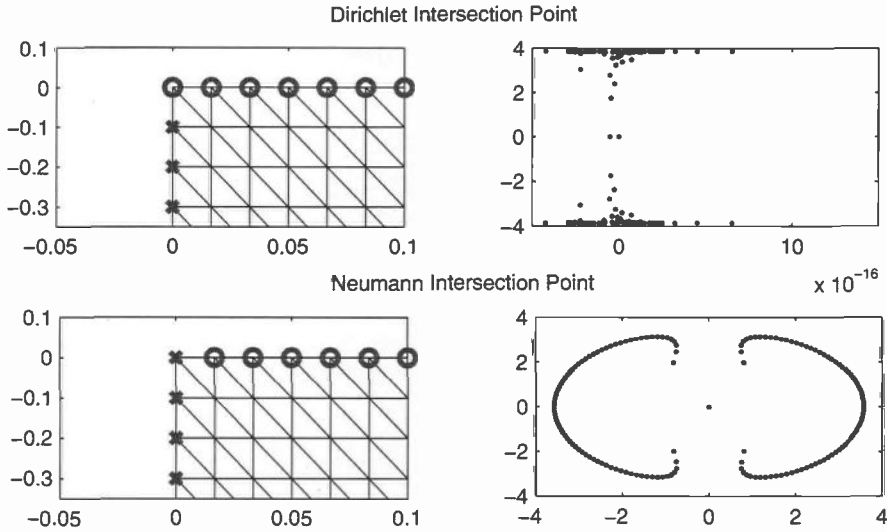
Figure 4.11: *Meshes and eigenvalues for a typical configuration with (0) being the nodes were a Dirichlet condition is applied.*

also found in preliminary nonlinear simulations of the second implementation. In retrospect, the instability is not so remarkable considering the following observation. The discretisation of the second implementation is equivalent to the implementation of a homogeneous Neumann condition over the free-surface boundary from $x = 0$ to $x = \Delta x$. Such an implementation is therefore clearly not consistent and marginal stability can therefore not be expected.

4.2   Wedge wave maker

In 1999 a comparative study was organised by the Numerical Wave Tank group of the International Society of Offshore and Polar Engineering (ISOPE). The results of the computations of all participants in the comparative study have been gathered, analyzed and published by Tanizawa (2000). In Fig. 4.12 on the following page the geometric configuration of a heaving wedge, used in the benchmark test, has been sketched. The wedge wave maker has a prescribed sinusoidal heave motion

$$Z = \bar{a} \cdot \sin(\omega t), \tag{4.24}$$

where Z is the vertical displacement with respect to the rest position of the wedge. ω and $\bar{a}$ are the frequency and the amplitude of the motion, respectively. As a result of the wedge-motion a regular wave with wavelength λ is generated. The ratio between the half breadth of the wedge a_w and the depth of the wedge d_w (both at rest) is
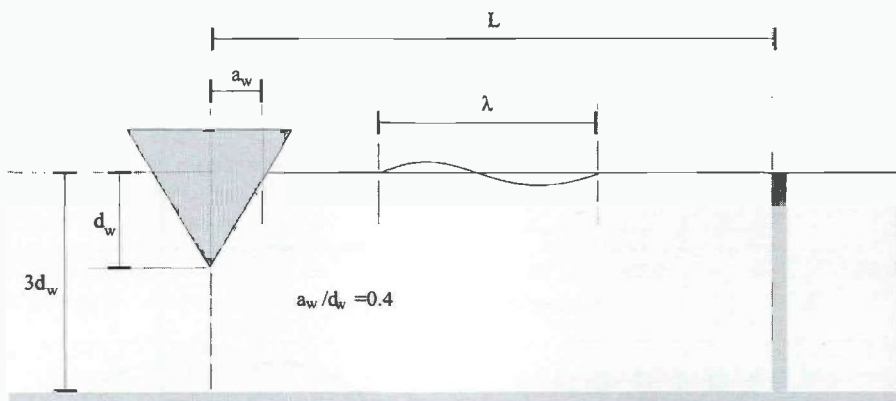
Figure 4.12: *Configuration of the wedge for the comparative study. Prescribed vertical motion of the wedge results in the generation of waves.*

$a_w/d_w = 0.4$. The wave tank has a depth $h = 3d_w$ and a length L of more than four times the wavelength λ. The domain is assumed to be unbounded for $x \to \infty$. Of course, in numerical simulations, a numerical beach must be employed to absorb the waves within a finite distance from the wedge. In Chapter 5 this aspect of the numerical simulation is treated in more detail. The numerical simulations are started from the rest situation with a start-up time of approximately four periods of the wedge motion and continue until the wave field is periodic.

The benchmark problem specifies a set of nine different combinations of the dimensionless frequency and dimensionless amplitude for the wedge motion. These nine combinations are given in Table 4.1 together with the wavelength according to linear theory and non-dimensionalised by the half breadth of the wedge a_w.

case nr.	$\bar{a}/a_w$	$\omega^2 a_w/g$	λ/a_w	case nr.	$\bar{a}/a_w$	$\omega^2 a_w/g$	λ/a_w
1	0.2	0.2	29.1	6	0.4	1.0	6.3
2	0.2	0.6	10.5	7	0.6	0.2	29.1
3	0.2	1.0	6.3	8	0.6	0.6	10.5
4	0.4	0.2	29.1	9	0.6	1.0	6.3
5	0.4	0.6	10.5				

Table 4.1: *Benchmark test cases with dimensionless amplitude and frequency of the wedge motion and the dimensionless wavelength. $\bar{a}$, ω and λ are non-dimensionalised by the half breadth of the wedge a_w and the gravitational acceleration g.*

The time signals of the following quantities were submitted for comparison with the

numerical results of the other participants: (i) the free-surface nodes for $0 \le x \le 4\lambda$ (ii) the free-surface velocity for $0 \le x \le \lambda$ and (iii) the hydrodynamic force on the wedge. In order to calculate the hydrodynamic force the pressure is integrated over the wetted surface S_0 of the body:

$$F = \int_{S_0} p \, \underline{n} \, dS. \tag{4.25}$$

The pressure can be calculated from the potential solution using Bernoulli's equation (2.19), which is repeated here for convenience:

$$\frac{p}{\rho} = -gz - \frac{1}{2}\nabla\Phi \cdot \nabla\Phi - \Phi_t . \tag{4.26}$$

Only the last term in Eq. (4.26), the time derivative Φ_t, cannot be approximated directly from a single available potential solution. This derivative can be approximated using potential solutions at different time steps by numerical differentiation, for example by backward differences or even by central differences if the pressures are calculated in a post-processing phase of the computation. This, however, can lead to poor estimates of Φ_t as has been mentioned by e.g. de St. Q. Isaacson (1982) and Celebi *et al.* (1998).

A more suitable method of approximating Φ_t is to construct a new boundary-value problem for Φ_t itself that can be solved after the solution of the boundary value problem for Φ has been obtained, as was pointed out by Tanizawa & Sawada (1990). This can be done at any time when a pressure calculation is required. The boundary value problem for $\Psi = \Phi_t$ on a domain with fixed impermeable walls is given by

$$\Delta\Psi \quad = \quad 0 \qquad\qquad\qquad \text{in } \Omega \tag{4.27}$$

$$\Psi \quad = \quad -g\eta - \frac{1}{2}\nabla\Phi \cdot \nabla\Phi \quad \text{on } z = \eta(x,t) \tag{4.28}$$

$$\Psi_n \quad = \quad 0 \qquad\qquad\qquad \text{on } z = \eta(x,t) \tag{4.29}$$

The Neumann boundary condition for Ψ on a moving boundary like a wave maker is more elaborate. A general method to derive the expression for Ψ_n is given by Tanizawa & Sawada (1990). For a two dimensional surface this expression at a point p on a moving surface Γ that rotates with an angular velocity θ around a moving hinge is given as

$$\frac{\partial}{\partial n}\frac{\partial\Phi}{\partial t} = a_n - \theta_t r + (v_n - \theta r)\left(\frac{\partial^2\Phi}{\partial s^2}\right) + \frac{\partial\Phi}{\partial s}\theta . \tag{4.30}$$

In Eq. (4.30), a and v are the acceleration and the velocity of the rotation point, respectively, and θ is the angular velocity of the plate Γ around the rotation point (see also Fig. (4.13 on the next page)). For a flap-type wave maker Eq. (4.30) reduces to Eq. (4.31)

$$\Psi_n = -\theta_t r - \theta r \frac{\partial^2\Phi}{\partial s^2} + \frac{\partial\Phi}{\partial s}\theta \tag{4.31}$$
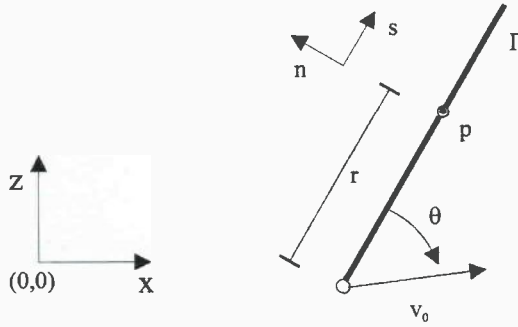
Figure 4.13: *Frame of reference and symbol notation for the determination of the normal derivative of Φ_t at a point p on a plate that is rotating around a moving point.*

and for the wedge type wave maker, Eq. (4.30) reduces to Eq. (4.32)

$$\Psi_n = Z_{tt}\sin(\alpha) + Z_t\sin(\alpha)\frac{\partial^2\Phi}{\partial s^2}. \tag{4.32}$$

In Eq. (4.32) , $Z(t)$ is the vertical position of the wedge (as e.g. in Eq. (4.24)) and α the constant angle of the wedge's face with the vertical, which is approximately 21.8 degrees for the wedge in the comparative study.

4.2.1   Analysis

Before proceeding to the comparison of the results of the test cases (Table 4.1) a linear stability analysis with respect to the spatial discretisation is performed. The main and important difference with the linear stability analysis of the flap and piston type wave maker is the non-rectangularity of the domain. Therefore the stability results from Section 3.2 cannot be directly applied.

Analogous to the derivation of the linearised discretised equations for the flap wave maker in Subsection 4.1.4, the linearised discretised equations for the wedge can be written as

$$\mathbf{q}_t = \mathbf{A}\mathbf{q} + \mathbf{b}T(t). \tag{4.33}$$

The matrix $\mathbf{A}$ is now constructed using a FEM and FD discretisation on a non-rectangular domain, see e.g. the grids in Fig. 4.14 on the facing page. In this figure one can already observe that, in contrast to the results from Chapter 3, the eigenvalues of $\mathbf{A}$ do not lie on the imaginary axis for all numerical parameters. When the wedge amplitude $a \rightarrow 0$, the eigenvalues always converged to the imaginary axis. The instability of some grid configurations is thus not solely due to the parameters β_1 , β_2 and nz_1 (the number of grid points on the wedge).
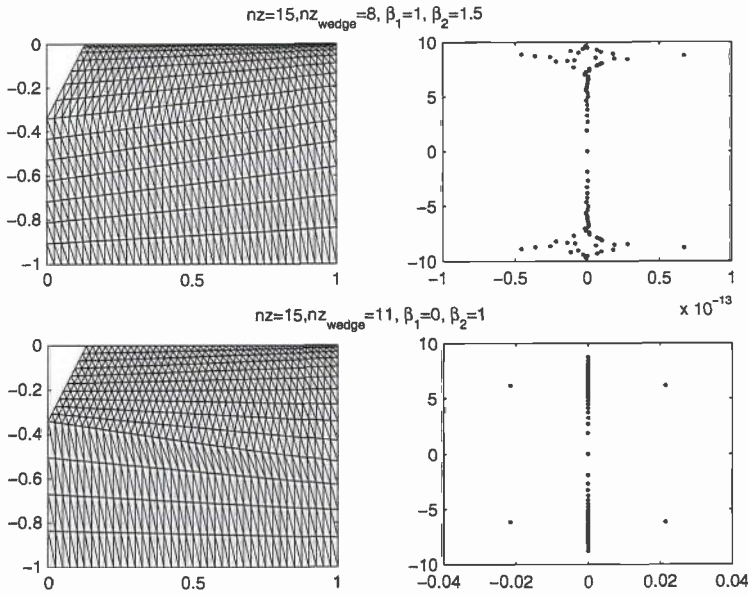
Figure 4.14: *A stable and an unstable grid configuration for the linear stability analysis of the heaving wedge.*

The stability of the different grid configurations was investigated and some of the results are presented in Table 4.2, 4.3 and 4.4. A discretisation is called unstable if the real part of at least one eigenvalue is larger than 10^{-3} and stable if the real part of all eigenvalues is smaller than 10^{-10}. In all investigated configurations the discretisation was found to be either stable or unstable by this definition. The results of the investigation however did not lead to a clear a priori criterion to establish the stability. However, the following observations were made

- The stability does not depend on the order of the polynomial approximation of the Finite Differences or on the triangular orientation of the elements.

- For the investigated range of values, increasing β_1 for the same number of nodes on the wedge may turn an unstable discretisation into a stable discretisation. The reverse has not been observed.

- Increasing the value of β_2 for $nx/h = 41$ has a positive effect when a low number of nodes are used on the wedge, while it has a negative effect when many nodes are used on the wedge.

- For finer horizontal mesh width ($nx/h = 81$) the increment of β_1 results in unstable discretisations for all investigated situations.

It is thus concluded that stable discretisations are not guaranteed for the heaving

wedge geometry. The stability depends on the grid and it is therefore recommended to perform a linear stability analysis before proceeding with the nonlinear simulations.

nz_1	$\beta_1 = 0$ $\beta_2 = 0$	$\beta_1 = 1/2$ $\beta_2 = 0$	$\beta_1 = 1$ $\beta_2 = 0$	$\beta_1 = 0$ $\beta_2 = 1$	$\beta_1 = 1/2,$ $\beta_2 = 1$	$\beta_1 = 1$ $\beta_2 = 1$
4	x	x	o	o	o	o
5	x	o	o	o	o	o
6	o	o	o	o	o	o
7	o	o	o	o	o	o
8	o	o	o	x	o	o

Table 4.2: *Stable (o) and unstable (x) grid configurations for the heaving wedge (nz = 11, L = 1, nx/h = 41, p[FD]=2, fixed triangular orientation).*

nz_1	$\beta_1 = 0$ $\beta_2 = 0$	$\beta_1 = 1/2$ $\beta_2 = 0$	$\beta_1 = 1$ $\beta_2 = 0$	$\beta_1 = 0$ $\beta_2 = 1$	$\beta_1 = 1/2,$ $\beta_2 = 1$	$\beta_1 = 1$ $\beta_2 = 1$
5	x	o	o	o	o	o
6	x	o	o	o	o	o
7	o	o	o	o	o	o
8	o	o	o	o	o	o
9	o	o	o	o	o	o
10	o	o	o	x	o	o
11	o	o	o	x	o	o

Table 4.3: *Stable (o) and unstable (x) grid configurations for the heaving wedge (L = 1, nz = 15, nx/h = 41, p[FD]=2), fixed triangular orientation*

4.2.2 Results

Seven researchers participated in the comparative study on the heaving wedge. Their computational methods and some details on the numerical parameters are given in Table 4.5 on the next page. In this table the column labelled with p denotes the order of polynomial base functions used in the discretisation method. Furthermore it is noted that $BEME$ is a second-order Taylor expansion method and thus not fully nonlinear. All methods, except the FVM, use the potential flow formulation of

nz_1	$\beta_1 = 0$ $\beta_2 = 0$	$\beta_1 = 1/2$ $\beta_2 = 0$	$\beta_1 = 1$ $\beta_2 = 0$	$\beta_1 = 0$ $\beta_2 = 1$	$\beta_1 = 1/2,$ $\beta_2 = 1$	$\beta_1 = 1$ $\beta_2 = 1$
4	x	x	o	x	x	x
5	x	o	o	x	x	x
6	o	o	o	x	x	x
7	o	o	o	x	x	x
8	o	o	o	x	x	x

Table 4.4: *Stable (o) and unstable (x) grid configurations for the heaving wedge (L = 1, nz = 11, nx/h = 81, p[FD]=2, fixed triangular orientation).*

indication	description	p	Δx	Δt	nz_{wedge}
BEM A	Fully Nonlin.	1	$\lambda/20$	$T/20 \sim T/40$	21
BEM B	Fully Nonlin.	2	$\lambda/20 \sim \lambda/30$	$T/25 \sim T/30$	21
BEM C	Fully Nonlin.	2	$\lambda/18$	$T/20 \sim T/160$	11
BEM D	Fully Nonlin.	1	$\lambda/6 \sim \lambda/25$	$T/50$	11
BEM E	2nd order	n.a.	$\lambda/60$	$T/60$	31
FEM	Fully Nonlin.	1	$\lambda/20 \sim \lambda/30$	$T/20 \sim T/30$	$4 \sim 27$
FVM	Fully Nonlin.	?	$\lambda/20$	$T/540 \sim T/700$	40

Table 4.5: *Brief description of the methods of the participants in the ISOPE benchmark tests. The FVM solves the incompressible NS equations, the other methods solve the potential flow problem.*

the free-surface wave problem. The FVM method is applied directly to the Navier-Stokes equations. Because of the difference in underlying equations and because this participant only contributed for a small number of test cases, the results of this method are not used in the present presentation of the results. For the numerical simulations with the present method, a numerical beach was used to absorb the radiated wave. This beach was designed to minimize reflections and more details can be found in Chapter 5. The actual numerical simulations were performed by Otto (1999). In Fig. 4.15 on the following page the free-surface elevation is plotted for $\bar{a}/a_w = 0.2$ and $\omega^2 a_w/g = 0.2$ (Case 1). The elevation of four different methods has been plotted and the results are found to be in reasonable good agreement. The results that were obtained with the present method are denoted by the label FEM. The free surface for the most extreme case 9 ($\bar{a}/a_w = 0.6$ and $\omega^2 a_w/g = 1$) is plotted in Fig. 4.16. This figure clearly shows some difference between the different numerical solutions. The linear and quadratic BEM and the FEM method show comparable results. It is
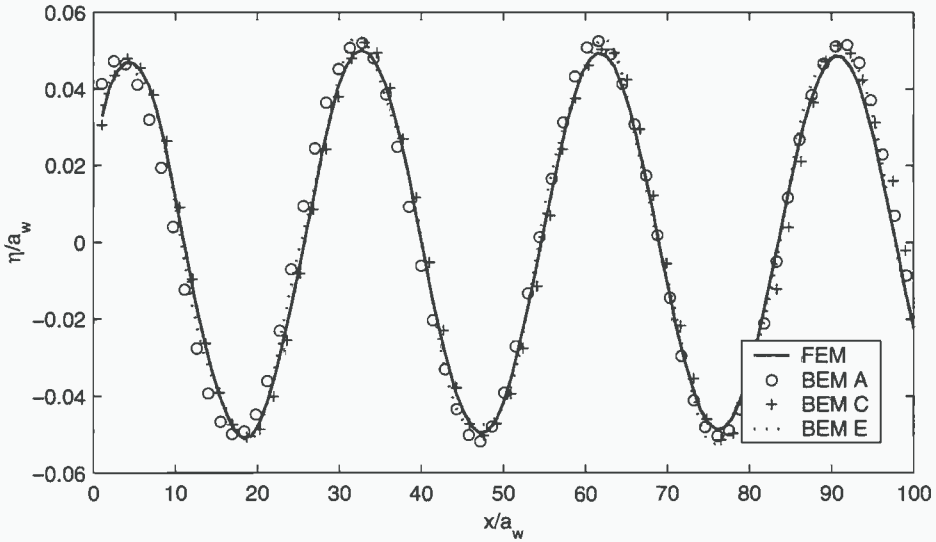
Figure 4.15: *The free surface elevation η computed by different numerical methods for low frequency and small amplitude waves (case 1 in Table 4.1).*

noted that the wave steepness $H/\lambda = 0.13$ which is more than 90% of the theoretical maximum. These extremely steep waves cannot be accurately reproduced by a second-order method, which is clearly visible in Fig. 4.16.

Besides the waves radiated by the heaving wedge, the forces on the wedge have been compared. Added mass and damping coefficients were computed and the second and third-order forces on the wedge have been determined for the different numerical methods. The results of this analysis are plotted in Fig. 4.17 on the next page. In general, the results of BEM A-C are in good agreement for all quantities and for all frequencies. The approximations of BEM D for the added-damping coefficients are relatively low. The second- and third-order forces on the heaving wedge are given in plot (c) and (d). The second-order Taylor expansion BEM E estimates the second-order forces for the higher frequencies rather high and evidently returns a zero valued third-order component. The BEM D appears to predict the third-order forces significantly higher than BEM A-C, while the FEM predicts a lower third-order force than BEM A-C for this frequency. Overall it is concluded that in general good mutual agreement is observed for the fully nonlinear BEM methods BEM A, BEM B and BEM C. The approximations obtained using the developed FEM are in reasonable agreement but show some deviation of the average result for the high frequencies.
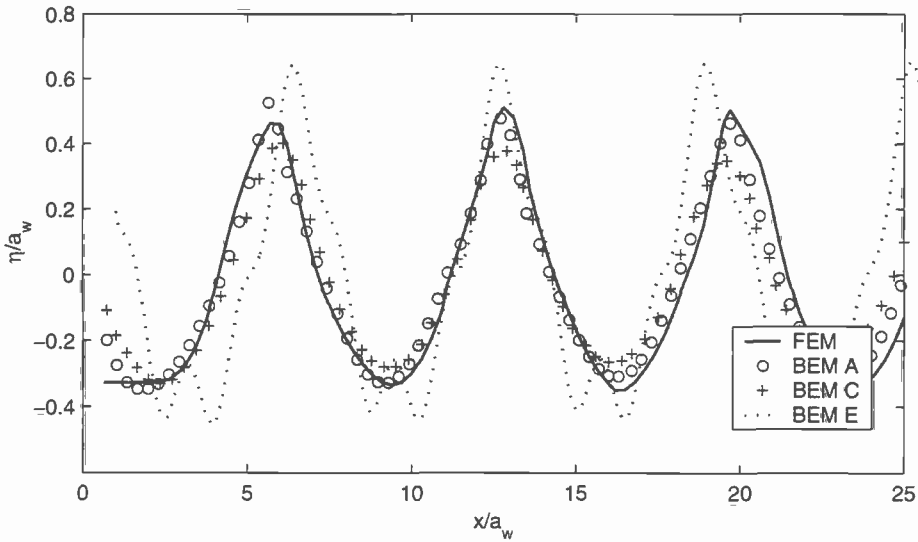
Figure 4.16: *The free-surface elevation η computed by different numerical methods for high frequency and large amplitude waves (case 9 in Table 4.1).*
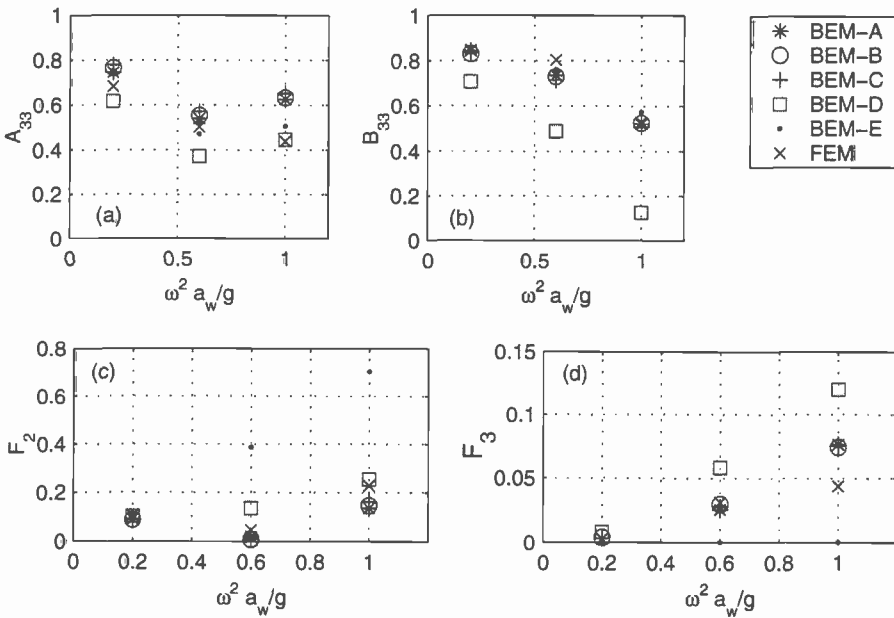

Figure 4.17: *Added mass (a) and damping (b) and the second and third-order forces on the wedge (c)-(d) (see also Table 4.5).*

4.3   Numerical velocity generation

The results from the analysis on the wedge indicate that the stability of the numerical method is influenced by the non-rectangular geometry of the domain. Remark however that for flap- and piston type wave makers, this cannot be concluded from linear stability analysis. For some applications of the numerical method, one is less interested in an exact physical representation of the wave maker. In these cases a numerical velocity generation mechanism can be employed on the inflow boundary. In this section we consider two special types of numerical velocity wave generation mechanisms that have been developed for practical applications. The first is a combined flux-displacement wave maker and the second mechanism is a combined generation-absorption wave maker for regular waves.

4.3.1   Combined flux-displacement wave maker

The idea of the combined flux-displacement wave maker is to allow an arbitrary correlation between the prescribed velocities on the inflow boundary and the actual displacement of that boundary. This concept was developed to increase the stability of the simulations. It was found that for very long simulations ($t > 100T$) the simulation might break down due to instabilities around the wave maker. It was already found by experience that when the wave board geometry was kept fixed and only velocities are prescribed, simulations could be carried out for longer times.

The correlation between the flux and the displacement of the wave maker is controlled by the parameter $\hat{\sigma}$ already introduced in Section 2.2. The parameter $\hat{\sigma}$ indicates to what extent a free-surface grid point is a material point. For $\hat{\sigma} = 0$, the free-surface grid point coincides with a material point, and for $\hat{\sigma} = 1$ the free-surface grid point is displaced along the tangent of the free surface in such a way that the x-coordinate remains unaltered. In physical modelling of piston-, flap- or wedge-type wave generators, the values of $\hat{\sigma}$ for the intersection point must be set to $\hat{\sigma} = 0$ because the grid point must remain on the wave maker surface.

When the value of $\hat{\sigma}$ at the free surface is chosen to be 1, the intersection point only moves up and down. However, the normal velocity along the wave maker boundary is still prescribed according to the virtual wave-maker motion. In this situation, the wave-maker boundary produces numerical flow and can be interpreted as a model for a complicated pump-system. For values of $\hat{\sigma}$ between 0 and 1 the intersection point, and thus the complete wave-maker boundary, varies between a non-moving flux generating boundary and a consistently moving boundary. The physical equivalence for e.g. $\hat{\sigma} = 1/2$ is a flap that moves with half the amplitude of the original wave maker but produces additional flux through its boundaries to compensate for this difference.

4.3.2 Absorbing wave maker

Both in experimental as in numerical wave tanks, active absorption mechanism are used. In an experimental wave tank, the active wave absorption mechanism measures the elevation on or near the wave generating flap and corrects the flap-displacement to absorb incoming waves. This mechanism can be reproduced in the numerical simulation method, but for regular waves a simpler numerical procedure is available for a numerical wave tank. The aim of this kind of wave generation is to construct a boundary condition that generates regular waves and absorbs waves with the same frequency that travel in the other direction.

The exact solution of a progressive linear wave moving to the right is given by

$$\overrightarrow{\phi}(x, z, t) = A \frac{\omega}{k} \frac{\cosh(k(z+h))}{\sinh(kh)} \cos(kx - \omega t). \tag{4.34}$$

One possibility to generate a regular wave is thus to impose the condition

$$\Phi_t = \frac{\partial \overrightarrow{\phi}}{\partial t} = A \frac{\omega^2}{k} \frac{\cosh(k(z+h))}{\sinh(kh)} \sin(\omega t) \quad \text{on} \quad \Gamma_W \tag{4.35}$$

on the *non-moving* wave-generating boundary. The boundary does not move, but an artificial potential satisfying a linear progressive wave is imposed as a Dirichlet condition on this boundary.

We assume that a second wave (caused by reflections against the opposing wall or an other obstruction) is propagating with the same frequency in the negative x-direction. The potential in the domain is thus thought to be build up as

$$\Phi = \overrightarrow{\phi} + \overleftarrow{\phi}. \tag{4.36}$$

The outgoing regular wave satisfies the travelling wave equation

$$\overleftarrow{\phi}_t + c_s \overleftarrow{\phi}_x = 0. \tag{4.37}$$

When this condition is restricted to the boundary it is often referred to as a Sommerfeld condition. Substitution of $c_s = \frac{\omega}{-k}$ and Eq. (4.34) in Eq. (4.36) and differentiation with respect to time at $x = 0$ leads to

$$\Phi_t \quad = \quad \overrightarrow{\phi}_t + \overleftarrow{\phi}_t \tag{4.38}$$

$$= \quad \overrightarrow{\phi}_t + \frac{\omega}{k} \overleftarrow{\phi}_x \tag{4.39}$$

$$= \quad \overrightarrow{\phi}_t + \frac{\omega}{k} \left(\Phi_x - \overrightarrow{\phi}_x \right) \tag{4.40}$$

$$= \quad A \frac{2\omega^2}{k} \frac{\cosh(k(z+h))}{\sinh(kh)} \sin(\omega t) + \frac{\omega}{k} \Phi_x \tag{4.41}$$

Imposing Eq. (4.41) as a boundary condition on the generating boundary thus combines the generation of a regular wave with the absorption of regular waves of the same

frequency and can thus be used as a combined wave-generating/absorbing boundary condition.

It is important to notice that the above derivation does not take nonlinear effects into account. Reflections of the transient waves during start-up and nonlinear interactions will result in many different frequency components that will be only partially absorbed by this condition. Another important aspect of this combined wave generator/absorber is the effect of the Sommerfeld condition on the stability of the numerical discretisation (see also Section 5.3.1 on page 129).

To illustrate this method, the following numerical simulation is performed. A small regular wave ($A = 0.01$, $\omega = 1.6$) is generated using the combined wave generator/absorber using a linear startup ramp for $0 < t < 1.25T$ to avoid large initial accelerations. The transient waves are completely reflected against the opposing wall. The combined wave-generator absorber should partially absorb the transient waves during startup and completely absorb the reflected regular waves. After sufficiently long time the transients should therefore be absorbed completely and a standing wave remains.

This can be observed in Fig. 4.18 on the next page were the x-t plots of the surface elevation have been plotted. In Fig. 4.18(a) the first 6 periods are shown in which the generation of the transients and their reflection can be observed. Along the $x = 0$ axis one can observe that the progressive wave is indeed of the correct amplitude. In Fig. 4.18(b) the x-t plot for $24T < t < 30T$ is visualised. Clearly, the regular standing wave can be observed with an amplitude of 0.02, confirming the applicability of the generating/absorbing regular wave generator. This absorbing wave maker was also used successfully in the fully nonlinear numerical studies on the wave forces acting on a captive heaved ship section (Huijsmans *et al.* (1999)).

4.4   Conclusions

In this chapter three types of numerical wave generation have been discussed. For flap- and piston-type wave generators the linear stability and convergence of the discretisation was established. The discrete Biésel transfer functions were determined for a number of numerical grids and compared with exact transfer function. It was found that the discrete wave maker produces slightly higher waves (up to 10% for high frequencies) than expected from linear theory. Additional grid resolution in the horizontal and vertical direction is necessary to obtain more accurate transfer functions and representation of the effect of the evanescent modes. If this resolution is not available for some reason, the proposed analysis should be performed on the numerical scheme to obtain the transfer functions of the discretised system. It has been observed both in fully nonlinear simulations, as well as from linear analysis, that on poorly resolved high frequency waves ($\frac{nx}{\lambda} < 6$), no progressive waves are generated at all.
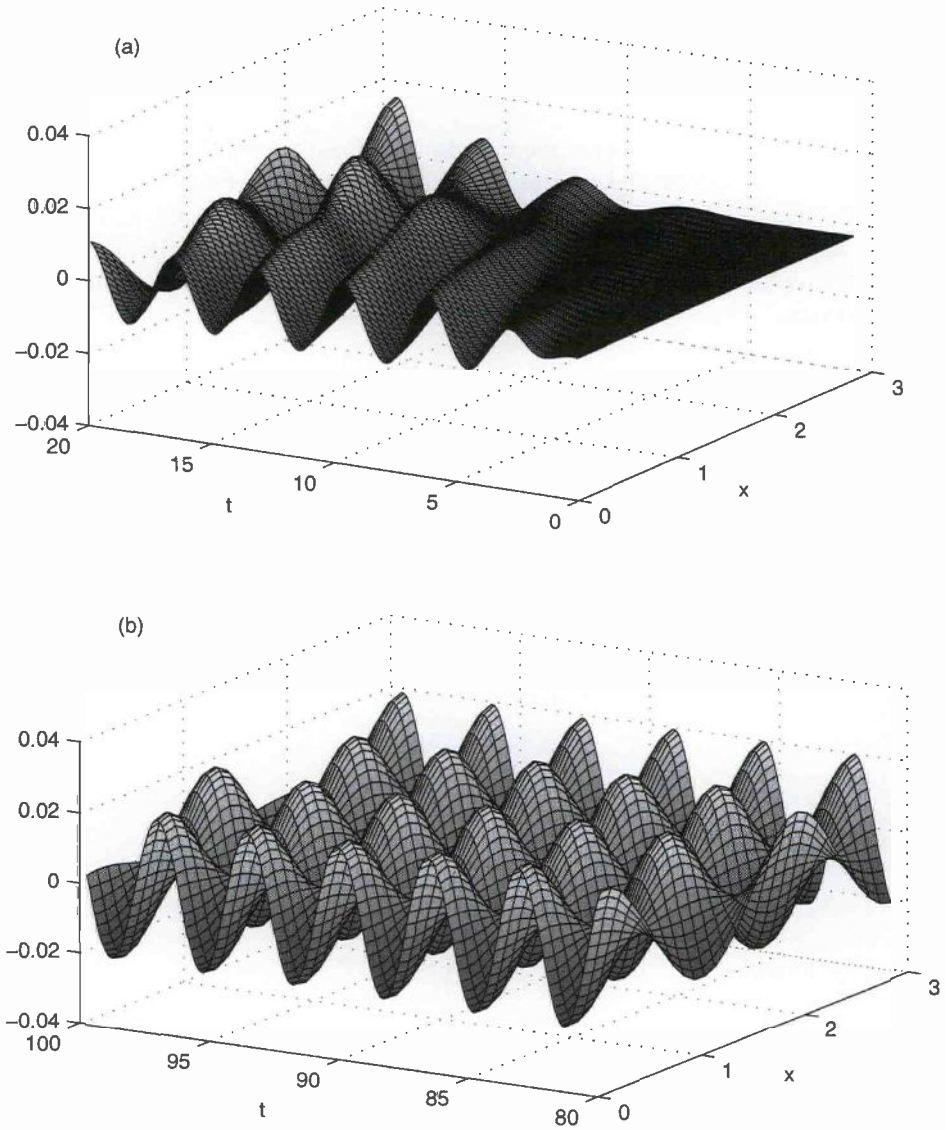
Figure 4.18: *x-t plots of the free surface when the combined absorbing/generating boundary condition Eq. (4.41) at $x = 0$ is used. (a) the first 6 periods showing the generation and reflection against the opposing wall. (b) after sufficiently long time, the transient wave components have been completely absorbed and a standing wave field is achieved.*

Linear stability analysis of the wedge wave maker showed that stability depends on the grid structure around the wedge. It is therefore recommended to perform a linear stability analysis to a planned grid when a wedge-type wave maker is used. Comparison of the forces on a heaving wedge with other numerical methods has been presented. In general good agreement is found between other methods and results of the present method.

Two specific numerical velocity wave makers have been presented: a combined flux-displacement wave maker and an absorbing/generating wave maker. The combined flux-displacement wave maker allows for more stable fully nonlinear long time simulations, and the absorbing/generating wave maker can be efficiently used when reflections from obstructions placed in the numerical wave tank need to be absorbed at the wave maker.

It has been found in nonlinear numerical simulations that for the generation of large amplitude waves, using either flap type or numerical velocity type of wave generation, stability of the simulation is not evident and additional refinement of the grid near the wave maker may be necessary to avoid growing instabilities at the free surface near the wave maker.

Chapter 5

Simulation of Wave Absorption

In this chapter the modelling and simulation of the absorption of waves in a model basin will be discussed. Firstly, different kind of physical wave absorption mechanisms will be presented. Measurements performed at MARIN to assess the quality of some artificial beach concepts will be discussed. The reflection coefficients obtained from the measurements do not support a low dimensional model for the artificial beach. Secondly, a number of numerical methods to model wave-absorption and -reflection are presented. The implementation of these methods is analyzed to investigate the corresponding reflection coefficients and the effect on the stability of the numerical scheme. Based on these investigations, two numerical beach concepts are developed, analyzed and implemented. The first beach concept aims at achieving minimal reflecting properties at low computational costs. The second concept aims at reproducing the obtained reflection coefficients from the measurements.

5.1   Experimental wave absorption

A model basin in a hydrodynamic laboratory is designed to act as a model environment for open sea conditions. To represent these conditions, the waves need to propagate through the basin as if the basin is not bound by horizontal walls. The incoming wave field is reproduced by a wave generation mechanism such as has been discussed in chapter 4. Against the walls opposite to the wave generators, wave absorbers are positioned to absorb the incoming waves. The aim of these wave absorbers is to minimize the reflective influence of the walls opposite to the wave generators.

Two types of wave absorption in an experimental wave tank are distinguished: active and passive wave absorbers. The most appealing example of a passive wave absorber

is a sand beach. An active wave absorber can be best compared to an inversely operating wave maker. These two absorption mechanisms are briefly discussed in the following two subsections.

5.1.1   Passive wave absorption

In a wave tank used for coastal or waterway model testing, physical models of sand beaches can be the subject of the investigations. However, in an experimental wave tank designed for hydrodynamic applications, the beaches are purely artificial and only intended to maximally absorb the waves. On the one hand, the artificial beach should take up as less space as possible to maximize the model testing area. On the other hand, the reflections against the beach should be small enough, not to influence the model testing significantly.

A straightforward but effective artificial wave absorber is a sloping bottom. In order to have small reflections from such an artificial beach, the slope must be very small. This requirement clearly conflicts with the requirement of maximal model testing space and is thus not frequently encountered in a hydrodynamic model basin.

When the previous seakeeping basin of MARIN was constructed in 1957, a study on artificial beaches was performed by van Lammeren & Vossers (1957). They reported on 12 different artificial beach concepts (including gravel beaches and overflows) and concluded that a curved plate with grating (investigated by Delft (1955)) yielded satisfactory results. Gratings of different size were investigated and the final choice was eventually constructed in wood. The concept of parabolic plates with gratings was also used for the artificial beaches at the Indonesian Hydrodynamic Laboratory (constructed in 1995). Hollow perforated stainless steel grating were used and measurements showed that these artificial beaches had better overall reflection characteristics. For the construction of the artificial beaches in the new SMB at MARIN, a new series of design tests was performed by Kapsenberg (1999). Some results of these tests are presented in Section 5.2.

Another kind of passive wave absorber is a construction composed of partially submerged layers of wire-netting. This wave absorber was used in front of the wave generators at the old seakeeping basin at MARIN to absorb spurious waves generated during the wave generation process. A similar wave absorption technique has been developed at the Canadian Hydraulics Center. An upright wave absorber composed of porous expanded metal sheets is placed in front of the opposing wall. An advantage of this absorber is that the absorption characteristics can be tuned by changing the number, placing and porosity of the sheets. A disadvantage is the amount of space required for the positioning of the sheets.

5.1.2   Active wave absorption

An active wave absorber is best compared to an inversely operating wave maker. Based on real-time measurements of e.g. the wave height or the pressure, a control mechanism steers the board of the active wave absorber in such a way that the incoming wave is transmitted. The main advantage of an active wave absorber is that it requires only very little space, thus leaving more space for model testing. Another advantage is that it can be tuned specifically to reduce resonant oscillations in the tank and to reduce the basin stilling time between experiments. There are however two major drawbacks of such an absorption mechanism when compared to passive absorbers. Firstly, it is much more expensive than passive wave absorption. Secondly, the active wave absorber is only suitable for a certain range of frequencies, depending on the geometry of the wave board. Although active wave absorbers are available in some wave tanks (e.g. Canadian Hydraulics Center, Danish Hydraulics Institute and MARIN), they are usually not used as a replacement of passive wave absorbers. Instead, the most common use of active wave absorption technology is to combine the absorption method with the existing wave generator. Such a system is also referred to as a reflection compensation system. Based on measurements on or near the wave maker instantaneous additional steering information is generated to adjust the motion of the board to absorb unwanted reflections. This technology has been implemented at the new Seakeeping and Manoeuvering Basin and Offshore Basin at MARIN. For a recent review on (two-dimensional and multi-directional) active wave absorption methods confer Schäffer & Klopman (2000).

5.2   Measurements of wave reflection on beaches

For the construction of the artificial beaches in the new SMB at MARIN, a series of design tests were performed. These experiments and the results have been reported by Kapsenberg (1999). The artificial beaches are to be placed both on the long (North) side as on the short (West) side of the SMB. The tank geometry of both sides is however not identical as can be observed in Fig. 5.1 on the following page.

The design of the artificial beach was made by Delft Hydraulics, Bos (1997), and consists of a straight (A), a curved (B) and again a straight part (C). These parts are depicted in Fig. 5.2 on the next page where the dimensions of the final configuration for the beach on the West side are also given. Reflection coefficients were determined for different values of the length of part (A), the relative height of the still water level, the angle of part (C) and two types of gratings. The plate (E) in Fig. 5.2 was placed to investigate the performance of the beach when placed in the West side of the SMB.
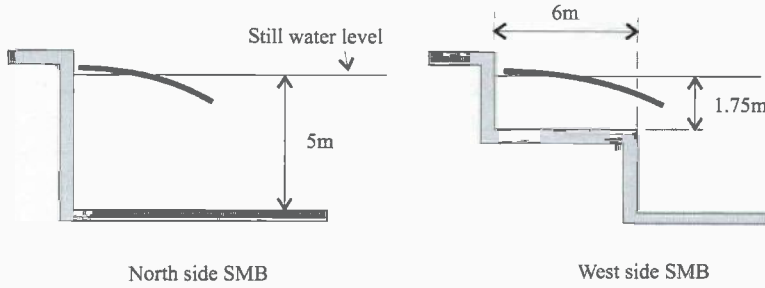
Figure 5.1: *Geometry of the Seakeeping and Manoeuvering BASIN (SMB) near the beaches at the West side (short side) and the North side (long side) of the basin.*
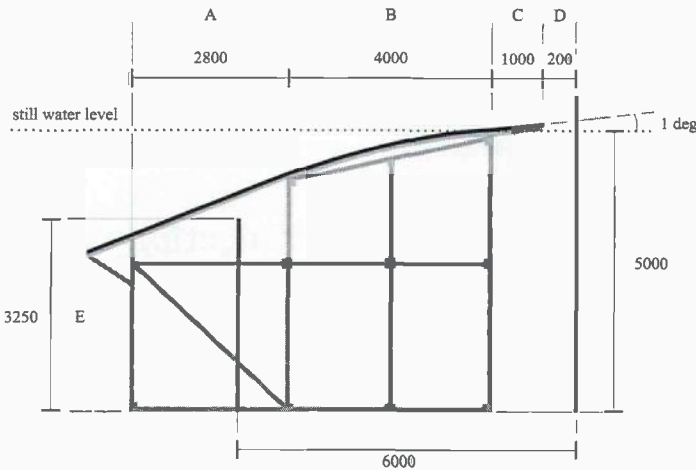

Figure 5.2: *Model of the beach used to examine the reflection coefficients of various geometry and roughness variations. Dimensions are given for the West-side beach configuration.*
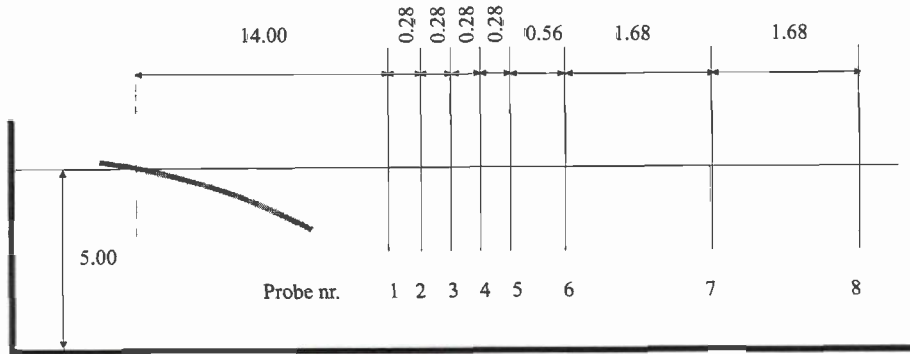
Figure 5.3: *Position of the wave elevation probes relative to the intersection of the still water with the beach. Dimensions are in [m] and are not depicted proportionally.*

5.2.1 Determination of the reflection coefficients

The measurements were performed in the High Speed Basin at MARIN using a model of the artificial beach designs. This basin is equipped with a hydraulic flap type wave generator (hinged 1.27 [m] above the bottom) and has a still water depth of 3.57 [m] and a length of 220 [m]. The measurements were scaled to a water depth of 5 [m] corresponding to the water depth in the SMB. Figures and results presented in this section are also scaled to 5 [m] water depth.

The wave elevation was measured at 9 positions using resistance type wave gauges. Fig. 5.3 shows the positions of the first 8 wave probes relative to the intersection of the still water and the beach. The nineth wave probe is positioned 70 [m] from this intersection point and is used to determine the incoming wave amplitude.

The reflection coefficient for a beach is defined by modelling the beach as a linear filter. A plane incident wave with frequency ω and complex amplitude $A_{inc}(\omega)$ is reflected by the beach and therefore another wave travelling in the opposite direction with the same frequency but complex amplitude $A_{ref}(\omega)$ is observed. The reflection coefficient $r(\omega)$ is then defined as

$$r(\omega) = \frac{A_{inc}(\omega)}{A_{ref}(\omega)}. \tag{5.1}$$

Note that the reflection coefficient is defined as a complex quantity. However, in practice one usually refers to the absolute value, $|r|$, as the reflection coefficient. Another used definition of the reflection coefficient is the ratio of the incoming and reflected wave energy, i.e. $|r|^2$. We will use the word reflection coefficient mostly in the second sense (i.e. $|r|$). A fixed wall has by this definition a reflection coefficient of 1 and a completely absorbing beach has a reflection coefficient of zero.

Not the complete time signal obtained from the wave probe measurements was used to determine the reflection coefficient. Only the time interval that contains the primary incoming and reflected wave is used for analysis. These time signals thus do not contain the contribution of the wave that has reflected from the beach and also reflected from the wave maker. There are two main methods to determine the reflection coefficient from the wave height measurements. These two methods will be discussed in the following paragraphs.

Wave envelope modulation

The first method to determine the reflection coefficient is based on the spatial modulation of the envelope of the wave elevation of a regular wave. The (linear) wave elevation due to an incoming wave with amplitude a and a reflected wave with reflection coefficient $r = |r|e^{i \arg(r)}$ is given by

$$\eta(x,t) = ae^{i(kx-\omega t)} + rae^{i(-kx-\omega t)} + c.c. \tag{5.2}$$

$$= \left(1 + re^{-2ikx}\right)ae^{i(kx-\omega t)} + c.c. \tag{5.3}$$

An asymptotic method, introduced by Ursell *et al.* (1960) can be used, to determine the reflection coefficient $|r|$. Determining the envelope variation A from Eq. (5.3) results in

$$A^2(x) = a^2(1 - 2|r|\cos(2kx - \arg(r)) + |r|^2). \tag{5.4}$$

Taking the square root of Eq. (5.4) and using a Taylor approximation one obtains

$$A(x) = a\left(1 - |r|\cos(2kx - \arg(r)) + \mathcal{O}\left(|r|^2\right)\right). \tag{5.5}$$

The spatial wavelength of the modulation of the envelope A is thus halve the wavelength of the incoming wave. The reflection estimate is based on the determination of the maximum and minimum of the envelope modulation. If the (constant) amplitudes of time signals at fixed different positions are determined, a $2k$ wave is fitted through these points. If the maximum and minimum of this fitted wave are denoted as A_{max} and A_{min} then the approximation of the reflection coefficient is given (from Eq. (5.5)) as

$$|r| = \frac{A_{max} - A_{min}}{A_{max} + A_{min}} + \mathcal{O}(r^2). \tag{5.6}$$

Kapsenberg (1999) uses a comparable method to determine the reflection coefficient by directly fitting r in Eq. (5.4) to the measured envelope data.

A priori knowledge of the expected envelope wavelength can be used to determine an optimal spacing of the wave probes. It is clear that the probes should in any case not be equally distributed at $\frac{1}{2}n\lambda$ distances if the expected wavelength is λ.

For small amplitudes and reflection coefficients, the variations in the envelope can be quite small (8 [cm] wave with 5% reflection leads to a wave envelope amplitude of 4 [mm]). Assume that the maximum and minimum envelope have a resulting error of e_{max} and e_{min} respectively. This leads to the following relation between the reflection coefficient estimate based on the actual values and the estimate based on the biased values.

$$|r|_{bias} = r + \frac{2(e_{max}A_{min} - e_{min}A_{max})}{(A_{max} + e_{max} + A_{min} + e_{min})(A_{max} + A_{min})} \tag{5.7}$$
$$= r + e_r \tag{5.8}$$

When $e_{max} = e_{min} = e$, the following estimate is obtained

$$\hat{e}_r = r\left(\frac{e}{a+e}\right) \tag{5.9}$$

which results in a relative error in $|r|$ smaller than 2.5% for practical values of e and a. Substitution of the undisturbed amplitude a and choosing the worst error scenario $e_{max} = -e_{min} = -e$, this reduces to a maximum error estimate of

$$\tilde{e}_r = \frac{e}{a}. \tag{5.10}$$

The error in the wave gauges used at the experiments is determined (from the still water level time signals) at approximately 0.1 [cm]. We assume that this is also the error level of the amplitude determination which leads to a worst case error estimate of $\tilde{e}$ for small wave amplitudes (2 cm) of approximately 5 percent points. For intermediate amplitudes (8 cm) and high amplitudes (15 [cm]) this leads to worst case error estimates of 1.25 percent points respectively 0.67 percent points. For the small amplitude waves this worst error estimate is of the same order as the expected reflection coefficients. For the high amplitude waves, the linearity assumption underlying the model for the reflection coefficient becomes questionable and errors in the model probably will be dominant over this measurement error.

To give an indication of this magnitude we substitute the measurement error term e with the first nonlinear Stokes term $\frac{1}{2}ka^2$ (see also Eq. (3.10) on page 44) and determine the best-case error estimate from Eq. (5.9) as

$$\tilde{e}_r = r\frac{ka}{1+ka}. \tag{5.11}$$

Based on this substitution one can observe that for a steep wave $H/\lambda = 0.08$ with $a = 0.1$ [m] this leads to a relative error indication of approximately 20%.

Spectral decomposition for irregular waves

The second method to determine the reflection coefficients is based on spectral analysis of the measurements and has been developed by Mansard & Funke (1980). The

spectrum of a measured signal $s(x_n, t)$ at some point $x = x_n$ is given as

$$\hat{s}_n(\omega) = \frac{1}{2\pi} \int_{-\infty}^{\infty} s(x_n, t)e^{i\omega t}dt. \tag{5.12}$$

Hence (assuming linearity of the equations governing the signal), at every measuring point x_n we should have the identity

$$A_{inc}(\omega)e^{ikx_n} + A_{ref}(\omega)e^{-ikx_n} = \hat{s}_n(\omega) \tag{5.13}$$

where k and ω are related by the dispersion relation. Instead of forcing strict equality the squared summed error

$$\sum_{n=1}^{p} \left(A_{inc}(\omega)e^{ikx_n} + A_{ref}(\omega)e^{-ikx_n} - \hat{s}_n(\omega)\right)^2 \tag{5.14}$$

is minimised for A_{inc} and A_{ref}. This procedure results in the following estimate for the reflection coefficient based on p measurements of the signal at the locations $x = x_n$, $n = 1 \ldots p$

$$r = \frac{\left|\sum_{n=1}^{p}\hat{s}_n(\omega)e^{-ikx_n} \sum_{n=1}^{p}e^{2ikx_n} - p\sum_{n=1}^{p}\hat{s}_n(\omega)e^{ikx_n}\right|}{\left|\sum_{n=1}^{p}\hat{s}_n(\omega)e^{ikx_n} \sum_{n=1}^{p}e^{-2ikx_n} - p\sum_{n=1}^{p}\hat{s}_n(\omega)e^{-ikx_n}\right|}. \tag{5.15}$$

The main advantage of this method is that it can be applied to irregular wave fields. The result of the procedure is the reflection coefficient over a range of frequencies instead of a an estimate at a single frequency. A disadvantage of the method is the accuracy of the estimate. This is related to the accuracy with which the spectrum can be estimated. Accurate estimates of the spectral power density would require very long time traces. This desired time interval is not available because secondary reflections against the wave board will contaminate the signal. Furthermore, the reflection estimates are only valid for the range of frequencies where (i) the energy density is significant and (ii) the coherency between the measurements of the different wave probes is close to 1.

It turns out that in practical experiments, these limitations are quite stringent and that the error estimates of the coefficients are in the same order of magnitude as the estimates themselves. As with the spacing of the probes for the wave-envelope method, careless positioning of the probes may lead to failure of the method. Suryanto (1999) extended this method for a nonlinear wave model but found that the results were only slightly influenced and negligible with respect to other errors in this analysis.

5.2.2   Results

Both the wave envelope method and the spectral decomposition method have been used to estimate the reflection coefficients of the artificial beach. The wave envelope

method was however mostly used because it allows for more control over the incoming waves (including the amplitude) and the envelope estimates could be easily checked visually. Several tests were performed to investigate the repeatability of the analysis (different time traces of the same experiment) and the repeatability of the experiments (different experiments and a different position of the wave-gauge array). From these tests it was found that the repeatability of the envelope analysis is reasonable for most frequencies. For small amplitude, high frequency waves, large deviations were found, which can be explained from the analysis in the previous section.

In the next two paragraphs some general remarks are made regarding the different experiments that were performed to chose the final beach configurations for the North and West side of the SMB at MARIN. It is remarked that all experiments were performed in oblique waves. The effect on the reflection coefficient of waves approaching the beach at an angle was not investigated.

North-side basin

For the experiments using the geometry configuration of the North side of the basin, the length of part (A) (see Fig. 5.2 on page 120) is 0.8 m and the plate (E) is removed. Variation of the slope of part (D) and variation of the mean water level showed that a zero water level together with a 1 degree slope results in the most favorable reflection coefficients. Adding small roughness and lengthening the beach showed no significant improvement. For a steepness of 0.02 the reflection coefficient was found to be smaller than 10 % for all investigated frequencies. The reflection coefficients were also determined for other steepness but unfortunately no relation was found between the steepness and the reflection coefficient.

West-side basin

Based on the optimal configuration for the North side of the SMB, the reflection coefficients were determined when plate E was positioned to model the geometry of the West-side basin. For a wave steepness of 0.02 these reflection coefficients were found to be higher for the low frequencies and smaller for the high frequencies. Lengthening of the beach with 2 meters (length of part A is now 2.8 [m]) showed significant improvement. Further lengthening showed a slight worsening of the reflection coefficients.

Discussion

Fig. 5.4 on the following page shows the reflection coefficients that were determined from the experiments on the final beach configurations. The crosses correspond to a single measurement and the numerical value plotted next to the cross corresponds to
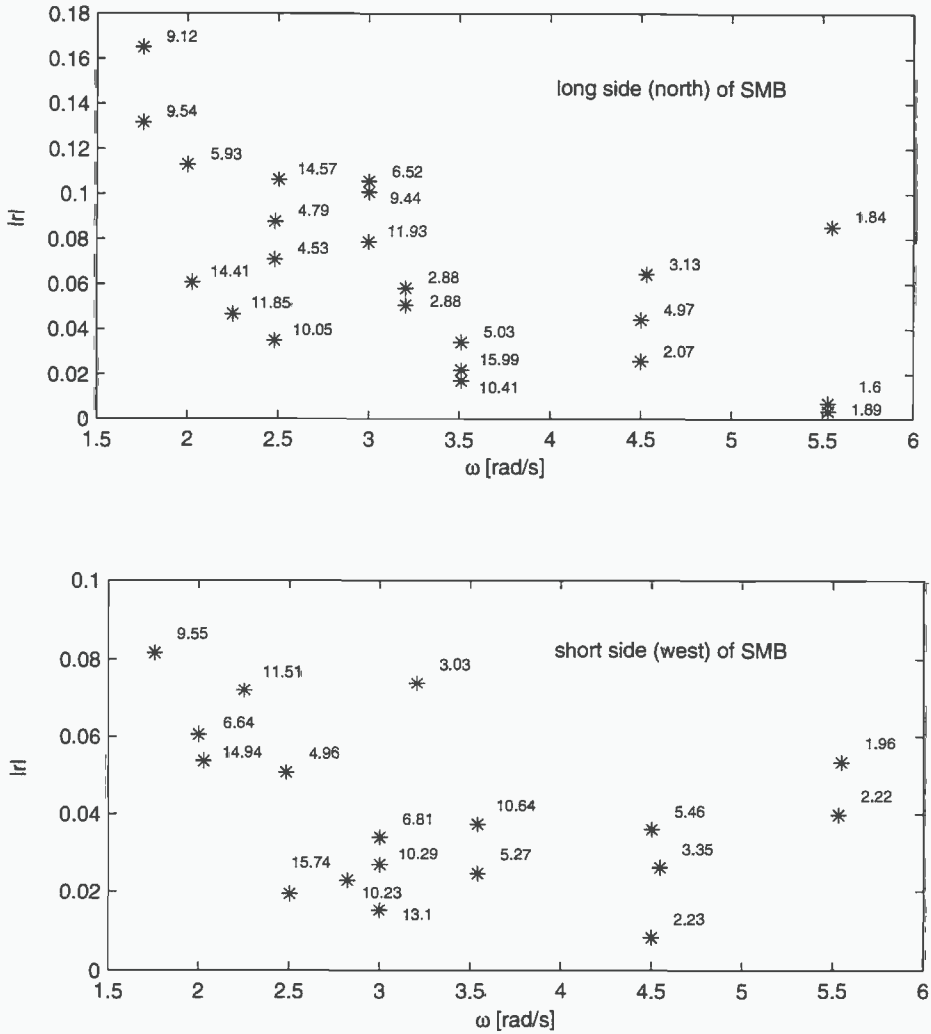
Figure 5.4: *Reflection coefficients (determined using the envelope modulation technique) for the final configurations of the beaches at the North and West side of the basin. The values near the measurements correspond to the amplitude of the incoming regular wave. ($h=5$ [m], $g=9.81$ [m/s^2]*

the amplitude (in cm) of the incoming wave.

Both configurations show that the amplitude influences the estimated reflection coefficient in an irregular fashion. Higher amplitudes do not lead to higher or lower reflection coefficients. The absence of this trend is also observed for the steepness. The results appear to support the observation that:

- the error in the measured reflection coefficient is significant for small amplitude waves.

- the linear filter model of the beach is not adequate for high amplitude waves.

Despite these shortcomings some conclusions can be made about the reflective properties of the artificial beaches. For the North (long) side of the basin the reflection coefficients are relatively high (10%-20%) for long waves ($\omega < 2$). With increasing frequency the reflection decreases, but seems to slightly increase at $\omega = 3$ [rad/s]. Between $\omega = 3$ and $\omega = 3.5$, the reflection coefficient further decreases to around 3 %. For frequencies larger than $\omega = 3.5$ the reflection coefficient slightly increases but remains under 10 %.

The beach at the West side has some noticeable differences with the North-side beach. The most important observation is that the reflection coefficients are overall smaller. This is most clearly visible in the relative low reflection coefficients around $\omega = 3$ [rad/s] compared to the reflection coefficient of the North-side beach for this frequency. The overall lower reflection coefficient is mainly due to the fact that the West-side beach is 2 meters longer than the North-side beach.

In general one should be careful to interpret the results of Fig. 5.4 on the preceding page because of the measurement and model errors that bias the results. Comparison of the results of these tests to similar tests on the artificial beaches in the previous basin and the new beaches at the IHL showed however that the new artificial beaches result in significantly smaller reflection coefficients.

5.3 Numerical wave absorption

Just as an experimental wave tank, a numerical wave tank is also modelled as a bounded region in space. The techniques that can be used in an experimental wave tank to minimize reflections have been summarised in the previous section. A wave absorption technique like the active wave absorber can be directly used as a concept for a numerical model. An artificial beach over which the waves spill, break and splash is however not easily translated into a numerical model. The direct numerical simulation of turbulent breaking and splashing would require elaborate numerical techniques and huge amounts of computer resources. The numerical simulation of wave breaking and splashing is a research topic by itself (cf. e.g. Guignard *et al.*

(1999) and Fontaine *et al.* (2000)) and may lead to important insights in the process. Most numerical wave tanks however, do not aim at modelling the experimental wave tank, but at modelling open sea conditions.

In this chapter we consider numerical wave absorption that aims at:

1. reproducing the reflection characteristics of the artificial beach in the experimental wave tank.

2. achieving minimal reflection from the numerical beach.

The numerical scheme must be able to simulate the evolution of a broad banded spectrum of waves on the same grid. Therefore the numerical wave absorption techniques must be 'blind' in the sense that they require no a priori knowledge on the incoming wave field. The implementation of the absorption technique will be evaluated by examining the reflection coefficient for waves with wavelength between $\lambda/h = 1/4$ and $\lambda/h = 4$.

First the different numerical methods available for numerical wave absorption will be discussed. Based on literature and experience, a numerical beach concept will be discretised and analyzed. It is then examined to what extent both of the above aims can be realised by this numerical beach. There are three main categories in which the numerical methods for wave absorption in a potential flow numerical wave tank can be divided:

- Open boundary conditions. In these methods, that have been reviewed by Romate (1992), (differential) equations are imposed on the outflow boundary. There are three types of methods that can be categorised as open boundary conditions:

  - Spatial periodic boundary conditions. These conditions were originally used by Longuet-Higgins & Cokelet (1976) in their pioneering paper on fully nonlinear wave simulation.

  - Matching boundary conditions. This technique is based on the matching of the inner solution with a (often linear) radiating solution on the exterior domain (cf. e.g. Dommermuth & Yue (1987)). A similar method is to construct a DtN relation at the boundary from the exterior problem and use this condition as a boundary condition on the interior (cf. e.g. Givoli (1992) and Sierevogel (1998)) .

  - Sommerfeld (1949) condition. This condition prescribes the partial differential equation $\Phi_t + c\Phi_x = 0$ on the absorbing boundary. This condition is transparent to fixed profiles that propagate with a constant speed c. An often used extension to the Sommerfeld condition, where the phase velocity is locally estimated every time step, was developed by Orlanski (1976) and applied to surface waves by Chan (1977). With this extension the method is often referred to as the Sommerfeld/Orlanski method.

- Dissipation zone. The governing equations are locally modified to dissipate the energy and thus damp out the wave energy locally (first introduced by Baker *et al.* (1981) and Israeli & Orszag (1981)). These dissipative zones can be used both at the downstream side of the tank and near the wave maker. Near the wave maker the damping is only applied on the difference between the desired outgoing wave and the undesired reflected wave.

- Active Wave absorption. This numerical technique is analogous to the active wave absorption techniques in an experimental model basin (see Section 5.1.2). However, more data is available for the control laws (potential, pressure, velocities, etc.). The control laws themselves are usually based on linear theory (cf. e.g. Duclos *et al.* (2000) for an application).

Instead of a single absorption technique, a combination of a Sommerfeld condition and a numerical dissipation zone, originally suggested by Israeli & Orszag (1981) is often used. This combination is known to have more favorable reflection properties for a broader range of frequencies than a single boundary condition and the concept has been adopted and extended by many authors (e.g. Ohyama & Hsu (1995), Clément (1996)). A disadvantage is that a relative long ($\approx 10\lambda$) dissipative zone is needed to obtain sufficiently low reflection coefficients, increasing the associated computational costs for some methods considerably. A recent comparative study of several numerical absorption techniques can be found in Clément (1999a).

5.3.1   Sommerfeld condition

The equation

$$\Phi_t + c_s \Phi_x = 0 \tag{5.16}$$

has as a general solution $\Phi = \tilde{\Phi}(x - c_s t)$. This condition (applied at e.g. $x = 0$) is transparent to profiles that move undisturbed and with fixed velocity c_s. For regular waves, with wave speed $\omega/k = c = c_s$ the Sommerfeld condition therefore acts as a perfect absorbing boundary condition. Regular waves with a different wave speed are however partially reflected. This reflection can be easily obtained by substitution of a regular wave solution

$$\Phi = e^{i(kx-\omega t)} + r e^{i(-kx-\omega t)} \tag{5.17}$$

in Eq. 5.16, and evaluate the expression at $x = 0$. The reflection r is then readily found to be

$$r = \frac{c_s - \omega/k}{c_s + \omega/k}. \tag{5.18}$$

Implementation of the Sommerfeld condition requires an a priori and fixed choice for the phase velocity c_s. To avoid this rigid choice, which conflicts with the 'blind-beach'

requirement, the parameter c_s can be constructed dynamically during numerical simulation. Based on information on the spatial-temporal history of $\widehat{\Phi}$, an approximation for the (time-local) c_s can be constructed. This was suggested by Orlanski (1976) and implemented for free-surface wave computations by Chan (1977). However, this method is not very robust as it will predict incorrect values for c_s if small reflections do occur.

Another way to improve the Sommerfeld condition to obtain more favorable reflection coefficients for a broader range of frequencies is to combine multiple phase velocities as

$$\prod_{i=1}^{N} [\partial_t + c_i \partial_x] \Phi = 0. \tag{5.19}$$

Using only two components in Eq. (5.19) ($c_1 = 1$ and $c_2 = 0.2$) will already result in a reflection coefficient $|r| < 0.13$ for $k \in [0 \ldots 25]$. However, accurate approximation of the higher-order derivatives in Eq. (5.19) can become a problem in the implementation of this condition.

For complex-valued potential functions and pseudo-differential operators a more general frame work can be constructed. Consider the differential equation

$$[\partial_t + P(\partial_x)] \Phi = 0 \tag{5.20}$$

the reflection coefficient r associated with Eq. (5.20) as a boundary condition is

$$r = \frac{i\omega - P(ik)}{i\omega - P(-ik)}. \tag{5.21}$$

For deep water waves, the dispersion relation can be simplified to $\omega^2 = k$ and therefore the choice of $\hat{P}(k) = \hat{f}(k) = \sqrt{ik}$ leads to low reflection coefficients for large k. The combination of this condition for large k with the standard Sommerfeld condition with $c = 1$ results to the equation

$$[\partial_t + \partial_x][\partial_t + f(\partial_x)] \Phi = 0. \tag{5.22}$$

Eq. (5.22) leads to a reflection coefficient $|r| < 0.007$ for $k \in [0 \ldots \infty)$. Unfortunately, the pseudo-differential operator $f(\partial_x)$ is not local and therefore computationally not suitable as an absorbing condition. A Taylor expansion of $\sqrt{k}$ around e.g. $k = 6$ can be used as an approximation of $\sqrt{k}$ as

$$\sqrt{k} \approx \sqrt{6} + 1/12\sqrt{6}(x - 6). \tag{5.23}$$

Using the approximation (5.23) in Eq. (5.22) results in the second-order complex partial differential equation

$$\Phi_{tt} + \frac{1}{2}\sqrt{6}(\Phi_t + \Phi_x) + \left(1 + i\frac{1}{12}\sqrt{6}\right)\Phi_{xt} + i\frac{1}{12}\sqrt{6}\Phi_{xx} = 0. \tag{5.24}$$

When this differential equation is used as an absorbing boundary condition a reflection coefficient $|r| < 0.055$ for $k \in [0\ldots25]$ can be obtained. The implementation of this boundary condition is however not straightforward because (i) the potential was assumed to be complex valued (ii) the presence of higher-order partial derivatives and (iii) the effect of this condition on the stability of the total numerical scheme.

5.3.2   Dissipation zone

A dissipation zone is a region in the discretised domain where the physical equations are modified in order to rapidly dissipate energy from the numerical solution. The equations for undisturbed free-surface potential are conservative. That no energy is dissipated can also be easily observed from the Hamiltonian structure of the equations for η and $\phi = \Phi|_{z=\eta}$. Consider the Hamiltonian

$$\mathcal{H} = \frac{1}{2} \int_{-h}^{\eta(x)} |\nabla \Phi|^2 dz + \frac{1}{2} g(\eta^2 - h^2). \qquad (5.25)$$

The free-surface elevation η and the potential at the free-surface ϕ are the canonical variables and the canonical equation

$$\begin{pmatrix} \phi \\ \eta \end{pmatrix}_t = \begin{pmatrix} 0 & -1 \\ 1 & 0 \end{pmatrix} \begin{pmatrix} \delta_\phi \mathcal{H} \\ \delta_\eta \mathcal{H} \end{pmatrix} \qquad (5.26)$$

is equivalent to the nonlinear free-surface conditions Eq. (2.23e)-(2.23f) without surface tension; Zakharov (1968) and Broer (1974). The Hamiltonian density (5.25) can be interpreted as the sum of the kinetic and potential energy. When natural boundary conditions are assumed, the time derivative of the total energy is given by $\partial_t \mathcal{H}$ as

$$\begin{aligned} \partial_t \mathcal{H} &= \langle \delta_\phi \mathcal{H}, \phi_t \rangle + \langle \delta_\eta \mathcal{H}, \eta_t \rangle & (5.27) \\ &= 0 & (5.28) \end{aligned}$$

from which it can be observed that energy is a conserved quantity. To construct a numerical dissipation zone, the equations have to be adapted in such a way that the energy will strictly decrease in the dissipative zone. Adding the functions $\alpha(x) \geq 0$ and $\beta(x) \geq 0$ to Eq. (5.26) as

$$\begin{pmatrix} \phi \\ \eta \end{pmatrix}_t = \begin{pmatrix} -\alpha(x) & -1 \\ 1 & -\beta(x) \end{pmatrix} \begin{pmatrix} \delta_\phi \mathcal{H} \\ \delta_\eta \mathcal{H} \end{pmatrix} \qquad (5.29)$$

results in

$$\begin{aligned} \partial_t \mathcal{H} &= \langle \delta_\phi \mathcal{H}, \phi_t \rangle + \langle \delta_\eta \mathcal{H}, \eta_t \rangle & (5.30) \\ &= \langle \delta_\phi \mathcal{H}, -\alpha(x) \delta_\phi \mathcal{H} \rangle + \langle \delta_\eta \mathcal{H}, -\beta(x) \delta_\eta \mathcal{H} \rangle & (5.31) \\ &\leq -\max\{\alpha\} \|\delta_\phi \mathcal{H}\|^2 - \max\{\beta\} \|\delta_\eta \mathcal{H}\|^2 & (5.32) \\ &\leq 0. & (5.33) \end{aligned}$$

Clearly, there are many ways to add non-physical damping by choosing α and β. We prefer to choose $\beta \equiv 0$ because this choice retains the kinematic boundary conditions. The additional contribution to the dynamic equation for $\alpha \neq 0$ can be incorporated in the atmospheric pressure p in Eq. (2.23e) as

$$p(x,t) = \alpha(x)\left(\Phi_z - \eta_x \Phi_x\right) = \alpha(x)\Phi_n \sqrt{1+\eta_x^2}. \tag{5.34}$$

The redefinition of the atmospheric pressure p by Eq. (5.34) is the only modification of Eqs. (2.23a)-(2.23f) and therefore mass conservation is still guaranteed. The air above the free surface is acting as a kind of damper with respect to the free surface. The pressure force always opposes the free-surface motion. Because $\sqrt{1+\eta_x^2} > 0$, energy decay is also guaranteed when $p(x) = \alpha(x)\Phi_n$ is chosen (redefinition of α). If the vertical unit vector is denoted as $\vec{e}$, the condition

$$\vec{e} \cdot \vec{n} > 0 \tag{5.35}$$

implies $sgn\,(\Phi_n) = sgn\,(\Phi_z)$ at $z = \eta(x,t)$ and therefore the damping function

$$p(x) = \alpha(x)\Phi_z|_{z=\eta(x,t)} \tag{5.36}$$

leads to guaranteed energy decay with mass conservation if $\alpha(x) > 0$. Condition (5.35) states that the free surface is not overturning which was already a condition for the introduction of η.

In Section 5.4 the effect of the dissipative zone using the damping function Eq. (5.36) will be investigated for simple polynomial functions α. Of course there are many other possibilities for the functions α and β. Grilli & Horillo (1997) e.g. proposed a method in which the coefficients of the dissipative zone are dynamically determined based on the energy flux entering the dissipation zone.

5.3.3   Grid stretching

If large reflections of short waves from the dissipating zone are to be avoided, the coefficient α in Eq. (5.36) should slowly increase from zero. Long waves will propagate quickly through the dissipation zone with relative small values of $|\phi_z|$ and are therefore slowly damped. As a consequence the length of the dissipation zone should be rather long to have good absorbing properties for both short and long waves. It was found that the length of the dissipative zone, should be in the order of $10h$ to obtain sufficiently small ($< 5\%$) reflection coefficients for all wavelengths of interest. The additional computational effort to include a dissipation is thus considerable with respect to a length of $40h$ for a typical basin.

To reduce the computational effort a horizontal grid stretching technique has been applied to the grid on which the dissipation zone is implemented. The distance between two nodes x_i (increasing i corresponds to the downstream direction) on the same horizontal grid line is increased as

$$|x_{i+1} - x_i| = \gamma |x_i - x_{i-1}|. \tag{5.37}$$
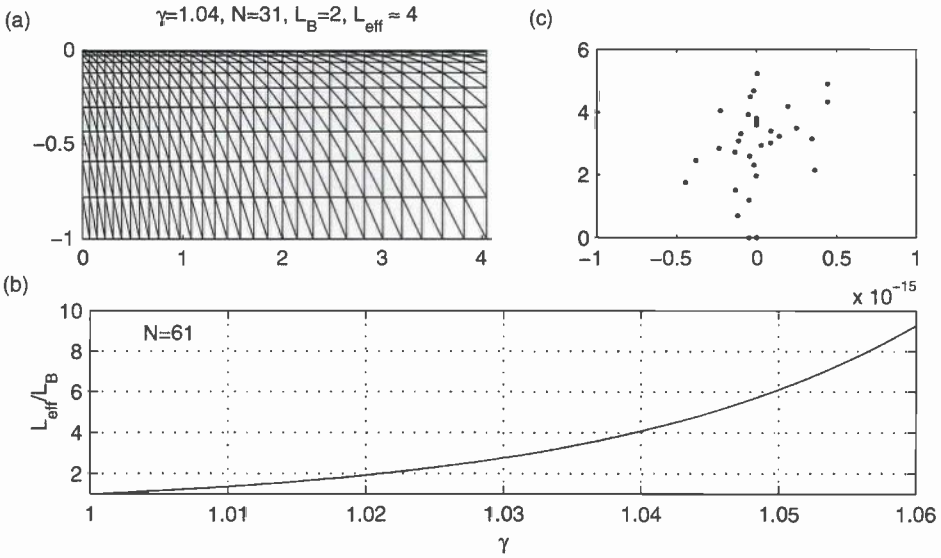
Figure 5.5: *(a) Horizontally stretched grid with $nx = 31$ and $\gamma = 1.04$. (b) The effective increment of the domain when $nx = 61$ for different values of γ. (c) Eigenvalues of the matrix associated with the grid in (a).*

If N nodes are used in the horizontal direction for the dissipation zone and these are stretched according to (5.37), the length of the zone L_{eff} is increased by a factor

$$\frac{L_{eff}}{L_B} = \frac{\gamma^N - 1}{N(\gamma - 1)}. \tag{5.38}$$

L_B denotes the length of the dissipative zone if the N points would have been equidistantly separated. In Fig. 5.5 the mesh structure (a) and the eigenvalues (c) associated with the linearised discretised equations using this mesh are plotted. The stability of the numerical scheme is not affected by the stretching of the grid. This property has been found to be independent of N, p[FEM], p[FD], β and triangular orientation of the elements.

5.3.4   Combined absorbing zone

When the velocity c_s of the Sommerfeld condition (Eq. (5.16)) is chosen to be 1, this condition will absorb the long waves relatively well, whereas the short waves are almost completely reflected as follows from Eq. (5.18). On the other hand a dissipation zone can be constructed that has good reflective properties for the shorter waves. The combination of this dissipation zone and the Sommerfeld condition can lead to the desired reflective properties for a broader range of frequencies, as was

suggested by Israeli & Orszag (1981) and implemented by Chapman (1985) for free-surface waves. In order to reduce the computational cost of this implementation the grid is stretched in the horizontal direction to increase the effective length of the dissipation zone without increasing the computational costs. In Subsection 5.4.1 the reflection coefficient of this combined beach concept is investigated analytically for different polynomial function $\alpha(x)$. In Subsection 5.4.2 on page 141 the reflection coefficients of the discretisation are determined and the effect of the grid stretching on the reflection, the computational effort and the time step is investigated.

5.4   Analysis of numerical wave absorption

In the following two subsections the reflection coefficients are determined for the dissipating zone with a Sommerfeld condition. In Subsection 5.4.1 the continuous equations are approximated and based on these approximations the reflection coefficients are estimated. In Subsection 5.4.2 the numerical discretisation of the pressure damping and the Sommerfeld condition is constructed. Based on this construction, the reflection coefficients for the linearised discretised dissipation zone are determined. The results of the continuous and numerical analysis are compared and discussed in Section 5.5.

5.4.1   Continuous analysis of reflection coefficients

In this subsection we obtain estimates for the reflection coefficients of a numerical beach that consists of a dissipation zone and a Sommerfeld condition. The results in this subsection have been presented by Westhuis (2000). In Dalrymple *et al.* (1991) the reflection coefficients are determined for a model of a porous structure. This model corresponds to the addition of a frequency dependent damping term proportional to $\omega\Phi$ to the dynamic boundary condition. Romate (1998) obtains reflection coefficients for a dissipation zone using the wave equation as an underlying model for wave propagation. In both references no Sommerfeld condition is included in the analysis. In the following region (I) refers to the part of the computational domain in which the waves can propagate undisturbed; region (II) denotes the numerical dissipation zone from $x = 0$ to $x = L_B$.

At the free surface of region (II) the pressure is varied in accordance with Eq. (5.36) as

$$p(x,t) = \alpha(x)\Phi_z(x,z,t) \quad \text{on} \quad z = \eta(x,t) \tag{5.39}$$

and at the downstream vertical boundary $x = L_B$ a Sommerfeld condition is applied

$$\Phi_t(x,z,t) + c_s\Phi_x(x,z,t) = 0 \qquad \text{at } x = L_B. \tag{5.40}$$

In order to find analytic estimates we simplify the problem by linearizing the free-surface equations and by assuming that region (I) is not bounded to the left. We therefore do not consider the wave maker in this analysis. Starting point of the analysis are thus the linear free surface equations:

$$\eta_t = \phi_z \tag{5.41}$$

$$\phi_t = -g\eta - p \tag{5.42}$$

where all functions are evaluated at $z = 0$. This set of first-order differential equations can also be written as:

$$\phi_{tt} = -g\phi_z - p_t. \tag{5.43}$$

In the current context a linear operator and its symbol are related by the following definitions (cf. e.g. Hörmander (1971) for an introduction to Fourier integral operators)

$$R\phi(x) = \int r(x - y) \ \phi(y)dy \tag{5.44}$$

where

$$r(x - y) = \frac{1}{2\pi} \int \hat{R}(k)e^{ik(x-y)}dk \tag{5.45}$$

The solution of Laplace's equation on the linearised geometry gives the linear dispersion operator R as

$$\hat{R} = \frac{\tanh(kh)}{k} \tag{5.46}$$

resulting in the kernel (cf. e.g. Broer (1974) and Dingemans (1997b))

$$r(x - y) = -\frac{1}{\pi} \ln \tanh \left(\frac{|x - y|}{h} \right) \tag{5.47}$$

which determines the relation between the horizontal and vertical velocity at the free surface by:

$$\phi_z = -\partial_x R\phi_x. \tag{5.48}$$

Assuming the solution of Eq. (5.43) to be harmonic in time,

$$\phi = \hat{\phi}e^{-i\omega t} \tag{5.49}$$

and substituting Eqs. (5.39), (5.48) and (5.49) for Eq. (5.43) results in the following equation for $\hat{\phi}$:

$$-\omega^2\hat{\phi} = gR\hat{\phi}_{xx} - i\omega\alpha(x)R\hat{\phi}_{xx}. \tag{5.50}$$

In region (I) (where $\alpha(x) = 0$) the solutions travelling to the right are given by

$$\hat{\phi}^I = d_1^I \left(e^{ikx} + \sum_{j=1}^{\infty} C_j e^{ik_j(x)} \right) \tag{5.51}$$

where d_1^I is a complex constant and k and k_j are the real and purely imaginary solutions, respectively, of the dispersion relation:

$$\omega^2 = gk^2 \hat{R}. \tag{5.52}$$

The coefficients of the imaginary wave number components C_j in Eq. (5.51) determine the evanescent modes. As has been pointed out by Dalrymple *et al.* (1991) the process of obtaining the solution ϕ across the interface between region (I) and (II) involves the coupling of the principal *and all* evanescent modes. To simplify the analysis the contributions of these evanescent modes will however be neglected. This commonly used assumption in the analysis of wave phenomena is called the plane-wave assumption. Because of the linearity of the equations, the reflected waves from region (II) have the same frequency, but travel in the opposite direction, the general solution in region (I) under these assumptions is thus given by:

$$\hat{\phi}^I = d_1^I e^{ikx} + d_2^I e^{-ikx}. \tag{5.53}$$

The general solution of Eq. (5.50) in region II is given as

$$\hat{\phi}^{II} = d_1^{II} A(x) + d_2^{II} B(x) \tag{5.54}$$

where $A(x)$ and $B(x)$ are two linearly independent solutions of Eq. (5.50) and d_1^{II} and d_2^{II} are again two complex constants. We assume that an incoming (i.e. $k \geq 0$) wave of unit amplitude (i.e. $d_1^I = 1$) is partially reflected from region (II) with complex amplitude $d_2^I = r$. For a unique solution to exist in the complete domain, continuity of ϕ and ϕ_x along the interface between region (I) and (II) is a necessary and sufficient condition (cf. e.g. Romate (1998). I.e. we require that

$$\hat{\phi}^I \Big|_{x=0} = \hat{\phi}^{II} \Big|_{x=0} \tag{5.55}$$

$$\hat{\phi}_x^I \Big|_{x=0} = \hat{\phi}_x^{II} \Big|_{x=0}. \tag{5.56}$$

Substituting Eqs. (5.53) and (5.54) in Eqs. 5.55) and (5.56) the following Eqs. (5.57) and (5.58) are derived:

$$1 + r = d_1^{II} A(0) + d_2^{II} B(0) \tag{5.57}$$

$$ik - ikr = d_1^{II} A_x(0) + d_2^{II} B_x(0) \tag{5.58}$$

The solution $\hat{\phi}^{II}$ also has to satisfy the Sommerfeld condition Eq. (5.40) at $x = L_B$, resulting in

$$i\omega \left[d_1^{II} A(L_B) + d_2^{II} B(L_B) \right] = c_s \left[d_1^{II} A_x(L_B) + d_2^{II} B_x(L_B) \right]. \tag{5.59}$$

Once the functions $A(x)$ and $B(x)$ are found from solving Eq. (5.50) for specified $\alpha(x)$, the set of Eqs. (5.57)-(5.59) can be solved directly for $(d_1^{II}, d_2^{II}$ and $r)$ and thus the absolute amplitude of the reflection coefficient $|r|$ can be determined.

Piecewise damping functions

From the previous analysis it follows that the reflection coefficient can be obtained for dissipation zones when the solutions $A(x)$ and $B(x)$ of Eq. (5.50) have been determined. This concept can be extended for piecewise defined damping functions α. Let the n intervals that partition the damping region (II) be denoted as $l_i = [x_i, x_{i+1}]$ and let $\alpha(l_i)$ be defined only on l_i. Let the general solution of Eq. (5.50) on the interval l_i be denoted as $d_1^{(i)} A^{(i)} + d_2^{(i)} B^{(i)}$. Continuity of the solution $\hat{\phi}$ and its derivative along the interfaces together with the boundary condition at $x = L$, results in a set of $2n + 1$ linear equations that can be solved for $d_j^{(i)}$, $i = 1 \ldots n$, $j = 1, 2$ and r.

When the independent solutions of Eq. (5.50) are available for certain functions $\alpha(x)$, the reflection coefficient can be obtained for dissipation zones consisting of a successive combination of these functions. In the next subsection (approximations of) the solutions for the functions $A(x)$ and $B(x)$ for constant, linear and parabolic damping functions $\alpha(x)$ are determined.

Solutions for constant damping

For a constant damping function

$$\alpha(x) = \alpha_0 \tag{5.60}$$

it can be verified directly that harmonic functions of the form

$$\hat{\phi}^{II} = d_1^{II} e^{i\tilde{k}x} + d_2^{II} e^{-i\tilde{k}x} \tag{5.61}$$

are solutions of Eq. (5.50). Here $\tilde{k}$ is essentially complex and ω and $\tilde{k}$ must be related by the dissipative dispersion relation

$$\omega^2 = \tilde{k}^2 \hat{R}(\tilde{k})(g - i\omega\alpha_0) \tag{5.62}$$

This equation can be solved exactly for ω

$$\omega = \pm\tilde{k}\sqrt{g\hat{R}(\tilde{k}) - \frac{1}{4}\tilde{k}^2\alpha_0^2\hat{R}^2(\tilde{k})} - \frac{1}{2}i\tilde{k}^2\alpha_0\hat{R}(\tilde{k}). \tag{5.63}$$

Remark that $\tilde{k} \neq k$ if $\alpha_0 \neq 0$ and is complex instead of the real valued k.

Solutions for linear damping

Equation (5.50) is rewritten as

$$R\hat{\phi}_{xx} = \frac{-\omega^2}{g - i\omega\alpha(x)}\hat{\phi}. \tag{5.64}$$

Solutions of Eq. (5.64) will in general not have spatial harmonic solutions so the operator R is not acting on a single mode and can thus not be reduced to pre multiplication with $\hat{R}$. In order to simplify Eq. (5.64) we assume however that there exists a complex $\tilde{\mu}$ such that the result of the operator R can be approximated by a pre-multiplication with $\tilde{\mu}$.

$$R\hat{\phi} \approx \tilde{\mu}\hat{\phi}. \tag{5.65}$$

If such a $\tilde{\mu}$ can be found, Eq. (5.64) simplifies to

$$\hat{\phi}_{xx} = \frac{-\omega^2}{\tilde{\mu}(g - i\omega\alpha(x))}\hat{\phi} \tag{5.66}$$

For the linear damping function

$$\alpha(x) = \alpha_0 + \alpha_1 x/L_B \tag{5.67}$$

and constant $\tilde{\mu}$ the general solution of Eq. (5.66) can be obtained by the transformation

$$\zeta = \tilde{\mu}\left[g - i\omega\left(\alpha_0 + \alpha_1 x/L_B\right)\right] \tag{5.68}$$

and substitution of

$$\vartheta_1 = \frac{\tilde{\mu}\alpha_1}{L_B} \tag{5.69}$$

in Eq. (5.66), resulting in

$$-\vartheta_1^2\hat{\phi}_{\zeta\zeta}\zeta + \hat{\phi} = 0 \tag{5.70}$$

The general solution of Eq. (5.70) is known (e.g. Whittaker & Watson (1965)) to be

$$\hat{\phi}(\zeta) = d_1\ \sqrt{\zeta}I_1\left(\frac{2\sqrt{\zeta}}{\vartheta_1}\right) + d_2\ \sqrt{\zeta}K_1\left(\frac{2\sqrt{\zeta}}{\vartheta_1}\right) \tag{5.71}$$

where $I_n(z)$ and $K_n(z)$ are the modified Bessel functions of the first and second kind, respectively. Thus, two linearly independent solutions are obtained and the reflection coefficient can be calculated from Eqs. (5.57)-(5.59).

Solutions for parabolic damping

The general parabolic damping term is denoted as

$$\alpha(x) = \alpha_0 + \alpha_1 x + \alpha_2 x^2 \tag{5.72}$$

where the scaling in x by L_B is included in the coefficients α_1 and α_2. Substitution of Eqs. (5.65) and (5.72) in Eq. (5.66) results in

$$\hat{\phi}_{xx} = \frac{-\omega^2}{\tilde{\mu}(g - i\omega(\alpha_0 + \alpha_1 x + \alpha_2 x^2))}\hat{\phi} \tag{5.73}$$

By introducing the transformation

$$\zeta = \frac{i\omega\alpha_2 \left(x - \frac{\alpha_1}{\alpha_2}\right)^2}{g - i\omega \left(\alpha_0 - \frac{\alpha_1^2}{4\alpha_2}\right)} - 2 \tag{5.74}$$

and the abbreviation

$$\vartheta_2 = \frac{2i\alpha_2\tilde{\mu}g}{\omega} \tag{5.75}$$

Eq. (5.73) can be transformed to

$$\zeta(1 - \zeta)\hat{\phi}_{\zeta\zeta} - \frac{1}{2}\zeta\hat{\phi}_\zeta - \frac{1}{2}\hat{\phi}_\zeta + \frac{1}{2\vartheta_2}\hat{\phi} = 0 \tag{5.76}$$

which is a differential equation of the hypergeometric type. The general solution of Eq. (5.76) is given by

$$\begin{aligned}\hat{\phi} &= d_1\ F([a,b],[c],\zeta)\ + \\ &\quad d_2\zeta^{1-c}F([a - c + 1, b - c + 1],[2 - c],\zeta)\end{aligned} \tag{5.77}$$

with

$$a = -\frac{1}{4}\sqrt{\frac{\vartheta_2 + 9}{\vartheta_2}} \tag{5.78}$$

$$b = -\frac{1}{4}\sqrt{\frac{\vartheta_2 - 7}{\vartheta_2}} \tag{5.79}$$

$$c = -\frac{1}{2} \tag{5.80}$$

The generalised hypergeometric function $F(\vec{n}, \vec{d}, z)$ in Eq. (5.77) is defined by

$$F(\vec{n}, \vec{d}, z) = \sum_{k=0}^{\infty} \frac{\left(\prod_{i=1}^{j} \frac{\Gamma(n_i+k)}{\Gamma(n_i)}\right) z^k}{\left(\prod_{i=1}^{m} \frac{\Gamma(d_i+k)}{\Gamma(d_i)}\right) k!} \tag{5.81}$$

where Γ is the gamma function, i.e.:

$$\Gamma(z) = \int_0^\infty e^{-t}t^{z-1}\mathrm{d}t \tag{5.82}$$

Choice of $\tilde{\mu}$

The solutions in the previous two paragraphs were obtained for modifications of equation (5.64). It was assumed that a constant $\tilde{\mu}$ satisfying Eq. (5.65) can be determined. A natural candidate for such a constant $\tilde{\mu}$ is the choice

$$\tilde{\mu} = 1/k. \tag{5.83}$$
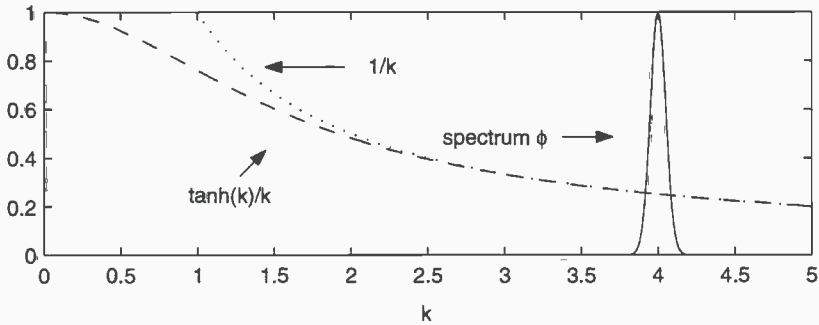
Figure 5.6: *The function $\hat{R}(k) = \frac{\tanh(k)}{k}$, its deep water approximation and a narrow banded spectrum. The operation $R\phi$ is the product in Fourier space of $\hat{R}$ with the spectrum of $\hat{\phi}$.*

This approximation is motivated by the observation that when $\alpha(x)$ is slowly varying, i.e. when α_1 and α_2 are small, the solution $\hat{\phi}$ is still assumed to be narrow banded around k and a zeroth-order approximation of R around k results in the approximation $\tilde{\mu} = 1/k$ (see also Fig. 5.6).

A different approximation is obtained if the coefficient $\tilde{\mu}$ is allowed to depend on the spatial coordinate. If the damping term is considered to be locally almost constant, the local wave number would be related to the damping coefficient in deep water as

$$\tilde{k} = \frac{\omega^2}{g - i\omega\alpha}. \tag{5.84}$$

Motivated by this observation, the coefficient $\tilde{\mu}(x)$ could be approximated as

$$\tilde{\mu}(x) = \frac{1}{\tilde{k}(x)} = \frac{g - i\omega\alpha(x)}{\omega^2}. \tag{5.85}$$

The result of this choice on the solution $\hat{\phi}$ for linear damping functions is that with

$$\zeta = g - i\omega\alpha(x) \tag{5.86}$$

and

$$\vartheta_3 = \frac{\alpha_1}{\omega L_B}, \tag{5.87}$$

Eq. (5.64) reduces to

$$-\vartheta_3^2 \zeta^2 \hat{\phi}_{\zeta\zeta} + \hat{\phi} = 0 \tag{5.88}$$

with general solution

$$\hat{\phi}(\zeta) = d_1 \zeta^{\left(\frac{\vartheta_3 + \sqrt{\vartheta_3^2 + 4}}{2\vartheta_3}\right)} + d_2 \zeta^{\left(\frac{\vartheta_3 - \sqrt{\vartheta_3^2 + 4}}{2\vartheta_3}\right)}. \tag{5.89}$$

In Section 5.5 the effect of these two approximations of equation (5.64) following from the different choices of $\tilde{\mu}$ on the estimated reflection coefficient are presented.

5.4.2   Discrete analysis of reflection coefficients

In this subsection, the linearised discretised equations are derived for the numerical implementation of the dissipation zone, stretching and Sommerfeld condition. The stretching only changes the grid on which the equations are discretised and therefore does not lead to a different structure of the equations.

Sommerfeld condition

The Sommerfeld condition is implemented by adding the equation

$$\Phi_t = -c_s \Phi_x \tag{5.90}$$

on the downstream vertical boundary. This equation is implemented as a Dirichlet condition on the downstream wall and is therefore treated analogous to the Dirichlet condition for the free surface. Let the index set containing the nodes that belong to the downstream boundary be denoted as $\mathcal{S}$ and the vector containing the approximated value of the potential be denoted as

$$\varphi = \begin{pmatrix} \varphi^{\mathcal{I}} \\ \varphi^{\mathcal{D}} \\ \varphi^{\mathcal{S}} \end{pmatrix}. \tag{5.91}$$

Taking this extra Dirichlet condition into account leads to the following extension of Eq. (4.18)

$$a\left(\sum_{i\in\mathcal{I}} \varphi_i N_i, N_j\right) = -a\left(\sum_{i\in\mathcal{D}} \varphi_i N_i, N_j\right) - a\left(\sum_{i\in\mathcal{S}} \varphi_i N_i, N_j\right)$$

$$+ b\left(\sum_{i\in\mathcal{N}} g_i N_i|_{\Gamma_W}, N_j|_{\Gamma_W}\right) \quad \forall j \in \mathcal{I}. \tag{5.92}$$

Remark that in this equation the index set $\mathcal{I} = \mathcal{V} \setminus (\mathcal{S} \cup \mathcal{D})$ instead of $\mathcal{I} = \mathcal{V} \setminus \mathcal{S}$. The linear operator that maps the values of φ to the approximation of the vertical and horizontal derivative in the nodes of φ is denoted as D^z and D^x, respectively. The components of D^* are ordered as

$$D = \begin{bmatrix} D_{\mathcal{I}\mathcal{I}} & D_{\mathcal{I}\mathcal{D}} & D_{\mathcal{I}\mathcal{S}} \\ D_{\mathcal{D}\mathcal{I}} & D_{\mathcal{D}\mathcal{D}} & D_{\mathcal{D}\mathcal{S}} \\ D_{\mathcal{S}\mathcal{I}} & D_{\mathcal{S}\mathcal{D}} & D_{\mathcal{S}\mathcal{S}} \end{bmatrix}. \tag{5.93}$$

With the definitions of

$$
\begin{array}{rcl}
L_{\mathcal{D}} & = & \left[-D^z_{\mathcal{DI}}A^{-1}_{\mathcal{II}}A_{\mathcal{ID}} + D^z_{\mathcal{DD}}\right] \\
L_{\mathcal{S}} & = & \left[-D^z_{\mathcal{DI}}A^{-1}_{\mathcal{II}}A_{\mathcal{IS}} + D^z_{\mathcal{DS}}\right] \\
L_{\mathcal{N}} & = & \left[D^z_{\mathcal{DI}}A^{-1}_{\mathcal{II}}B_{\mathcal{IN}}\right]
\end{array}
$$

$$
\begin{array}{rcl}
K_{\mathcal{D}} & = & \left[-D^z_{\mathcal{SI}}A^{-1}_{\mathcal{II}}A_{\mathcal{ID}} + D^z_{\mathcal{SD}}\right] \\
K_{\mathcal{S}} & = & \left[-D^z_{\mathcal{SI}}A^{-1}_{\mathcal{II}}A_{\mathcal{IS}} + D^z_{\mathcal{SS}}\right] \\
K_{\mathcal{N}} & = & \left[D^z_{\mathcal{SI}}A^{-1}_{\mathcal{II}}B_{\mathcal{IN}}\right]
\end{array}
$$

(5.94)
(5.95)
(5.96)
(5.97)
(5.98)
(5.99)
(5.100)
(5.101)

the discretisation of the Sommerfeld condition leads to

$$
\varphi^{\mathcal{S}}_t \ = \ -c_{\mathrm{s}}\left[D^x\varphi\right]_{\mathcal{S}} \tag{5.102}
$$
$$
-c_{\mathrm{s}}K_{\mathcal{D}}\varphi^{\mathcal{D}} - c_{\mathrm{s}}K_{\mathcal{S}}\varphi^{\mathcal{S}} - c_{\mathrm{s}}K_{\mathcal{D}}\widehat{g}. \tag{5.103}
$$

The linearised discretised equations including wave generation and Sommerfeld absorption, can thus be written as

$$
\frac{\partial}{\partial_t}\begin{pmatrix}\widehat{\eta}\\\varphi^{\mathcal{D}}\\\varphi^{\mathcal{S}}\end{pmatrix} = \begin{pmatrix} 0 & L_{\mathcal{D}} & L_{\mathcal{S}} \\ -gI & 0 & 0 \\ 0 & -c_{\mathrm{s}}K_{\mathcal{D}} & -c_{\mathrm{s}}K_{\mathcal{S}} \end{pmatrix}\begin{pmatrix}\widehat{\eta}\\\varphi^{\mathcal{D}}\\\varphi^{\mathcal{S}}\end{pmatrix} + \begin{pmatrix}L_{\mathcal{N}}\\0\\-c_{\mathrm{s}}K_{\mathcal{N}}\end{pmatrix}\widehat{g} \tag{5.104}
$$

Pressure damping

Discretisation of the additional pressure damping terms

$$
p(x,t) = \alpha(x)\Phi_z(x,t) \tag{5.105}
$$

is straightforward by definition of the vector

$$
\widehat{\alpha}_i = \alpha\left(x_{\mathcal{D}(i)}\right) \quad i = 1\ldots|\mathcal{D}| \tag{5.106}
$$

where x_i is the horizontal coordinate of the node N_i. In the region outside the dissipation zone, the value of $\alpha(x)$ in Eq. (5.105) is zero. The inclusion of the linearisation of the discretised damping terms (5.105) results in

$$
\mathbf{q}_t = \mathbf{A}\mathbf{q} + \mathbf{b}\widehat{g} \tag{5.107}
$$

with

$$
\mathbf{q} = \begin{pmatrix}\widehat{\eta}\\\varphi^{\mathcal{D}}\\\varphi^{\mathcal{S}}\end{pmatrix} \quad \mathbf{A} = \begin{pmatrix} 0 & L_{\mathcal{D}} & L_{\mathcal{S}} \\ -gI & \Upsilon L_{\mathcal{D}} & \Upsilon L_{\mathcal{S}} \\ 0 & -cK_{\mathcal{D}} & -cK_{\mathcal{S}} \end{pmatrix} \quad \mathbf{b}\begin{pmatrix}L_{\mathcal{N}}\\0\\-cK_{\mathcal{N}}\end{pmatrix} \tag{5.108}
$$
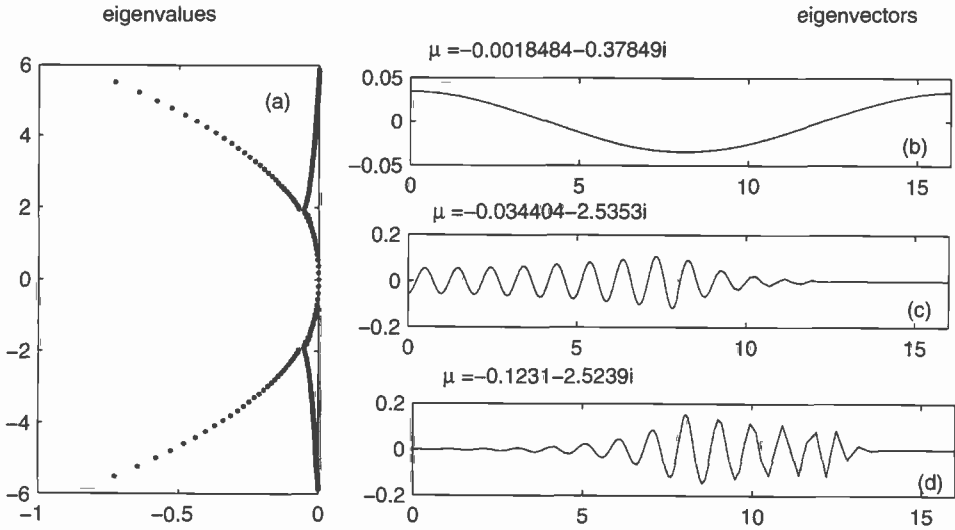
Figure 5.7: *(a) The eigenvalues of* **A** *in (5.108)and (b)-(d) the real part of the eigen-
vectors for three specific eigenvalues related to* $\widehat{\eta}$. *(p[FD]=2, p[FEM]=1,
nx/h=21, nz=10, $\beta = 1.5$, $\gamma = 1.06$, $L_0 = 10$, $\alpha(x) = 0.05$ for x > 8,
without a Sommerfeld condition)*

where

$$\Upsilon = \text{diag}\{\widehat{\alpha}\}. \tag{5.109}$$

In Fig. 5.7 the eigenvalues of **A** in (5.108) are plotted for $\alpha(x) = 0.05$, $x > 8$,
using grid stretching but without a Sommerfeld condition. The most characteristic
observation is the appearance of two spectral branches. The eigenvectors associated
with the branch of eigenvalues closest to the imaginary axis are mainly restricted to
the undamped region. The eigenvectors associated with the branch that is positioned
further away from the imaginary axis are mainly restricted to the dissipation zone.
One can also observe that, even for this very long dissipating zone, the eigenvectors
associated with long waves (like in subfigure (b)) are not well damped.

The effect on the spectrum when the discretisation of the Sommerfeld condition with
$c_s = 1$ is added can be observed in Fig. 5.8 on the next page. The result of the
additional Sommerfeld equation is twofold. Firstly, an additional set of negative
real eigenvalues associated with the new equations is observed near $Re(\mu) \approx -3$.
Secondly, the eigenvalues with small imaginary component around the origin have a
larger negative real part than in Fig. 5.7. This indicates that also the longer waves
are more rapidly damped.

Although the inspection of the eigenvalues may hint at the qualitative effect of the
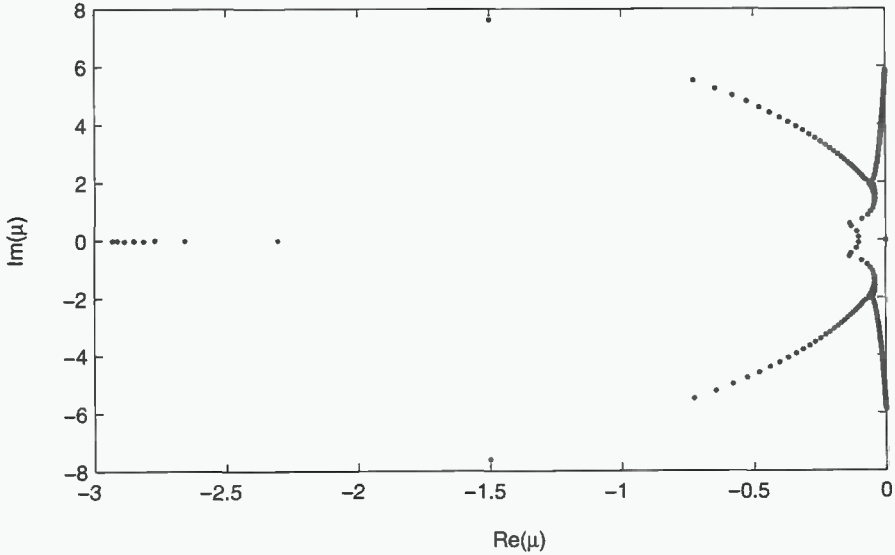
Figure 5.8: *The eigenvalues of* **A** *for the same configuration as in Fig. 5.7 on the preceding page with an additional Sommerfeld condition with* $c_s = 1$.

absorbing layer, one is primarily interested in the reflection coefficient r. This coefficient can be obtained by determining the envelope variations from Eq. (5.107) and using the Ursell formula (5.6). By prescribing $\widehat{g} = \bar{g}e^{i\omega t}$ where $\bar{g}$ corresponds to a profile of a wave maker and seeking solutions of the form $\mathbf{q} = \tilde{\mathbf{q}}e^{i\omega t}$, the complex amplitude $\tilde{\mathbf{q}}$ can be found by solving

$$(i\omega\mathbf{I} - \mathbf{A})\tilde{\mathbf{q}} = \mathbf{b}\bar{g}. \tag{5.110}$$

Eq. (5.110) is solved using a preconditioned Conjugate Gradient Squared (CGS) method with incomplete Cholesky factors (ICF) as preconditioners. When the drop tolerance of the ICF is set to 10^{-4} the relative residue converges typically to a value $< 10^{-12}$ within 10 iterations. The envelope of the solution is determined as

$$A_{env} = |\tilde{\mathbf{q}}|. \tag{5.111}$$

For reflection coefficient determination, we have typically used a domain of length $12h$ (without horizontal stretching) and the numerical beach starts at $x = 10h$. The effect of the evanescent modes on the wave envelope is not significant further than $3h$ from the wave maker and $3h$ from the beach interface at $x = 10h$. The maximum A_{max} and minimum A_{min} value of the envelope A_{env} are thus determined over the interval $[3h, 7h]$ and Eq. (5.6) is applied to obtain the reflection coefficient estimate.

In order to verify the applicability and the accuracy of the above reflection coefficient approximation, the method is used to estimate the reflection coefficient when a piston wave-maker is used in combination with a Sommerfeld condition on the opposing wall
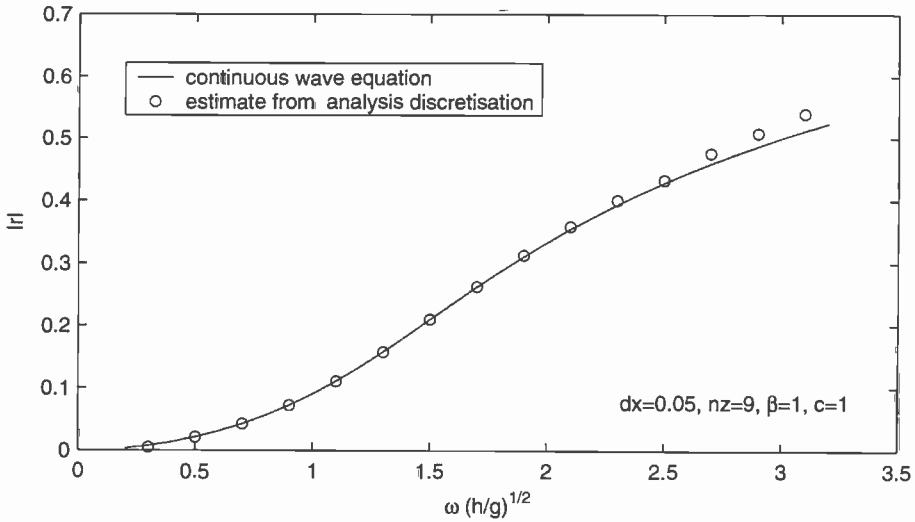
Figure 5.9: *Comparison of the exact reflection coefficients of the Sommerfeld condition for the 1 dimensional wave equation and the reflection coefficients obtained by linear analysis of the discretised equations.*

with $c_s = 1$. The reflection coefficient estimate is compared to the exact reflection coefficient (5.18) of the Sommerfeld condition for the wave equation with the exact dispersion relation.

As can be observed from Fig. 5.9 the approximation using the envelope variations obtained from the linear solution of the discretised equations, results in an accurate estimate of the reflection coefficient for small values of this coefficient.

Intersection point with Sommerfeld boundary

Until now we have not commented on the intersection point between the free surface and the boundary where the Sommerfeld condition is applied. In the derivation at the beginning of this section, the intersection point was chosen to belong to the free surface. Therefore the vector $\varphi^{\mathcal{D}}$ and $\widehat{\eta}$ are both of the same length and the Bernoulli equation is applied to the free surface, while the Sommerfeld condition is applied to the nodes below the free surface.

When the Sommerfeld condition is applied at the free-surface node instead of the Bernoulli equation, the vector $\varphi^{\mathcal{D}}$ and $\widehat{\eta}$ are not of the same length and the matrices change due to the redefinition of the index sets. The first index of the index set $\mathcal{D}$ corresponds to the leftmost node at the free surface. Nodes at the free surface are then numbered sequentially. The first index in the index set $\mathcal{S}$ corresponds to the
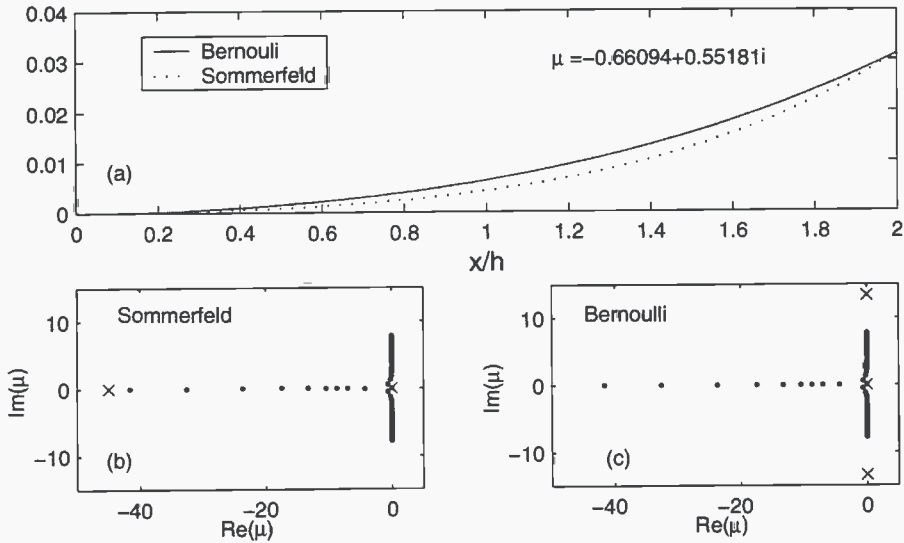
Figure 5.10: *(a) the eigenvector belonging to an eigenvalue for the Bernoulli- and Sommerfeld-type intersection point. (b)-(c) spectrum of the linearised discretisation; the eigenvalues marked with (x) correspond to special eigenfunctions.*

node on or closest to the free surface (depending on the implementation).

In Fig. 5.10 (b)-(c) the two spectra of **A** are drawn. Both implementations lead to a stable discretisation. The difference between the two discretisations can be observed (i) in the slightly different eigenvectors (see (a)) corresponding to the same (up to 5 digits) eigenvalue and (ii) the eigenvalues in (b)-(c) that are marked by a cross (x) instead of a point (·). For both implementations, the eigenvalues (x) correspond to special eigenvectors that appear to lack any physical significance and are a pure numerical artefact. In the following paragraphs, these eigenvectors are constructed explicitly. For both constructions we assume that the triangular element that has the intersection point as a vertex, has no interior point as a vertex.

Consider the case where the intersection point belongs to the free surface. The vector $\mathbf{q} = \mathbf{v} \in R^{d+d+s}$ constructed as

$$\mathbf{v} = \begin{pmatrix} \eta^{\mathcal{D}} \\ v^{\mathcal{D}} \\ v^s \end{pmatrix}, \tag{5.112}$$

where

$$\eta^{\mathcal{D}} = \begin{pmatrix} 0 \\ \vdots \\ 0 \\ i \end{pmatrix} , v^{\mathcal{D}} = \begin{pmatrix} 0 \\ \vdots \\ 0 \\ 1 \end{pmatrix} , v^{\mathcal{S}} = \begin{pmatrix} 0 \\ \vdots \\ 0 \end{pmatrix}. \tag{5.113}$$

The vector $\mathbf{v}$ is an eigenvector with *complex* eigenvalue $-i$ of the matrix

$$\mathbf{A} = \begin{pmatrix} 0 & L_{\mathcal{D}} & L_{\mathcal{S}} \\ -I & 0 & 0 \\ 0 & -K_{\mathcal{D}} & -K_{\mathcal{S}} \end{pmatrix} \tag{5.114}$$

that follows from the linearisation of the discretisation of the free-surface equations and the Sommerfeld condition. This property is independent of p[FD], β, nx and nz. The proof follows easily when it is shown that $L_{\mathcal{D}}v^{\mathcal{D}} = -i\eta^{\mathcal{D}}$ (for the definition of $L_{\mathcal{D}}$ see (5.94)). That this is true follows from two observations

1. The triangular element that has the intersection point as a vertex, has no interior point as a vertex. Therefore the contribution of the intersection point to $A_{\mathcal{ID}}$ is zero. Therefore the only non-zero contributions in the last row of $L_{\mathcal{D}}v^{\mathcal{D}}$ come from $D_{\mathcal{DD}}^{z}$.

2. Because the 1-dimensional finite-difference method uses only a single point on the free surface for the approximation of the vertical derivative of Φ at a single point, the matrix $D_{\mathcal{DD}}^{z}$ is a diagonal matrix. [1] The elements in this matrix are normalised to one, without loss of generality.

By definition of $L_{\mathcal{D}}$ it follows that the vector $L_{\mathcal{D}}v^{d}$ is zero everywhere except a unity value at the last index and is thus equal to $-i\eta^{\mathcal{D}}$.

When the intersection point is modelled to belong to the Sommerfeld boundary, a similar special eigenvector exists. Recall that for this situation the vectors $\eta^{\mathcal{D}}$ and $v^{\mathcal{D}}$ are not of equal length. Consider the vector $\mathbf{v} \in R^{d+(d-1)+s}$ as

$$\mathbf{v} = \begin{pmatrix} \eta^{\mathcal{D}} \\ v^{\mathcal{D}} \\ v^{s} \end{pmatrix}, \tag{5.115}$$

---

[1] Remark that this property is not true for 2-dimensional polynomial approximations

where

$$
\eta^{\mathcal{D}} = \begin{pmatrix} 0 \\ \vdots \\ 0 \\ 1 \end{pmatrix} \ , \ v^{\mathcal{D}} = \begin{pmatrix} 0 \\ \vdots \\ 0 \end{pmatrix} \ , \ v^{\mathcal{S}} = \begin{pmatrix} -1 \\ 0 \\ \vdots \\ 0 \end{pmatrix} . \tag{5.116}
$$

This vector is an eigenvector of

$$
\mathbf{A} = \begin{pmatrix} 0 & L_{\mathcal{D}} & L_{\mathcal{S}} \\ \begin{pmatrix} 0 \\ -I & \vdots \\ 0 \end{pmatrix} & 0 & 0 \\ 0 & -K_{\mathcal{D}} & -K_{\mathcal{S}} \end{pmatrix} \tag{5.117}
$$

with *real* eigenvalue $\mu = -1$. The proof follows directly if $L_{\mathcal{S}} v^s = -\eta^{\mathcal{D}}$ and $-K_{\mathcal{S}} v_s = -v_s$. This can be shown by following a reasoning similar to the one in the previous paragraph. For $L_{\mathcal{S}} v^{\mathcal{S}}$, the contributions of $-D_{\mathcal{D}\mathcal{I}}^z A_{\mathcal{I}\mathcal{I}}^{-1} A_{\mathcal{I}\mathcal{S}}$ become identical zero and only the contribution of $D_{\mathcal{D}\mathcal{S}}^z$ remains. Except for the last row, the matrix $D_{\mathcal{D}\mathcal{S}}^z$ is equal to zero because the values at the Sommerfeld boundary contribute only to the approximation of the vertical derivative at the intersection point. Again the element in the first column of the last row can be normalised without loss of generality, leading to the desired result $L_{\mathcal{S}} v^s = -\eta^{\mathcal{D}}$. The second condition, $-K_{\mathcal{S}} v_s = -v_s$ follows directly by observing that $D_{\mathcal{S}\mathcal{S}}^z$ is a diagonal matrix that can be normalised.

The above derivations depend on whether or not the triangular element at the intersection point has a vertex whose corresponding node belongs to $\mathcal{I}$. When this condition is not satisfied, there is a non-zero contribution in $A_{\mathcal{I}\mathcal{D}}$ or $A_{\mathcal{I}\mathcal{S}}$ from the intersection point leading to very small but non-zero contributions in the last row of e.g. $-D_{\mathcal{D}\mathcal{I}}^z A_{\mathcal{I}\mathcal{I}}^{-1} A_{\mathcal{I}\mathcal{D}}$. The corresponding special eigenvalues and eigenvectors for these situation were however found to be almost identical to the situation for which the triangular element satisfies the condition.

Based on the observation that the eigenvalues of the special eigenvectors for the Sommerfeld implementation are (i) real and (significantly) negative and thus quickly damp and (ii) impose less stringent conditions on the RK stability region, the implementation of the Sommerfeld-type for the intersection point is preferred over the Bernoulli-type.

Stability of the Sommerfeld condition

In the previous paragraphs it was already observed that the extra eigenvalues associated with the additional equations due to the Sommerfeld condition are real. Based
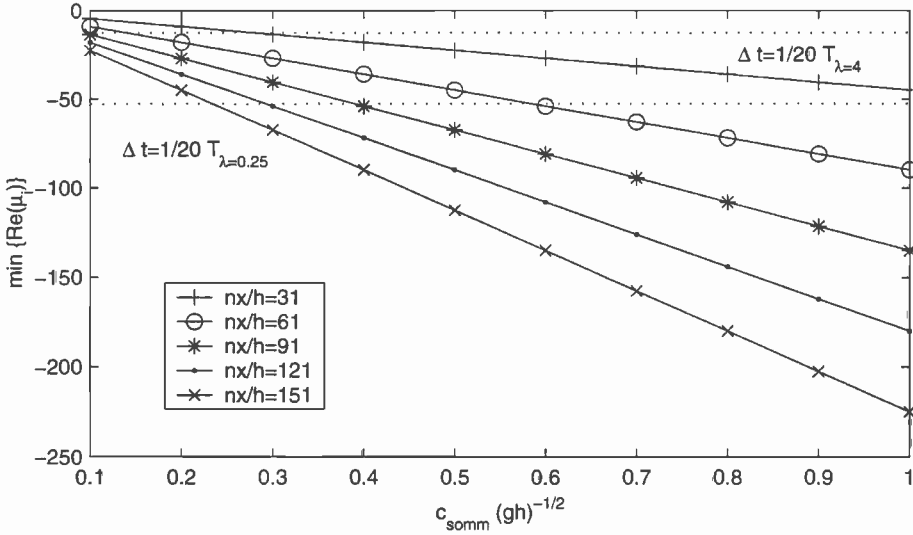
Figure 5.11: *Minimum value of eigenvalues when the Sommerfeld condition is applied related to the stability constraints imposed by the imaginary eigenvalues related to the wave propagation.*

on the analysis of the second-order discretisation of the Sommerfeld condition for uniform meshes,

$$\Phi_t^{(i,nx)} = -c_s \frac{3\Phi^{(i,nx)} - 4\Phi^{(i,nx-1)} + \Phi^{(i,nx-2)}}{2\Delta x}, \tag{5.118}$$

the position of these eigenvalues is thought to depend linearly on the value c_s and on the value of Δx^{-1} near the boundary.

The eigenvalues are negative and therefore the spatial discretisation is stable. The negative values might however lie outside the RK-stability interval (see also Chapter 3 Section 3.2.2). Variation of the number of nodes in the vertical direction nz and β showed no significant influence on the position of these eigenvalues. In Fig. 5.11 the minimal real eigenvalue μ_{min} due to the additional Sommerfeld condition is plotted for different values of c_s and for different nx/h. The minimum real eigenvalue is indeed observed to be proportional to c_s and $1/\Delta x$ as

$$\mu_{min} \approx -\frac{3}{2} \frac{c_s}{\Delta x}. \tag{5.119}$$

In fully nonlinear simulations with narrow banded spectra around a central period T a common choice for the time step is $\Delta T = 1/20T$. Given this time step, the intersection of the 5 stage Runge-Kutta stability region with the real axis is approximately $-3.2167/\Delta t$. This value has been plotted as a horizontal line in Fig. 5.11 for the smallest $\lambda = 1/4h$ and longest $\lambda = 4h$ wave considered in Chapter 3. From

the intersection of these horizontal lines with the curves representing the minimal eigenvalue due to the Sommerfeld condition, one can observe that the time step has to be decreased for many configurations if a Sommerfeld condition is added. E.g. for a time step of $1/20$ of the period associated with the $\lambda/h = 1/4$ wave on a grid with $nx/h = 61$ nodes, the discretisation becomes unstable for $c > 0.6$.

Remark that the smallest wave has a frequency of approximately $\sqrt{\pi \Delta x}$. If the time step is chosen such that this wave is stable, the intersection of the stability region with the negative real axis is at $\mu \approx -20.64$ for the finest $nx/h = 151$ grid. Given the stability region of an RK method, denote the intersection with the largest modulus of this region with the positive imaginary axis with z_{im} and the intersection with the negative real axis as z_{re}. The value of the minimal real eigenvalue only depends on the local horizontal mesh width at the Sommerfeld boundary and will be denoted as Δx^0. The RK integration is thus stable if

$$\Delta t < \min \left\{ |z_{im}| \sqrt{\frac{\Delta x}{\pi}} \ , \ |z_{re}| \frac{2\Delta x^0}{3c_s} \right\} \tag{5.120}$$

where Δx is the smallest appearing horizontal mesh width in the discretisation. From condition (5.120) one can observe that the previous stability condition is not affected by the Sommerfeld condition if

$$\Delta x^0 > \frac{|z_{im}|}{|z_{re}|} \frac{3c_s}{2\sqrt{\pi}} \sqrt{\Delta x}. \tag{5.121}$$

Because the maximum value of c_s is 1 and the maximum ratio $\frac{|z_{im}|}{|z_{re}|}$ is 1.0554 for the RK schemes investigated in Section 3.2.2, the more rigorous condition on Δx^0,

$$\Delta x^0 > \sqrt{\Delta x} \tag{5.122}$$

will result in a stable method if the method without the Sommerfeld condition was also stable.

The suggested stretching of the grid in the horizontal direction to increase the effective range of the dissipation zone, has the additional benefit that the local horizontal mesh width near the downstream boundary is significantly increased. When N nodes in the horizontal direction are used in the dissipation zone, the horizontal mesh width near the free surface is a factor γ^N larger. For the situation with $N = 61$ and $\gamma = 1.04$, this means a reduction of almost a factor 11 in μ_{min}, resulting e.g. for $nx/h = 61$ in stable simulations for all c_s and ΔT within the range plotted in Fig. 5.11 on the page before. The effect of stretching on the eigenvalues due to the Sommerfeld discretisation can also be observed in Fig. 5.8 on page 144. If no stretching would have been used, these eigenvalues are situated around $\mu \approx -30$. To assure that the additional Sommerfeld condition does not influence the stability of the numerical scheme, a combination of N and γ needs to be chosen such that

$$\gamma^N > \sqrt{1/\Delta x}. \tag{5.123}$$
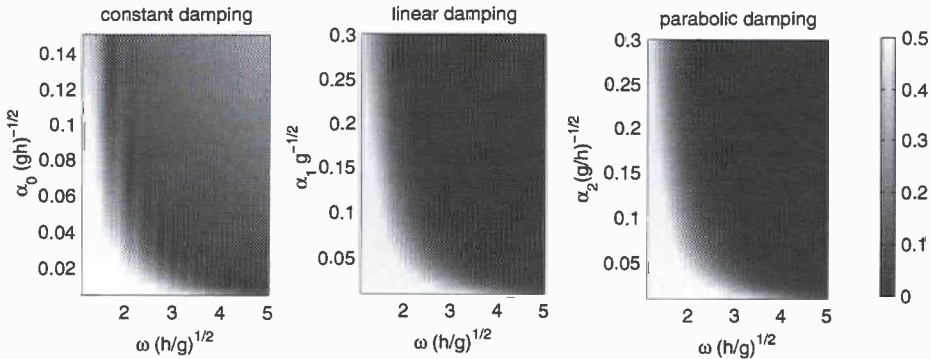
Figure 5.12: *The reflection coefficients of constant, linear and parabolic damping functions. (nx/h=31, nz=11, $\beta = 1.5$, $L = 12$, $L_B = 2$, $g = 1$, $h = 1$)*

A similar analysis can be performed on the additional equations following from a discretisation of the absorbing wave maker boundary condition of Subsection 4.3.2 on page 113. For this situation, the local mesh width cannot be easily stretched and small time steps may be necessary to obtain stable discretisations.

Effect of damping and stretching

In Fig. 5.12 the reflection coefficients are plotted for constant $\alpha(x) = \alpha_0$, linear $\alpha(x) = \alpha_1 x$ and parabolic damping functions $\alpha(x) = \alpha_2 x^2$. The length of the dissipation zone is $L_B = 2$ and no Sommerfeld condition is applied. From this figure it can be observed that for small values of α_0 long waves are significantly reflected. For larger values of α_0 the reflection coefficient decreases for these long waves but the short waves reflect against the sudden jump in α across the interface. The reflection coefficients for linear and parabolic damping are quite similar. For larger values of α_1 and α_2 the short waves are damped quite well, but the long waves still reflect with reflection coefficients of $|r| > 0.3$. Although this is not depicted in Fig. 5.12 one can easily envision that for larger values of α_1 the short waves will again reflect against the quick change in α. It is also noticed that the parabolic damping function does not show a characteristic different behavior than the linear damping function. We therefore focus on constant and linear damping and do not consider parabolic damping functions in detail further.

Fig. 5.13 on page 153 shows the reflection coefficients for a combination of linear damping functions $\alpha(x) = \frac{\alpha_1}{L_{eff}} x$, a Sommerfeld condition with velocity c and stretching of the grid in horizontal direction with a factor γ. The length of the beach without stretching is $L_B = 2$. From this figure it can be observed that the additional Sommerfeld condition greatly reduces the reflection coefficients when compared to Fig. 5.12. It is also observed that for small damping coefficients α_1, the reflections against the stretching grid become significant for larger values of γ. Recall that larger values of γ

also imply larger values of L_{eff} and therefore a smaller slope α_1/L_{eff} of the damping function. The value of c slightly changes the reflection profiles and it can be observed that for intermediate values of α_1, $c = 0.8$ results in lower reflection coefficients for long waves when the grid is stretched than the reflection coefficients for $c_s = 1$. This is due to the reduction in phase speed of the regular wave after propagation through the stretched dissipation zone.

5.5   Results and discussion

In this section the expressions for the reflection coefficient estimates derived in Section 5.4.1 and 5.4.2 are compared and discussed. Based on the linear analysis of the discretised equations, a combination of parameters is determined that results in a combined absorbing beach that approximates a transparent boundary. Based on the results from these sections and the measurements that have been described in Section 5.2, a numerical beach will be constructed that has approximately the same reflection coefficients as the artificial beach in the SMB at MARIN.

5.5.1   Continuous equations and numerical results

We recall that the method to obtain the reflection coefficient from the continuous equations is based on a plane wave assumption. Therefore, no equivalence is to be expected with the results obtained by analysis of the linearised discretised equations. Firstly, the reflection coefficients for $\alpha = 0$ (no damping) will be compared. Fig. 5.14 on page 154 shows the continuous reflection coefficient and the reflection coefficients obtained from linear analysis of the discretised equations for $c_s = 1$. In general, good agreement is observed but the estimated numerical reflection coefficients are slightly higher than the continuous reflection coefficients.

Constant damping

After substitution of the solution (5.61) in Eqs. (5.57)-(5.59), the complex valued solution for the reflection coefficient is obtained as

$$r = \frac{e^{2i\tilde{k}L_B}\left(\omega - c_s\tilde{k}\right)\left(\tilde{k} + k\right) + \left(\omega + c_s\tilde{k}\right)\left(\tilde{k} - k\right)}{e^{2i\tilde{k}L_B}\left(\omega - c_s\tilde{k}\right)\left(k - \tilde{k}\right) - \left(\omega + c_s\tilde{k}\right)\left(k + \tilde{k}\right)} \tag{5.124}$$

where k is a function of ω and related by the dispersion relation

$$\omega^2 = k \tanh k \tag{5.125}$$

and $\tilde{k}$ is related to ω as

$$\omega^2 = (1 - i\alpha_0\omega)\,\tilde{k} \tanh \tilde{k}. \tag{5.126}$$
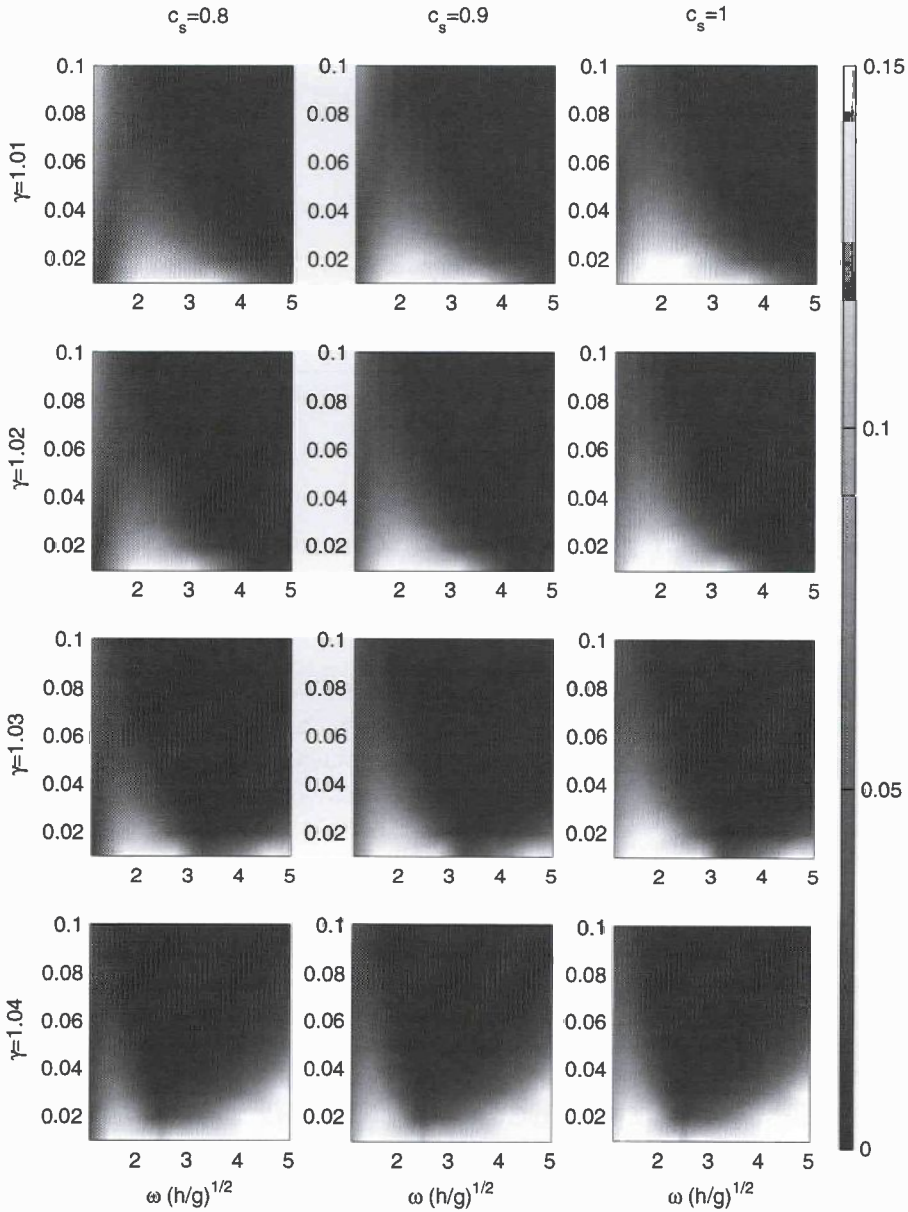
Figure 5.13: *The reflection coefficients for linear damping functions and different values of the Sommerfeld velocity c_s and the horizontal grid stretching parameter γ. The value on the vertical axis is α_1/L_{eff}. (nx/h=31, nz=11, $\beta = 1.5$, $L = 12$, $L_B = 2$, $g = 1$, $h = 1$)*
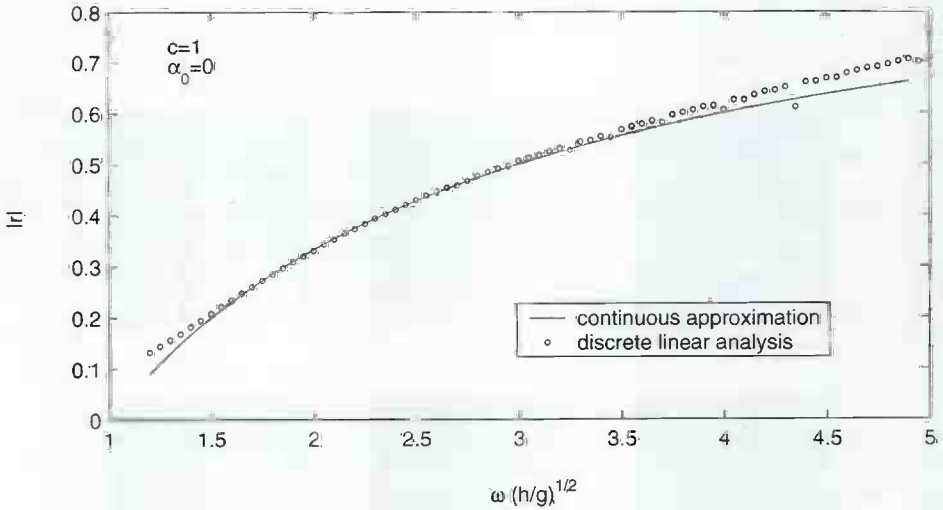
Figure 5.14. *Reflection coefficients obtained using the continuous equations from 5.4.1 and the the analysis of the linearised discretised equations for $c = 1$ and $\alpha = 0$ (g=1, h=1, $L_B = 2$, $\gamma = 1$, $\beta = 1.5$, $nx/h = 31$, $nz = 11$, $L = 8$)*

The solutions $\tilde{k}$ of Eq. (5.126) for given ω are non-trivially distributed over the complex plane. A direct procedure to obtain all solutions has been developed by McIver (1998) using a Riemann-Hilbert approach by Ioakimidis (1988). As pointed out by McIver even double roots of Eq. (5.126) may exist. A complete eigenfunction expansion of Eq. (5.43) with p as in Eq. (5.39) with $\alpha(x) = \alpha_0$ may therefore include generalised eigenfunctions at these double roots.

In Fig. 5.15 on the next page the zero-contours of the real and imaginary part of $\tilde{k} \tanh \tilde{k} - \frac{\omega^2}{1 - i\alpha_0\omega}$ are plotted for $\omega = 2$ and two values of α_0. The intersection of these zero-contours where $k \neq \pm i(2n + 1)\frac{\pi}{2}$ ($\tanh(k)$ is not defined) correspond to the solutions of Eq. 5.126. The points $k = \pm i(2n + 1)\frac{\pi}{2}$ are the dots in the figure. The cross plotted in the right-upper plane corresponds to the deep water approximation $\tilde{k} = \omega^2/(1 - i\alpha_0\omega)$. As can be observed, the deep water assumption still results in good approximations of the principal wave number. In the following paragraphs the deep water assumption will be used to approximate the 'most progressive' wave number $\tilde{k}$.

In Fig. 5.16 on page 157 the reflection coefficients for a dissipation zone consisting of a linear damping function $\alpha(x) = \alpha_0$ and a Sommerfeld condition with $c_s = 1$ are compared for different values of α_0. Investigation of the wave patterns showed that the 'wiggling' part of the reflection curve for small values of $\alpha_0\omega$ corresponds to waves that:

1. are partially reflected against the discontinuity in α at the interface with the
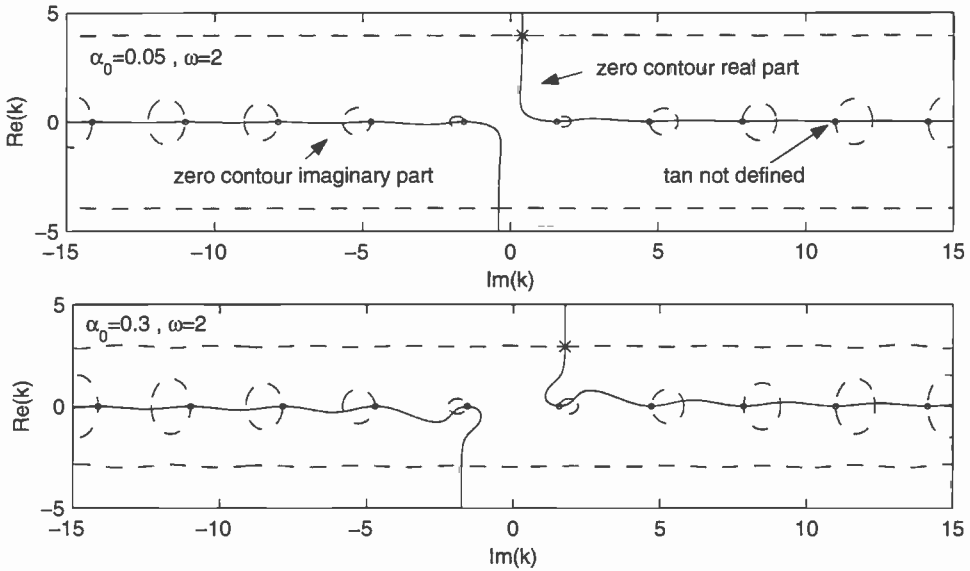
Figure 5.15: *The zero-contours of the real component (solid line) and imaginary component (dashed line) of $\tilde{k}\tanh\tilde{k} - \frac{\omega^2}{1-i\alpha_0\omega}$. The intersections where $k \neq \pm i(2n+1)\frac{\pi}{2}$ correspond to solutions of Eq. 5.126.*

numerical dissipation zone.

2. have propagated through the dissipation zone, partially reflected against the Sommerfeld condition and travelled back through the dissipation zone.

The wiggling is due to the interference between these two left-going waves and is predicted both by the continuous analysis as by the discrete analysis for small values of $\alpha_0\omega$. For larger values of $\alpha_0\omega$ the reflection coefficient is completely determined by the first type of reflections. The part of the wave that travels through the dissipation zone and reflects against the Sommerfeld condition is completely damped before it reaches the start of the dissipation zone for the second time. Therefore no interference between the two type of reflections occurs and the reflection coefficient is determined as if $L_B \to \infty$. We therefore examine the reflections coefficient for $kL_B \to \infty$. Multiplication of the nominator and denominator by $e^{-2i\tilde{k}^*}$ in Eq. (5.124) results in

$$r = \frac{e^{-2\text{Re}(2i\tilde{k}^*L_B)}\left(\omega - c_s\tilde{k}\right)\left(\tilde{k}+k\right) + e^{-2i\tilde{k}^*L_B}\left(\omega + c_s\tilde{k}\right)\left(\tilde{k}-k\right)}{e^{-2\text{Re}(2i\tilde{k}^*L_B)}\left(\omega - c_s\tilde{k}\right)\left(k-\tilde{k}\right) - e^{-2i\tilde{k}^*L_B}\left(\omega + c_s\tilde{k}\right)\left(k+\tilde{k}\right)} \quad (5.127)$$

from which it can be directly observed that

$$\lim_{kL\to\infty} r = \frac{k-\bar{k}}{k+\bar{k}}, \quad (5.128)$$

which results in deep water in

$$\lim_{kL \to \infty} r = \frac{i\omega\alpha_0}{i\omega\alpha_0 - 2}. \tag{5.129}$$

Taking the absolute value of Eq. (5.129) results in

$$\lim_{L \to \infty} |r| = \sqrt{\frac{\omega^2\alpha_0^2}{\omega^2\alpha_0^2 + 4}}. \tag{5.130}$$

The conclusion of the previous analysis is that for large values of kL_B but for $\omega\alpha_0 \ll 2$

$$|r| \approx \frac{\omega\alpha_0}{2}, \tag{5.131}$$

which is in agreement with the results of both the linear analysis and the discretised equations as can be observed in figure 5.16 on the next page.

For smaller values of kL_B the continuous and discrete reflection coefficients are not in mutual agreement. A series of grid refinement studies confirmed that the reflection coefficients of the discrete analysis had converged. The discrepancy between the continuous estimate and the numerical estimate must therefore be due to the plane wave assumption used in the continuous analysis. Apparently, neglecting the evanescent modes in the constant dissipating zone results in an overestimate of the reflection coefficients.

Linear damping

The expression for the reflection coefficient using a linear damping function $\alpha(x) = \alpha_1 x$ when the limit $kL_B \to \infty$ for the approximation $\mu(x) = \frac{1 - i\omega\alpha(x)}{\omega^2}$ with the deep water assumption is

$$\lim_{kL \to \infty} |r| = \frac{2\omega + \alpha_1 - \sqrt{\alpha_1^2 + 4\omega^2}}{2\omega - \alpha_1 + \sqrt{\alpha_1^2 + 4\omega^2}}. \tag{5.132}$$

This expression simplifies for $\alpha_1 \ll 2\omega$ in

$$|r| \approx \frac{\alpha_1}{4\omega}. \tag{5.133}$$

For large values of ω the reflection coefficient therefore strictly decreases with increasing ω which is a significant difference compared to the asymptotic behavior for constant $\alpha(x) = \alpha_0$.

Fig. 5.17 on page 158 shows the reflection coefficient for linear damping functions $\alpha(x) = \alpha_1 x/L_B$ and a Sommerfeld absorption boundary with $c_s = 1$. In every subfigure 3 curves are plotted. The solid curve is the graph of the reflection coefficient obtained by linear analysis of the discretised equations. The dashed curve is the reflection coefficient obtained using the simplified continuous plane wave model,
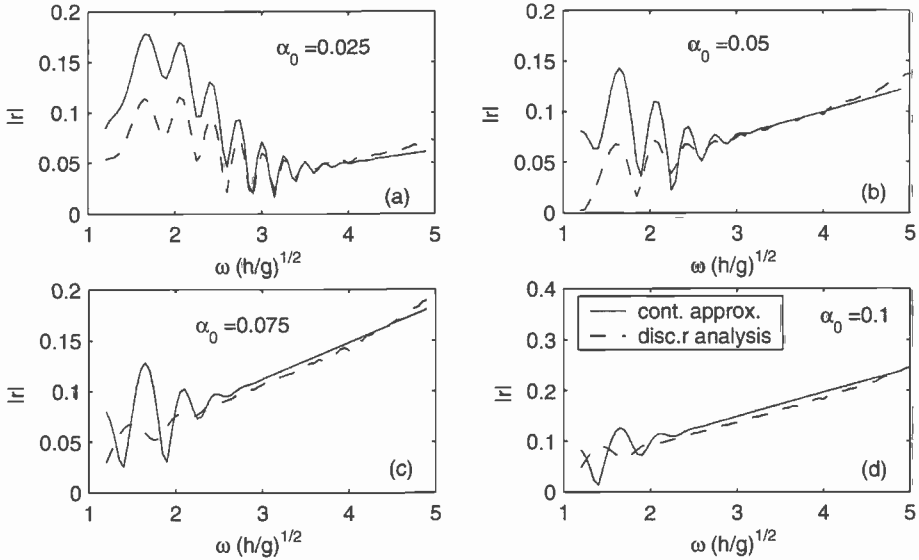
Figure 5.16: *Reflection coefficient estimates obtained from linear analysis of the continuous equations and of the discretisation. (constant damping function) (g=1, h=1, c=1, $L_B = 2$, $\gamma = 1$, $\beta = 1.5$, $nx/h = 31$, $nz = 11$, $L = 12$)*

Eq. (5.64)-(5.65), with the approximation $\tilde{\mu} = \frac{1}{k}$. The dotted curve is the reflection coefficient obtained using the approximation $\tilde{\mu}(x) = \frac{1-i\omega\alpha(x)}{\omega^2}$ as in Eq. (5.85). Again the convergence of the reflection curve obtained by the discretisation has been verified.

From this figure and the above analysis it is concluded that:

- For the investigated range of parameters, the approximation using $\tilde{\mu}(x) = \frac{1-\omega\alpha(x)}{\omega^2}$ in the simplified continuous model Eq. (5.66) results in smaller reflection coefficients than the choice $\tilde{\mu} = \frac{1}{k}$. The latter choice for $\tilde{\mu}$ results in an overprediction of the reflection coefficients from discrete analysis for almost the complete range of investigated frequencies.

- The simplification of the continuous equations for linear damping functions - the plane wave assumption and the operator approximation - results in poor estimates of the reflection coefficient.

- The reflection coefficient on a long numerical dissipation zone using a linear damping function $\alpha(x) = \alpha_1 x$ for small waves is proportional to α_1/ω.
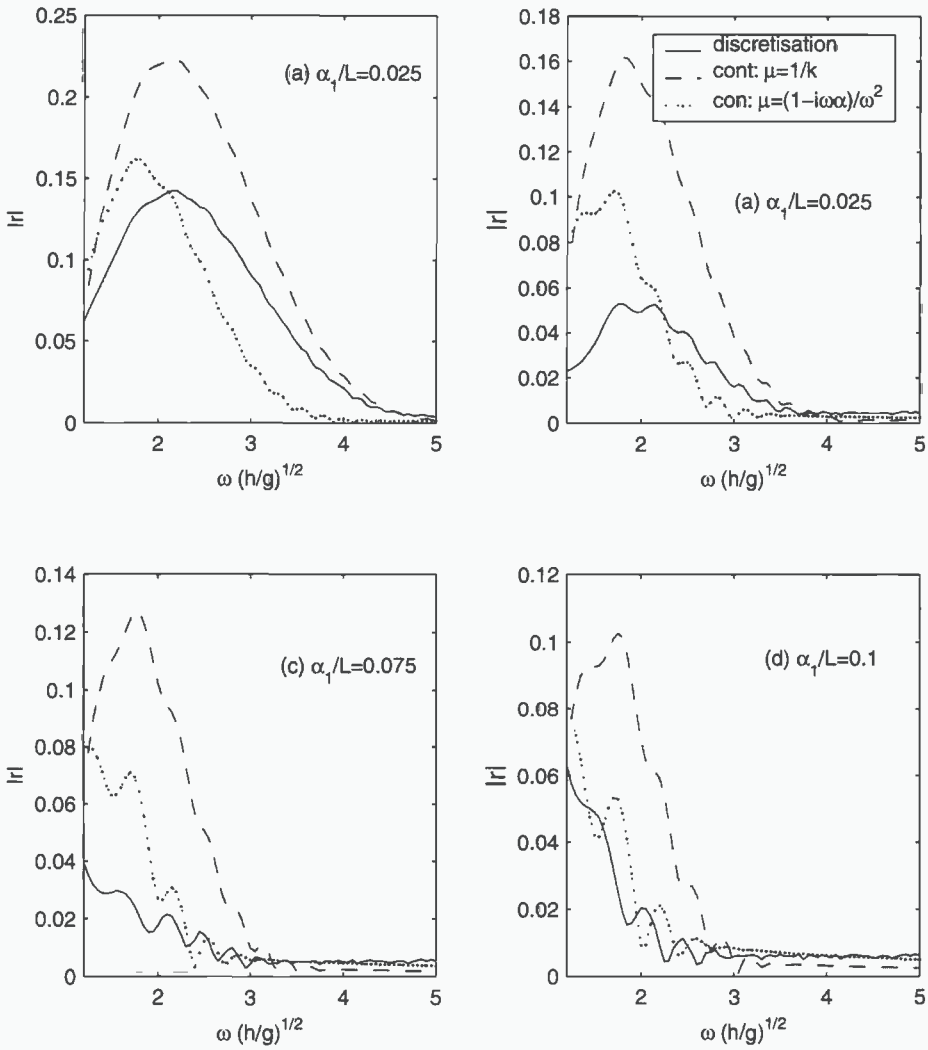
Figure 5.17: *Reflection coefficients of the continuous model using the approximations Eq. (5.83) (dashed) and Eq. (5.85) (dotted) and the result of the analysis of the linearised discretised equations (solid line) for $c_s = 1$ and different values of α_1 (linear damping function). (g=1, h=1, $L_B = 2$, $\gamma = 1$, $\beta = 1.5$, $nx/h = 31$, $nz = 11$, $L = 12$)*
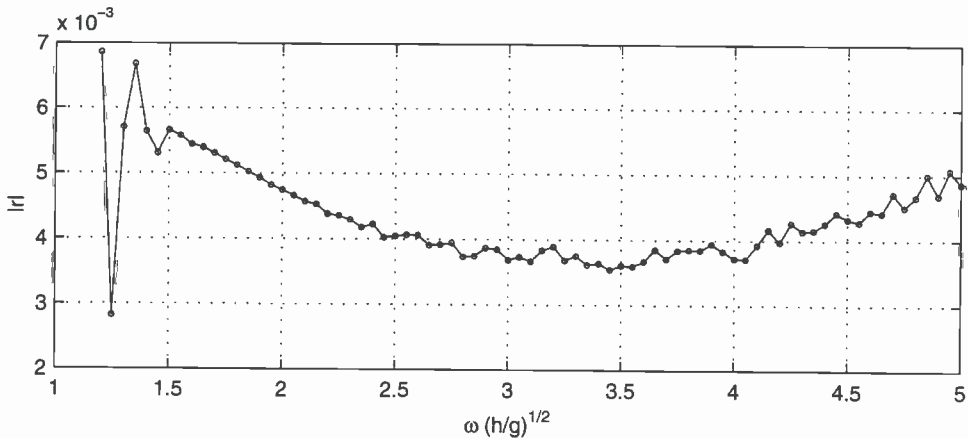
Figure 5.18: *The reflection coefficients for the beach configuration α_1 = $0.3/L_{eff}$ [1/g], γ = 1.04, c_s = 0.7 nx/h=31, nz=11, β = 1.5, $L = 12$, $L_B = 2$, $g = 1$, $h = 1$)*

5.5.2   Transparent beach

It was found that for the grid configuration used in Fig. 5.13 on page 153 (i.e. nx/h=31, nz=11, $\beta = 1.5$, $L = 12$, $L_B^0 = 2$, $g = 1$, $h = 1$) the smallest reflection coefficients were obtained for $\alpha_1/L_{eff} = 0.3$, $\gamma = 1.04$ and $c_s = 0.7$. The reflection coefficients are plotted in Fig. 5.18 and show that all reflection coefficients are smaller than 0.7 %. The slow increase of the reflection coefficient for the higher values of ω is due to reflections on the stretching of the grid.

Although the configuration $L_B = 2$, $\gamma = 1.04$, $c_s = 0.7$ and $\alpha_1/L_{eff} = 0.3$ results in minimal reflection coefficients for the principal range of frequencies, the choice $c_s = 1$ over $c_s = 0.7$ is sometimes preferable when shallow water waves (like solitary waves) also need to be absorbed. Remark that these very small reflections ($< 0.7\%$) over the range of waves between $\lambda = \frac{1}{4}h$ and $\lambda = 4h$ is achieved at the relatively small computational cost of increasing the computational domain with a length of 2h. Choosing $c_s = 1$ over $c_s = 0.7$ results in an increase of the reflection coefficient at $\omega = 1.2$ and $\omega = 1.25$ to approximately 0.019 and 0.008, respectively. The reflection coefficients at all other frequencies do not significantly change. Because of the very small reflections, the above configuration with either $c_s = 0.7$ or $c_s = 1$ will be referred to as the transparent numerical wave absorber.

To illustrate the effectiveness of this configuration in the fully nonlinear case, the following numerical simulations are presented: (i) comparison of the free-surface elevation for two different positions of the beach and (ii) the investigation of the evolution of an initial condition resulting in a broad continuous spectrum of travelling waves.
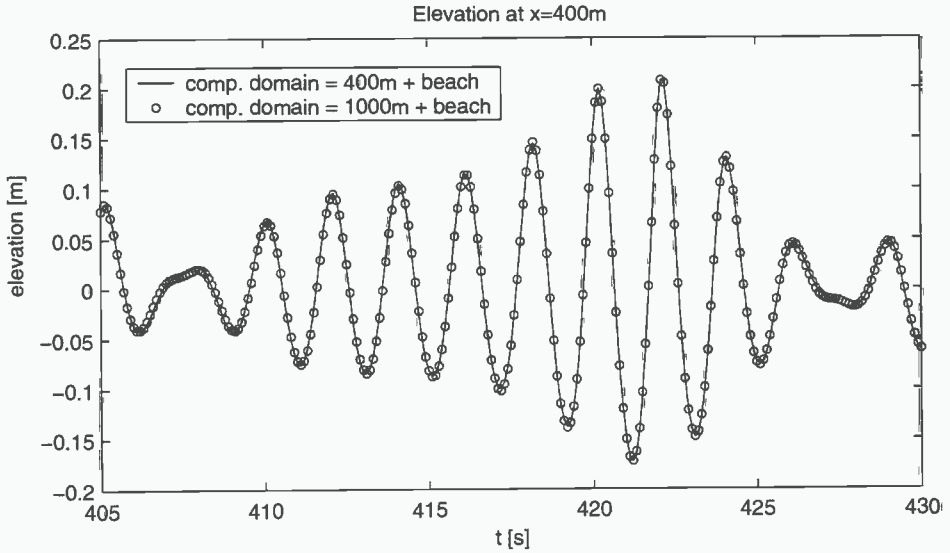
Figure 5.19: *The wave elevation of a nonlinear bichromatic wave for $405 < t < 430$ at $x = 400$ [m] and two configurations using the optimal configuration of Fig. 5.18: (solid line) dissipation zone starts at $x = 400$ [m] ; (open dot) dissipation zone starts at $x = 1000$ [m])*

Effect of translated beach

A highly nonlinear bichromatic wave ($h = 5$ [m], $g = 9.81$ [m^2/s], T_1=1.8 [s], T_2=2.2 [s], q_1=q_2=0.08 [m], $\Delta T = 0.1$ [s]) is generated using a flap-type wave maker and the numerical beach is placed at $x = 80h$ from the wave maker. The wave elevation is recorded at $x = 80h$ and compared to the wave signal for the same simulation, but with the numerical beach translated to $x = 200h$. The two signals are plotted in Fig. 5.19 and are seen to be almost identical. It is concluded that the effect of the numerical beach on the simulation is negligible and therefore performs adequately as a transparent boundary.

Broad banded spectrum

An initially prescribred free-surface method is used to generate a wave train containing many frequency components. As a numerical absorption the optimal beach of this section is used. For this simulation $h = 5$ [m], $g = 9.81$ [m/s^2], $nx/h = 26$ and $\Delta T = 0.1$ [s]. As an initial condition the profile

$$\eta(x, 0) = a \operatorname{sech}(2x) \tag{5.134}$$

is taken. The numerical dissipation zone starts at $x = 12h$. The graphs in Fig. 5.20 on the following page are x-t plots of η where values of $\eta > 5 \times 10^{-4}$ are plotted as black dots. The plots in Fig. 5.20 (a)-(c) are the result of simulations with $a = 0.2$ [m] while in (d)-(f) $a = 0.6$ [m] was chosen. In plots (a) and (d) no dissipation zone is used but only a Sommerfeld condition with $c = 1$. In plots (b) and (e) only a linear dissipation zone is used but no Sommerfeld condition. In (c) and (f) the combination of the damping and Sommerfeld condition is used. From this figure the effectiveness of the Sommerfeld condition for long waves and the effectiveness of the dissipation zone for short waves can be observed. Also, for nonlinear time-domain simulations for waves with many frequency components, the concept of combined linear damping, stretching and a Sommerfeld condition proves to be a robust, stable and adequate numerical beach concept for a relatively small computational effort (extension of the domain by 2h).

5.5.3 Approximation of the physical beach

In the previous subsection the numerical parameters that result in the smallest achievable reflection coefficients using the numerical wave absorber have been presented. In this subsection, parameters are sought that will result in a reasonable representation of the measurements presented in Subsection 5.2. It has also been investigated whether geometric modelling of the West-side basin (see Fig. 5.1 on page 120) could improve correspondence between the numerical and measured reflection coefficients; this was however not observed. It is stressed that there is no physical connection between the numerical models (Sommerfeld condition, pressure damping and grid stretching) and the artificial beach used in the experiments. Matching of the results is therefore an ad hoc procedure of trial and error that is guided by the following three observations:

- The value of c_s determines a local minimum on a desired frequency in the lower frequency part of the spectrum.

- The value of α_1 determines the value of the reflection coefficients for the central frequencies

- The values of γ influences the slope of the reflection curve in the high-frequency range.

Based on extensive variations keeping $nx/h = 31$ fixed of the above parameters the following two configurations of numerical parameters were chosen:

$$\text{North side SMB} \quad L_B = 2, \ \gamma = 1.0365, \ c_s = 0.5, \ \alpha_1/L_{eff} = 0.015 \quad (5.135)$$

$$\text{West side SMB} \quad L_B = 2, \ \gamma = 1.04, \ c_s = 0.45, \ \alpha_1/L_{eff} = 0.02 \quad (5.136)$$

During the investigations it was observed that by adding a threshold to $\alpha(x)$ as

$$\alpha(x) = \begin{cases} \alpha(x) = \alpha_0 & 0 < x < 0.4h \\ \alpha(x) = \frac{\alpha_1/L_{eff}}{x} & 0.4h \leq x < L_{eff} \end{cases} \quad (5.137)$$
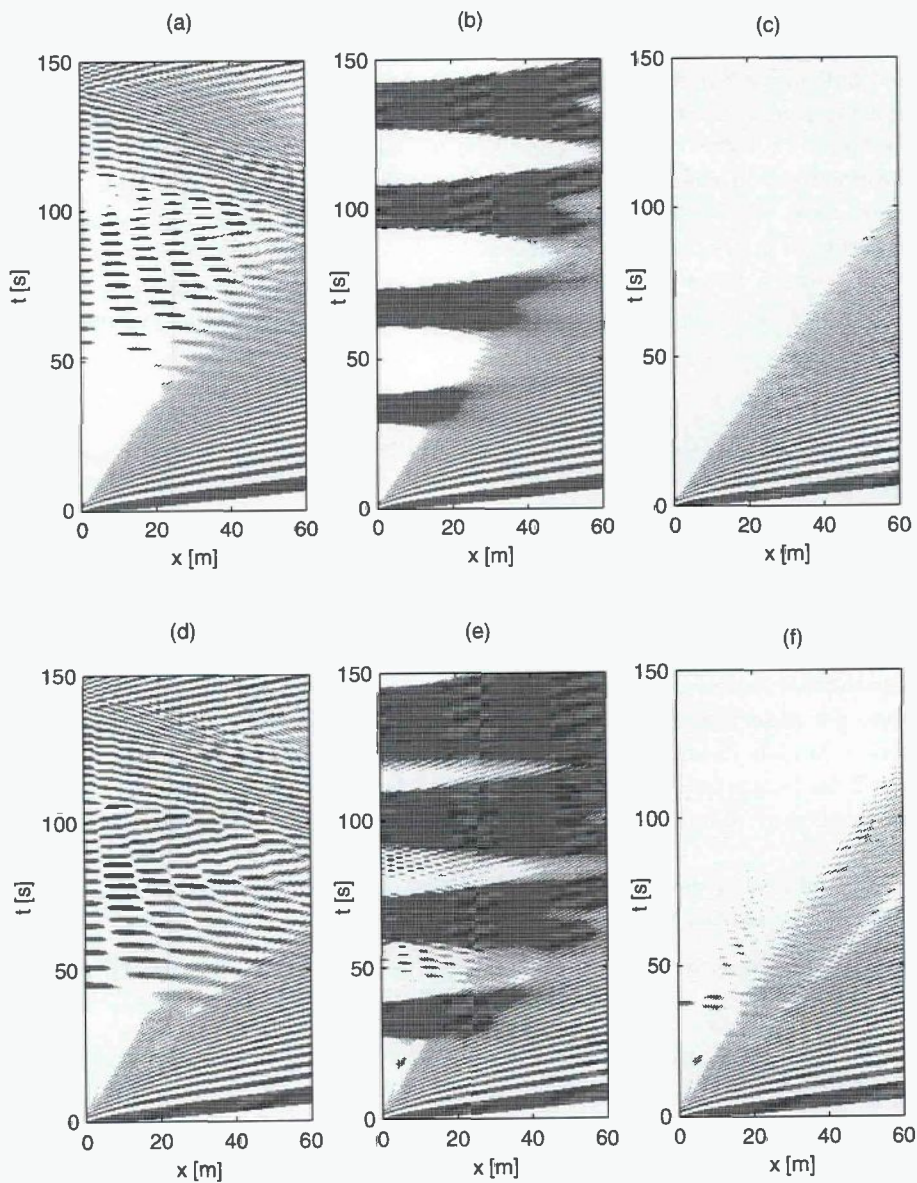
Figure 5.20: *x-t plots of η given the initial condition (5.134) where values of η > 2 5 × 10⁻⁴ are plotted as black dots. for (a)-(c) a = 0.2 and for (d)-(f) a = 0.6. 1st column: only Sommerfeld; 2nd column: only pressure damping; 3rd column: combination of Sommerfeld and pressure damping.)*
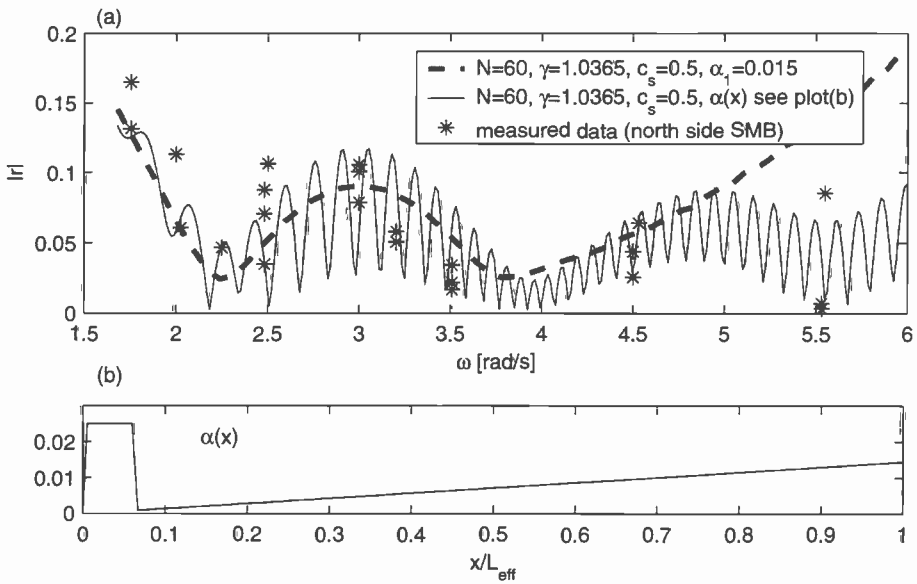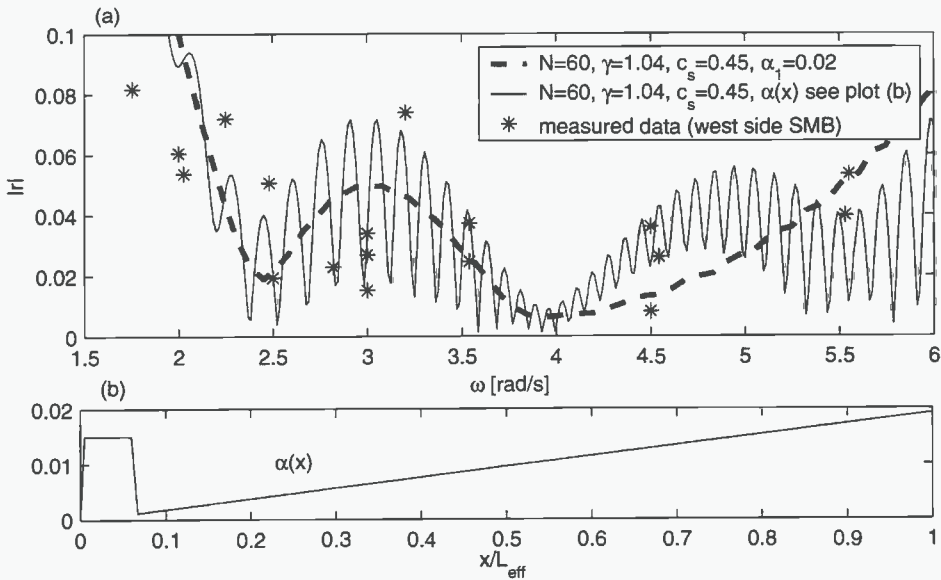
Figure 5.21: *Measured reflection coefficients and the reflection coefficients for two numerical damping models for the beach on the North side of the SMB*

resulted in a highly oscillating reflection curve. The reflection curves both with and without this threshold and the measured reflection coefficients (see also Fig. 5.4 on page 126) are plotted in Fig. 5.21 and Fig. 5.22. The oscillations due to the additional threshold are probably due to the interference of the waves reflected against the two jumps in $\alpha(x)$.

One reason to include the threshold in the function $\alpha(x)$ could be to introduce a similar spreading of the reflection coefficients as was found in the measurements. Very small variations in ω lead to quite different reflection coefficients. However, it must again be stressed that there is no physical representative model underlying the numerical beach, let alone the choice of α.

5.6 Conclusions

In this chapter the numerical modelling of artificial beaches in a wave tank has been discussed. Firstly, the measurements on the artificial beaches of the new SMB and OT at MARIN have been described. The reflection coefficients at the West side of the SMB are < 10% for all investigated regular waves. The reflection coefficients on the North side are slightly higher than the coefficients on the West side which is due to the fact that the beach on the North side is two meters shorter. Examination of the measurements showed that the estimated reflection coefficients are not independent

Figure 5.22: *Measured reflection coefficients and the reflection coefficients for two numerical damping models for the beach on the West side of the SMB.*

of the wave amplitude. Also no strong correlation was found between the steepness of the wave and the reflection coefficient.

A combination of three numerical methods is porposed as a numerical model for the artificial beach: (i) an energy dissipation zone (ii) a Sommerfeld radiation condition on the downstream vertical boundary and (iii) stretching of the grid in the horizontal direction along the dissipation zone. The energy is dissipated through the additional term $\alpha(x)\phi_z$ in the dynamic free-surface condition. For positive $\alpha(x)$ strict energy decay is guaranteed and mass is still conserved. This combined numerical beach model was investigated both before and after numerical discretisation.

In the continuous analysis a plane-wave assumption was made to simplify the analysis. Comparison with the converged reflection coefficients of the discretised equations showed that this simplification leads to an overestimate of the reflection coefficients for constant functions $\alpha(x) = \alpha_0$ for small values of $\omega\alpha_0$. The approximation of the dispersion operator by Eq. (5.65), to obtain analytical solutions for the governing equations when $\alpha(x) = \alpha_1 x$, resulted in poor estimates of the reflection coefficient when compared to the discrete results. It is therefore concluded that models based on the suggested operator approximation are inadequate, although higher-order (Padé) approximations of the symbol $\hat{R}$ may lead to better approximations.

Linear analysis of the discretisation of the equations showed that stretching of the grid does not affect the linear stability of the numerical scheme. The Sommerfeld radiation

condition, that was implemented as a Dirichlet boundary condition, will influence the stability of the time integration as the additional eigenvalues due to this condition can be situated outside the stability region of the RK scheme. Analysis showed that the position of this eigenvalue on the real axis is inversely proportional to the horizontal mesh width near the downstream boundary and may result in a severe restriction on the time step. Stretching of the grid has therefore two main advantages: (i) the effective length of the dissipating zone is greatly increased without any additional computational cost and (ii) the local horizontal mesh width near the Sommerfeld boundary is much enlarged leading to no additional constraints on the time step. If the horizontal grid is stretched too fast short waves will significantly reflect against the grid. An optimal configuration of the three numerical concepts is constructed with the property that $|r| < 0.007$ for all waves with wavelength $h/4 < \lambda < 4h$ for a computational effort equivalent to an extension of the domain with $2h$. This optimal beach was tested in the fully nonlinear case by measuring the effect of the translation of the beach and by examining the effect on a broad banded wave train. It is concluded that the constructed optimal configuration is both efficient and effective as a transparent boundary for a wide range of frequencies. A numerical parameter variation study of the combined beach concept was performed to tune the reflection coefficients to the measured data. A combination of parameters was found to result in a reasonable approximation of the scattered data from the measurements. It was found that an additional threshold in the damping function $\alpha(x)$ resulted in oscillatory behavior of the reflection coefficients.

Chapter 6

Nonlinear Wave Groups

The investigations of the Chapters 3-5 dealt with the generation, propagation and absorption of waves in a numerical wave tank based on the principles outlined in Chapter 2. In this chapter, the developed numerical scheme will be applied to investigate the long-time evolution of nonlinear wave groups. Firstly, the evolution of a confined wave group and the effect of a specific bottom topography in a coastal region will be investigated. Secondly, the evolution of bichromatic wave groups will be examined. Predictions of the numerical simulations are validated against experiments that have been performed at MARIN. Good agreement is observed between the experimental and the numerical results. Both the numerical and experimental results show a strong nonlinear deformation of the wave group envelope. The numerical method is then used to predict the long-time evolution beyond the spatial dimension of the physical wave tank. This long-time evolution of the wave group shows intriguing temporal structure and spatial recurrence phenomena. Investigation of the spatial variation of the wave spectrum and analysis of the nonlinear equations motivates the introduction of a parameter governing the deformation process of these bichromatic waves.

6.1 Previous investigations

The nonlinear evolution of (confined) wave groups has been the subject of investigations since the 1960's. The subject is directly related to the instability of uniform wave trains. The reason is that the first experimental evidence of wave train instability showed grouping of the wave. The grouping evolves from (exponentially) growing symmetric side bands close to the central frequency of the wave train, resulting in a modulated wave train.

6.1.1   Modulated wave trains

Although the first existence proofs of periodic deep water solutions to the nonlinear free-surface equations were already given at the beginning of the previous century, the stability of these solutions was taken for granted until the 1960's. Lighthill (1965) used Whitham (1965) averaged Lagrangian theory to examine the solution of a smooth initial wave packet for deep water waves. His solution predicted that the nonlinearity would lead to a focussing of energy towards the center of the pulse as the packet evolved in time, but the solution became singular in finite time. Lighthill commented that such behavior is indicative of the presence of an instability associated with non-linear deep-water waves. Benjamin & Feir (1967) were however the first to prove that a uniform continuous wave train is indeed unstable to modulational perturbations of its envelope. Both Benjamin (1967) as Feir (1967) give experimental proof to provide some evidence for their theoretical proven instability. They speculate that as a result of the exponential growth of the unstable sideband band frequencies, the wave train would finally disintegrate and the energy would spread over a broad spectrum. Feir (1967) also showed experimentally the disintegration of a single confined wave group into two wave group pulses. Hasselmann (1967) speculates that the results of Benjamin & Feir supports his claims that due to the resonant nonlinear interactions the wave energy will be evenly spread over all wave numbers in any wave spectrum (Hasselmann (1963)).

Lighthill (1967) uses Whitman's theory to examine the same problem as Benjamin & Feir and also shows instability, but gives different conditions for the instability. The solution again leads to a singularity in finite time (Whitman's theory should be asymptotically valid). Zakharov (1968) shows that the nonlinear free-surface boundary conditions are Hamiltonian and that if the wave number variation is small, the governing equations can be reduced to the Non-Linear Schrödinger (NLS) equation for the wave envelope. His mode-interaction equations are also known as the Zakharov integral equations. Later is has been shown by Caponi *et al.* (1982) that the Zakharov equations itself are not Hamiltonian, while the free-surface equations have a Hamiltonian structure (cf. also Broer (1974) and Miles (1977)).

Chu & Mei (1970, 1971) use a multiple-scale method to derive the NLS equations. Their equations are similar to the ones of Lighthill except for an additional term in the dispersion relation proportional to $\frac{a_{xx}}{a}$, which eliminates the singularity encountered by Lighthill. Their numerical scheme however, breaks down when the amplitude a becomes zero. The experiments that they preformed however showed that the envelope of a deep water Stokes train tends to disintegrate into smaller envelope pulses of permanent form. Zakharov & Shabat (1972) give an exact solution to the initial value problem of the NLS for sufficiently fast vanishing initial values. The exact solution predicts that an arbitrary smooth initial wave packet will eventually disintegrate into a definite number of envelope solitons which are stable to collisions.

Both Hasimoto & Ono (1972) as Davey (1972) report that the wave envelope for small wave number variations satisfies the NLS. Hasimoto & Ono propose that the

end state of the instability of nonlinear wave trains might be a series of solitary envelope pulses of permanent form. Bryant (1974) shows that permanent waves can be identified with Stoke waves for deep water and with cnoidal waves for shallow water, with a continuous range of wave profiles in between. Yuen & Lake (1975) prove that Whitman's theory when applied consistently to the order considered, also yields the NLS and they experimentally confirm the soliton properties of confined wave packets. Now the discrepancies between Whitman's theory and the Benjamin-Feir instability are resolved because the NLS produces the Benjamin-Feir instability for an initially uniform wave train. This is also later shown by Stuart & Diparma (1978).

Yuen & Lake (1975) also perform detailed experiments to confirm that the NLS provides a quantitatively satisfactory description of the long-time evolution of wave packets. Lake & Yuen (1977) then re-examined the experiments of the initial reported instabilities by Benjamin and Feir. They showed that the long-time evolution of a modulated continuous wave train exhibits Fermi-Pasta-Ulam (FPU, Fermi et al. (1940)) recurrence. The previously observed disintegration of the modulated wave train into a pulse was only an intermediate state. They also show numerically that the NLS exhibits this kind of recurrence. Later it has been shown (see e.g. Akhmediev & Ankiewicz (1997), pp. 50-57) that the BF-instability is related to an exact solution of the NLS. Lake & Yuen (1977) accounted for the apparent discrepancies between the numerical and experimental results by correcting the theoretical wave steepness with the measured wave steepness ($ka = 0.78(ka)_{\text{meas}}$). Yuen & Ferguson (1978b) further explored the relationship between the Benjamin-Feir instability and recurrence in the NLS, also in two space dimensions (Yuen & Ferguson (1978a)).

Longuet-Higgins (1978a,b) presents fully numerical simulations using periodic boundary conditions establishing reference material for the stability regions and initial growth rates. Dysthe (1979) extends the nonlinear Schrödinger equation to be applicable to wave packets of broader bandwidth by adding a higher-order term correction. The correction for the wave steepness previously introduced by Lake & Yuen (1977) was shown to be fictional by the same authors (Yuen & Lake (1982)) and they concluded that theories should be improved. They propose the use of the Zakhorov integral equations and obtained better agreement of the side-band growth-rates than given originally by Benjamin and Feir. Stiasnie (1983) showed that Dysthe's equation can be deduced from Zakharov's integral equation by using the narrow bandwidth approximation. Janssen (1981) obtains a nonlinear evolution equation for the amplitude of the sidebands from analysis of Dysthe's equation and the result exhibits the FPU recurrence phenomena and are in qualitative agreement with the experimental findings. Bryant (1982) show that there is a critical depth as a point of bifurcation between permanent waves and wave groups of permanent envelope. Melville (1982) conducts a series of sideband evolution experiments (all including breaking) from which he concludes that the end state of the evolution is inevitably a breaking event followed by partial recurrence, tending to lower frequencies. He did not observe any recurrence of the FPU type as reported by Lake et al. (1977). However his initially used wave steepness was a factor two higher ($ka = 0.2$) than that used by the

previous authors. Lo & Mei (1985) numerically compute the long-time evolution of nonlinear wave trains using Dysthe's equation showing wave train disintegration and FPU recurrence phenomena. Trulsen (1989) later improved this numerical method for solving Dysthe's equation. The stability analysis on the Zakharov equation is extended by Crawford *et al.* (1991) who obtain an expression of the initial growth rates for finite values of ka and find better agreement with experimental and numerical results. Their results also show restabilisation for large values of ka. Krasitskii (1994) modifies the Zakharov integral equations preserving the Hamiltonian structure of the free-surface problem. Colin *et al.* (1995) show that the stability does not depend on the irrotationality assumption.

Nonlinear simulations on the evolution of nonlinear unstable wave trains have been performed by several authors using periodic boundary conditions. Landrini *et al.* (1998) however compared several numerical surface methods (NLS, Dysthe, Krasitskii) to fully numerical simulations (using the code developed by Wang *et al.* (1995)) and concluded that the Krasitskii model shows the closest agreement to the fully nonlinear solution for long-time unstable waves. Tulin & Waseda (1999) report extensively on fully nonlinear numerical results and measurements on the occurrence and the effect of breaking in the unstable wave train.

For further references we refer to the review article of Yuen & Lake (1980) on wave instabilities and the review of Hammack & Henderson (1993) on Resonant Interaction Theory. A thorough mathematical description and numerous references on issues related to the nonlinear instability of water waves can be found in Debnath (1994), Chapters 7-8.

6.1.2   Bichromatic waves

Most of the previous reported investigations have been focused on the stability of a slightly modulated uniform wave train. Lo & Mei (1985) are the first to report on the long-time evolution of an unstable bichromatic wave group. Their measurements (performed by G.J. Keller, 1982) show the steepening of the waves at the front and the asymmetric evolution of the wave group envelope. Comparison with numerical experiments based on Dysthe's equation showed reasonable agreement. Lo & Mei use their numerical scheme for long-time calculations and observe the splitting of the bichromatic wave group in two groups with different speeds. Cointe & Boudet (1991) present some measurements and gives some fully nonlinear numerical computations on bichromatic wave groups. The measurements and computations are not directly compared. They also observe the asymmetric evolution of the wave group but do not report on recurrence or long-time evolution. Comparable experimental results on bichromatic waves as presented by Lo & Mei, have also been provided by Stansberg (1997). In Moubayed & Williams (1994) the full second-order solution of bichromatic waves produced by a wave maker in a wave flume is presented. However, a second-order theory cannot account for (third-order) resonant interactions. Taylor & Ohl

(1999) uses the method by Graig & Sulem (1993) (spectral method based on expansion of the Dirichlet-Neumann operator with symmetric spatial boundary conditions) to investigate bichromatic wave groups and observe focussing. The spatial and time scales are however far too small to comment on long time evolution and they mention that more data on vast times scales is necessary to obtain conclusive results.

It is surprising that systematic experimental results on the fully nonlinear evolution of bichromatic wave groups are not available in the literature. We also did not found systematic fully nonlinear numerical investigations on the long-time evolution of these waves.

6.2   Confined wave groups

During the initial course of our investigations, questions concerning the validation of the developed computer program frequently arose. One of the first (cf. Westhuis & Andonowati (1998)) validation studies that was performed, considered the simulation of the evolution of a confined wave group. Similar calculations had been performed by de Haas (1997) who used a Domain Decomposition Boundary Integral Method to solve the evolution of these large wave structures. Initially, he used the first-order solution of the potential and elevation for a confined wave group and investigated the effect of second-order contributions to the stationarity of the propagating wave group. De Haas found that the addition of bound second-order contributions could compensate partially the generation of free second-order components. However, a stationary propagating confined wave group was not achieved. In this section we examine the same first-order confined wave group and use an engineering approach to isolate the stationary part. After it has been confirmed that this approach leads to a reasonable stationary evolution of a confined wave group, the effect of the evolution of this wave group is investigated when the water depth is slowly decreased to half of the original depth.

NLS coefficients

As an initial condition for the simulation of confined waves, a modulated carrier wave with wavenumber $\bar{k}$ is used. It is well known that the modulation amplitude satisfies the Non Linear Schrödinger equation. This equation describes the evolution of the complex-valued amplitude envelope of a narrow-banded spectrum. To obtain the coefficients of the NLS-equation (3.21) the method of multiple-scale expansion has been used. This method was also originally employed by Hasimoto & Ono (1972) for two-dimensional and Davey & Stewartson (1974) for three-dimensional wave packages.

The potential and free surface are expanded as

$$\Phi = \sum_{n=0}^{\infty} \sum_{m=n}^{\infty} \Phi_{nm} \varepsilon^m e^{in\theta} + c.c. \tag{6.1a}$$

$$\eta = \sum_{n=0}^{\infty} \sum_{m=n}^{\infty} \eta_{nm} \varepsilon^m e^{in\theta} + c.c. \tag{6.1b}$$

where $\theta = \bar{k}x - \bar{\omega}t$ and $\eta_{nm}(\xi, \tau)$ and $\Phi_{nm}(\xi, \tau)$ are functions of the slowly varying variables ξ and τ, with

$$\xi = \varepsilon(x - c_g(\bar{k})t) \tag{6.2a}$$

$$\tau = \varepsilon^2 t. \tag{6.2b}$$

Substitution of (6.1a)-(6.1b) in the equations governing the nonlinear free-surface evolution (2.23a)-(2.23f) on page 19, ignoring surface tension and equating the coefficients for $\varepsilon^m e^{in\theta}$, $m = 1, 2, 3$ and $n = 0, 1, 2$ to zero leads after lengthy algebra to expressions for η_{11} and Φ_{11} as

$$\Phi_{11} = A \frac{\cosh(\bar{k}(z + h)}{\cosh(\bar{k}h)} \tag{6.3}$$

$$\eta_{11} = \frac{i\bar{\omega}}{g} A \tag{6.4}$$

Where $A(\xi, \tau)$ is a slowly varying complex-valued amplitude function. To avoid resonance in the $n = 1, m = 3$ expressions, this amplitude has to satisfy

$$iA_\tau + \beta' A_{\xi\xi} - \gamma' |A|^2 A. \tag{6.5}$$

The coefficients β' and γ' in the NLS-equation (6.5) are given as

$$\beta' = \frac{1}{2} \left. \frac{\partial^2 \omega}{\partial k^2} \right|_{k=\bar{k}} \quad \text{and} \tag{6.6}$$

$$\gamma' = \frac{k^4}{4\omega\sigma_1^2} \left\{ (9 - 10\sigma_1^2 + 9\sigma_1^4) + \frac{2\sigma_1^2}{c_g^2 - gh} \left(4c^2 + 4cc_g(1 - \sigma_1^2) + gh(1 - \sigma_1^2)^2 \right) \right\} \tag{6.7}$$

with

$$c = \bar{\omega}/\bar{k} \tag{6.8}$$

$$c_g = \left. \frac{\partial \omega}{\partial k} \right|_{k=\bar{k}} \tag{6.9}$$

$$\sigma_1 = \tanh(kh). \tag{6.10}$$

It is noted that these coefficients determine the evolution of the amplitude of the potential. A simple scaling argument shows that the γ' coefficient for the amplitude
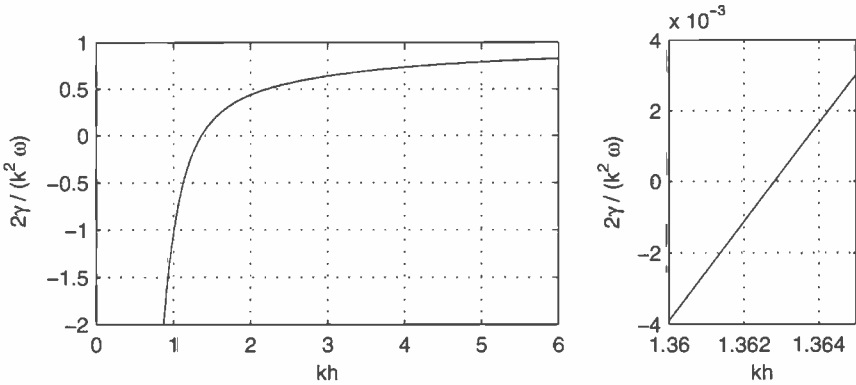
Figure 6.1: *The normalised coefficient $2\gamma^\eta/(\bar{k}^2\omega)$ governing the nonlinearity in the NLS equation.*

of the free surface is $\gamma^\eta = \gamma'\left(\frac{g}{2\omega}\right)^2$. This value of γ^η coincides with the result obtained by e.g. Dingemans (1997*b*) pp. 918 [1] who found γ^η as

$$\gamma^\eta = \left(\frac{\bar{\omega}k_\infty c_g}{2g\sinh^2 q} + \bar{k}\right)\frac{\frac{\bar{k}g^2}{2\bar{\omega}} + \frac{\bar{\omega}^2 c_g}{4\sinh^2 q}}{c_g^2 - gh} + k_0\omega_0\kappa \tag{6.11}$$

with

$$\kappa = \frac{1}{16\sinh^4 q}\left(\cosh 4q + 8 - 2\tanh^2 q\right), \tag{6.12}$$

$$k_\infty = \frac{\bar{\omega}^2}{g} \quad , \quad q = \bar{k}h \tag{6.13}$$

The normalised value of γ^η is plotted in Fig. 6.1 from which it can be observed that it changes sign around $kh \approx 1.363$. For $\beta'\gamma' < 0$, Eq. (6.5) is known as the self-focussing NLS allowing confined solitary solutions for A. Because for gravity waves always $\beta' < 0$, this condition is equivalent to the condition $\gamma' > 0$ which results in the condition $kh > 1.363$ in order for solitary solutions of the envelope to exist. The soliton solution of Eq. (6.5) in physical coordinates is given by

$$A(x,t) = a_0\text{sech}\left(\sqrt{\frac{-\gamma'}{2\beta'}}a_0\ (x - c_g t)\right)e^{-i\frac{\gamma'a_0^2}{2}t}. \tag{6.14}$$

---

[1] This reference contains a misprint: the second power instead of the fourth power of the sinh in the denominator of κ has been printed.

Disintegrating wave trains

Before the NLS was introduced as a model equation for the modulation of narrow
banded wave train, Feir (1967) already reported on the appearance of a second wave
group from a wave pulse experiment. Later systematic experiments were performed
by Yuen & Lake (1975) for $ka < 0.1$ and Su (1982) for $ka > 0.1$ on confined wave
trains. Their results are in agreement with the predictions of Zakharov & Shabat
(1972) that a wave train that sufficiently fast decays for $\|x\| \to \infty$ will disintegrate
in solitary wave groups and a small oscillatory tail. The results of Su have been
reproduced qualitatively by numerical simulations of Lo & Mei (1985) using Dysthe's
equation. Shemer *et al.* (1998) also performed some experiments for wave groups
on intermediate water depth and compare the results to numerical solutions of the
NLS-equation. Although symmetric initial data remain symmetric under the NLS-
equation, they consider the NLS-equation as a robust model for the description of
wave groups in water of intermediate depth.

The experiments of Su (1982) have been simulated using the numerical method of
Chapter 2 and for the cases that no breaking events occurr ($ka < 0.14$) disintegration
of the wave train in solitary wave groups was found. Some simulations that were
performed showed however a slightly different behavior than the experiments of Su
suggest for further downstream wave signals. Similar to the experiments of Su (1982),
a wave train is generated by modulating a regular wave ka with a ramp function $s(t)$.
For the results presented in this paragraph, this ramp function is given in Eq. (6.15).

$$
s(t) = \begin{cases}
1/4\, t & 0 \le t \le 4 \\
1 & 4 < t \le 24 \\
1 - (t - 24)/4 & 24 < t \le 28 \\
0 & t > 28
\end{cases}
\tag{6.15}
$$

The depth is $h = 5$ [m] and for the carrier wave we choose $a = 0.1$ [m], $T = 2$ [s]
from which it follows that $ka \approx 0.10$ and $kh \gg 1.363$. The numerical simulation
was performed with the following numerical parameters: $nx = 5122$, $L = 1000$ [m],
$\Delta x = 0.2$, $nz = 9$, $\beta = 1$, $\Delta t = 0.1$, RK45M time integration, p[FEM]=1 and
p[FD]=2. The velocity generating type of numerical wave generation as described in
Subsection 4.3.1 was used and for the absorbing beach the optimal configuration of
Section 5.5.2 was employed. The results of this simulation are plotted in Fig. 6.2 on
the facing page. The figure shows the time signals at different positions along the
numerical tank. From $x = 5$ [m] to $x = 450$ [m], the disintegration and focussing
of the wave train into several wave groups can be clearly observed. Although one
might expect the further separation of the groups (as suggested by Su and also by Lo
& Mei), this is in fact not observed at $x = 600$ [m] and $x = 750$ [m]. It is possible
that this is just an intermediate step in the splitting process. However, it shows that
based on the observations until $x = 450$ [m] one may not conclude that the distinct
solitary groups are established and will propagate independently and with their own
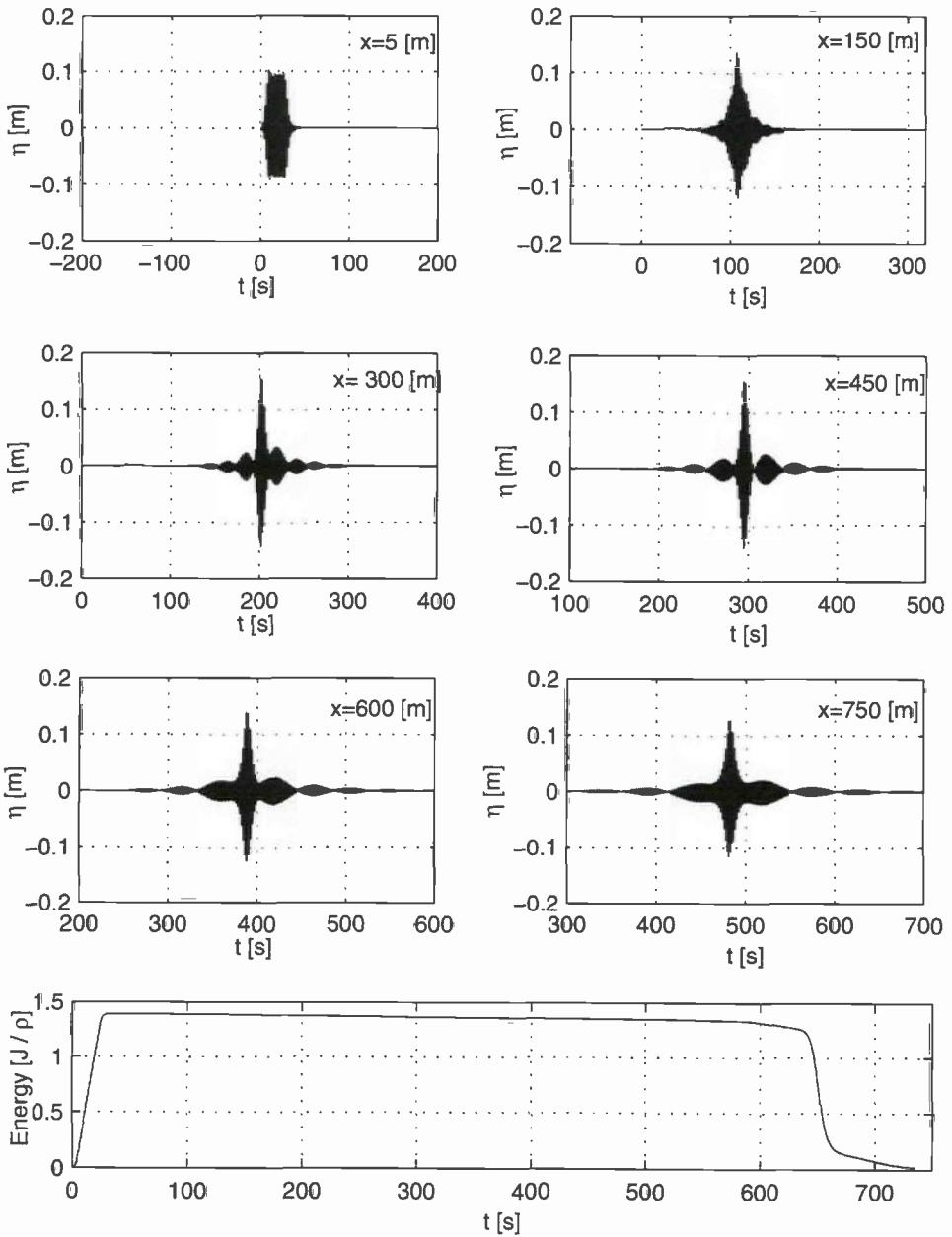
Figure 6.2: *Evolution of a confined wave train (ka = 0.1, h = 5 [m]). Lowest plot shows the total discrete energy during the numerical simulation.*

velocities.

The lower plot in Fig. 6.2 shows the total discrete energy (see Eq. (3.55)) as a function of the simulation time. One can observe that after the wave train has been generated ($t > 28$), the total energy slowly decreases, which is due to numerical dissipation and mass-loss through the Sommerfeld condition. This energy decay is in agreement with the findings of Section 3.4. Between $t = 28$ [s] and $t = 600$ [s] approximately 3.6 % of the energy has been dissipated. The experiments and numerical simulations of Yuen & Lake, Su, Lo & Mei and our own numerical simulations support the concept of interpreting deep water ocean waves as interacting wave groups of permanent form. The simulation of a single confined solitary wave group over a bottom topography is therefore representative to the understanding of the properties of ocean waves heading to shore.

6.2.1 Propagation over an even bottom

To directly compare the results with the results obtained by de Haas (1997) and de Haas *et al.* (1997) the depth is set to $h = 12$ [m], and the carrier wave frequency is given by $\bar{\omega} = \frac{2\pi}{6}$ [rad/s]. The wave number is $\bar{k} \approx 0.12385$ and the wavelength $\lambda \approx 50.73$. The simulation is performed with an initial envelope wave amplitude of 1 [m] and the center of the wave group is positioned at $x = 1500$ [m]. Remark that $kh = 1.486 > 1.363$ and thus a solitary wave solution to the NLS-equation exists.

Using this data the potential is prescribed according to Eq. (6.14) and the corresponding first-order free-surface elevation η_{11} are prescribed as the initial values for the simulation. The numerical parameters used for the simulation are $nx = 6000$, $\Delta x = 1.25$ [m], $nz = 9$, $\Delta t = 0.1$ [s], RK45M time integration and natural boundary conditions were used at both sides (implying full reflection of the waves against these walls). Both the time step as the horizontal mesh width were chosen small in order to accurately represent $2\bar{k}$-waves. For this case, the simulation of a single time step on a 500 [Mhz] Pentium III processor takes approximately 8.4 [s]. A simulation over 500 [s] for this configuration thus takes approximately 12 hours of computer time. The memory usage is approximately 61 [Mb] which poses no severe problem on a contemporary PC computer configuration.

Directly after the simulation was started the envelope of the wave group was observed to start oscillating. Second- and zeroth-order wave components (η_{22} and η_{02}) are bound to the wave group and compensated by generation of their associated free $2\bar{k}$ harmonic waves and nonharmonic solitary wave. The generation of these free waves was also observed by de Haas and can be found in other quadratic free-surface models (cf. e.g. Pelinovsky *et al.* (1999) for a KdV application).

The top plot in Fig. 6.3 on the next page shows the wave elevation at $t = 500$ [s]. The dashed line is the initial wave group envelope and the different free components that can be observed in the upper plot are labelled with (a)-(d) and are shown in more
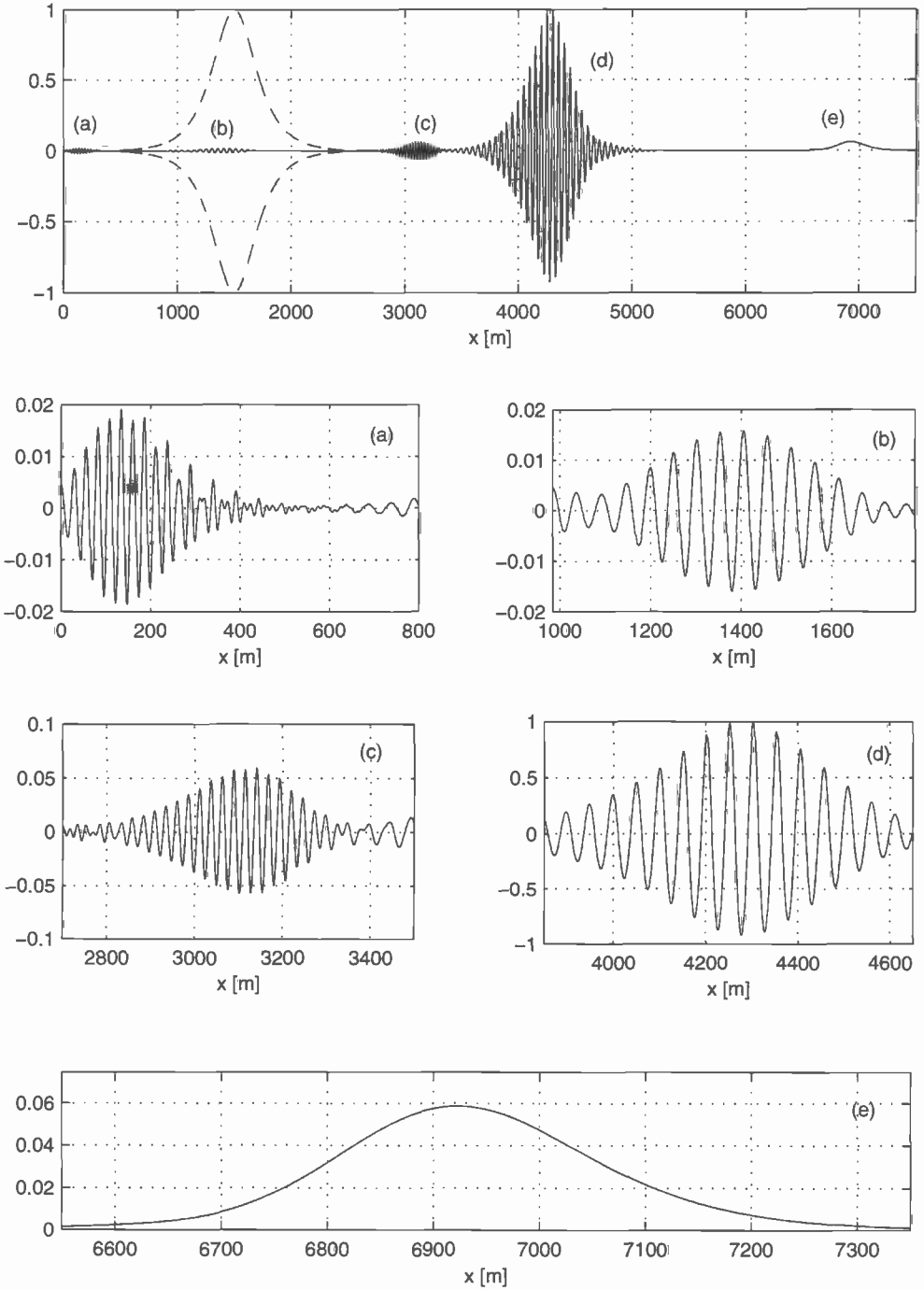
Figure 6.3: *Free-surface elevation at* $t = 500$ *[s] using a first-order confined wave group as initial values. Dashed line in top figure is initial envelope.*
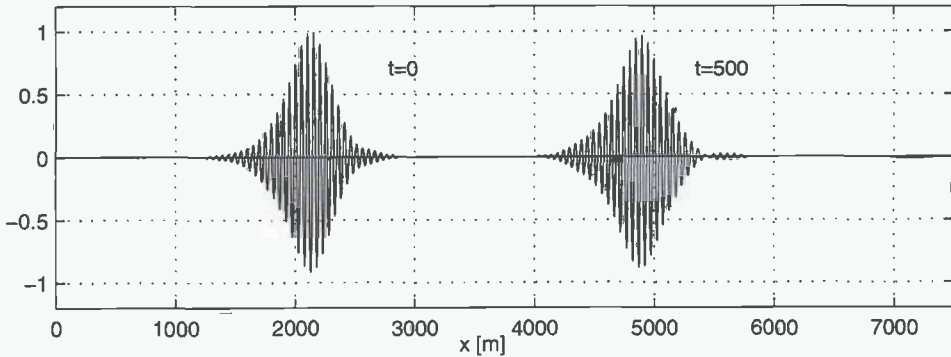
Figure 6.4: *Wave group at t = 0 is isolated from the solution at t = 500 in Fig. 6.3 and used as an initial condition. The elevation at t = 500 [s] using this condition has also been plotted.*

detail in the other plots of the figure. The center of the main group (d) is around $x = 4280$ implying a wave group velocity of approximately speed of 5.56 [m/s] which is slightly faster than the linear group velocity $c_g \approx 5.52$ [m/s]. The central wave group has a bound set-down that was compensated by the free solitary wave (e) which has a phase speed of approximately 10.84 [m/s] which is in good agreement with the critical speed $c_\infty \approx 10.85$. The free $2\bar{k}$ waves that are generated by the adapting wave group are visible in subplot (c) in which it can be clearly observed that the wavelength of the carrier wave in this group is half the original wave length. The group velocity of this wave group is estimated at approximately 3.24 [m/s] which is in good agreement with the linear group velocity for a free $2\bar{k}$ wave of 3.24.

The two other observed free-surface disturbances (a) and (b) are the result of a free $\bar{k}$ wave group and a free $2\bar{k}$ wave group that have propagated to the left after the simulation was started. This is possibly due to the mismatch in potential and thus the mismatch in velocity that was initially imposed. At t=500 [s], the wave group (b) is travelling to the right because it was completely reflected against the wall at $x = 0$ [m]. Based on its position, the average speed of this group must have been approximately 5.80 [m/s] which is considerably higher than the expected speed of approximately 5.56 [m/s]. The left travelling $2\bar{k}$ wave group is just reflecting from the left wall and its speed is estimated to be 3.32 [m/s] which is again slightly faster than the expected speed. A very small negative valued solitary wave was also observed to travel to the left after starting the simulation. At $t = 500$ [s] this wave is not visible because it is just interacting with the main wave group (d). In de Haas *et al.* (1997) different initial conditions (inclusion of higher-order terms and using Taylor series to better approximate the potential at the free surface given the first-order solution) are examined but the above described free waves still emerge from the initial wave group. In order to obtain an initial condition that produces a confined wave group without significant secondary waves, the simulation in Fig. 6.3 is continued for another
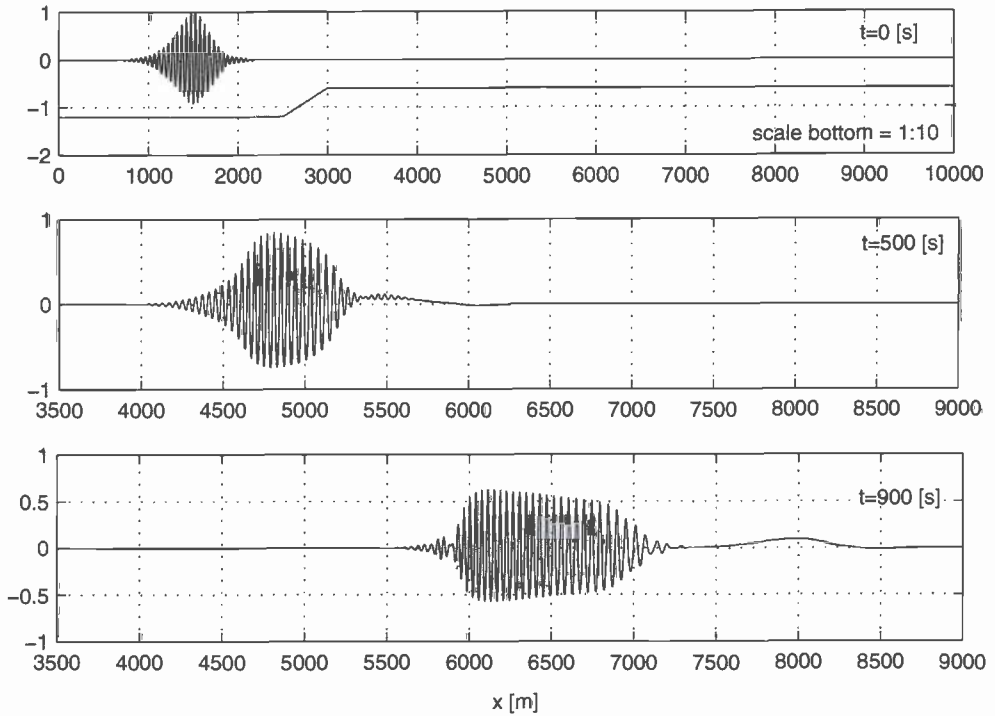
Figure 6.5: *Free-surface elevation of the wave group propagating over the bottom to-pography visualised (scale 1:10) in the upper plot.*

100 seconds after which the central group is considered to be fairly isolated from all secondary free waves. The wave group potential and free surface are then 'cut' and used as new initial conditions when centered around $x = 2120$ [m]. The free surface of this initial condition and the elevation after another 500 [s] of simulation are plotted in Fig. 6.4 on the facing page. From this figure it can be observed that there are still some spurious waves emerging from the wave group. However, significantly less disturbances are present than in the original simulation. It is also observed that the group does not appear to remain symmetric and slightly flattens. Despite these minor shortcomings the initial condition obtained from 'cutting' the solution of the previous calculation can be used as a practical initial condition for examination of the effect of an uneven bottom.

6.2.2   Propagation over a slope

The evolution of a stationary wave group is examined when the bottom is slowly (with respect to the carrier wave length) raised. The depth is constant at $h = 12$ [m] from $x = 0$ to $x = 2500$ [m] and increases linearly to $h = 6$ [m] from $x = 2500$ [m] to

$x = 3000$ [m]. As an initial condition the 'cut' wave group from the previous subsection is used and now positioned at $x = 1500$ [m]. The length of the computational domain was increased to $10,000$ [m] and thus $nx = 8000$ grid points are used in the horizontal direction. All other numerical parameters are kept identical. The simulation time is extended to $t = 900$ [s] which resulted in a computational time of 28 hours on a Pentium III 500 [Mhz] PC and approximately 82 [Mb] of memory resources were used.

The resulting wave elevation of the wave group propagating over this bottom topography is plotted for two different time steps in Fig. 6.5 on the page before. The top plot shows the initial solitary wave group (scale 1:1) and the bottom topography (scale 1:10). The two other plots in Fig. 6.5 show the wave group at $t = 500$ [s] and $t = 900$ [s]. At $t = 500$ [s], the wave group has propagated almost 2 [km] over the new depth and it can be observed that the group is flattening and widening. Because on the new depth $h = 6$ [m] the wavelength is $\lambda \approx 42$ and therefore $kh \approx 0.922 < 1.363$. The NLS-equation describing the envelope of the wave group is no longer self-focussing and therefore the energy is spread over the group instead of focused in the center. This is in agreement with the observed shape of the wave group for $t = 900$ [s] and with the observations of Barnes & Peregrine (1995). The decreasing depth thus leads to a drop of the maximum wave height. Another remarkable phenomena that can be observed from Fig. 6.5 is the long free solitary wave that is generated from the adapting wave group. In front of this wave a very small depression of the elevation of approximately 0.02 [m] is observed. The length of this solitary wave is of the same order as the length of the confined wave group and its amplitude is approximately 0.1 [m].

6.3 Bichromatic wave groups

A bichromatic wave group is the periodic signal resulting from the linear superposition of two regular waves with different frequencies (bichromatic). Consider the superposition of two regular waves with frequencies ω_1 and ω_2 and equal amplitude q

$$
\begin{aligned}
\eta(x,t) &= q\cos(k_1 x - \omega_1 t) + q\cos(k_2 x - \omega_2 t) &\qquad (6.16) \\
&= 2q\cos\left(\frac{1}{2}(\Delta k x - \Delta\omega t)\right)\cos(\bar{k}x - \bar{\omega}t) &\qquad (6.17) \\
&= A(x,t)\frac{1}{2}\left(e^{i\bar{\theta}(x,t)} + c.c.\right) &\qquad (6.18)
\end{aligned}
$$

where $\Delta k = k_1 - k_2$, $\Delta\omega = \omega_1 - \omega_2$, $\bar{k} = \frac{k_1+k_2}{2}$, $\bar{\omega} = \frac{\omega_1+\omega_2}{2}$ and $\bar{\theta}(x,t) = \bar{k}x - \bar{\omega}t$. From Eq. (6.17) it is observed that the wave group can be interpreted as a carrier wave $(\bar{k}, \bar{\omega})$, modulated by an envelope wave $(\Delta k, \Delta\omega)$. The phase speed of this latter wave envelope is $\frac{\Delta\omega}{\Delta k}$ and is referred to as the wave group velocity of the bichromatic wave.

Although for many practical purposes linear theory produces satisfactory approximations of the underlying nonlinear process, this is not the case for the propagation of

certain classes of bichromatic waves. This was clearly demonstrated by Stansberg (1997) in which an experimental study in a wave tank was reported. The measured wave groups that were generated using only two frequencies, showed large deviations from linear theory at some distance from the wave maker.

These observations motivated the investigations presented here for the following reasons. Firstly, the observed profoundly nonlinear wave behavior provided an interesting test case for the fully nonlinear wave simulations. Not only could be investigated to what extent the results can be reproduced numerically, but the numerical simulations can be extended over a much larger domain (cf. Westhuis *et al.* (2000)). Secondly, the numerical simulations would provide valuable information for the development and benchmarking of analytical wave models (e.g. van Groesen *et al.* (2001) and Suryanto *et al.* (2001)). In contrast to measurements, the numerical simulation provides high resolution spatial information and parameters can be easily varied. The cost of numerical simulations is also a fraction of actual experiments in a wave tank. Thirdly, the evolution of (extreme) bichromatic waves is also of direct interest for the hydrodynamic laboratory. It is an extreme but relevant example that shows the non-stationarity of the wave spectrum with respect to the length scale of the model basin. The extreme nonlinearity can however also be used to control the generation of freak waves.

In the next sections the results of both experimental as numerical simulations on a variety of bichromatic wave groups are presented. In Subsection 6.3.1 the experimental setup and results will be described in detail. The next subsection (6.3.2) describes the numerical simulations that have been performed. It will be shown that numerical and experimental data are in good mutual agreement. Next, the numerical simulations are carried out over an extended spatial domain and the observed recurrence and wave group envelope dynamics will be presented and discussed.

In Subsection 6.3.3 the observed nonlinear dynamics will be related to the Benjamin-Feir instability and NLS-theory. From these relations a parameter is motivated that governs the non-stationarity of the nonlinear bichromatic wave group evolution.

6.3.1   Measurements

The experimental results presented in Stansberg (1997) consisted of the time signals of a bichromatic wave train at different positions. Using the same wave data, these experiments were in first instance simulated numerically using the fully nonlinear method described in this thesis and the results showed good qualitative agreement. Next, the initial wave data was slowly varied and the numerical simulations were repeated to see the effect of wave amplitude and frequency differences. Based on these numerical results, a series of experimental investigations was setup to validate the observed asymmetries and focussing of the wave group. Also, these carefully controlled experiments could be used for direct comparison with the results from numerical simulations.
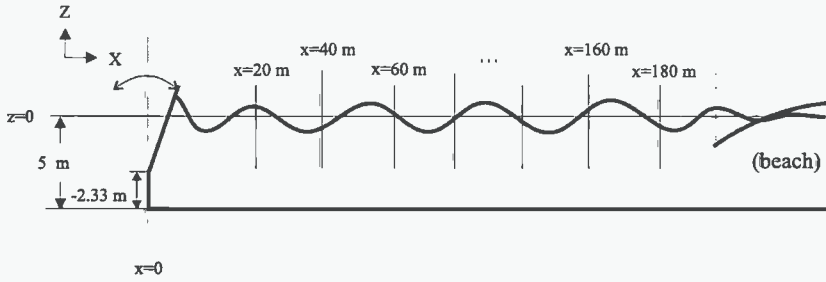
Figure 6.6: *Scaled sketch of the experiment setup performed at the MARIN high speed basin (actual depth h=3.6 [m]). The wave elevation was measured at the center line of the tank at $x = 0$, 10, 40, 60, ... , 180 [m] and at $x = 80$ [m] and $x = 120$ [m] at $\frac{1}{4}$ of the tank width.*

The measurements on bichromatic wave groups were performed at the High Speed Basin at MARIN and have been reported by Westhuis & Huijsmans (1999). A schematic sketch of this facility and the position of the measurement probes is depicted in Fig. 6.6. In order to measure the spatial evolution of the travelling wave group, resistance type wave probes were positioned at $x = 0$ [m], $x = 10$ [m] and $x = 40, 60, ... , 180$ [m] at the centerline of the tank. At $x = 80$ [m] and $x = 120$ [m], additional probes were positioned at $1/4$ of the tank breadth to investigate possible 3D effects. The probe at $x = 0$ [m] is mounted on the wave generator and thus measures the run-up against the wave board. The time interval during which the signals were measured is 700 [s]. Data was acquired on model scale at a sample frequency of 50 [Hz], which corresponds to a sample frequency of $50\sqrt{3.6/5}$ [Hz] at $h = 5$ [m].

The steering signal Eq. (6.19) for the stroke of the flap was sent directly to the wave maker and is strictly bichromatic

$$S(t) = R(t) \left(\bar{q}_1 \cos(\omega_1 t) + \bar{q}_2 \cos(\omega_2 t) \right), \tag{6.19}$$

so no second-order wave maker theory was used to correct the signal. Using the linear theory from Chapter 4 the value of $\bar{q}_i$ is related to the desired value of the wave amplitude q_i. In Table 6.1 on the next page the experiments performed for different combinations of periods T_1 and T_2 and the amplitudes $q_1 = q_2 = q$ are summarised. All experiments and simulations were performed around the central period $T = 2$ [s].

$$T_1 = T - \frac{1}{2}\Delta T \tag{6.20}$$

$$T_2 = T + \frac{1}{2}\Delta T \tag{6.21}$$

For future reference and to interpret the results in scaled variables, we note that for $T = 2$ one can identify $\frac{\Delta\omega}{\bar{\omega}} = \frac{1}{2}\Delta T$ and $ka \approx q$.

The experiments and numerical simulations for $q = 0.08$ [m] and $\Delta T = 0.2$ [s] correspond to the experiment reported by Stansberg (1997). The performed measurements

	ΔT = 0.4		ΔT = 0.3		ΔT = 0.2		ΔT = 0.15		ΔT = 0.1	
	E	S	E	S	E	S	E	S	E	S
$q = 0.03$						×			×	×
$q = 0.04$		×				×	×	×	×	×
$q = 0.05$				×	×	×	×	×	×	×
$q = 0.06$	×	×		×	×	×	×	×	×	×
$q = 0.07$				×	×	×	b	b	b	b
$q = 0.08$	×			×	×	×	b			b
$q = 0.09$					b	b	b			b
$q = 0.10$	×									

Table 6.1: *A × marks the bichromatic wave experiment (E) or a numerical simulation (S) with the periods $T_i = 2 \pm \Delta T/2$, and amplitude q that were performed. (b) indicates that the experiment/simulation was performed but that either wave breaking was observed in the wave tank or that the numerical scheme was terminated due to onset of breaking.*

are in the columns identified by (E) and cells marked with (×). When wave breaking was observed during the experiment, the cell is marked with (b). The wavelength of the carrier wave of the linear wave group is almost the same for all experiments and satisfies ($L \approx 6 = 1.25h$). After the transient start-up effects have passed, the time signals at all probe-positions, showed that the signals are periodic in the modulation period $T_{mod} = \frac{T_1 T_2}{\Delta T}$. Because in all experiments and numerical simulations $T = 2$ [s], the modulation period is $T_{mod} = \frac{4}{\Delta T} - \frac{1}{4}\Delta T$. Examination of the signals from the probes that were placed at $\frac{1}{4}$ tank breadth at $x = 80$ [m] and $x = 120$ [m] showed no signs of standing waves across the breadth of the tank for any of the experiments.

For small initial amplitudes the wave elevation differs only very little from linear theory. Figs. 6.7-6.10 show part of the time traces of the free-surface elevation at the different positions in the tank for the highest amplitude waves for every tested combination of (T_1, T_2). For $(T_1, T_2)=(1.8,2.2)$ [s] and $q = 0.1$ [m], Fig. 6.7 on page 185 shows that the wave group appears to have a fairly constant shape at the different positions in the tank. Although locally steep waves ($H/\lambda \approx 0.09$) are measured, they do not give direct indications for asymmetries of the evolving wave group. When the period difference is however slightly decreased to $(T_1, T_2)=(1.9,2.1)$ [s] (see also Fig. 6.8) the symmetry of the wave group clearly breaks. Steepening at the front of the wave group is observed as a prelude to the apparent splitting of the group in two wave groups. At $x = 80$ [m] a local extreme wave can be observed also with a steepness of approximately 0.09. However, examination of the video's of the experiment showed

spilling breakers indicating the presence of even steeper waves.

A similar breaking of the symmetry and the appearance of a second wave group is visible in the results presented in Fig. 6.9 on page 187. The combination (T_1, T_2)=(1.925,2.075) [s] with $q = 0.09$ [m] shows similar envelope evolution as (T_1, T_2)=(1.9,2.1) [s], $q = 0.09$ [m], but at a slower spatial pace. Remark also that if a ship model would have been positioned at $x = 100$ [m], it would experience almost no significant wave heights (< 0.05 [m]) for approximately 8 seconds. Then, within 4 seconds a 0.55 [m] high wave passes the ship after which the wave height drops to 0.25 [m] and then slowly decreases to the initial calm situation in about 13 seconds. Such a wave system can thus be used to repeatedly measure the effect of a steep wave impact on the model. The periodicity of the event allows to obtain enough data to apply accurate statistics. Both in these measurements as in the previous measurements, the maximum measured wave height exceeds the prediction of linear theory by more than 150 %.

In Fig. 6.10 on page 188 the time signals are plotted for (T_1, T_2)=(1.95,2.05) [s] and $q = 0.07$ [m]. This figure confirms the same wave group envelope deformation process of steepening and shows the possible onset of splitting. Again, the spatial pace at which the deformation is observed is slower than in the previous figures. Remark the resemblance of the wave group envelope at $x = 60$ [m] in Fig. 6.8, at $x = 80$ [m] in Fig. 6.9 and at $x = 140$ [m] in Fig. 6.10. It is noticed however that the maximum wave height measured in Fig. 6.10 on page 188 is approximately the same as for the other two experiments while the initial amplitude is lower. This indicates that for the other experiments, the steepening of the wave group was interrupted by breaking. Therefore smaller initial amplitudes can lead to a higher ratio between the maximum measured wave height and linear prediction which is confirmed by the experiments. Although in some of the experiments breakers have been observed, these breaking events were typical spilling breakers that do not dissipate much energy.

6.3.2   Numerical simulations

Numerical simulations have been performed using the same initial data as for the experiments described in the previous subsection. It should be noted that during the investigations, these numerical simulations were performed prior to the experiments that were used to verify the numerical predictions. The numerical simulations were performed with the following numerical parameters: $h = 5$ [m], $g = 9.81$ [m/s^2], $\Delta x = 0.2$ [m], $L = 200$ [m], $nz = 9$, $\beta = 1$, $\Delta t = 0.1$ [s], RK45M time integration, p[FEM]=1 and p[FD]=2. The flux-displacement wave generator (Section 4.3.1) was used with the consistency parameter set to zero, implying that only flux is generated through the boundary and no physical displacement of the wave maker. The l and d flap parameters (see also Section 4.1) are identical to the wave generator of the basin used for the experiments. The vertical grid density parameters are set to $\beta_1 = 0$, $\beta_2 = 1$ and 5 grid points are used on the flap. The effect of using different values
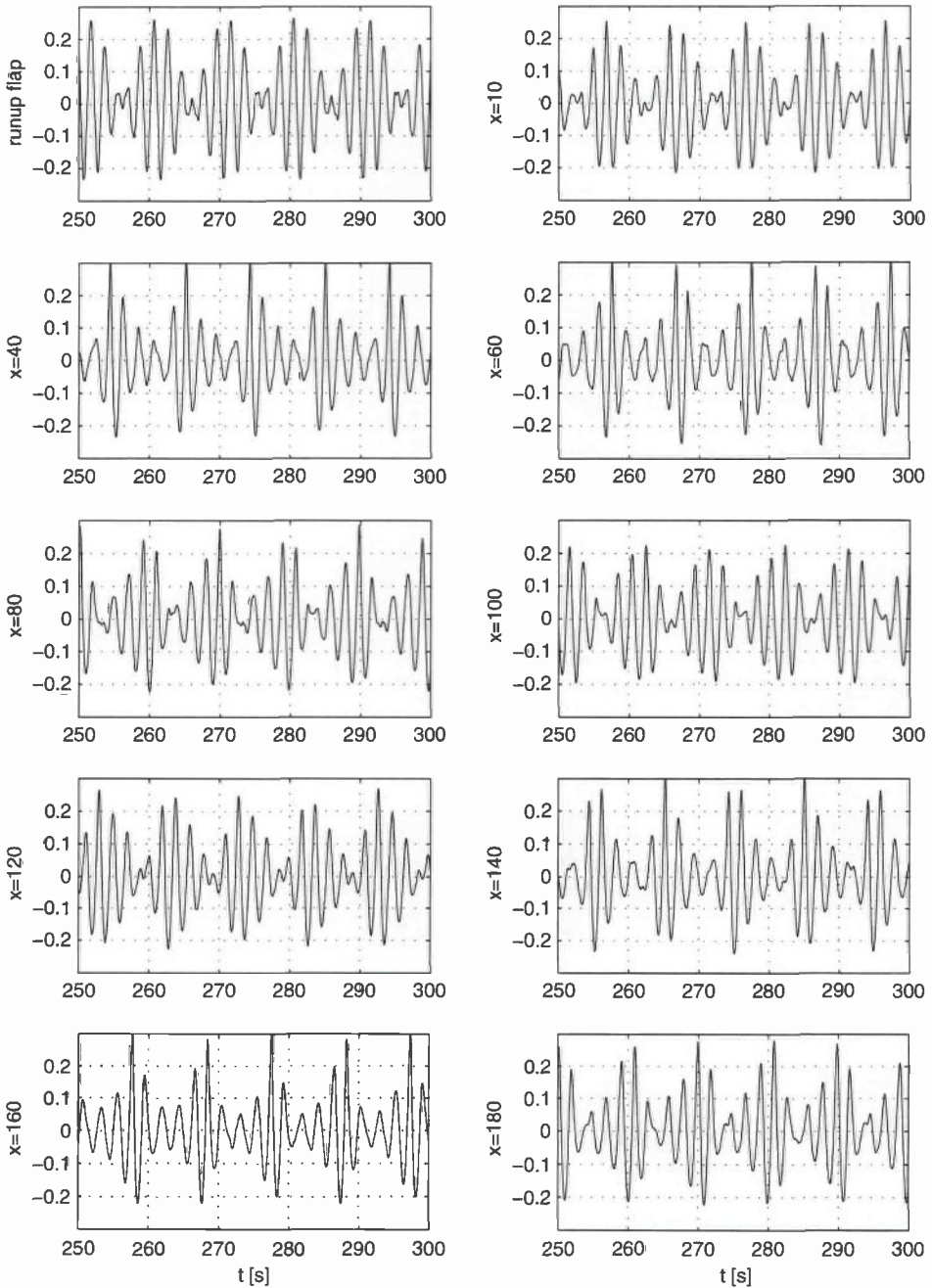
Figure 6.7: *Measured wave elevation of bichromatic wave ($\Delta T = 0.4$ [s], $q = 0.10$ [m]) at different positions in the tank. ($T_1 = 1.8$ [s], $T_2 = 2.2$ [s], h=5 [m], MARIN test no. 6371), no breaking waves observed)*
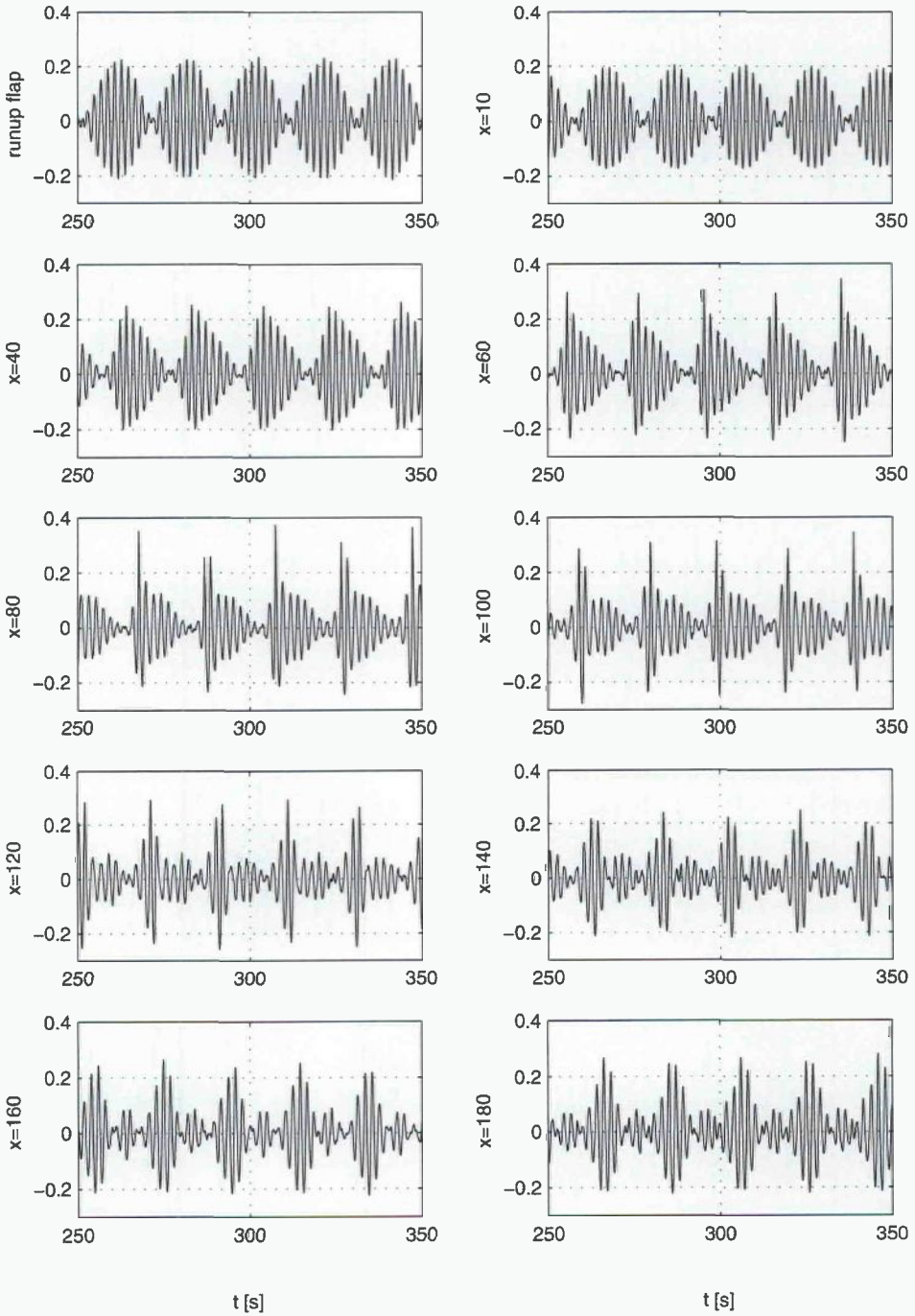
Figure 6.8: *Measured wave elevation of bichromatic wave ($\Delta T = 0.2$ [s], $q = 0.09$ [m]) at different positions in the tank. ($T_1 = 1.9$ [s], $T_2 = 2.1$ [s], $h=5$ [m], MARIN test no. 6376), breaking waves were observed)*
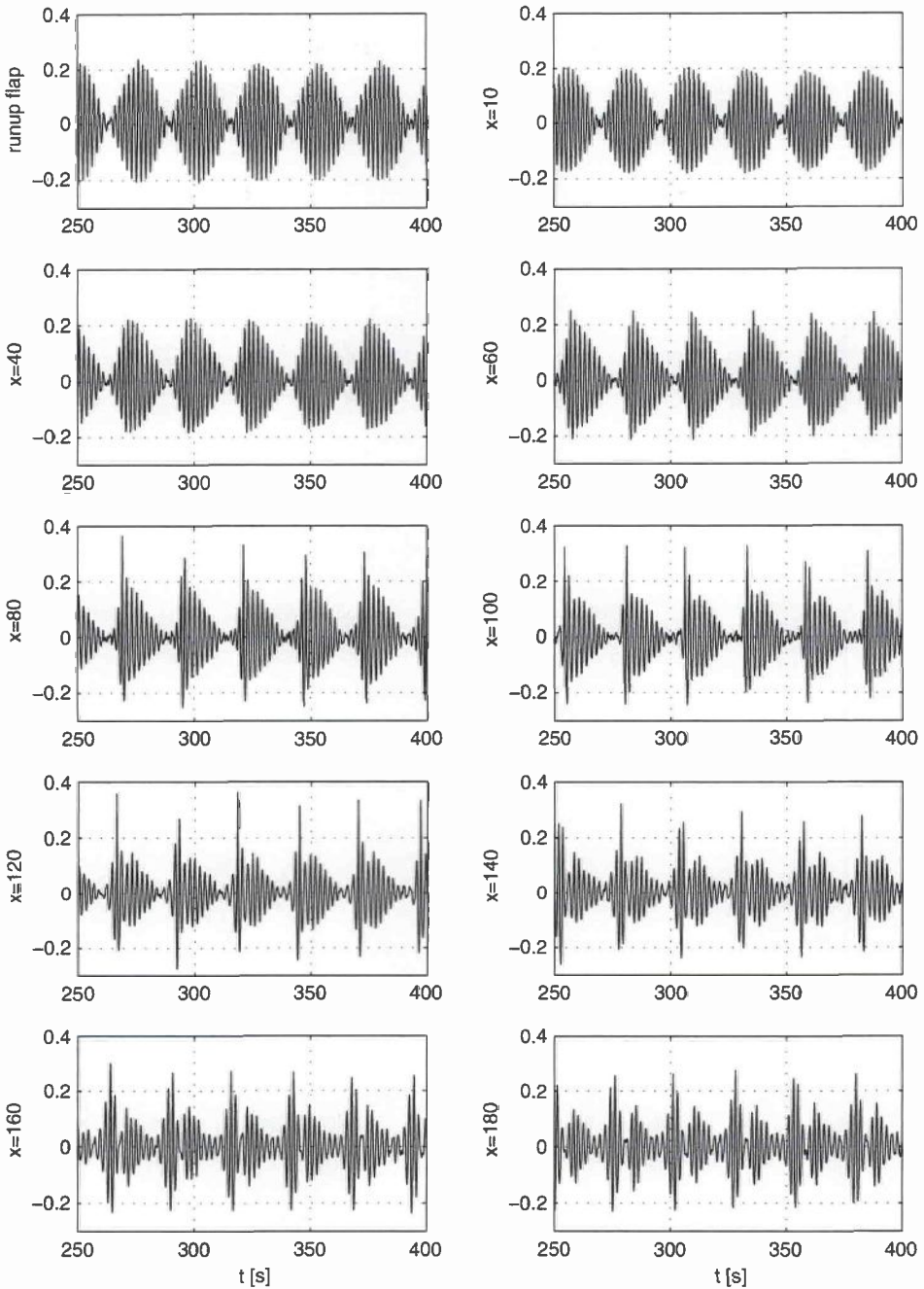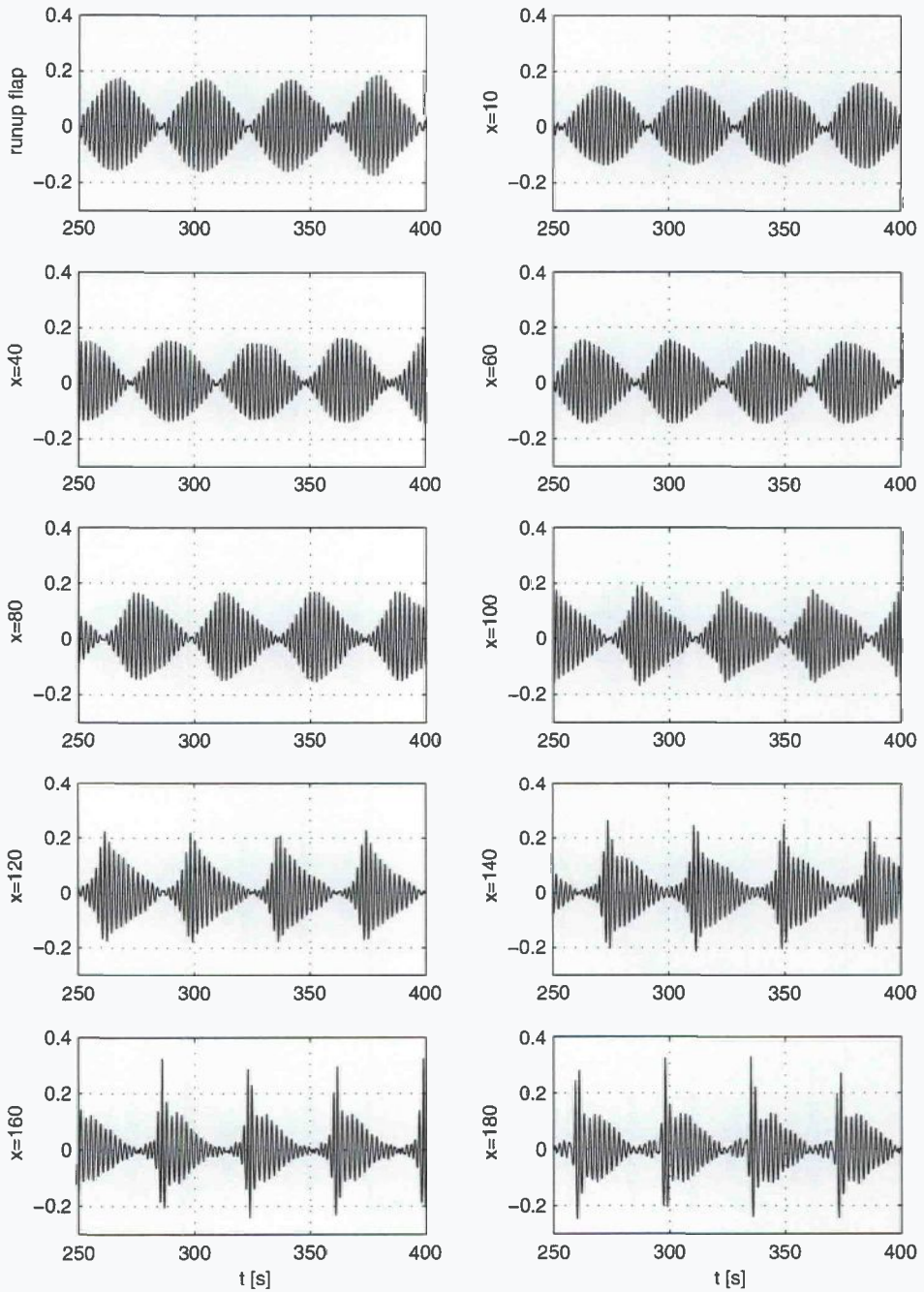
Figure 6.9: *Measured wave elevation of bichromatic wave ($\Delta T = 0.15$ [s], $q = 0.09$ [m]) at different positions in the tank. ($T_1 = 1.925$ [s], $T_2 = 2.075$ [s], $h=5$ [m], MARIN test no. 6382), breaking waves were observed)*

Figure 6.10: *Measured wave elevation of bichromatic wave ($\Delta T = 0.1$ [s], $q = 0.07$ [m]) at different positions in the tank. ($T_1 = 1.95$ [s], $T_2 = 2.05$ [s], $h=5$ [m], MARIN test no. 6387), breaking waves were observed)*

of the consistency parameter have been investigated and except for phase-differences, the data is in mutual agreement. The steering signal sent to the numerical wave maker is identical to the signal used for the experiments (Eq. (6.19) on page 182). The linear ramp function

$$R(t) = \begin{cases} t/t^* & 0 \leq t \leq t^* \\ 1 & t > t^* \end{cases} \tag{6.22}$$

was used to slowly increase the wave maker to avoid large initial accelerations. For the absorbing beach the optimal configuration described in Section 5.5.2 was employed. The optimal beach was used instead of a model because no measurement data was available on the artificial beach in the basin. Furthermore, the investigations of this chapter are more concerned with the properties of evolving wave groups, rather than with the simulation of the beaches. Therefore the effect of reflections is kept as low as possible. The simulations over an effective tank length of 200 [m] ($= 40h \approx 30\lambda$) use approximately 11 [Mb] of memory. On a single 500 [Mhz] Pentium III processor every 5 minutes of simulation time ($= 150T$) takes about 1 hour of computational time.

Using this configuration, all numerical simulations were found to be stable for as long as the simulations were continued. The numerical beach has been translated to investigate this effect on the time signals, but no deviations were found. The combinations of parameters (T_1, T_2) and q for which a numerical simulation has been performed can be found in Table 6.1. It is noted again that during the investigations, these numerical simulations preceded the physical experiments. The amplitude and period parameters of these experiments were chosen based on the numerical simulations.

Comparison with measurements

In Fig. 6.11 on the following page the time signals of the evolving wave group using $(T_1, T_2) = (1.9, 2.1)$ and $q = 0.08$ [m] are plotted. The solid lines represent the measured wave elevation and the dots are the results of the numerical simulation. The interval of the horizontal axis in the consecutive plots is shifted using the linear group velocity of the wave group. Remark that the speed of the wave group is slightly faster than the linear wave group velocity. Because of the differences in the start-up function and the flux model that were used for wave generation, the phases of the signals are not aligned and one of the phases needs to be adapted. The additional time-shift, added to the computational signal was determined such that the wave group zero-crossings fitted at $x = 40$ [m]. As can be observed, the asymmetry of the wave group is very well predicted by the numerical simulation for $x = 40$ until $x = 100$ [m]. At $x = 120$ [m] and $x = 140$ [m] the numerical simulations appear to overpredict the wave behind the peak-wave, although further downstream the agreement becomes better again.

To investigate the agreement in more detail the power spectra of the measured and
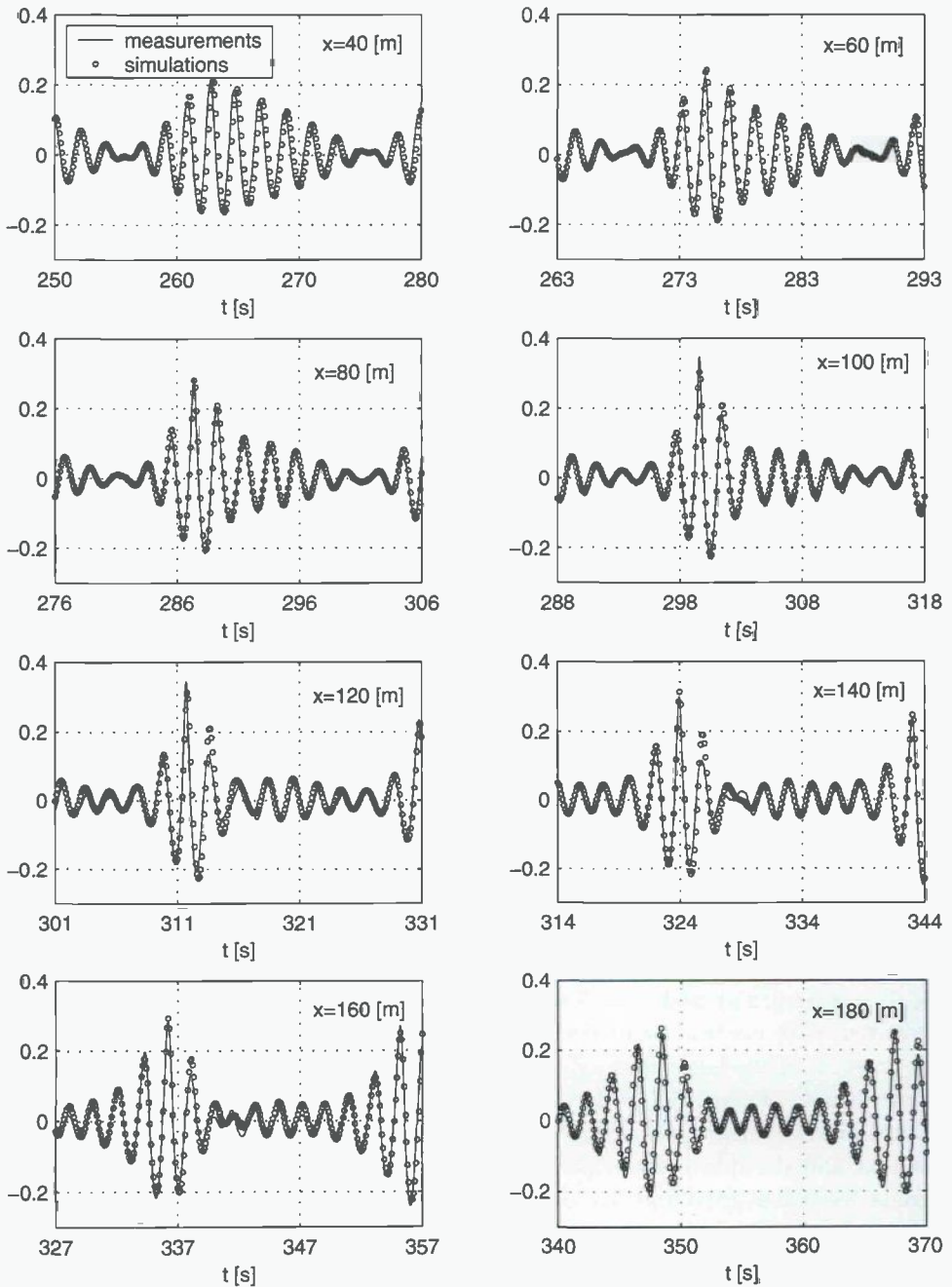
Figure 6.11: *Experiments (solid line) and numerical simulation (dots) for a strongly nonlinear bichromatic wave, $T_1 = 1.9$ [s], $T_2 = 2.1$ [s], $q = 0.08$ [m], h=5 [m], g=9.81 [ms^{-2}]*

numerical signal are compared. The model scale sampling frequency of the experiment
was 50 [Hz] and the sampling frequency at SMB scale is thus approximately 42.42
[Hz]. For the comparison of the spectra, the experimental data is resampled by
skipping every three measurements, thus resulting in time signals with a sampling
frequency of approximately 10.61 [Hz]. The time-step between two successive data-
points of the resampled signal is now quite close to the numerical time step $\Delta T = 0.1$.
To determine the power spectral density accurately, an interval of length 300 [s] of
the periodic signal is taken and divided in 10 overlapping intervals containing 2048
data points, resulting in a spectral resolution of approximately 0.0307 [rad/s] for the
simulations and 0.0325 for the measurements. These signals are then detrended and
windowed (Hanning window) and standard spectral analysis is performed to obtain
power spectral density estimates. These 10 estimates are then averaged to obtain
the final, more accurate, estimate. In Fig. 6.12 a log-plot of the spectral densities
of the measurement and the numerical simulation are plotted for the wave group of
Fig. 6.11. From Fig. 6.12 it can be observed that at $x = 10$ [m] the power density of
the two spectra are in good agreement except for the high frequencies around $\omega = 8.5$
[rad/s]. Further downstream the results are in excellent agreement for the whole range
of frequencies. At $x = 120$ [m], the energy is spread over a wide range of frequencies,
mostly to the higher sidebands. The results also show that the energy in the second-
order wave components does not exceed 1% of the energy of the original primary
bichromatic components. The primary sidebands however, may grow significantly to
the same order as the primary waves themselves.

Prolongation of the domain

The wave signals from the experiments and simulations in the previous paragraphs
showed significant deformation of the wave group envelope for $0 \leq x < 180$ [m]. Be-
cause of the excellent agreement of numerical and experimental results, it is expected
that the numerical simulations can also accurately predict the evolution over longer
domains. The computational effort of the numerical method increases linear with
simulation time and tank length. The computational domain is prolonged by a factor
of 5 and the evolution is simulated for 900 [s] (=450 T). Such a case requires approx-
imately 61 [Mb] of memory and takes 21 hours on a Pentium III 500 [Mhz] PC. The
results of these simulations are presented in figures 6.13-6.16.

The upper two plots of Fig. 6.13 on page 193, $(T_1, T_2) = (1.8, 2.2)$, show the power
spectrum density estimate of the periodic time signals at different positions in the nu-
merical tank. It can be clearly observed that there is no significant energy transfer to
the sidebands for both amplitudes. The evolution of this bichromatic wave is therefore
almost completely linear. In the lower three figures the spectrum of the bichromatic
wave $(T_1, T_2) = (1.85, 2.15)$ is shown at different positions. The appearance of the
sideband energy is clearly visible for $q = 0.08$ [m]. The lower figure shows the values
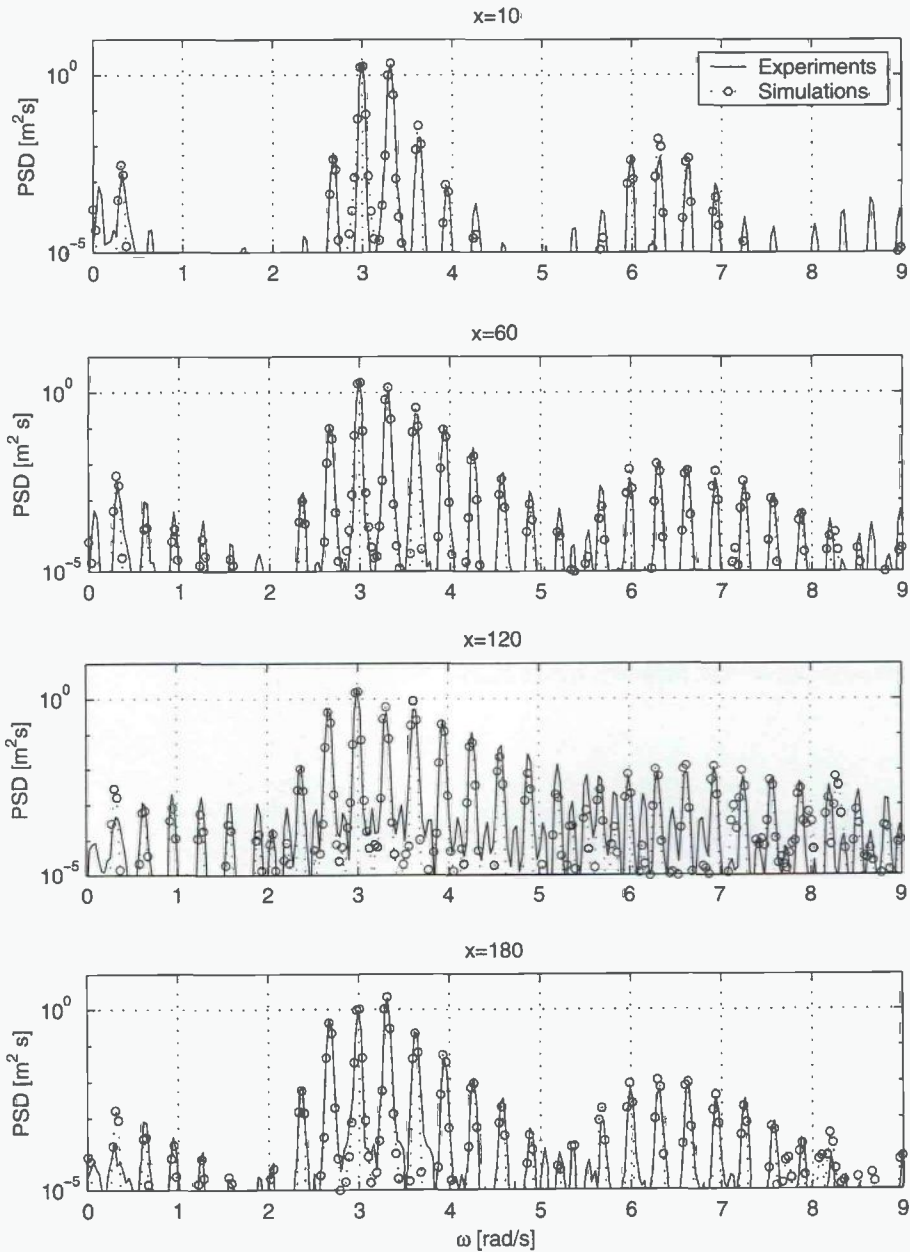
Figure 6.12: *Log-plot of power spectral density estimates of free surface at different locations. Experiments (dotted line with markers) and numerical simulation (solid line without markers) (wave data as in Fig. 6.11)*
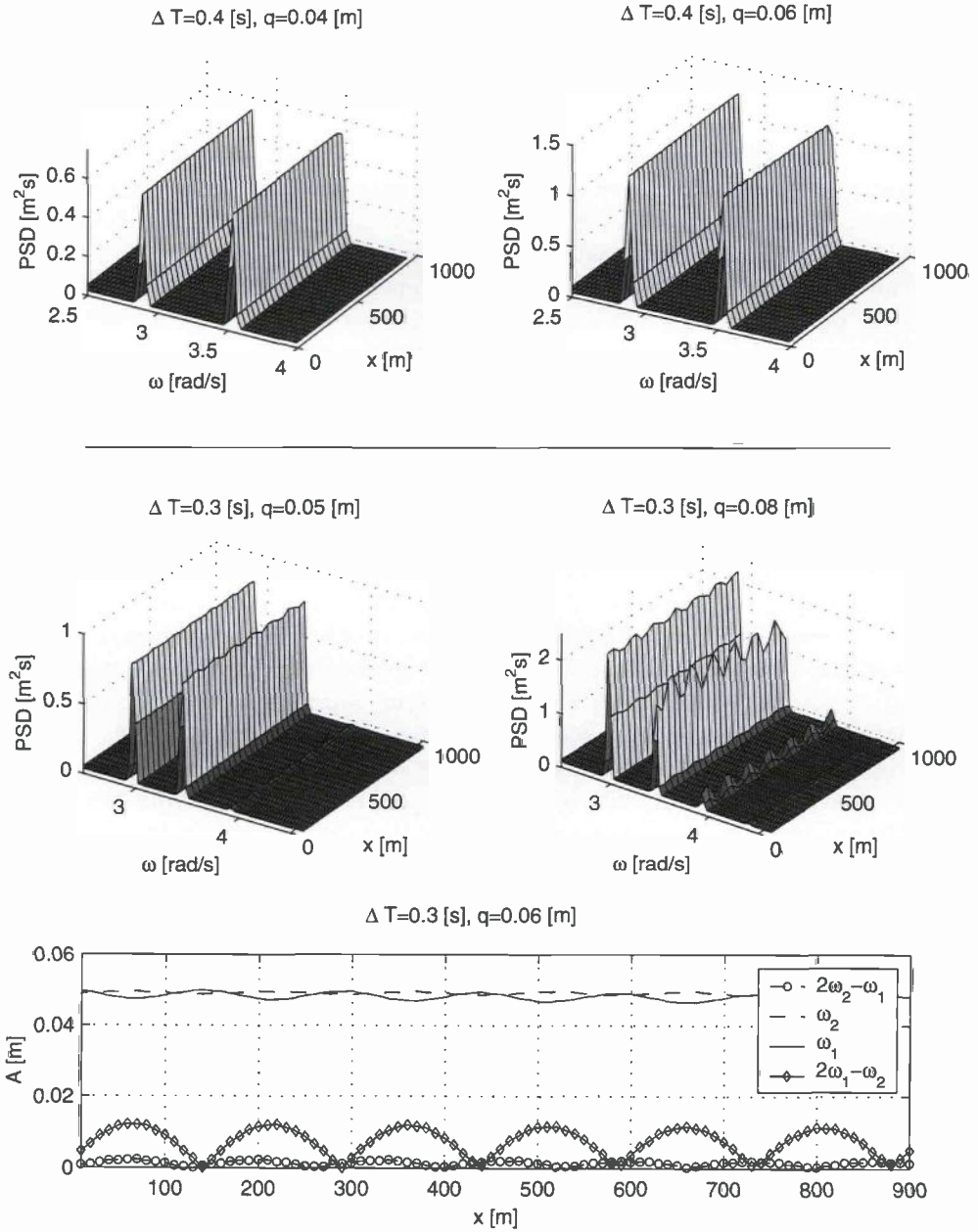
Figure 6.13: *Power spectral density of the periodic wave elevation signals at different positions along the numerical tank. The lower figure shows the integrated PSD associated with the primary bichromatic waves and bichromatic side bands.*

of

$$a_i(x) = \sqrt{2 \int_{\omega_i - \frac{1}{2}\Delta\omega}^{\omega_i + \frac{1}{2}\Delta\omega} \mathrm{PSD}(\omega, x) d\omega} \qquad (6.23)$$

where the range of integration is such that the energy content can be identified with a discrete sideband. The coefficients a_i can be interpreted as the amplitude of the discrete wave component with frequency ω_i. From the lower plot in Fig. 6.13 on the preceding page it can be observed that the energy transfer appears periodic in space. Careful examination however reveals that the upper and lower sideband do not have the same period and therefore there is no exact recurrence. The steady periodicity remains remarkable and is not a consequence of the numerical method but a feature of the dynamic equations. It is also noticed that the relative amplitude of the sidebands to the amplitude of the primary bands increases with q.

In Fig. 6.14 on the next page the results of the simulations for $(T_1, T_2) = (1.9, 2.1)$ are summarised. For the small initial amplitudes $q \leq 0.06$, the spatial periodicity of the sideband amplitudes is observed. As was also noted for $(T_1, T_2) = (1.85, 2.15)$, the spatial period of the $2\omega_2 - \omega_1$ is not identical to the period of $2\omega_1 - \omega_2$. With increasing amplitude the period of the $2\omega_2 - \omega_1$ sideband increases, while that of the $2\omega_1 - \omega_2$ decreases. For $q = 0.06$ [m], one can also observe that the second upper sideband $3\omega_1 - 2\omega_2$ becomes significant and its spatial period appears to follow that of $2\omega_2 - \omega_1$. The second lower sideband contains almost no energy and even for $q = 0.08$ one can observe that almost no energy is present in this band. For this large ($q = 0.09$ leads to breakers) value of q, the simple periodicity is lost and a more complicated pattern arises. With some imagination, one observes a symmetry around $x = 560$ [m] for all energy components. Remark that the energy transfer between the different bands has lead to the fact that at some points the energy of the side band is larger than the energy of the primary band. The lower figure shows a density plot of the power spectral density estimate for $q = 0.08$ [m] from which it is observed that the energy is still well separated in the different bands and the possible symmetry around $x = 560$ [m] can be observed. The results are in qualitative agreement with the numerical predictions of Lo & Mei (1985) using Dysthe's equation.

Fig. 6.15 on page 196 shows that for $q = 0.04$ [m] almost complete recurrence appears to be attained. For this specific configuration of q and (T_1, T_2), the periods of the lower and upper sidebands appear identical. Based on the results of the previous simulations, it appears however likely that even further downstream the periods will show to be slightly different. It is further noticed that the evolution of the modes appears similar with the results of Fig. 6.14 on the next page. Examine for example the spatial interval $[0, 900]$ for $q = 0.06$ [m] in Fig. 6.15 with the interval $[0, 510]$ for $q = 0.08$ [m] in Fig. 6.14.

Fig. 6.16 on page 197 shows that for higher values of q the evolution of even the main frequencies cannot be considered sinusoidal. Although some similarity with previous figures is again observed for the smaller values of q. The difference with the lower
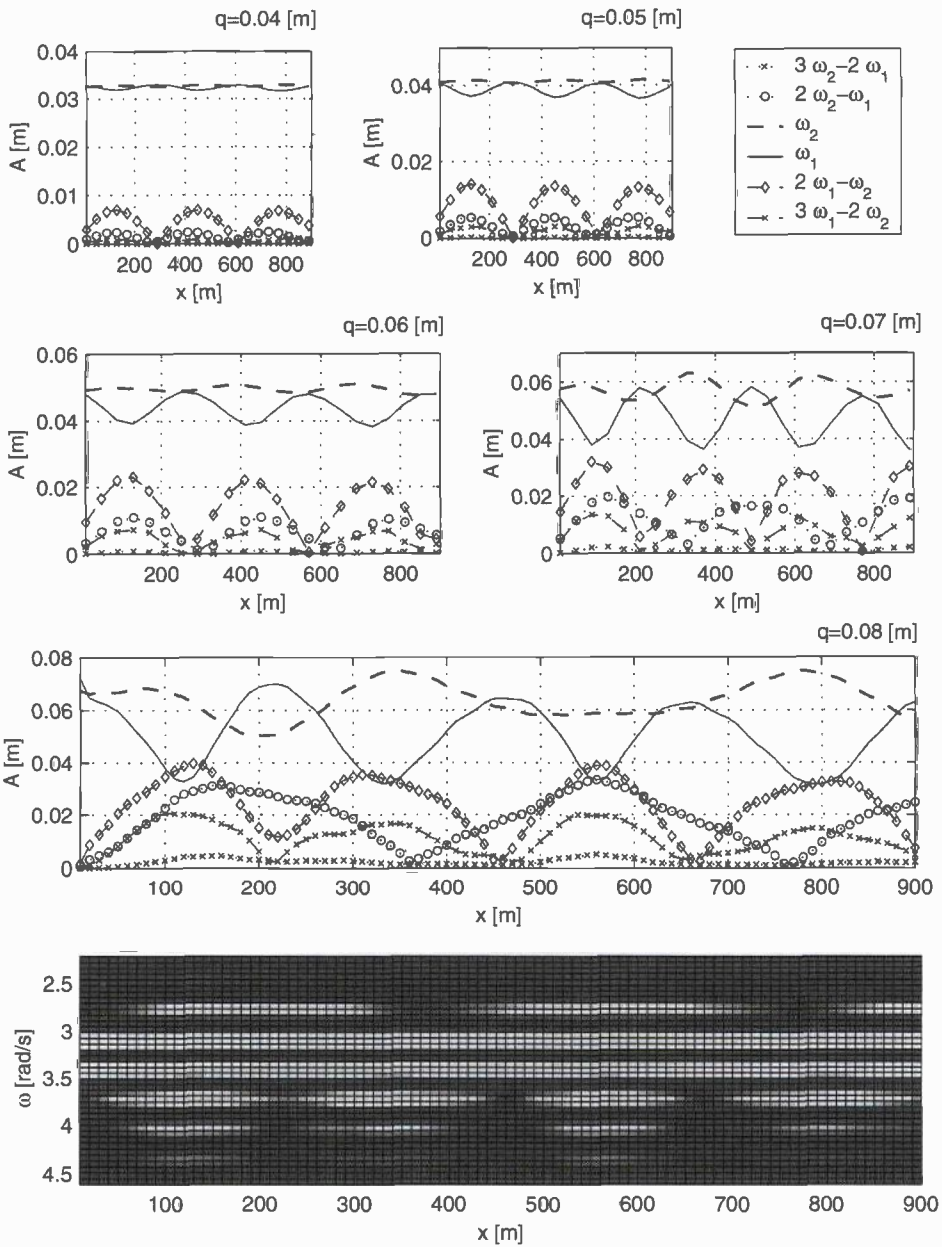
Figure 6.14: *Spatial evolution of the amplitudes of the bichromatic sidebands for the simulations with $T_1 = 1.9$, $T_2 = 2.1$. Lower plot shows a density plot of the power spectral density estimate for $q = 0.08$ [m].*
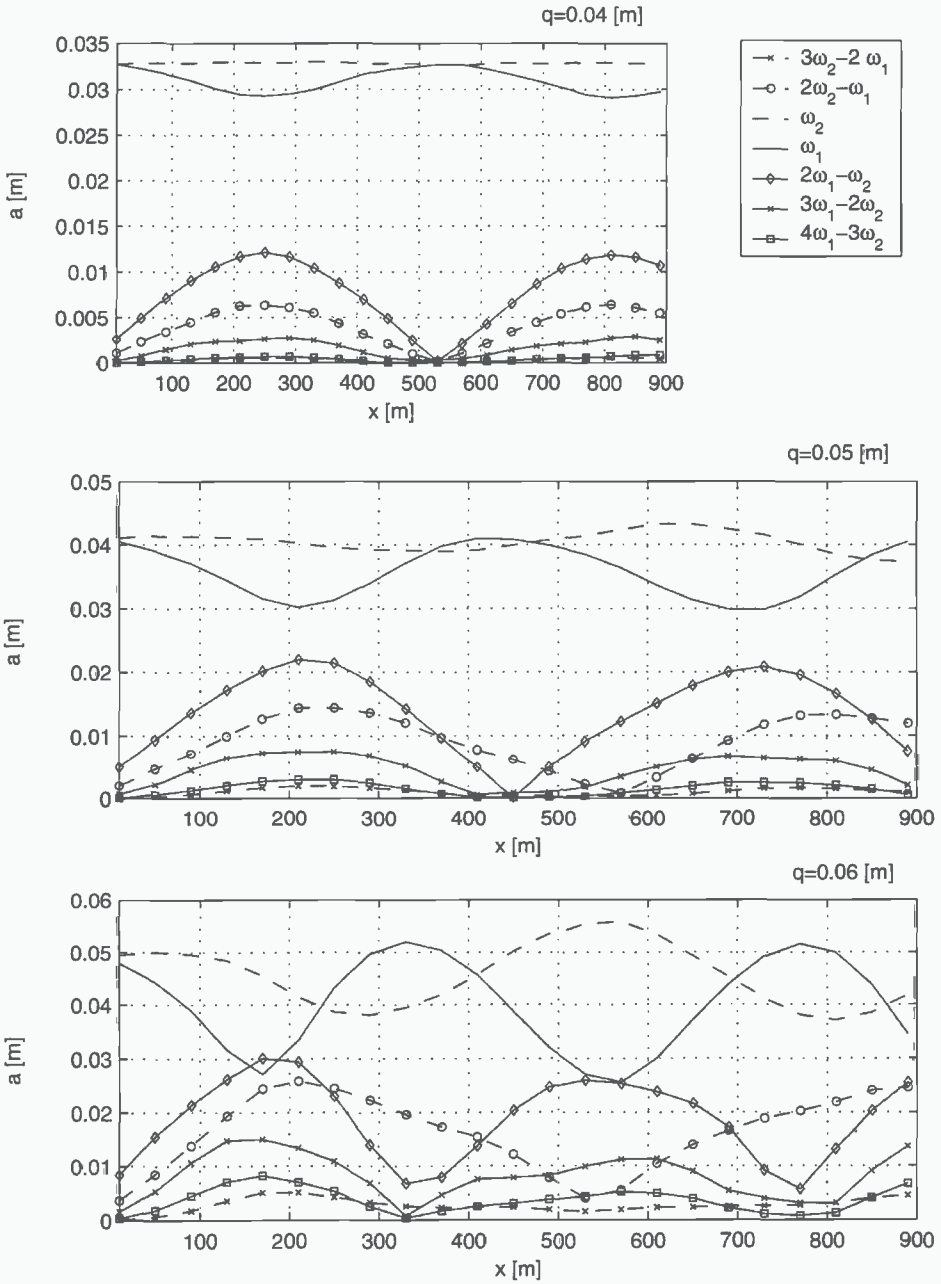
Figure 6.15: *Spatial evolution of the amplitudes of the bichromatic frequencies and sidebands for $T_1 = 1.925$, $T_2 = 2.075$*
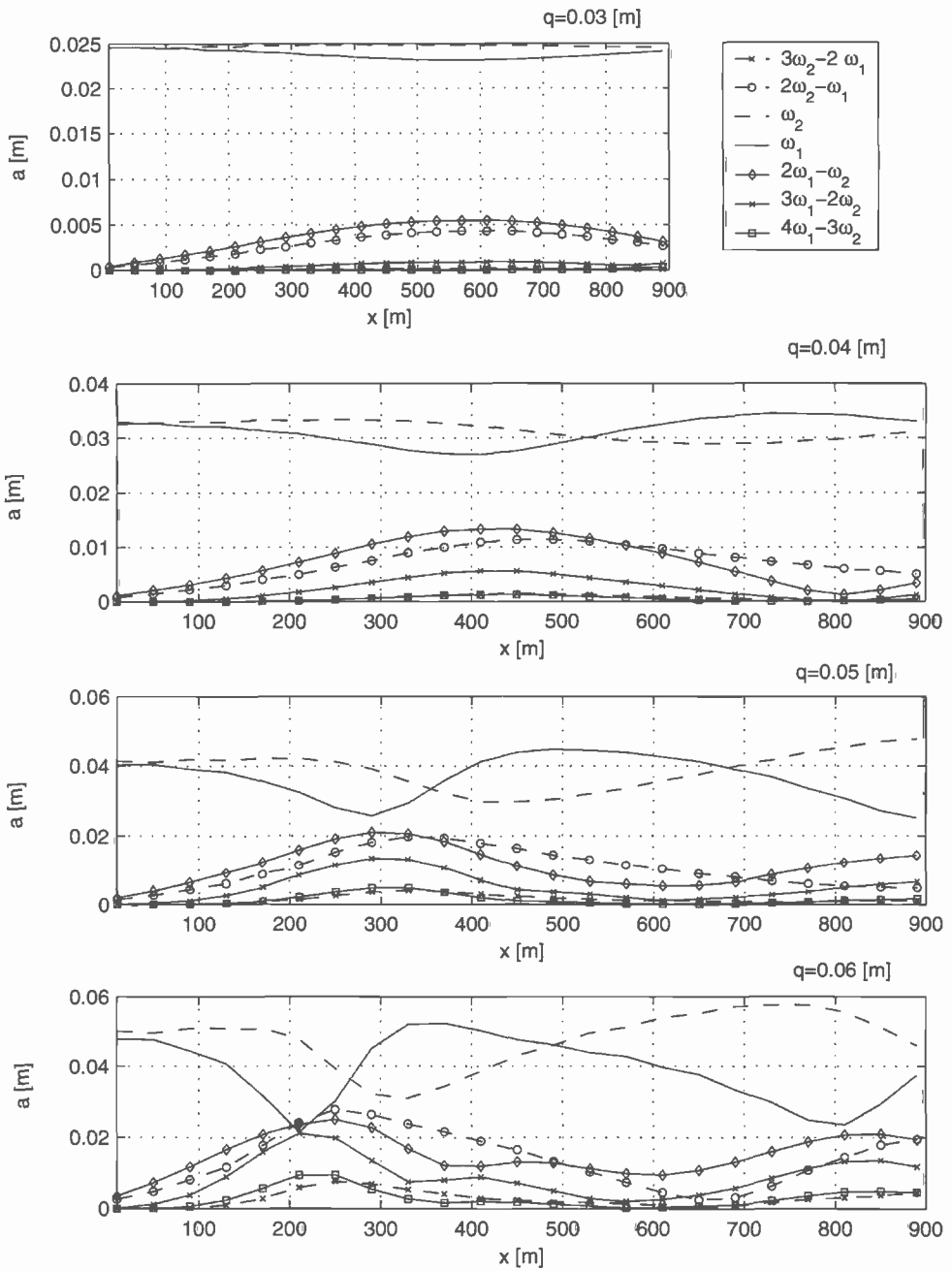
Figure 6.16: *Spatial evolution of the amplitudes of the bichromatic frequencies and sidebands for $T_1 = 1.95$, $T_2 = 2.05$*

$\Delta T = 0.3$ [s]			$\Delta T = 0.2$ [s]			$\Delta T = 0.15$ [s]			$\Delta T = 0.1$ [s]		
q [m]	λ_+[m]	λ_- [m]	q	λ_+	λ_-	q	λ_+	λ_-	q	λ_+	λ_-
0.05	137	128	0.04	300	285	0.04	520	520	0.03	1200	1200
0.06	148	136	0.05	306	295	0.05	450	555	0.04	800	
0.08	148	147	0.06	285	320	0.06	380	550			
			0.07	245	345						
			0.08	222	382						

Table 6.2: *Spatial periods obtained from Fig. 6.13-6.16 of the higher side bands (λ_+) and the lower side bands (λ_-) for different values of q and ΔT.*

plot of Fig. 6.13 is however striking.

6.3.3   Non stationarity

In this subsection the spatial non-stationarity of the wave group, observed from the numerical and experimental results, will be discussed further. The spatial periods of the upper and lower frequency bands will be related to non-dimensional parameters. Also a relation with the Benjamin-Feir instability and the nonlinear Schrödinger equation will be examined.

Spatial period

Firstly it is observed from the numerical simulations presented in the previous paragraphs that the spatial periods for all higher side bands ($\omega > \omega_1$) seem identical. The same is observed for the lower sidebands. In Table 6.2 the spatial periods obtained from Figs. 6.13-6.16 have been gathered. It should be noted that these figures are the periods of the (almost) zero crossings and that they cannot be very accurately determined in all cases. Because of the observed similarity between the different spatial evolutions, we seek for a suitable way to scale the results and thus establish some non-dimensional parameter that governs the dynamics.

From the figures of the previous subsection it was already observed that similar patterns arise for different combinations of q and ΔT. Closer examination of the results shows that similarity (up to a scaling in x) is observed when $\Delta T/q$ is approximately constant. Using this observation, it is found that the appropriate scaling for x is approximately a factor $\frac{1}{\Delta T^2}$. These scalings are translated in terms of ω and non-dimensionalised with ωk resulting in the graphs plotted in Fig. 6.17.

This figure shows that, given the errors in the determination of the spatial periods, the
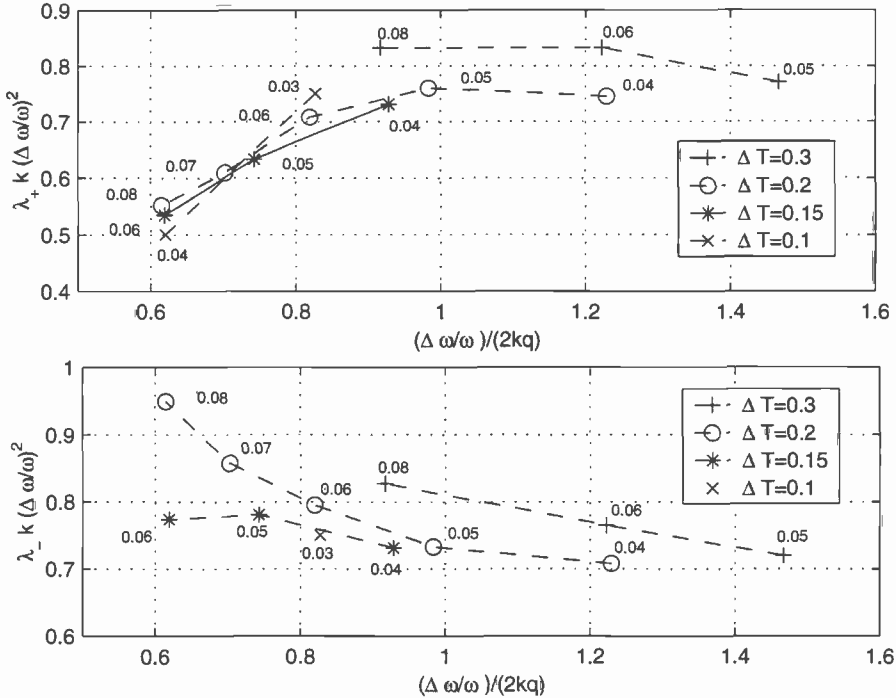
Figure 6.17: *Scaled spatial periods of the upper and lower scaled frequency bands. Un-scaled data from Table 6.2.*

spatial dynamics of the evolving wave group is rather consistent under the introduced scalings. The spatial period of the higher sidebands first increases for $(\Delta\omega/q)/(\omega k) < 1$ and appears to slowly decrease for $(\Delta\omega/q)/(\omega k) > 1$. The spatial periods of the lower frequency bands show in general a decreasing trend for increasing $(\Delta\omega/q)/(\omega k)$.

It should be noted that all simulations are performed with almost the same value for ωk and the scaling of $\Delta\omega/q$ with ωk has not been validated by other simulations. However, $(\Delta\omega/q)/(\omega k) = (\Delta\omega/\omega)/(ka)$, the latter being the appropriate scaling for the growth rates resulting from the Benjamin-Feir instability. This relation with the Benjamin-Feir instability is further discussed in the next paragraph.

Benjamin-Feir instability

Remark that the modulation amplitude A in Eq. (6.18) on page 180 is not always positive and therefore one must be careful to interpret this modulation function as an envelope. One could suggest to interpret the absolute value of A_{mod} as the envelope.

The function

$$|A(x,t)|\frac{1}{2}\left(e^{i\bar{\theta}(x,t)} + c.c.\right) \tag{6.24}$$

differs however from Eq. (6.18) by a sign-jump (or equivalently phase jump of π) of the carrier wave at the zero crossings of A_{mod}. We will refer to wave trains that are modulated by a *positive* envelope simply as modulated waves.

To investigate the difference between the modulated and the bichromatic wave, the bichromatic steering signal with parameters $T_1 = 1.9$ [s], $T_2 = 2.1$ [s] and $q = 0.08$ [m], is adapted as

$$s(t) = 2\bar{q}\left|\cos\left(\frac{1}{2}\Delta\omega\right)\right|\cos\left(\bar{\omega}t\right). \tag{6.25}$$

All other numerical parameters (mesh, start-up function and numerical methods) have been kept constant. The wave elevation resulting from (6.25) can therefore be directly compared with the results of Fig. 6.11 on page 190. This comparison is visualised in Fig. 6.18 where the thick solid line is the result from the original simulation on the bichromatic steering signal. From this figure the sign change of the carrier wave between two wave groups can be clearly observed at $x = 1$ [m] from the wave maker. At $x = 40$ [m], the most noticeable difference between the two signals is around the 'zero-crossing' of the envelope. The envelopes of two signals, except near the zero-crossing, are however still in quite good agreement. Although from $x = 80$ [m] to $x = 160$ [m] qualitatively the same envelope deformation is observed, there are some differences. Firstly, the group of the modulated wave propagates slightly faster than the bichromatic group. Secondly, the wave heights due to the modulated group are a fraction higher than the bichromatic wave. These two differences are even more clearly visible further downstream as can be seen in Fig. 6.19 on page 202 where part of the time signals of the wave elevation at $x = 560$ [m] and $x = 700$ [m] are plotted. Although the envelopes of the wave are not in alignment, the original sign and phase differences are remarkably well preserved.

Despite the differences in wave group velocities further downstream and some small differences in the envelopes around the zero-crossings, the simulations indicate that the evolution of the modulated and the bichromatic wave train are quite similar. In Fig. 6.20 on page 203 the spatial evolution of the spectrum is visualised. Firstly it is noticed from subplot 6.20(a) that (in contrast to the results from the bichromatic simulations) the wave elevation clearly shows a 'meta' group structure, i.e. a group-of-groups structure. Furthermore, the almost recurrence of the evolution is visible in the plots $(c_1) - (c_4)$ where the PSD has been plotted for four positions in the tank. Notice that the frequency containing most energy at $x = 180$ [m] and $x = 540$ [m] is the sideband frequency $\omega - \Delta\omega$. The spatial evolution of all the sidebands can be examined in more detail in Fig. 6.20(d). Comparison of this figure with Fig. 6.14 on page 195 ($q = 0.08$ [m]) shows some remarkable differences. The spatial evolution of the spectrum from $x = 300$ [m] to $x = 450$ [m] in Fig. 6.20(d) is quite slow (which is also suggested by 6.20(a)) and this is not observed in Fig. 6.14.
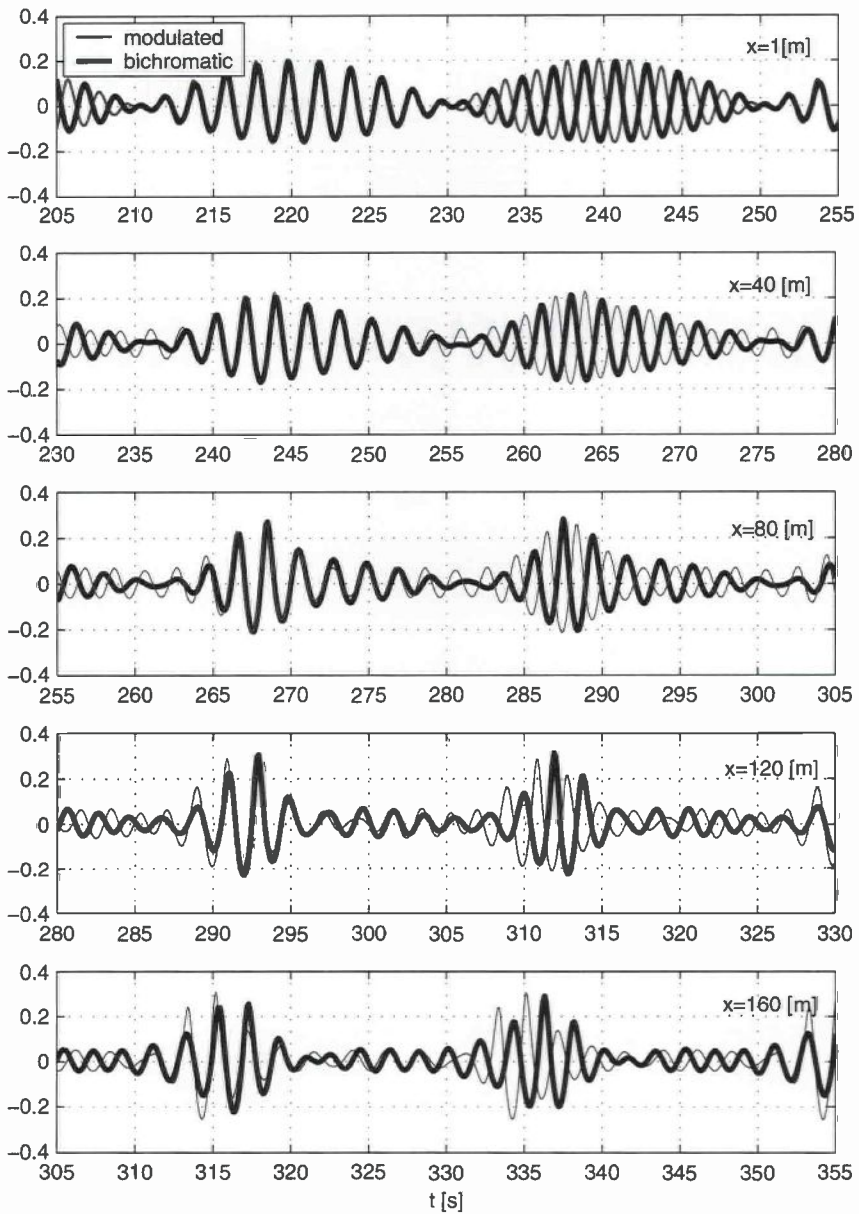
Figure 6.18: *Comparison between the numerical simulation of the evolution of a bichromatic wave (carrier wave has phase jump at zero crossing envelope) and a (positive) modulated wave (no phase jump).*
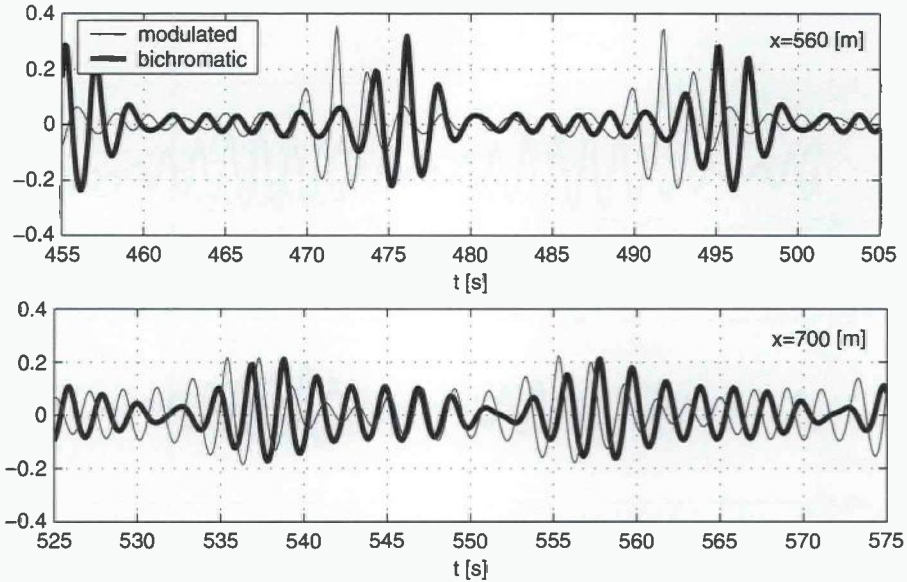
Figure 6.19: *Comparison between the numerical simulation of the evolution of a bichromatic wave and the modulated wave (no phase jump) at $x = 560$ [m] and $x = 700$ [m] from the wave maker.*

The spectrum of a linear bichromatic linear wave consists of two distinct frequencies at ω_1 and ω_2. The spectrum of the positive regularly modulated linear wave has most of its energy at the central frequency $\bar{\omega}$ and in numerous side bands $\bar{\omega} \pm j\Delta\omega$. To illustrate the spectral relation between bichromatic, positively modulated and a classical modulated (only two sidebands are used for modulation) wave train, the PSD of the bichromatic and positively modulated driving signals are compared to the PSD of the classical modulated signal

$$s(t) = \left(\frac{1}{2} + \frac{1}{2}\cos(\Delta\omega t)\right)\cos(\bar{\omega}t) \tag{6.26}$$

$$= \frac{1}{2}\cos(\bar{\omega}t) + \frac{1}{4}\cos((\bar{\omega} + \Delta\omega)t) + \frac{1}{4}\cos((\bar{\omega} - \Delta\omega)t) \tag{6.27}$$

in Fig. 6.21 on page 204. This latter signal represents a regular wave modulated by two symmetrical sidebands. The spatial-temporal evolution of such modulations has been studied in detail by several authors since Benjamin & Feir (1967) showed that these modulations are unstable and will grow exponentially for small t. The similarity of the initial wave group evolutions observed for the bichromatic and modulated waves (Fig. 6.18) and the initial dominance of the first sidebands $\omega - \Delta\omega$ and $\omega + \Delta\omega$ in Fig. 6.20(d), suggests that (i) a relation exists between the spectral components of the modulated and the bichromatic wave and (ii) the initial evolution of sidebands of the modulated wave can be described using the Benjamin-Feir instability.
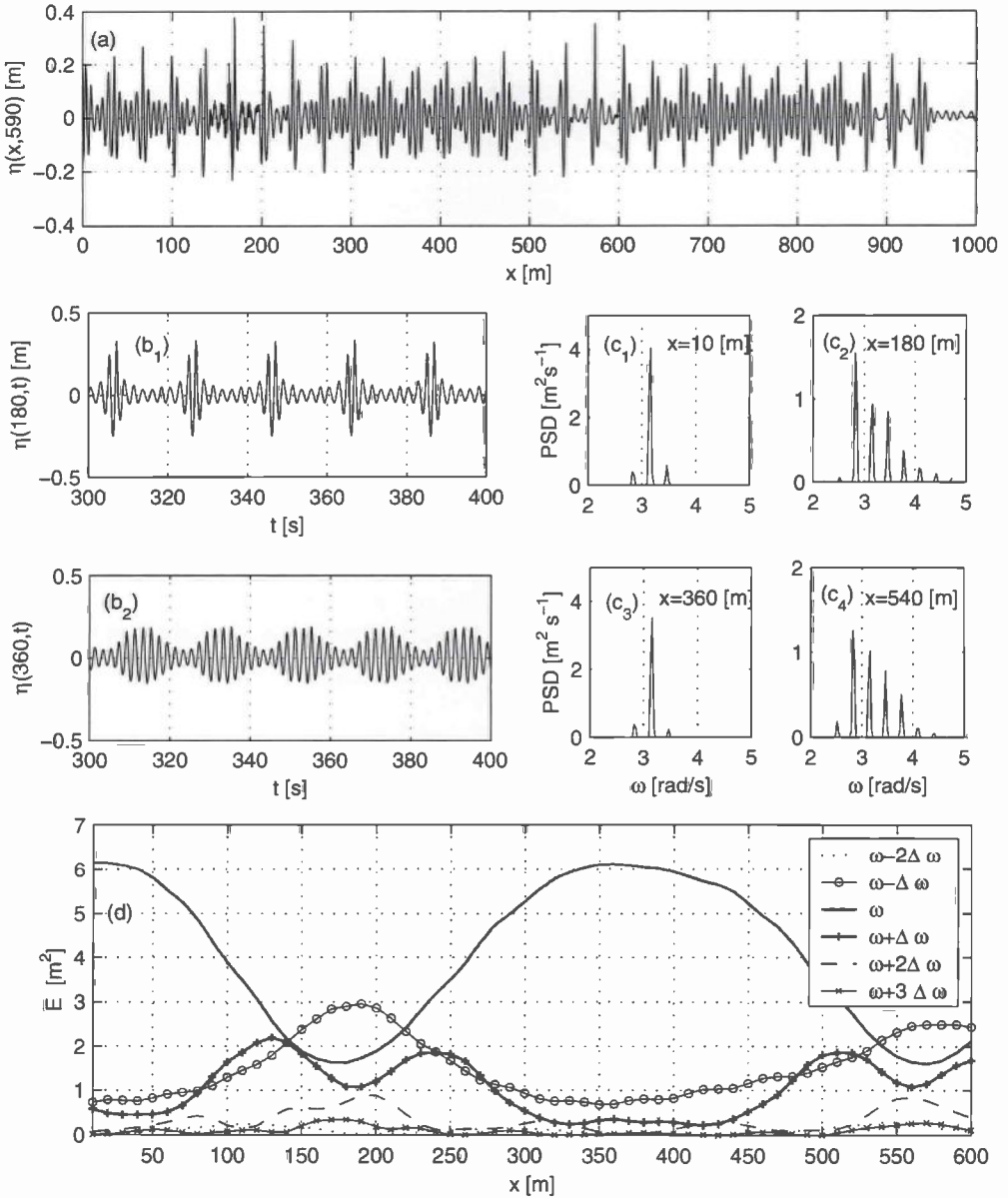
Figure 6.20: *Numerical simulations of modulated wave. Stroke steering signal: $s(t) = 2\bar{q}|\cos(\frac{1}{2}\Delta\omega t)|\cos(\omega t)$. (a) wave elevation at $t = 590$ [s] (b) time signals (c) spectral density (d) evolution of energy in frequency bands. ($h=5$, $g=9.81$, $\omega = \bar{\omega} = \pi$, $\Delta\omega \approx 0.315$*
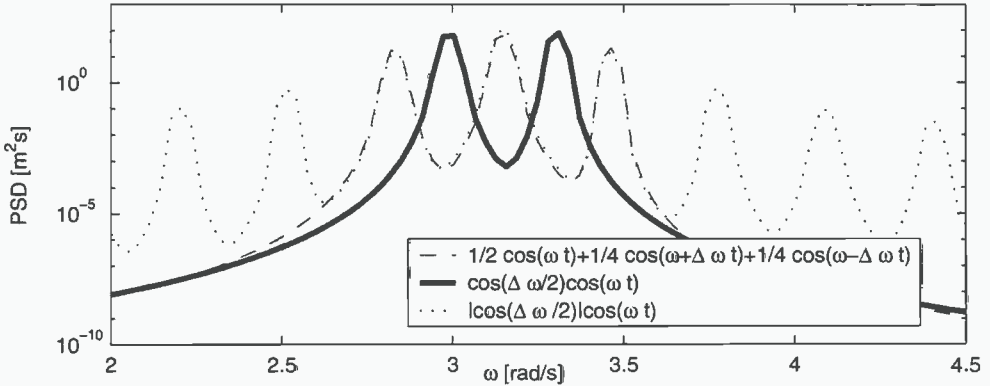
Figure 6.21: *Power spectral density of sampled functions (-.-) wave group with two sideband modulations; (-) bichromatic wave $A\cos(\omega t)$; ($\cdots$) modulated wave $|A|\cos(\omega t)$*

Benjamin & Feir (1967) showed that for $kh > 1.363$ the Stokes wave train (see also Eq. (3.10) on page 44) is unstable to modulations. In the presence of a regular Stokes wave with phase $\theta(x,t) = kx - \omega t$ and on infinitely deep water, the regular wave modes with phases

$$\theta_\pm = k(1 \pm \kappa)x - \omega(1 \pm \delta')t \tag{6.28}$$

will grow exponentially in time if

$$0 < \delta' \le \sqrt{2}ka. \tag{6.29}$$

The exponential growth rate for small time of the sideband waves is obtained as

$$\frac{\delta'}{2}\sqrt{2(ka)^2 - \delta'^2}. \tag{6.30}$$

This instability region and exponential growth rate can also be derived by performing a modulational stability analysis (cf. Stuart & Diparma (1978)) of the NLS equation (which can be derived from Zakharov's integral equation). The properties of the instability and the associated growth rates are however only approximations for small ka. Crawford et al. (1991) extend these results by direct analysis of the Zakharov integral equation, obtaining growth rates and stability regions for finite ka as a function of $\kappa/(ka)$.

It is noted that the Benjamin-Feir instability cannot completely account for the observed non-stationarity of the bichromatic waves. If the linear bichromatic wave with carrier frequency k and maximum height $2q$ is compared to an unstable regular wave with amplitude kq modulated by two sidebands (see also Fig. 6.21) then these sidebands would not grow (according to BF) if $(\Delta\omega/\omega)/(kq) > \sqrt{2}$, or $(\Delta\omega/\omega)/(2kq) >$

$\frac{1}{2}\sqrt{2}$ for bichromatic waves. However, from Fig. 6.17 it is clearly visible that growing side bands are present for this latter condition.

In the following paragraphs we will establish a relation between the spectral content of the positively modulated wave and the bichromatic wave, so that Eq. (6.30) can be used to predict the initial growth rates of the bichromatic components.

Consider the function

$$F(t) = \begin{cases} f_1(t) & 0 \leq t < T \\ f_2(t) & T \leq t \leq 2T \end{cases}, \tag{6.31}$$

where the functions f_1 and f_2 are both $\bar{T}$-periodic and can be identified with their Fourier-series data $\left\{c_n^{(1)}\right\}$ and $\left\{c_n^{(2)}\right\}$, respectively, as

$$f_j(t) = \sum_{-\infty}^{\infty} c^{(j)}{}_n e^{in\tilde{\Omega}t} , \quad c^{(j)} = \frac{1}{T} \int_0^T f_j(t) e^{-in\tilde{\Omega}t} \mathrm{d}t, \quad \tilde{\Omega} = \frac{2\pi}{T}. \tag{6.32}$$

The Fourier series coefficients C_n of $F(t)$ are thus given as

$$\begin{aligned} C_n &= \frac{1}{2T} \int_0^{2T} F(t) e^{-in\frac{2\pi}{2T}t} \mathrm{d}t \tag{6.33} \\ &= \frac{1}{2T} \left\{ \int_0^T f_1(t) e^{-in\frac{1}{2}\tilde{\Omega}t} \mathrm{d}t + \int_T^{2T} f_2(t) e^{-in\frac{1}{2}\tilde{\Omega}t} \mathrm{d}t \right\} \tag{6.34} \\ &= \frac{1}{2T} \int_0^T \left(f_1(t) + (-1)^n f_2(t) \right) e^{-in\frac{1}{2}\tilde{\Omega}t} \mathrm{d}t. \tag{6.35} \end{aligned}$$

For the $(T_1 = 1.9\,[\mathrm{s}], T_2 = 2.1\,[\mathrm{s}])$ bichromatic evolution and corresponding modulated evolution we assume that for sufficiently small distances from the wave maker (say $x < 120\,[\mathrm{m}]$):

- the time signal of the elevation due to the modulated signal is T_{mod} periodic and identify it with f_1,

- the time signal of the bichromatic wave is $2T_{mod}$ periodic and is identified with $F(t)$ where $f_2 = -f_1$. The latter identification is a simplification of the actually observed smoothing of the original zero crossing phase jump and the fact that the signal $F(t)$ has a non-zero mean.

Under these assumptions we find from Eq. (6.35) that

$$C_n = 0 \quad \text{if } n \text{ is even} \tag{6.36}$$

and for n is odd we find:

$$C_n = \frac{1}{T} \int_0^T f_1(t) e^{-in\frac{1}{2}\tilde{\Omega}t} dt \tag{6.37}$$

$$= \frac{1}{T} \int_0^T \sum_{-\infty}^{\infty} c_k^{(1)} e^{ik\tilde{\Omega}t} e^{-in\frac{1}{2}\tilde{\Omega}t} dt \tag{6.38}$$

$$= \sum_{-\infty}^{\infty} c_k^{(1)} \frac{1}{T} \int_0^T e^{i(k-\frac{1}{2}n)\tilde{\Omega}t} dt \tag{6.39}$$

$$= \sum_{-\infty}^{\infty} c_k^{(1)} \frac{2i}{\pi(2k-n)} \quad \text{if } n \text{ is odd.} \tag{6.40}$$

Eq. (6.40) gives the Fourier series components of the function $F(t)$, given the components of the function $f(t)$. The fact that $C_n = 0$ for n even is in agreement with the observations that the energy bands of the bichromatic wave, $(k+1)\omega_i - k\omega_j$, $i \neq j = 1,2$ $k = 1,2,\ldots$ lie exactly between the energy bands of the modulated wave, $\bar{\omega} \pm k\Delta\omega$. Under the made assumptions, this equation can thus in principle be used to relate the growth rate of the side bands of the bichromatic wave to the growth rates of Eq. (6.30).

The above relation between the Fourier series components of the modulated and bichromatic wave was based on the specific observations for $T = 2$ and $\Delta T = 0.2$, but can be generalised as follows. In general, the number of periods $\tilde{T} = \frac{4\pi}{\omega_1+\omega_2}$ in a (positive) wave group envelope period $T_{\text{mod}} = \frac{2\pi}{\omega_1-\omega_2}$ is

$$n_{mod} = \frac{T_{\text{mod}}}{\tilde{T}} = \frac{\bar{\omega}}{\Delta\omega} = \frac{T}{\Delta T}. \tag{6.41}$$

In the previous described case with $T = 2$ and $\Delta T = 0.2$, this leads to $n_{mod} = 10$, from which the periodicity of the signals and the subsequent analysis follows. In the case that n_{mod} is not an integer but rational, the following more elaborate relation can be obtained between the fourier components.

Because of the assumed rationality of n_{mod} there exists a minimal period $\hat{T}$ such that the signal $f_1(t) = \cos(\frac{1}{2}\Delta\omega t) \cos(\bar{\omega}t)$ is $\hat{T}$ periodic and $f_2(t) = |\cos(\frac{1}{2}\Delta\omega t)| \cos(\bar{\omega}t)$ is also $\hat{T}$ periodic. It follows that there exists a N such that $\hat{T} = 2NT_{\text{mod}}$ The signals f_1 and f_2 are clearly related as

$$f_2(t) = s(t) f_1(t) \tag{6.42}$$

with

$$s(t) = \begin{cases} 1 & \text{if } (j-1)T_{\text{mod}} < t < jT_{\text{mod}}, \quad j = 1,3,\ldots,2N-3,2N-1 \\ -1 & \text{if } (j-1)T_{\text{mod}} < t < jT_{\text{mod}}, \quad j = 2,4,\ldots,2N-2,2N \end{cases}. \tag{6.43}$$

The Fourier series coefficients $\left\{c_n^{(1)}\right\}$ and $\left\{c_n^{(2)}\right\}$ are thus related as

$$c_n^{(2)} = \frac{1}{\hat{T}}\int_0^{\hat{T}} f_2(t)e^{-in\frac{2\pi}{\hat{T}}t}\mathrm{d}t \tag{6.44}$$

$$= \frac{1}{\hat{T}}\int_0^{\hat{T}} s(t)f_1(t)e^{-in\frac{2\pi}{\hat{T}}t}\mathrm{d}t \tag{6.45}$$

$$= \frac{1}{\hat{T}}\int_0^{\hat{T}} \left(\sum_{k=-\infty}^{\infty} c_k^{(s)}e^{ik\frac{2\pi}{\hat{T}}t}\right)\left(\sum_{l=-\infty}^{\infty} c_k^{(1)}e^{il\frac{2\pi}{\hat{T}}t}\right)e^{-in\frac{2\pi}{\hat{T}}t}\mathrm{d}t \tag{6.46}$$

$$= \frac{1}{\hat{T}}\sum_{k=-\infty}^{\infty}\sum_{l=-\infty}^{\infty} c_k^{(s)}c_l^{(1)}\int_0^{\hat{T}} e^{i(k+l-n)\frac{2\pi}{\hat{T}}t}\mathrm{d}t \tag{6.47}$$

$$= \sum_{k=-\infty}^{\infty}\sum_{l=-\infty}^{\infty} c_k^{(s)}c_l^{(1)}\left[\frac{i\left(1-e^{i2\pi(k+l-n)}\right)}{2\pi(k+l-n)}\right]. \tag{6.48}$$

The Fourier series coefficients $\left\{c_k^{(s)}\right\}$ of $s(t)$ are given by

$$c_k^{(s)} = \frac{1}{\hat{T}}\int_0^{\hat{T}} s(t)e^{-ik\frac{2\pi}{\hat{T}}t}\mathrm{d}t \tag{6.49}$$

$$= \sum_{j=1}^{2N}(-1)^{j-1}\frac{1}{\hat{T}}\int_{(j-1)T_{\mathrm{mod}}}^{jT_{\mathrm{mod}}} e^{-ik\frac{2\pi}{\hat{T}}t}\mathrm{d}t \tag{6.50}$$

$$= \sum_{j=1}^{2N}(-1)^{j-1}\frac{1}{\hat{T}}\int_0^{T_{\mathrm{mod}}} e^{-ik\frac{2\pi}{\hat{T}}(t+(j-1)T_{\mathrm{mod}})}\mathrm{d}t \tag{6.51}$$

$$= \sum_{j=1}^{2N}(-1)^{j-1}e^{-ik(j-1)\pi/N}\left[\frac{i\left(1-e^{ik\pi T_{\mathrm{mod}}/N}\right)}{k\pi T_{\mathrm{mod}}}\right]. \tag{6.52}$$

In the last equality use has been made of the relation $\hat{T} = 2NT_{\mathrm{mod}}$. Combination of Eq. (6.48) and Eq. (6.52) leads to a complicated but exact relation between the Fourier series coefficients of the signals f_1 and f_2. If we assume that sufficiently close to the wave generator the signals of the bichromatic and modulated wave elevation satisfy the condition (6.42), the derived relation can be used to compute the growth rates of the components of the bichromatic wave from the growth rates of the unstable modes from the Benjamin-Feir instability.

Envelope evolution

In this paragraph the envelope evolution of the bichromatic wave is investigated. First the correspondence between the predictions of the NLS-equation (governing the slowly varying amplitude) are compared to the measurements. The solution of the NLS-equation in non-moving coordinates is approximated as an initial value boundary

problem (IBVP). The initial value is the still water solution $A(0, x) = 0$ and at the generating boundary, the prescribed boundary condition is the bichromatic steering signal

$$Re(A(t,0)) = s(t)2q\cos\left(\frac{1}{2}\Delta\omega\right)$$ (6.53)

$$Im(A(t,0)) = 0$$ (6.54)

where $s(t)$ is a smooth start-up function. The length of the computational domain was taken such that the generated waves did not reach the opposing wall on which the condition $A(t, L) = 0$ was imposed, thus avoiding the implementation of absorbing boundary conditions for the NLS-equation. The solution of the IVBP is approximated using an implicit Crank-Nicolson scheme for time integration with a central finite differences approximation for the spatial derivatives. This scheme was originally developed by Taha & Ablowitz (1984) and its results compare favorably with results of other difference schemes (see Chang *et al.* (1999)). The computer code used for the simulation was adapted from a computer code written by A. Suryanto. The time step of the simulations ($h = 1$, $g = 1$) is $\Delta t = 0.5$ and the mesh width is $\Delta x = 0.1$ with $L = 80$ and $T_{\text{end}} = 300$. For these dimensions the following values were used $\beta' = 0.0111$, $\gamma' = 22.874$, $c_g = 0.2213$ and $q = 0.016$. These values correspond to $q = 0.08$ [m] and $(T_1, T_2) = (1.9, 2.1)$ [s] in tank dimensions ($h = 5$ [m]).

This numerical simulation method of the NLS-equation differs from the simulations of Lo & Mei (1985) on Dysthe's equation and Shemer *et al.* (1998) on the NLS-equation. The latter use periodic spatial boundary conditions and solve the equations in a moving frame of reference. Solving the NLS-equation with symmetric initial data and periodic boundary conditions will retain the symmetry of the solution. The fourth-order terms in Dysthe's equation do allow for asymmetric evolution of symmetric data, which has been an important reason for this equation to be adopted by many authors.

In the present numerical simulations of the NLS-equation, a time periodic signal for $|A(x, t)|$ is observed after the transient startup waves have passed. The periodic signals are plotted in Fig. 6.22 on page 210 in which the NLS-envelope $|A(x, t + x/c_g)|$ (dashed line), the shifted envelope $-|A(x, t + x/(c_g + 0.05))|$ (solid thick line) and the experiments (solid line) for $q = 0.08$, $(T_1, T_2) = (1.9, 2.1)$ (see also Subsection 6.3.1) have been plotted. In contrast to simulations using periodic boundary conditions, the IVBP simulations presented in Fig. 6.22 on page 210 do show the symmetry breaking by the NLS-equation. Moreover, the simulations show reasonable qualitative agreement between the experiments and the NLS-envelope. There are however some noticeable differences:

- The group velocity of the NLS solution is lower than observed experimentally. Using the nonlinear deep water dispersion relation Eq. 3.11 on page 45 the

nonlinear deep water group velocity c_g^{nl} is obtained as

$$c_g^{nl} \approx \frac{g\left(2 + 3a^2k^2\right)}{\sqrt{8k\left(2 + a^2k^2\right)}}.$$

(6.55)

Substitution of $k = 1.0112$, $a = 2q = 0.16$ and $g = 9.81$ in Eq. (6.55) results in $c_g^{nl} = 1.608$, and therefore $c_g^{nl} - c_g = 0.0506$. The additional shift due to nonlinear group velocity results in the thick lines in Fig. 6.22 on the following page and shows good agreement with the experimentally found velocity.

- From $x = 100$ [m] and further downstream, the NLS envelope does not properly reproduce the splitting of the second group which is observed from the measured data. The NLS first underpredicts ($x = 100$ [m]) and then overpredicts ($x = 180$ [m]) the wave height behind the primary group.

Based on numerical simulations of Dysthe's equation (an extension of the NLS-equation) Lo & Mei (1985) speculate that the long-time evolution of a bichromatic wave consists of the splitting of the original group into two groups. These two groups have different group velocities and thus overtake each other periodically, thus establishing recurrence as an end-state. The results of the numerical simulations in Subsection 6.3.2 already provide evidence of the contrary. The spatial evolution of the upper and lower sidebands do not have exactly the same period and recurrence is therefore not simply established. The overtaking that was observed by Lo & Mei for the specific group that they examined (similar to the $(T_1, T_2) = (1.9, 2.1)$ group that we also examined) can be confirmed by our fully nonlinear numerical simulations. The envelope of the numerical data is determined using the Hilbert transform technique and low-pass filtering. The original time signals and the obtained envelopes for the $(T_1, T_2) = (1.9, 2.1)$ [s], $q = 0.08$ [m] numerical simulations are shown in Fig. 6.23 on page 211. From these figures one can observe from $x = 200$ [m] to $x = 550$ [m] that a small group splits and is slowly overtaken by the original group. This has also been visualised in Fig. 6.24 on page 212 where a density plot is shown of the envelope (in a moving frame of reference ($V_0 = 1.68$ [m/s]), determined experimentally from the group velocity of the primary (largest) group. From this figure the splitting and interacting of the two group envelopes is clearly visible. This indicates that envelope recurrence indeed will occur as was suggested by Lo & Mei. However, this overtaking wave group concept was not observed for all investigated bichromatic groups.

As an example we show the simulated fully nonlinear long-time evolution of the $(T_1, T_2) = (1.95, 2.05)$ [s], $q = 0.06$ [m] wave group. The simulation was performed on a computational domain with a length of more than 2000 [m] ($\approx 400\lambda$) over 1600 [s] ($\approx 800T$) with $\Delta x = 0.2$ [m], $nx = 10100$, $nz = 9$, $\beta = 1.5$ and RK45M time integration with a time step $\Delta t = 0.1$ [s]. Simulation of this long-time evolution involved 80,000 constructions and solutions of a boundary value problem for 90,900 unknowns using more than 160,000 elements per problem.

Time signals at different positions in the numerical tank and their corresponding envelopes are plotted in Fig. 6.25 on page 213. This figure clearly shows the splitting
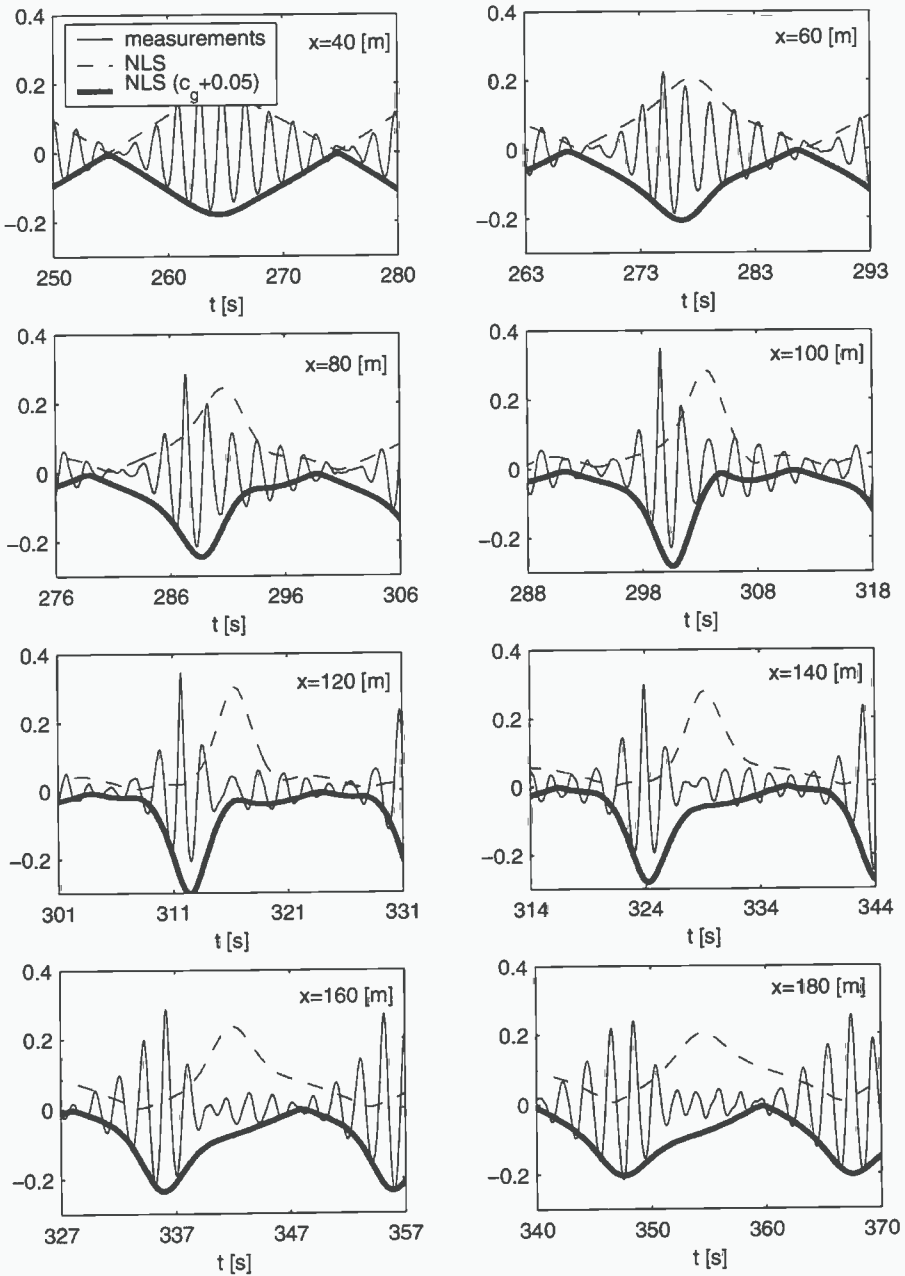
Figure 6.22: *Experiments (see also Fig. 6.11) and IVBP simulations of the NLS. The dashed line plots the NLS envelope $|A(t + c_g/x)|$ and the solid thick line plots the NLS envelope $-|A(t + (c_g + 0.05)/x)|$.*
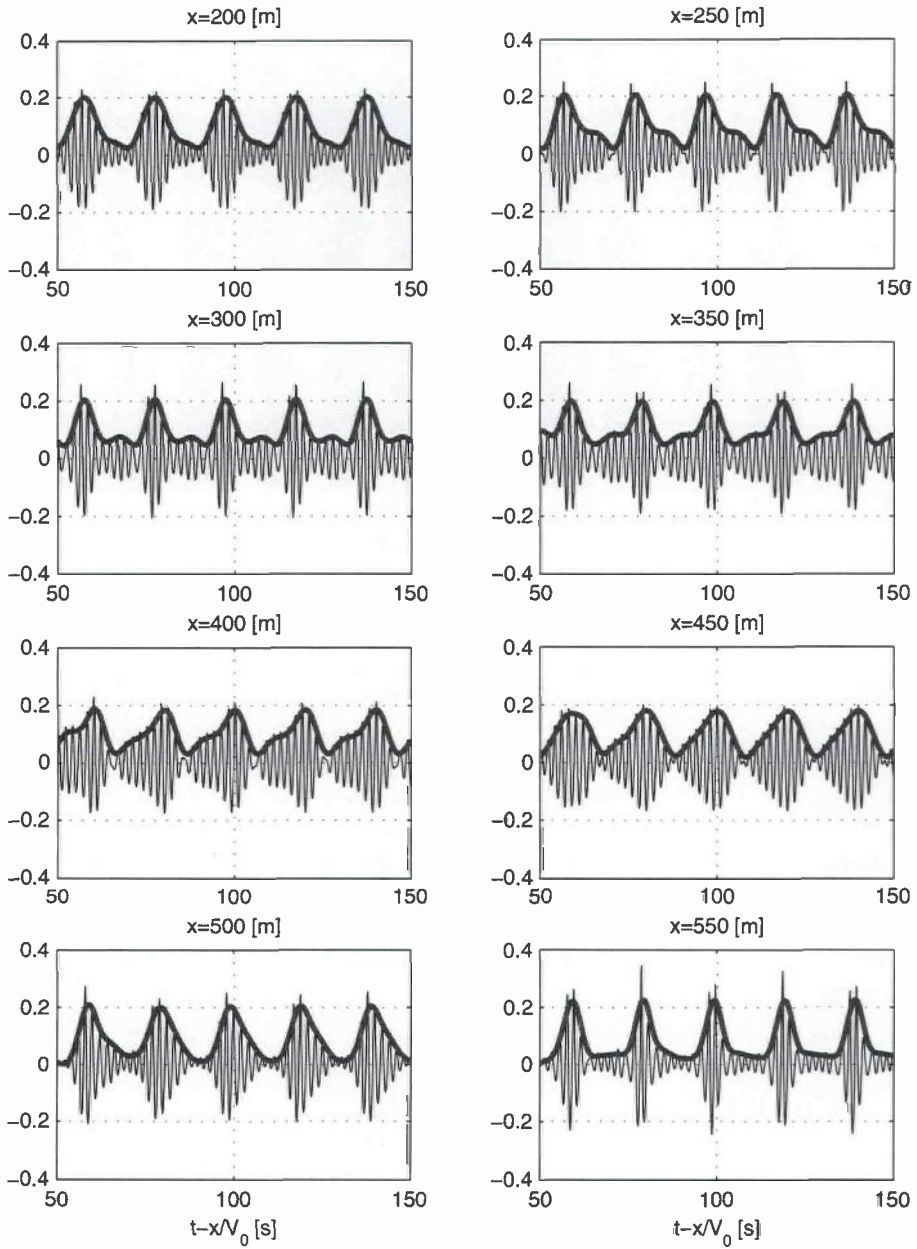
Figure 6.23: *Time signals and envelope evolution $T_1 = 1.9$ [s], $T_2 = 2.1$ [s], $q = 0.08$ [m], $h = 5$ [m]. Envelope is determined using the Hilbert transform and low pass filtering.*
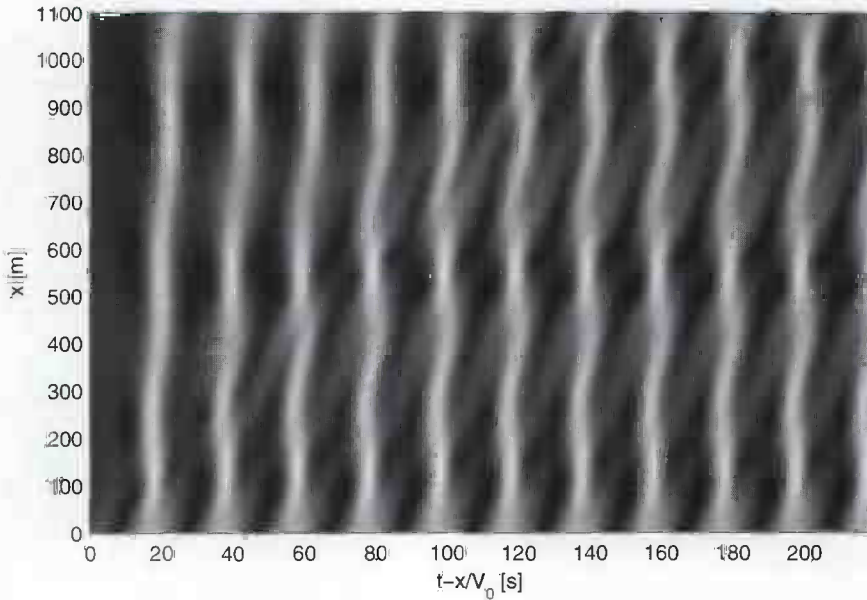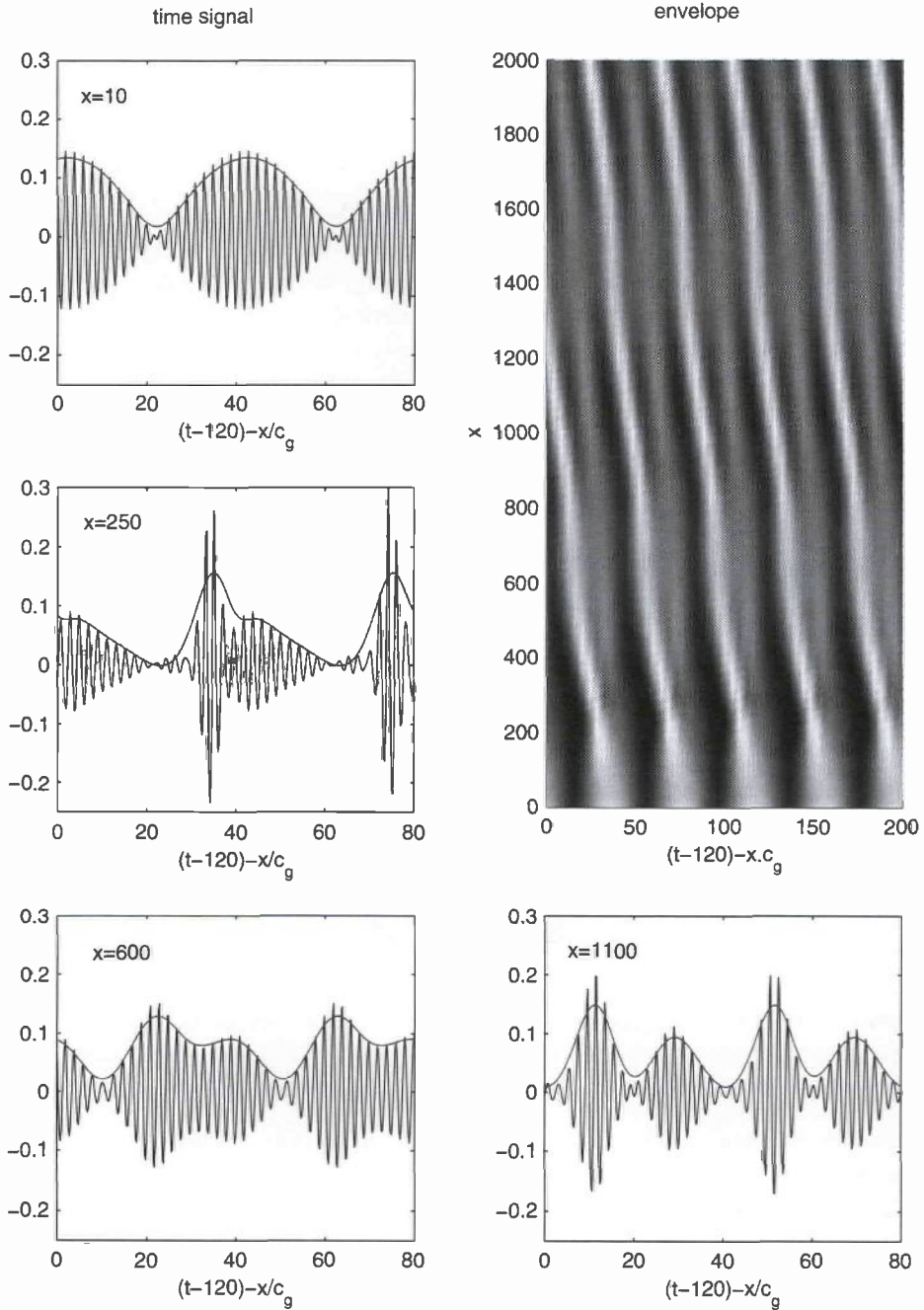
Figure 6.24: *Density plot of the envelope evolution $T_1 = 1.9$, $T_2 = 2.1$, $q = 0.08$ [m]. The envelope is determined using the Hilbert transform and low pass filtering. See also Fig. 6.23.*

of the wave group and the formation of two distinct wave groups at $x = 1100$ [m]. However, as the envelope density plot shows, the end state appears not to indicate overtaking wave groups as in Fig. 6.24. Closer examination of the signals shows that the group that has split off 'bounces' between its two neighboring larger groups. It is thus concluded that at least two qualitatively different ('overtaking' and 'bouncing') long-time (seemingly recurrent) end states exist for the initially bichromatic nonlinear wave group.

6.4   Conclusion and discussion

In this chapter the numerical method developed to simulate nonlinear water waves has been applied to study the long-time evolution of wave groups. Due to the efficiency of the method, the evolution has been explored on time-scales previously not attainable.

The evolution of a confined wave train is examined which shows good qualitative agreement with published results. The disintegration of the train in groups has been observed but the suggested complete splitting into clearly separated groups cannot be rigorously confirmed by the numerical results. Investigation if the evolution of a confined (NLS-soliton) wave group showed the generation of second-order free waves

Figure 6.25: *Time signals and envelope evolution for $T_1 = 1.95$ [s], $T_2 = 2.05$ [s], $q = 0.06$ [m]. The envelope is determined using the Hilbert transform and low pass filtering.*

due to first-order initial conditions. After isolating the primary confined wave group and establishing the relative permanency of its envelope, the effect of an uneven bottom on this group is examined. The results show that the group flattens and the maximum wave height decreases when the bottom increase such that $kh < 1.363$ on the new depth. Also the generation of a relative large solitary wave from the original wave group due to the bottom topography is observed.

A series of experimental and numerical simulations on bichromatic wave trains have been reported showing large deformation of the wave group due to nonlinearity. It is shown that on the length scale of the physical basin, the numerical and experimental results are in satisfactory agreement. The numerical simulations are then extended over a vastly larger domain to examine the possible end state of the observed deformations. Also the amplitude and modulation period are varied to examine the effect of these parameters on the evolution. For moderate amplitudes, periodic evolution of the wave spectrum was found, indicating recurrence. An appropriate scaling was experimentally constructed that relates the ratio between the frequency difference and the amplitude ($\frac{\Delta\omega}{q}$) to the observed spatial periods.

The experimental results on the bichromatic simulations are compared to a modulated wave and based on the similarities it is suggested that the initial growth rates of the side bands of the bichromatic wave can be related to the growth rates of the side bands of a simple modulated regular wave (Benjamin-Feir instability). It is noticed however, that sideband growth was also observed outside the B.-F.instability interval, indicating a different kind of instability.

Most numerical simulations of the NLS-equation in water wave evolution are based on the application of periodic boundary conditions in a moving frame of reference. The NLS-equation is often rejected as an appropriate model for the evolution of periodic wave groups (in favor of the fourth-order extension by Dysthe), because initial data remains periodic for the NLS-equation. Numerical simulation of the solution of the NLS-equation in physical coordinates as an initial boundary value problem however shows asymmetric envelope evolution that is in qualitative agreement with the measured data. This shows that the NLS-equation can be used for qualitative understanding of the asymmetric envelope deformations as long as it is treated in the context of an initial value problem.

Further examination of the envelope evolution due to fully nonlinear simulations of bichromatic waves shows the splitting of the original envelope in two distinguishable envelopes. These distinguished groups are observed to interact in at least two qualitatively different ways ('overtaking' and 'bouncing'), both showing envelope recurrence.

Chapter 7

Conclusions and recommendations

The preceding chapters contain a separate last section in which detailed conclusions concerning the topic of the chapter are summarised. These detailed conclusions are not repeated here, but only the more general conclusions are presented and some recommendations for further research are given.

In this thesis a numerical algorithm for the simulation of nonlinear free surface waves in a model test basin has been described and investigated. The aim of the research was to develop, implement and investigate an algorithm for the deterministic and accurate simulation of two-dimensional nonlinear waves in a model test basin. The simulated wave field may be generated from a broad-banded target spectrum and the simulations should be carried out by an efficient algorithm in order to be applicable in practical situations. The developed algorithm is based on a combination of Runge-Kutta (for time integration), Finite-Element (boundary-value problem) and Finite-Difference (velocity recovery) methods. The scheme is further refined and investigated using different models for wave generation, propagation and absorption.

The accuracy and stability of the numerical scheme are investigated and the numerical dispersion error is determined for several discretisation parameters. It was found that stable, second-order accurate discretisations can be obtained using first-order Finite Elements and second-order Finite Differences. The results also showed that a global projection method, using Finite Elements for velocity recovery, results in unstable discretisations. By a suitable choice of the grid density parameter the dispersion error of a small amplitude regular numerical wave can be annihilated by cancellation of errors. A physically relevant error measure for broad-banded wave simulations is introduced and discrete mass and energy conservation are investigated. It was found that the mass and energy decay due to numerical dissipation is mainly caused by the geometrical approximation but is sufficiently small for accurate simulations.

Wave generation methods based on models of physical wave makers and methods for numerical wave generation are described and evaluated. The discrete wave board transfer functions for flap- and piston type wave generators are determined and it is concluded that the numerical wave generator produces slightly higher waves than expected from continuous analysis. It was also found that application of the algorithm to wave simulation may result in unstable discretisations for specific geometries in combination with some grids.

Measurements that were performed on the reflection properties of beaches in the model basin are compared to the results of a numerical wave absorption method. This absorption method consists of the combined pressure damping, horizontal grid stretching and application of a Sommerfeld condition. Strict energy decay is guaranteed and the combination allows for effective absorption for a broad range of frequencies. Reflection coefficients smaller than 0.7 % can be achieved at relative low computational cost. It is also shown that by suitable choice of parameters the combined absorption method can reasonably approximate the measured reflections on artificial beaches in the basin.

The algorithm was further applied to several benchmark tests confirming the validity of the results. Also the direct comparison with measurements showed satisfactory agreement. The implementation of the numerical algorithm in an Object Oriented programming language allows for easy extension and maintenance of the computer code, allowing for the development of more general applications.

The numerical scheme is used to investigate the long-time evolution of nonlinear wave groups. A study on the propagation of a confined wave group over a bottom topography, the disintegration of a confined wave train and an elaborate study involving numerous measurements and simulations on the evolution of bichromatic wave groups are presented. The efficiency of the numerical algorithm allowed to explore the dynamics of these waves on an unprecedented time and spatial scale. The disintegration of a wave train in groups has been observed, but the complete splitting into clearly separated groups cannot be rigorously confirmed by the numerical results. Investigation of the evolution of a confined (NLS-soliton) wave group over a bottom topography showed the defocussing of the group and the generation of a large free solitary wave. The long-time evolution of bichromatic waves showed spatial periodic variations of the wave spectrum, indicating recurrence as an end state of the evolution. An appropriate scaling was experimentally constructed that relates the ratio of amplitude and original frequency difference $(\Delta\omega/q)$ to the observed spatial periods. Examination of the envelope evolution of the bichromatic waves show the splitting of the original envelope in two distinguishable envelopes. These distinguished groups are observed to interact in at least two qualitatively different ways, both showing envelope recurrence.

Based on the investigations of this thesis, the following recommendations for further research are given: (i) further development of the existing three-dimensional extension of the algorithm to investigate the evolution of extreme waves interacting in three dimensions; (ii) adaption of the top-level algorithm to include arbitrary numerical grid

structures, this will allow for more accuracy control near complex geometries; (iii) implementation of the local near-boundary C_B^N continuous finite elements to investigate whether accuracy or stability improvements can be achieved (iv) further investigation of mathematical models and measurements of artificial beaches. The current numerical model lacks physical justification and measurements are not conclusive; (v) extension of the stability investigations to the nonlinear discretisation, resulting in more rigorous stability results; (vi) verification of the suggested relation between the Benjamin-Feir growth rates and the nonlinear bichromatic wave evolution.

Appendices

Appendix A

Equivalence of strong and weak formulation

In this appendix an outline of the proof of the equivalence of the strong and weak formulation of the boundary value problem in section 2.2.4 is given. For full details we refer to the lecture notes of Girault & Raviart (1981) and the paper of Kawohl (1980) for further references therein.

A.1   Sobolev spaces

First, some notations and definitions are introduced. Let $\Omega \subset \mathbb{R}^d$ be an open set with boundary Γ. $\mathcal{D}(\Omega)$ is defined as the linear space of infinitely differentiable functions with compact support on Ω. The space of distributions on Ω, $\mathcal{D}'(\Omega)$, is defined as the dual space of $\mathcal{D}(\Omega)$. Locally integrable functions f can be identified with a distribution by

$$\langle f, \phi \rangle = \int_\Omega f\phi \, d\Omega \quad \forall \phi \in \mathcal{D}(\Omega) \tag{A.1}$$

The Sobolev space $W^{m,p}(\Omega)$ is defined as

$$W^{m,p} = \{v \in L^p \mid \partial^\alpha v \in L^p, \ \forall |\alpha| \le m\} \tag{A.2}$$

which is a Banach space for the norm

$$\|u\|_{m,p,\Omega} = \left(\sum_{|\alpha| \le m} \int_\Omega |\partial^\alpha u(x)|^p dx \right)^{1/p} \qquad p < \infty \tag{A.3}$$

221

$W^{m,p}(\Omega)$ can also be equipped with the following seminorm

$$|u|_{m,p,\Omega} = \left(\sum_{|\alpha|=m} \int_\Omega |\partial^\alpha u(x)|^p dx \right)^{1/p} \qquad p < \infty \qquad (A.4)$$

In the special case where $p = 2$, $W^{m,2}(\Omega)$ is denoted as $H^m(\Omega)$ and the subscript $p = 2$ is dropped from the norm and seminorm. $H^m(\Omega)$ is a Hilbert space for the scalar product

$$(u,v)_{m,\Omega} = \sum_{|\alpha|\le m} \int_\Omega \partial^\alpha u(x)\partial^\alpha v(x)dx. \qquad (A.5)$$

The scalar product of $L^2(\Omega$ is denoted (explicitly without any subscripts) as

$$(u,v) = \int_\Omega f(x)g(x)dx$$

The space $H_0^m(\Omega)$ is defined as the closure of $\mathcal{D}(\Omega)$ with respect to the $\| \cdot \|_{m,\Omega}$ norm and its dual space is denoted as $H^{-m}(\Omega)$. There exists a linear and continuous mapping $\gamma_0 \in \mathcal{L}\left(H^1(\Omega), L^2(\Gamma)\right)$ where $\gamma_0 u$ denotes the value of u on Γ. The range space of γ is denoted as $H^{1/2}(\Omega)$ which is a proper and dense subspace of $L^2(\Gamma)$. Equipped with the norm

$$\|f\|_{1/2,\Gamma} = \inf_{v\in H^1(\Omega)\ \gamma_0 v=f} \|v\|_{1,\Omega} \qquad (A.6)$$

$H^{1/2}(\Gamma)$ is a Hilbert space. Its corresponding dual space is denoted $H^{-1/2}(\Gamma)$ and the duality bracket as $\langle \cdot, \cdot \rangle_\Gamma$ which is an extension of the scalar product on $L^2(\Gamma)$.

A.2 Extended Green's formula for the Laplace operator

Green's formula states that if $u \in H^2(\Omega)$ and $v \in H^1(\Omega)$

$$(\nabla u, \nabla v) = -(\Delta u, v) + \int_\Gamma (\nabla u \cdot n)\, v \; d\Gamma. \qquad (A.7)$$

Consider now the function space

$$H(\nabla; \Omega) = \left\{ w \in \left[L^2(\Omega)\right]^n \mid \nabla \cdot w \in L^2(\Omega) \right\}. \qquad (A.8)$$

$\mathcal{D}(\bar{\Omega})$ is dense in $H(\nabla; \Omega)$ and therefore a linear and continuous map $\gamma_n w \to w \cdot n|_\Gamma$ from $H(\nabla; \Omega)$ into $H^{-1/2}(\Gamma)$ exists. From this also follows that

$$(w, \nabla u) + (\nabla \cdot w, u) = \langle \gamma_n w, \gamma_0 v \rangle_\Gamma \quad \forall w \in H(\nabla, \Omega),\ \forall u \in H^1(\Omega) \qquad (A.9)$$

which finally leads to the following extension of Green's formula.

If $u \in \mathbf{H}^1(\Omega)$ and $\Delta u \in \mathbf{L}^2(\Omega)$ then $\nabla u \cdot n \in H^{-1/2}(\Gamma)$ and

$$(\nabla u, \nabla v) = -(\Delta u, v) + \int_\Gamma (\nabla u \cdot n)\, v\, d\Gamma \quad \forall v \in H^1(\Omega). \tag{A.10}$$

A.3 Lax-Milgram theorem

Let V be a real Hilbert space with dual space V'; let $a(u,v)$ be a real bilinear form on $V \times V$ and $l \in V'$. Consider the problem

Find $u \in V$ such that

$$a(u,v) = \langle l, v \rangle \quad \forall v \in V. \tag{A.11}$$

If there exits two constants M and $\alpha > 0$ such that

$$|a(u,v)| \le M\|u\|\|v\| \qquad \forall u,v \in V \tag{A.12}$$
$$a(v,v) \ge \alpha\|v\|^2 \qquad \forall v \in V \tag{A.13}$$

then there exists a unique $u \in V$ satisfying (A.11). Moreover the mapping $l \to u$ is an isomorphism from V' onto V.

A.4 Equivalence

Let the boundary Γ be partitioned as $\Gamma = \Gamma^D \cup \Gamma^N$ and denote

$$H^1_{0,\Gamma^D} = \left\{ u \in H^1(\Omega) \,|\gamma_0 u = 0 \text{ on } \Gamma^D \right\} \tag{A.14}$$

which is also a Hilbert space with the norm of $H^1(\Omega)$.

Now consider the following two problems:

(A) Find a function Φ such that for $g \in H^{-1/2}(\Gamma^N)$ and $f \in H^{1/2}(\Gamma^D)$ that satisfies

$$\Delta\Phi = 0 \qquad \text{in } \Omega \tag{A.15a}$$
$$\Phi = f \qquad \text{on } \Gamma^D \tag{A.15b}$$
$$\nabla\Phi \cdot n = g \qquad \text{on } \Gamma^N \tag{A.15c}$$

(B) Find a function $\Phi \in H^1(\Omega)$ such that for a $\Phi_0 \in H^1(\Omega)$ that satisfies $\gamma\Phi_0 = f$ on Γ^D and $a(u,v) = (\nabla u, \nabla v)$

$$\Phi - \Phi_0 \in H^1_{0,\Gamma^D} \tag{A.16a}$$
$$a(\Phi - \Phi_0, v) = -a(\Phi_0, v) + \langle g, v \rangle_\Gamma \qquad \forall \in H^1_{0,\Gamma^D}. \tag{A.16b}$$

It is noted that $f \in H^{1/2}(\Gamma^D)$ so there exists a $\Phi_0 \in H^1(\Omega)$ such that $\gamma_0 \Phi_0 = f$ on Γ^D. Consider now problem (B) and define $l : v \to -a(\Phi_0, v) + \langle g, v \rangle_\Gamma$. Clearly $u, v \to (\nabla u, \nabla v)$ is continuous and $a(v, v) = \|\nabla v\|_{0,\Omega}^2 = |v|_{1,\Omega}^2 \geq c_1 \|v\|_{1,\Omega}^2$ where the last inequality follows from the Poincaré-Friedrichs' inequality. With the identification of V with H_{0,Γ^D}^1 and the observation that $\|l\|_{V'} \leq \|v\|_V + \|g\|_{-\frac{1}{2},\Gamma}$ and therefore $l \in V'$, the conditions of the Lax-Milgram theorem are satisfied and a unique $\Phi - \Phi_0 \in H_{0,\Gamma^D}^1$ exists.

(B) $\to$ (A) Clearly (A.16a) implies (A.15b) and from Eq. (A.16b) follows by partial integration that

$$a(\Phi, v) = (\nabla\Phi, \nabla v) = (-\Delta u, v) = 0 \quad \forall v \in \overline{D(\Omega)}. \tag{A.17}$$

and therefore $\Delta\Phi = 0$ in $H^{-1}(\Omega)$ which implies (A.15a). Eq. (A.16b) therefore also implies

$$\begin{aligned}
a(\nabla\Phi, \nabla v) &= \langle g, v \rangle_\Gamma \quad \forall v \in H_{0,\Gamma^D}^1 & (A.18) \\
&= \langle g, v \rangle_\Gamma + (\Delta\Phi, v) \quad \forall v \in H_{0,\Gamma^D}^1. & (A.19)
\end{aligned}$$

Application of the extended Green's formula results in

$$\langle g, v \rangle_\Gamma = \langle \nabla\Phi \cdot n \rangle_\Gamma \quad \forall v \in H^1(0, \Gamma^D) \tag{A.20}$$

and thus $\nabla\Phi \cdot n = g$ in $H^{-1/2}(\Gamma)$ on Γ^N.

(A) $\to$ (B) Multiplication of (A.15a) by $v \in H^1(\Omega)$ and application of the extended Green's formula, and substitution of the conditions results directly in (B)).

Appendix B

Details of the numerical methods

B.1 Lagrangian interpolation and simplex coordinates

In this appendix some details are given on the construction of the triangular elements and interpolation functions that were used for the approximation of the Laplace boundary value problem. Furthermore, the formulas for the exact computation of the necessary integrals over arbitrary triangles are given. More details on these methods and techniques can be found in e.g. Silvester & Ferrari (1983) and Zienkiewicz & Taylor (1994).

Simplex coordinates

First of all simplex coordinates are introduced as the new coordinates for a triangular element. An arbitrary point inside a triangle divides the triangle into three areas. Given the areas of these three sub-triangles with respect to the total area uniquely defines the original point. These area fractions thus define a new set of coordinates called simplex coordinates. The resulting relation between original and simplex coordinates can be written as (A is the total area of the triangle, and (x_i, y_i) is the coordinate of the i'th vertex):

$$\begin{bmatrix} \xi_1 \\ \xi_2 \\ \xi_3 \end{bmatrix} = \frac{1}{2A} \begin{bmatrix} x_2 y_3 - x_3 y_2 & y_2 - y_3 & x_3 - x_2 \\ x_3 y_1 - x_1 y_3 & y_3 - y_1 & x_1 - x_3 \\ x_1 y_2 - x_2 y_1 & y_1 - y_2 & x_2 - x_1 \end{bmatrix} \begin{bmatrix} 1 \\ x \\ y \end{bmatrix}. \tag{B.1}$$
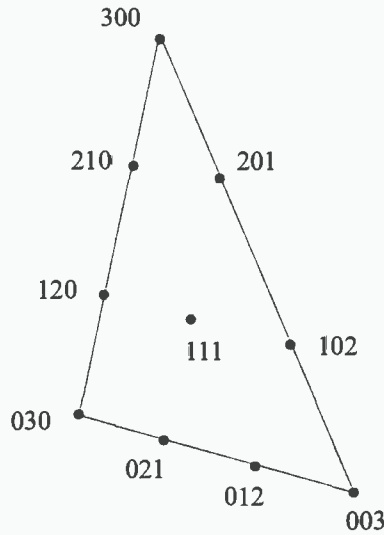
Figure B.1: *Example of natural numbering of regular spaced nodes on a triangle. The node number triple (ijk) can be identified with the simplex coordinates $(\xi_1, \xi_2, \xi_3) = (i/3, j/3, k/3)$*

Simplex coordinates are by definition bounded and define a natural numbering for regular spaced nodes on the triangle (see Fig. B.1). The node number ijk can be identified with the simplex coordinates $(\xi_1, \xi_2, \xi_3) = (i/n, j/n, k/n)$ where $n = i+j+k$. The next section describes how to construct a polynomial interpolation function on the triangle.

Piecewise polynomials on a triangle

Consider the auxiliary polynomials $R_m(n, \xi)$ which are polynomial functions of degree m having m equi-spaced nodes to the left of $\xi = m/n$ and none to the right and has unity value at $\xi = m/n$.

$$R_m(n, \xi) = \prod_{k=0}^{m-1} \frac{\xi - k/n}{m/n - k/n} = \frac{1}{m!} \prod_{k=0}^{m-1} (n\xi - k) \tag{B.2}$$

On a triangular simplex the following interpolation functions are defined

$$N_{ijk} = R_i(n, \xi_1) R_j(n.\xi_2) R_k(n, \xi_3) \tag{B.3}$$

with $i + j + k = n$. These interpolation formulae are just the classical Lagrange interpolation polynomials, expressed with respect to the simplex coordinates of the triangle. The function N_{ijk} defines a polynomial of degree n which is zero in all nodes $klm \neq ijk$. If sufficient and well-placed nodes are available, a polynomial

function of arbitrary order can be represented on the triangle as a combination of these interpolation polynomials.

The nodes are regularly spaced and a node lying on a side can belong to another triangle. When the same technique for constructing polynomials is used for all elements, the polynomial approximations on different neighboring triangles are continuous over triangle sides. A global base function N_i associated with a node x_i consists of the union of all local polynomials N_{ijk} associated with the node x_i on triangles to which x_i belongs and is zero everywhere else.

Evaluation of $a(N_i, N_j)$

From Eq. 2.40 one can observe that the main effort in the construction of the linear system to approximate the solution of the boundary value problem is the evaluation of the integrals

$$a(N_m, N_n) = \int_\Omega \nabla N_m \cdot \nabla N_n \, d\Omega = \sum_{K_e \in \mathcal{T}} \int_{K_e} \nabla N_m \cdot \nabla N_m \, d\Omega, \qquad \text{(B.4)}$$

where N_n and N_m are the global base functions. An element-by-element computational procedure is used which first determines all the integrals for all base functions per element and than adds the values to the appropriate integral. It is therefore sufficient to consider the evaluation of the integral

$$S_{mn} = \int_{K_e} \nabla N_m \cdot \nabla N_n \, d\Omega. \qquad \text{(B.5)}$$

Transformation to simplex coordinates of a partial derivative of N results in

$$\partial_x N_m = \sum_{i=1}^3 \frac{\partial N_m}{\partial \xi_i} \frac{\partial \xi_i}{\partial x}. \qquad \text{(B.6)}$$

and the derivatives of the simplex coordinates with respect to the spatial coordinates can be expressed as

$$\frac{\partial \xi_i}{\partial x} = \frac{y_{i+1} - y_{i-1}}{2A}, \qquad \text{(B.7a)}$$

$$\frac{\partial \xi_i}{\partial y} = \frac{x_{i-1} - x_{i+1}}{2A}. \qquad \text{(B.7b)}$$

where the indices are numbered modulo 3; so $y_{i+1} = y_1$ iff $i = 3$. Introducing the definition of

$$b_i = y_{i+1} - y_{i-1} \qquad \text{(B.8a)}$$

$$c_i = x_{i-1} - xi + 1 \qquad \text{(B.8b)}$$

and substitution of Eq. (B.6)-(B.8b) in Eq. (B.5) results in

$$S_{mn} = \frac{1}{4A^2} \sum_{i=1}^{3} \sum_{j=1}^{3} (b_i b_j + c_i c_j) \int \frac{\partial N_m}{\partial \xi_i} \frac{\partial N_n}{\partial \xi_j}. \tag{B.9}$$

For any triangle the following identities hold

$$b_i b_j + c_i c_j = -2A \cot \theta_k \qquad i \neq j \tag{B.10a}$$

$$b_i^2 + c_i^2 = 2A(\cot \theta_j + \cot \theta_k \qquad i = j \tag{B.10b}$$

where θ_k is the angle of the vertex with number $k \neq i \neq j$. Using Eq. (B.10a)-(B.10b) , Eq.(B.9 reduces to

$$S_{mn} = \sum_{k=1}^{3} \cot \theta_k \int \left(\frac{\partial N_m}{\partial \xi_{k+1}} - \frac{\partial N_m}{\partial \xi_{k-1}} \right) \left(\frac{\partial N_n}{\partial \xi_{k+1}} - \frac{\partial N_n}{\partial \xi_{k-1}} \right) \frac{d\Omega}{2A} = \sum_{k=1}^{3} Q_{mn}^{(k)} \cot \theta_k \tag{B.11}$$

The matrices $Q^{(}k)$ on the right hand side are now completely determined in terms of simplex coordinates and can thus be computed once and for all using the interpolation formula (B.3). When the resulting expression for S_{mn} is written only integrals $I(i, j, k)$ remain hat consist of products of powers of the simplex coordinates multiplied by some constant. Transforming the integral I from Cartesian coordinates to simplex coordinates results in

$$I(i, j, k) = \int \xi_1^i \xi_2^j \xi_3^k \frac{d\Omega}{2A} = 2 \int_0^1 \int_0^{1-\xi_1} \xi_1^i \xi_2^j (1 - \xi_1 - \xi_2)^k \, d\xi_1 \, d\xi_2. \tag{B.12}$$

The area A is canceled against the determinant of the Jacobian of the transformation. The integral (B.12) can be evaluated exactly by performing partial integrations. Partial integration with respect to ξ_2 evaluates as

$$I(i, j, k) = \frac{2k}{j+1} \int_0^1 \int_0^{1-\xi_1} \xi_1^i \xi_2^{j+1} (1 - \xi_1 - \xi_2)^{k-1} \, d\xi_1 \, d\xi_2 = \frac{k}{j+1} I(i, j+1, k-1), \tag{B.13}$$

so

$$I(i, j, k) = \frac{k!}{(j+k)!/j!} I(i, j+k, 0) = \frac{j!k!}{(j+k)!} I(i, j+k, 0). \tag{B.14}$$

If the partial integrations are then performed with respect to ξ_1, Eq.(B.14) reduces to

$$I(i, j, k) = \frac{i!j!k!}{(i+j+k)!} I(0, i+j+k, 0). \tag{B.15}$$

The right hand side in Eq. (B.15) can be evaluated exactly as

$$I(0, i+j+k, 0) = 2 \int_0^1 \int_0^{1-\xi_1} \xi_2^{i+j+k} \, d\xi_2 \, d, \xi_1 = \frac{1}{i+j+k+1} \frac{1}{i+j+k+2}. \tag{B.16}$$

which leads to the exact evaluation of the integral (B.12) as

$$I(i, j, k) = \frac{i!j!k!2}{(i + j + k + 2)!} \tag{B.17}$$

After the matrices $Q^{(k)}$ are tabulated and stored all integral evaluations up to any order can be evaluated exactly. Remark that $Q_{mn}^{(k)}$ does only need to be computed for a single k and that the other follow from permutations of the vertices.

B.2   Modified Butcher tables

Consider the ODE

$$q_t = f(q, t) \tag{B.18}$$

Given the time step ΔT we denote $q_n = q(n\Delta t)$. The explicit s stage Runge-Kutta integration method determines the value of the vector q_{n+1} using the formula

$$q_{n+1} = q_n + \Delta t_n \sum_{i=1}^{s} b_i f_i$$

where

$$
\begin{aligned}
f_1 &= f(q_n, t_n) \\
f_i &= f\left(q_n + \Delta t_n \sum_{j=1}^{i-1} a_{ij} f_j, \ t_n + c_i \Delta t_n\right)
\end{aligned}
$$

The following modified Butcher tables (from Dormand (1996) and van der Houwen & Sommeijer (1972)) give the coefficients a, b and c for three different explicit RK methods (RK44M, RK45M and RK35D).

c_i	a_{ij}			b_i
0				11/72
2/5	2/5			25/72
3/5	−3/20	3/4		25/72
1	19/44	−15/44	10/11	11/72

Table B.1: *Butcher array of RK44M: a 4'th order 4 stage RK method with minimised principal error and dispersive order 4.*

c_i	a_{ij}				b_i
0					13/96
1/5	1/5				0
2/5	0	2/5			25/48
4/5	6/5	−12/5	2		25/96
1	−17/8	5	−5/2	5/8	1/12

Table B.2: *Butcher array of RK45M: a 4'th order 5 stage RK method with minimised principal error and dispersive order 4.*

c_i	a_{ij}				b_i
0					−5/56
1/5	1/5				25/112
1/3	0	1/3			75/112
1/2	0	0	1/2		−1/14
1	0	0	0	1	15/56

Table B.3: *Butcher array of RK35D: a 3'rd order, 5 stage RK method with dispersive order 8.*

Appendix C

Nondimensional wave quantities

In most chapters of this thesis the wave quantities are given in non-dimensionalised form. Length scales are normalised with the depth h and time scales are normalised using the gravitational acceleration as $\sqrt{h/g}$. For reference and look-up purposes the graph below is provided. The graph relates the different non-dimensionalised wave quantities ω, λ, T, c and c_g according to the dispersion relation for linear waves Eq. (3.7). The values for the group velocity c_g and the phase velocity c have been scaled by a factor (4π and 2π respectively). For the SMB ($h = 5$ [m]) one obtains quick estimates by approximating $\sqrt{h/g} \approx 7/10$ and $\sqrt{gh} \approx 7$. For the HT ($h = 3.6$ [m]) these values are $\sqrt{h/g} \approx 6/10$ and $\sqrt{gh} \approx 6$.
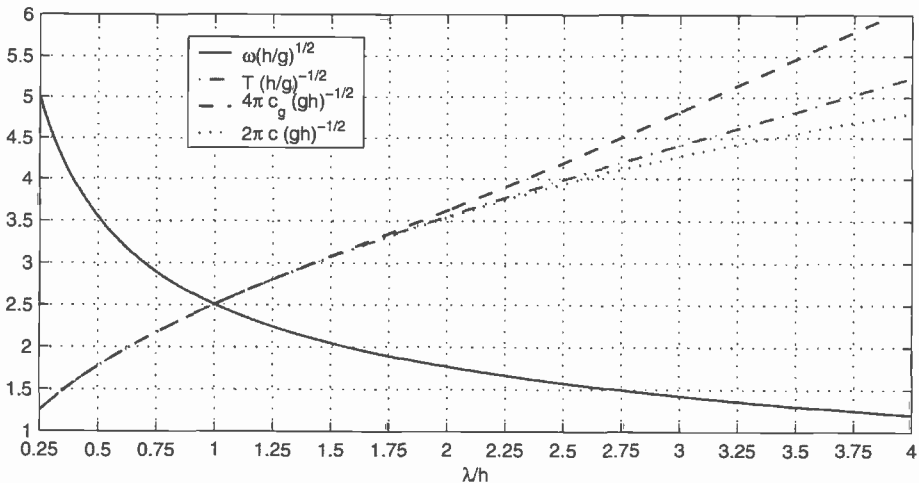
Bibliography

AKHMEDIEV, N. N. & ANKIEWICZ, A. 1997 *Solitons, Nonlinear Pulses and Beams*. London: Chapman & Hall.

AXELSSON, O. & BARKER, A. 1984 *Finite element solution of boundary value problems. Theory and computation*. Academic Press, Orlando.

AXELSSON, O. & VASSILEVSKI, P. S. 1990 Algebraic multilevel preconditioning methods, II. *SIAM J. Numer. Anal.* **27**, 1569–1590.

BABUSKA, I., STROUBOULIS, T., UPADHYAY, C. S. & GANGARAJ, S. K. 1996 Computer-based proof of the existence of superconvergent points in the Finite Element Method. Superconvergence of the derivatives in Finite Element Solutions of Laplace's, Poison's and the elasticity equations. *Numer. Methods for PDE's* **12**, 347–392.

BAKER, G. R., MERION, D. J. & ORSZAG, S. A. 1981 Applications of a generalized vortex method to nonlinear free-surface flows. In *3rd Int. Conf. Num. Ship Hydrodyn*, pp. 179–191. Paris.

BANNER, M. L. 1998 On the determination of the onset of breaking for modulating surface gravity water waves. *J. Fluid Mech.* **367**, 107–137.

BARNES, T. & PEREGRINE, D. H. 1995 Wave groups approaching a beach: Full irrotational flow computations. In *Proc. Coast. Dyn. '95, Abstracts*, pp. 7–8. Gdanks, Poland.

BARRET, R., BERRY, M., CHAN, T. F., DEMMEL, J., DONATO, J., DONGARRA, J., EIJKHOUT, V., POZO, R., ROMINE, C. & VAN DER VORST, H. 1994 *Templates for the Solution of Linear Systems: Building Blocks for Iterative Methods*. Philadelphia, PA: SIAM.

BELYTSCHKO, T., KRONGAUZ, Y. K., FLEMING, D. & KRYSL, P. 1996 Meshless methods: An overview and recent developments. *Comput. Meth. Appl. Mech. Engrg.* **139**, 3–47.

BENJAMIN, T. B. 1967 Instability of periodic wave trains in nonlinear dispersive systems. *Proc. Roy. Soc. A* **299**, 59.

BENJAMIN, T. B., BONA, J. L. & MAHONY, J. J. 1972 Model equations for long waves in non-linear dispersive systems. *Phil. Trans. Roy. Soc. London* **A 272**, 47–78.

BENJAMIN, T. B. & FEIR, J. E. 1967 The disintegration of wave trains in deep water. Part 1. Theory. *J. Fluid Mech.* **27**, 417.

BIÉSEL, F. 1951 Etude théorique d'un type d'appareil á houle. *La Houille Blanche* **6**, 152–165.

BÖRGERS, C. & WIDLUND, O. B. 1990 On finite element domain imbedding methods. *SIAM J. Numer. Anal.* **27**, 963–978.

BOS, K. J. 1997 Passieve golfdempers, vooronderzoek fysisch modelonderzoek. *Tech. Rep.* 3262. Delft Hydraulics.

BOUSSINESQ, M. J. 1872 Théorie des ondes et des remous qui se propagent le long d'un canal rectangulaire horizontal, en communiquant au liquide contenu dans ce canal des vitesses sensiblement pareilles de la surface au fond. *Journal de Mathématique Pures et Appliquées, deuxi'eme série* **17**, 55–108.

BRAESS, H. & WRIGGERS, P. 2000 Arbitrary Lagrangian Eulerian Finite Element analysis of free surface flow. *Comput. Methods Appl. Mech. Engrg* **190**, 95–109.

BREZZI, F. & FORTIN, M. 1991 *Mixed and Hybrid Finite Element Methods. Springer Series in Computational Mathematics* 15. Springer-Verlag.

BROER, L. J. F. 1974 On the Hamiltonian theory of surface waves. *Appl. Sci. Res.* **29**, 430.

BROEZE, J. 1993 Numerical modelling of nonlinear free surface waves with a 3d panel method. PhD thesis, University Of Twente.

BRORSEN, M. & LARSEN, J. 1987 Source generation of nonlinear gravity waves with the boundary integral equation method. *Coastal Eng.* **11**, 93–113.

BRYANT, P. J. 1974 Stability of periodic waves in shallow water. *J. Fluid Mech.* **66**, 81–96.

BRYANT, P. J. 1982 Modulation by swell of waves on the ocean. *J. Fluid Mech.* **114**, 443.

CAI, X., LANGTANGEN, H. P., NIELSEN, B. F. & TVEITO, A. 1998 A finite element method for fully nonlinear water waves. *J. Comput. Phys.* **143**, 544–568.

CAPONI, E. A., SAFFMAN, P. G. & YUEN, H. C. 1982 Instability and confined chaos in a nonlinear dispersive wave system. *Phys. Fluids* **25**, 2159.

CELEBI, M. S., KIM, M. H. & BECK, R. F. 1998 Fully nonlinear 3-d numerical wave tank simulation. *J. Ship Res.* **42**, 33–45.

CHAN, R. K. C. 1977 Finite difference simulation of the planar motion of a ship. In *Proc. 2nd Int. Conf. Num. Ship Hydrodyn.* (ed. J. W. *et al.*), pp. 39–51. Berkeley: Univ. Extension Publ.

CHANG, Q., JIA, E. & SUN, W. 1999 Difference scheme's for solving the generalized nonlinear Schrödinger equation. *J. Comput. Phys.* **148**, 397–415.

CHAPMAN, D. C. 1985 Numerical treatment of cross-shelf open boundaries in a barotropic coastal ocean model. *J. Phys. Oceanogr.* **15**, 1060–1075.

CHU, V. H. & MEI, C. C. 1970 On slowly varying Stokes waves. *J. Fluid Mech.* **41**, 873.

CHU, V. H. & MEI, C. C. 1971 The nonlinear evolution of Stokes waves in deep water. *J. Fluid Mech.* **47**, 337.

CLÉMENT, A. H. 1996 Coupling of two absorbing boundary conditions for 2d time-domain simulations of free surface gravity waves. *J. Comp. Phys.* **126**, 139–151.

CLÉMENT, A. H. 1999*a* Benchmark test cases for numerical wave absorption: 1st workshop of ISOPE Numerical Wave Tank group. *Proc. 9th ISOPE Conf.* **4**, 266–288.

CLÉMENT, A. H. 1999*b* The spinning dipole: An efficient unsymmetrical numerical wavemaker. In *Proc. 14th Int. Workshop on Water Waves and Floating Bodies*. Port Huron, Michigan.

COINTE, R. & BOUDET, L. 1991 Nonlinear and breaking waves in bichromatic wave-trains: Experiments and numerical simulations. In *Proc. 1st ISOPE Conf.*, pp. 517–522. ISOPE.

COLIN, T., DIAS, F. & GHIDAGLIA, J. 1995 On rotational effects in the modulations of weakly nonlinear water waves over finite depth. *Eur. J. Mech. B/Fluids* **14**, 775–793.

CONNOR, J. J. & BREBBIA, C. A. 1976 *Finite Element Techniques for Fluid Flow*. Newnes-Butterworths.

CRAWFORD, D. R., LAKE, B. M., SAFFMAN, P. G. & YUEN, H. C. 1991 Stability of weakly
nonlinear deep-water waves in two and three dimensions. *J. Fluid Mech.* **105**, 177–179.

VAN DAALEN, E. 1993 Studies of water waves and floating bodies. PhD thesis, University of
Twente.

VAN DAALEN, E. F. G., VAN GROESEN, E. & PUDJAPRASETYA, S. R. 1997 BEM-numerics
and KdV-model analysis for solitary wave split-up. *Computational Mechanics* **19**, 179–187.

VAN DAALEN, E. F. G., KLEEFSMAN, K. M. T., GERRITS, J., LUTH, H. R. & VELDMAN,
A. E. P. 1999 Anti roll tank simulations with a Volume of Fluid (VOF) based Navier
Stokes solver. In *Proc. 7th Int. Conf. Numerical Ship Hydrodynamics.* Nantes, France.

DALRYMPLE, R., LOSADA, M. & MARTIN, P. 1991 Reflection and transmission from porous
structures under oblique wave attack. *J. Fluid Mech.* **224**, 625–644.

DAVEY, A. 1972 The propagation of weak nonlinear waves. *J. Fluid Mech.* **53**, 769.

DAVEY, A. & STEWARTSON, K. 1974 On three-dimensional packets of surface waves. *Proc.
Roy. Soc. Lond.* **A338**, 101–110.

DEBNATH, L. 1994 *Nonlinear Water Waves.* San Diego, CA: Academic Press.

DELFT, W. L. 1955 Golfdempend talud N.S.P. verslag modelonderzoek. *Tech. Rep.* M490.
Waterloopkundig Laboratorium Delft.

DESILVA, S. J., GUENTHER, R. B. & HUDSPETH, R. T. 1996 Irregular points in 2-d free
surface flows with surface tension for the wavemaker boundary value problem. *Appl. Ocean
Res.* **18**, 293–302.

DIAS, F. & KHARIF, C. 1999 Nonlinear gravity and capillary-gravity waves. *Annu. Rev.
Fluid Mech.* **31**, 301–346.

DINGEMANS, M. W. 1997a *Water Wave Propagation over Uneven Bottoms, Part 1 - Linear
Wave Propagation, Advanced Series on Ocean Engineering,* vol. 13. World Scientific.

DINGEMANS, M. W. 1997b *Water wave propagation over uneven bottoms, Part 2 - Non-linear
Wave Propagation, Advanced Series on Ocean Engineering,* vol. 13. World Scientific.

DOLD, J. W. 1992 An efficient surface-integral algorithm applied to unsteady gravity waves.
J. Comput. Phys. **103**, 90–115.

DOMMERMUTH, D. G. & YUE, D. K. P. 1987 Numerical simulation of nonlinear axisym-
metric flows with a free surface. *J. Fluid Mech.* **178**, 195–219.

DOMMERMUTH, D. G., YUE, D. K. P., LIN, W. M., RAPP, R. J., CHAN, E. S. & MELVILLE,
W. K. 1988 Deep-water plunging breakers: A comparison between potential theory and
experiments. *J. Fluid Mech.* **189**, 423–442.

DORMAND, J. R. 1996 *Numerical Methods for Differential Equations.* CRC Press.

DUCLOS, G., CLÉMENT, A. H. & CHATRY, G. 2000 Absorption of outgoing waves in a
numerical wave tank using a self-adaptive boundary condition. In *Proc. 10'th Int. Offshore
Polar Engin. Conf.,* pp. 185–192. Seatle, USA: ISOPE.

DYSTHE, K. B. 1979 Note on a modification to the nonlinear Schrödinger equation for
application to deep water waves. *Proc. Roy. Soc. A* **369**, 105.

FEIR, J. E. 1967 Discussion: some results from wave pulse experiments. *Proc. Roy. Soc. A*
299, 54.

FEKKEN, G., VELDMAN, A. E. P. & BUCHNER, B. 1999 Simulation of green water loading
using the Navier Stokes equations. In *Proc. 7th Int. Conf. Numerical Ship Hydrodynamics.*
Nantes, France.

FERMI, E., PASTA, J. & ULAM, S. 1940 Studies of nonlinear problems. *Collected Papers of
Enrico Fermi, University of Chicago Press,1962* **2**, 978.

FERZIGER, J. H. & PERIĆ, M. 1999 *Computational Methods for Fluid Dynamics*, 2nd edn. Springer-Verlag.

FONTAINE, E., LANDRINI, M. & TULIN, M. P. 2000 On modelling the post breaking phase: Splashing. In *Proc. 15'th Int. Workshop on Water Waves and Floating Bodies* (ed. T. Miloh & G. Zilman), pp. 51–54.

GIRAULT, V. & RAVIART, P.-A. 1981 *Finite Element Approximation of the Navier-Stokes Equations*. Berlin, Germany: Springer-Verlag.

GIVOLI, D. 1992 *Numerical Methods for Problems in Infinite Domains*. Amsterdam, The Netherlands: Elsevier.

GIVOLI, D. & VIGDERGAUZ, S. 1994 Artificial boundary conditions for 2d problems in geophysics. *Comp. Meth. Appl. Mech. Eng.* **110**, 87–102.

GRAIG, W. & SULEM, C. 1993 Numerical simulation of gravity waves. *J. Comp. Phys.* **108**, 73–83.

GREAVES, D. M., BORTHWICK, A. G. L., WU, G. X. & EATOCK TAYLOR, R. 1997 A moving boundary finite element method for fully nonlinear wave simulations. *Journal of Ship Research* **41** (3), 181–194.

GRILLI, S. T. & HORILLO, J. 1997 Numerical generation and absorption of fully nonlinear periodic waves. *J. Eng. Mech.* **123**, 1060–1069.

GRILLI, S. T., SKOURUP, J. & SVENDSEN, I. A. 1989 An efficient boundary element method for nonlinear water waves. *Engineering Analysis with Boundary Elements* **6** (2), 97–107.

GRIMSHAW, R. 1970 The solitary wave in water of variable depth. *J. Fluid Mech.* **42**, 639–656.

VAN GROESEN, E. 1998 Wave groups in uni-directional surface wave models. *J. Eng. Math.* **34**, 215–226.

VAN GROESEN, E., CAHYONO, E. & SURYANTO, A. 2001 Uni-directional models for narrow banded and broad banded pulse propagation in second order nonlinear media. In *Int. Symp. On Modern Optics and its Applications*. Bandung, Indonesia: ITB, for review in Journal of Nonlinear Optical Physics and Materials.

GUIGNARD, S., GRILLI, S. T., MARCER, R. & REY, V. 1999 Computation of shoaling and breaking waves in nearshore area's by the coupling of BEM and VOF methods. In *Proc. 9th ISOPE conf.*, pp. 304–309.

DE HAAS, P. C. A. 1997 Numerical simulation of nonlinear water waves using a panel method: decomposition and applications. PhD thesis, University of Twente.

DE HAAS, P. C. A., DINGEMANS, M. W. & KLOPMAN, G. 1997 Simulation of propagating nonlinear wave groups. In *Proceedings of the 25th international conference on Coastal Engineering*, pp. 165–174. Orlando.

DE HAAS, P. C. A. & ZANDBERGEN, P. J. 1996 The application of domain decomposition to time-domain computations of non-linear water waves with a panel method. *Journal of Computational Physics* **129**, 332–344.

HAMMACK, J. L. & HENDERSON, D. M. 1993 Resonant interactions among surface water waves. *Ann. Rev. Fluid Mech.* **25**, 55.

HARLOW, F. 1964 The Particle-in-Cell computing method for fluid dynamics. *Methods of Computational Science* **3**, 313–343.

HASIMOTO, H. & ONO, H. 1972 Nonlinear modulation of gravity waves. *J. Phys. Soc. Japan* **33**, 805.

HASSELMANN, K. 1963 On the nonlinear energy transfer in a gravity-wave spectrum. Part 2. Conservation theorems; wave-particle analogy; irreversibility. *J. Fluid Mech.* **15**, 273.

HASSELMANN, K. 1967 Discussion. *Proc. Roy. Soc. A* **299**, 76.

HAVELOCK, T. H. 1929 Forced surface waves on water. *Philos. Mag., series F* **8**, 569–576.

HIRT, C., AMSDEN, A. & COOK, J. 1974 An Arbitrary Lagrangian Eulerian computing method for all speeds. *J. Comput. Phys.* **14**, 227–253.

HÖRMANDER, L. 1971 Fourier integral operators I. *Acta Math.* **127**, 79–183.

VAN DER HOUWEN, P. J. & SOMMEIJER, B. P. 1972 Explicit Runge-Kutta (-Nyström) methods with reduced phase errors for computing oscillating solutions,. *SIAM J. Numer. Anal.* **24**, 595–617.

HUIJSMANS, R. H. M., WESTHUIS, J. & BALLAST, A. 1999 Non-linear diffraction around heeled ship sections. In *Proc. 9th Int. Offshore and Polar Eng. Conf.*, pp. 651–657.

IOAKIMIDIS, N. 1988 A unified Riemann-Hilbert approach to the analytical determination of zeros of sectionally analytic functions. *J. Math. Anal. Applic.* **129**, 134–141.

DE ST. Q. ISAACSON, M. 1982 Nonlinear wave effects on fixed and floating bodies. *J. Fluid Mech.* **120**, 267–281.

ISRAELI, M. & ORSZAG, S. A. 1981 Approximation of radiation boundary conditions. *J. Comp. Phys.* **41**, 115–135.

JANSSEN, P. A. E. M. 1981 Modulational instability and the Fermi-Pasta-Ulam recurrence. *Phys. Fluids* pp. 23–36.

JOHNSON, R. S. 1973 On the development of a solitary wave moving over an uneven bottom. *Proc. Cambridge Phil. Soc.* **73**, 183–203.

JOHNSON, R. S. 1994 Solitary wave, soliton and shelf evolution over variable depth. *J. Fluid Mech.* **276**, 125–138.

KAPSENBERG, G. 1999 Reflection measurements of beaches to be used for the new seakeeping and offshore facilities. *Tech. Rep.* 85504-1-HT. MARIN.

KAWOHL, B. 1980 On nonlinear mixed boundary value problems for second order elliptic differential equations on domains with corners. *Proc. Roy. Soc. Edinburg* **87A**, 35–51.

KEADY, G. & NORBURY, J. 1978 On the existence theory for irrotational water waves. *Proc. Cambr. Phil. Soc.* **83**, 137.

KIM, C. H., CLÉMENT, A. H. & TANIZAWA, K. 1999 Recent research and development of numerical wave tanks - a review. *Int. J. of Offshore and Polar Eng.* **9**, 241–256.

KORTEWEG, D. J. & DE VRIES, G. 1895 On the change of form of long waves advancing in a rectangular canal, and on a new type of long stationary waves. *Phil. Mag. and J. of Science* **39**, 422–443.

KRASITSKII, V. P. 1994 On reduced equations in the hamiltonian theory of weakly nonlinear surface waves. *J. Fluid Mech.* **272**, 1.

KRASOVSKII, Y. P. 1960 On the theory of steady waves of not small amplitude (in russian). *Dokl. Akad. Nauk SSSR* **130**, 1237.

KRASOVSKII, Y. P. 1961 On the theory of permanent waves of finite amplitude (in russian). *Zh. vychisl. Mat. mat. Fiz.* **1**, 836.

LAKE, B. M. & YUEN, H. C. 1977 A note on some nonlinear water-wave experiments and the comparison of data with theory. *J. Fluid Mech.* **83**, 75.

LAKE, B. M., YUEN, H. C., RUNGALDIER, H. & FERGUSON, W. E. 1977 Nonlinear deep water waves: theory and experiment. II. Evolution of a continuous wavetrain. *J. Fluid Mech.* **83**, 49.

LAMB, S. H. 1932 *Hydrodynamics*, 1995th edn. Cambridge University Press.

VAN LAMMEREN, W. P. A. & VOSSERS, G. 1957 New facilities of the netherlands ship model basin at wageningen. *Tech. Rep.* 141a. N.S.M.B.

LANDAU, L. D. & LIFSHITZ, E. M. 1987 *Fluid Mechanics*, 2nd edn. Oxford: Butterworth-Heinemann.

LANDRINI, M., OSHRI, O., WASEDA, T. & TULIN, M. P. 1998 Long time evolution of gravity wave systems. In *13th International Workshop on Water Waves and Floating Bodies* (ed. A. Hermans), p. 75.

LEVI-CIVITA, T. 1925 Détermination rigoureuse des ondes permanentes d'ampleur finie. *Math. Ann.* **93**, 264.

LIGHTHILL, M. J. 1965 Contributions to the theory of waves in nonlinear dispersive systems. *J. Inst. Math. Appl.* **1**, 269.

LIGHTHILL, M. J. 1967 Some special cases treated by the Whitham theory. *Proc. Roy. Soc. A* **299**, 28.

LO, E. & MEI, C. C. 1985 A numerical study of water-wave modulation based on a higher-order nonlinear Schrödinger equation. *J. Fluid Mech.* **150**, 395.

LONGUET-HIGGINS, M. 1978a The instabilities of gravity waves of finite amplitude in deep water. I. Superharmonics. *Proc. R. Soc. London Ser. A* **360**, 471–488.

LONGUET-HIGGINS, M. 1978b The instabilities of gravity waves of finite amplitude in deep water. II. Subharmonics. *Proc. R. Soc. London Ser. A* **360**, 489–505.

LONGUET-HIGGINS, M. S. & COKELET, E. D. 1976 The deformation of steep surface waves on water - I. a numerical method of computation. *Proceedings of The Royal Society London* **A350**, 233–251.

MANSARD, E. P. D. & FUNKE, E. R. 1980 The measurement of incident and reflected spectra using a least squares method. In *Proc. 17th Coastal Engrg. Conf.*, pp. 154–172.

MARGERETHA, H., VAN GROESEN, E. & HUIJSMANS, R. H. M. 2001 Experiments and model equations for generating waves on top of currents. *Journal of Applied Ocean Research* p. submitted.

MCIVER, P. 1998 The dispersion relation and eigenfunction expansions for water waves in a porous structure. *J. Eng. Math.* **34**, 319–334.

MELVILLE, W. K. 1982 The instability and breaking of deepwater waves. *J.Fluid Mech.* **115**, 165.

MILES, J. W. 1977 On Hamilton's principle for surface waves. *J. Fluid Mech.* **83**, 153.

MOLIN, B. 1999 Numerical and physical wavetanks: Making them fit. Twenty-Second Georg Weinblum Memorial Lecture, IWWWFB, Michigan.

MONAGHAN, J. 1992 Smoothed Particle Hydrodynamics. *Annu. Rev. Astron. Astrophys.* **30**, 543–574.

MONAGHAN, J. 1994 Simulating free sruface flows with SPH. *J. Comput. Phys.* **110**, 399–406.

MOUBAYED, W. I. & WILLIAMS, A. N. 1994 Second-order bichromatic waves produced by a generic planar wavemaker in a two-dimensional wave flume. *J. Fluids Struc.* **8**, 73–92.

NABORS, K., KORSMEYER, F. T., LEIGHTON, F. T. & WHITE, J. 1994 Preconditioned, adaptive, multipole -accelerated iterative methods for three-dimensional first-kind integral equations of potential theory. *SIAM, J. Sci. Comp.* **15** (3), 713–735.

NESTEGÅRD, A. 1994 Comparative study of fully non-linear wave simulation programs. *Tech. Rep.* 94-2041. Det Norske Veritas, Oslo.

OHYAMA, T. & HSU, J. R. C. 1995 Nonlinear wave effect on the slow drift motion of a floating body. *Appl. Ocean Res.* **17**, 349–362.

ORLANSKI, I. 1976 A simple boundary condition for unbounded hyperbolic flows. *J. Comp. Physics* **21**, 251–269.

OTTO, R. M. 1999 A study on the intersection point of free surface and wavemaker. *Tech. Rep.*. University of Twente, tWAIO report Computational Mechanics.

PELINOVSKY, E., TALIPOVA, T., KIT, E. & ETIAN, O. 1999 Nonlinear wave packet evolution in shallow water. In *Int. Symp. Prog. Coast. Eng. Ocean.*, pp. 53–62. Seoul, Korea.

PHILLIPS, O. M. 1981 Wave interactions-the evolution of an idea. *J. Fluid Mech.* **106**, 215–227.

POWER, H. & WROBEL, L. C. 1995 *Boundary Integral Methods in Fluid Mechanics.* Southampton, UK: Computational Mechanics Publications.

PUDJAPRASETYA, S. R. 1996 Evolution of waves above slightly varying bottom: a variational approach. PhD thesis, University of Twente.

RIENECKER, M. M. & FENTON, J. D. 1981 A fourier approximation method for steady water waves. *J. Fluid Mech.* **104**, 119–137.

ROACH, P. J. 1994 Perspective: A method for uniform reporting of grid refinement studies. *ASME J, Fluids Engrg.* **116**, 405–413.

ROBERTSON, I. & SHERWIN, S. 1999 Stabilisation and simulation of nonlinear free surface flow using high order algorithms. MARNET-CFD First Workshop, barcelona.

ROMATE, J. E. 1989 The numerical simulation of nonlinear gravity waves in three dimensions using a higher order panel method. PhD thesis, Twente University.

ROMATE, J. E. 1992 Absorbing boundary conditions for free surface waves. *J. Comp. Phys.* **99**, 135/145.

ROMATE, J. E. 1998 Analytical aspects of an artificial damping layer for the wave equation. *Tech. Rep.* 1454. Twente University.

SCARDOVELLI, R. & ZALESKI, S. 1999 Direct numerical simulation of free-surface and interfacial flow. *Annu. Rev. Fluid Mech.* **31**, 567–603.

SCHÄFFER, H. A. 1996 Second-Order wavemaker theory for irregular waves. *Ocean Engng.* **23**, 47–88.

SCHÄFFER, H. A. & KLOPMAN, G. 2000 Review of multidirectional active wave absorption methods. *J. Waterway, Port, Coastal and Ocean Engin.* **126**, 88–97.

SCHWARTZ, L. & FENTON, J. D. 1982 Strongly non-linear waves. *Annu. Rev. Fluid Mech.* **14**, 39–60.

SCORPIO, S., BECK, R. & KORSMEYER, F. T. National Academic Press, Washington DC Nonlinear water wave computations using a multipole accelerated, desingularized method. In *21'st Symposium on Naval Hydrodynamics*, pp. 64–73. National Research Council.

SHEMER, L., KIT, E., JIAO, H. & ETIAN, O. 1998 Experiments on nonlinear wave groups in intermediate water depth. *Journal of Waterway, Port, Coastal and Ocean Engineering* nov/dec, 320–327.

SIEREVOGEL, L. 1998 Time-domain calculations of ship motions. PhD thesis, Delft University.

SILVESTER, P. P. & FERRARI, R. L. 1983 *Finite Elements for Electrical Engineers.* Cambridge: University Press.

SMITH, B., BJÖRSTAD, P. & GROPP, W. 1997 *Domain Decomposition: Parallel Multilevel Methods for Elliptic Partial Differential Equations.* Cambridge University Press.

SOMMERFELD, A. 1949 *Partial Differential Equations in Physics*. New York, USA: Academic Press.

STANSBERG, C. 1997 On the nonlinear behaviour of ocean wave groups. *proc. Waves '97* **2**, 1227–1241.

STIASNIE, M. 1983 Note on the modified Nonlinear Schrödinger Equation for deep water waves. *Wave Motion* **5**, 10–15.

STOKES, G. G. 1847 On the theory of oscillatory waves. *Trans. Cambr. Phil. Soc.* **8**, 441.

STRUIK, D. J. 1926 Détermination rigoureuse des ondes irrotationelles périodiques dans un canal a profondeur finie. *Math. Ann.* **95**, 595.

STUART, J. T. & DIPARMA, R. C. 1978 The Eckhaus and Benjamin-Feir resonance mechanisms. *Proc. Roy. Soc. A* **362**, 27.

SU, M. Y. 1982 Evolution of groups of gravity waves with moderate to high steepness. *Phys. Fluids* **25**, 2167–2174.

SURYANTO, A. 1999 Model for reflection properties of hydrodynamic beaches. Master's thesis, Twente University.

SURYANTO, A., VAN GROESEN, E. & HOEKSTRA, H. 2001 Deformation of modulated wave groups in third order nonlinear media. *Optical and Quantum Electronics* p. to appear in april.

TAHA, T. R. & ABLOWITZ, M. J. 1984 Analytical and numerical aspects of certain nonlinear evolution equations. II Numerical, Nonlinear Schrödinger equation. *J. Comput. Phys.* **55**, 203.

TANIZAWA, K. 2000 Benchmark test 1999. In *Proc. Conf. ISOPE 2000*.

TANIZAWA, K. & SAWADA, H. 1990 A numerical method for nonlinear simulation of 2-d body motions in waves by means of BEM (in japanese). *J. Soc. Naval Architects Japan* **168**, 221–226.

TAYLOR, P. H. & OHL, C. O. G. 1999 Focussed wave groups II: Global nonlinearity and resonant wave-wave interactions. In *Proc. OMAE '99*. ASME.

TOLAND, J. F. 1978 On the Existence of a Wave of Greatest Height and Stoke's Conjecture. *Proc. Roy. Soc. A* **363**, 469.

TRULSEN, K. 1989 Frequency downshift through self modulation and breaking, a numerical study. Master's thesis, Univeristy of Tromso.

TSAI, W. & YUE, D. K. P. 1996 Computation of non linear free surface flows. *Annu. Rev. Fluid Mech.* **28**, 249–278.

TULIN, M. P. & WASEDA, T. 1999 Laboratory observations of wave group evolution, including breaking effects. *J. Fluid Mech.* **378**, 197.

TURKEL, E. 1999 Preconditioning techniques in computational fluid dynamics. *Ann. Rev. Fluid. Mech.* **31**, 385–416.

UNVERDI, S. & TRYGGAVSON, G. 1992 Computation of multifluid flow. *Physica D* **60**, 70–83.

URSELL, F., DEAN, R. G. & YU, Y. S. 1960 Forced small-amplitude water waves: A comparison of theory and experiment. *J. Fluid Mech.* **7**, 33–52.

VINJE, T. & BREVIG, P. 1981 Numerical simulation of breaking wave. In *Proc. 3rd Int. Conf. On Finite Elements in Water Resources*, pp. 196–210. Oxford: Univ. of Mississippi, vol. 5.

WANG, P., YAO, Y. & TULIN, M. P. 1995 An efficient numerical tank for non-linear water waves, based on the multi-subdomain approach with BEM. *International journal for numerical method in fluids* **20**, 1315–1336.

WASHIZU, K. 1982 Some applications of finite element techniques to nonlinear free surface fluid flow problems. In *Finite Element Flow Analysis, Proc. 4'th Int. Symp. On FEM in Flow Problems*, pp. 3–15.

WESTHUIS, J. 1997 Measuring and modelling of non linear water waves. Master's thesis, University of Twente.

WESTHUIS, J. 2000 Approximate analytic solutions and numerical wave tank results for the reflection coefficients of a class of numerical beaches. In *Proc. of the 10th ISOPE conference*.

WESTHUIS, J. & ANDONOWATI, A. 1998 Applying FEM in numerically solving the two dimensional free surface water wave equations. In *13th IWWW&FB* (ed. A. Hermans), p. 171. Alphen a/d Rijn, the Netherlands.

WESTHUIS, J., VAN GROESEN, E. & HUIJSMANS, R. H. M. 2000 Long time evolution of unstable bichromatic waves. In *15th IWWW&FB* (ed. T. Miloh). Caesarea, Israël.

WESTHUIS, J. & HUIJSMANS, R. H. M. 1999 Unstable bichromatic wave groups: Experimental results. *Tech. Rep.* 15309.152. MARIN.

WHITHAM, G. B. 1965 A general approach to linear and non-linear dispersive waves using a Lagrangian. *J. Fluid Mech.* **22**, 273.

WHITTAKER, E. T. & WATSON, G. N. 1965 *A course of modern Analysis*. Cambridge University Press.

WU, G. X. & EATOCK TAYLOR, R. 1994 Finite element analysis of two-dimensional nonlinear transient water waves. *Appl. Ocean Res.* **16**, 363–372.

WU, G. X. & EATOCK TAYLOR, R. 1995 Time stepping solutions of the two-dimensional nonlinear wave radiation problem. *Ocean Engineering* **22** (8), 785–798.

YEUNG, R. W. 1982 Numerical methods in free-surface flows. *Ann. Rev. Fluid Mech.* **14**, 395–442.

YUEN, H. C. & FERGUSON, W. E. 1978*a* Fermi-Pasta-Ulam recurrence in the two-space dimensional nonlinear Schrödinger equation. *Phys. Fluids* **21**, 2116.

YUEN, H. C. & FERGUSON, W. E. 1978*b* Relationship between Benjamin-Feir instability and recurrence in the nonlinear Schrödinger equation. *Phys. Fluids* **21(8)**, 1275.

YUEN, H. C. & LAKE, B. M. 1975 Nonlinear deep water waves: theory and experiment. *Phys. Fluids* **18**, 956.

YUEN, H. C. & LAKE, B. M. 1980 Instabilities of waves on deep water. *Ann. Rev. Fluid Mech.* **12**, 303.

YUEN, H. C. & LAKE, B. M. 1982 Nonlinear dynamics of deep-water gravity waves. *Adv. Appl. Mech.* **22**, 67.

ZAKHAROV, V. E. 1968 Stability of periodic waves of finite amplitude on the surface of a deep fluid. *Sov. Phys. J. Appl. Mech. Tech. Phys.* **4**, 86.

ZAKHAROV, V. E. & SHABAT, A. B. 1972 Exact theory of two-dimensional self-focussing and one-dimensional self-modulating waves in nonlinear media. *Sov. Phys. J. Exp. Theor. Phys.* **34**, 62.

ZIENKIEWICZ, O. C. & TAYLOR, R. L. 1994 *The Finite Element Method*. McGraw-Hill.

ZIENKIEWICZ, O. C. & ZHU, J. Z. 1992 The superconvergent patch recovery and a postiori error estimates. Part 1: The recovery technique. *Int. J. Numer. Methods Eng.* **33**, 1331–1364.

Index

Samenvatting

Dit proefschrift beschrijft het onderzoek naar een numeriek algoritme ten behoeve van de simulatie van niet-lineaire golven in een model basin. Het doel van het onderzoek is om een algoritme voor de deterministische en nauwkeurige simulatie van twee dimensionale golven in een model basin te ontwikkelen, te implementeren en haar eigenschappen te onderzoeken. Het golfveld dat gesimuleerd moet worden kan uit golven van verschillende golflengte bestaan en het algoritme dient efficiënt genoeg te zijn opdat het toegepast kan worden in praktische situaties. Het ontwikkelde schema is gebaseerd op een combinatie drie methoden: Runge-Kutta (voor de tijds integratie), Eindige Elementen (voor het randwaarde probleem) en Eindige Differenties (voor de benadering van de snelheden). Het schema is verder verfijnd en onderzocht met behulp van verschillende modellen voor de opwekking, de voortplanting en de absorptie van golven.

De nauwkeurigheid en stabiliteit van het numerieke schema zijn onderzocht en de fout in de dispersie-eigenschappen is bepaald voor verschillende discretisatie-parameters. Er is gevonden dat stabiele, tot op tweede orde nauwkeurige, discretisaties kunnen worden geconstrueerd op basis van eerste orde Eindige Elementen en tweede orde Eindige Differenties. De resultaten laten ook zien dat een globale projectie methode waarbij Eindige Elementen gebruikt worden om de snelheden te benaderen, tot niet stabiele discretisaties leidt. Door een geschikte keuze van een gridparameter, kan de numerieke fout in de voortplantingssnelheid van een golf met een kleine amplitude tot nul worden gereduceerd doordat verschillende fouttermen in de benadering elkaar opheffen. Voor golven met een breed spectrum wordt een fysisch relevante foutmaat ingevoerd en het discrete massa- en energie-behoud wordt onderzocht. Het blijkt dat de geringe afname in de massa en energie voornamelijk wordt bepaald door de benadering van de geometrie, maar dat deze afname voldoende klein is om nauwkeurige simulaties uit te voeren.

Verschillende methodes voor de opwekking van golven, gebaseerd op modellen van fysische golfopwekkers en op numerieke goflopwekkings modellen, worden geintroduceerd en onderzocht. De discrete overdrachtsfunctie tussen de slag van de golfopwekker en de amplitude van de golf wordt bepaald en hieruit volgt dat de numerieke golfopwekker een iets hogere golf opwekt dan verwacht kan worden op basis van exacte analyse. Er werd ook waargenomen dat voor sommige toepassingen met een specifieke

combinatie van geometrie en numeriek grid, de discretisatie niet stabiel kan zijn.

Metingen die gedaan zijn aan de reflectie eigenschappen van de stranden in een model basin worden vergeleken met een numerieke golfabsorptie methode. Deze numerieke golf absorptie methode bestaat uit de gecombineerde toepassing van demping door het aanbrengen van kunstmatige atmosferische drukverschillen, het oprekken van het numerieke grid in de voortplantingsrichting en het toepassen van een Sommerfeld randconditie op de uitstroom wand. De demping zorgt voor strikte afname van de golf energie en de combinatie zorgt voor effectieve absorptie voor een breed interval aan frequenties. Reflectie coëfficiënten lager dan 0.7 % zijn haalbaar ten koste van een relatief geringe hoeveelheid extra rekentijd. Er wordt ook aangetoond dat door een bepaalde combinatie van parameters van de numerieke absorptie methode, een redelijke benadering van de gemeten reflectie eigenschappen van de kunstmatige stranden in het model basin kan worden gerealiseerd.

Verder is het algoritme toegepast op enkele vergelijkende testen die de validiteit van de numerieke resultaten bevestigen. Ook zijn de numerieke resultaten direct vergeleken met metingen hetgeen goede overeenstemming liet zien.

Als een apart behandeld onderwerp is met behulp van de onderzochte methode de evolutie van niet lineaire golfgroepen bekeken. Een studie naar de voortplanting van een begrensde golfgroep over een bodemprofiel en het uiteen vallen van de samenhang in een begrensde golftrein worden gepresenteerd. Daarnaast wordt een uitgebreide studie, waarbij talrijke metingen en simulaties betrokken zijn, naar de ontwikkeling van een bichromatische golfgroep besproken. De efficiëntie van het numerieke algoritme zorgt dat de dynamica van deze golven kan worden onderzocht over zeer grote afstanden. Het uit elkaar vallen van de begrensde golftrein wordt waargenomen, maar de verwachte splitsing in afzonderlijke groepen kan niet worden bevestigd. Onderzoek naar de evolutie van een begrensde (NLS-soliton) golfgroep over een bodemprofiel laat zien dat de begrensde solitaire groepsstructuur overgaat in een golftrein. Verder wordt waargenomen dat tijdens dit proces een lange vrije solitaire golf word gegenereerd die voor de golftrein uitsnelt. De evolutie van een bichromatische golf laat zien dat het ruimtelijk verloop van het golf spectrum een periodiek patroon vertoont hetgeen wijst op FPU herhaling. Een toepasselijke schaling wordt gevonden die de verhouding tussen de amplitude en het frequentie verschil relateert aan de geobserveerde periode. Verdere beschouwing van de evolutie van de omhullende van de golf laat een splitsing van de oorspronkelijke omhullende in twee afzonderlijk herkenbare golfomhullende zien. De wisselwerking tussen de omhullende van deze twee groepen laat twee kwalitatief verschillende patronen zien die beide wijzen op een herhaling van de evolutie.

Curriculum Vitae

The author of this thesis was born on the 23'rd of August in 1973 in Amsterdam. After primary school in Maarssenbroek (1978-1981) and Brussels (1982-1985), he completed secondary school education (Gymnasium) at the Comenius College in Hilversum in 1991. From 1991 until 1997 he studied Applied Mathematics at the University of Twente and was an active member of a student society and co-founder of a not-for-profit consultancy organisation. In 1996 he conducted a practical research assignment at the Gerechterlijk Laboratorium (Forensic Laboratory) in Rijswijk on 'Image Restoration using Variational Methods'. This work was supervised by prof.dr.ir. E.C.W. van Groesen who also supervised the authors Master's Thesis on 'Measuring and Modelling of Nonlinear Water Waves', which was conducted at MARIN, Wageningen. After obtaining his Master's degree in 1997, the author started in the spring of 1997 doing research to obtain a PhD degree under supervision of his promotor prof. van Groesen. This research work was carried out at MARIN under supervision of dr.ir. R.H.M. Huijsmans. In the summer of 1997 he was one of the co-ordinators of a two-month research workshop on aspects of fluid dynamics at the Institute Technology Bandung (ITB), Indonesia. During the PhD research he was involved in several other research activities at MARIN and attended several summerschools at the University of Twente. From 1998 until 2001 the author was president of a student alumni society and from March 2000 until May 2001 he was editor of ITW-nieuws (Newsletter for Industrial and Applied Mathematics). After the public defence of his dissertation in May 2001, he and his girlfriend will travel around the world until May 2002.